

# Ground Vibration from Underground Railways: How Simplifying Assumptions Limit Prediction Accuracy



A dissertation submitted to the University of Cambridge  
for the degree of Doctor of Philosophy

by

Simon William Jones

Churchill College

September 2010



# Preface

The work detailed herein was performed at the University of Cambridge, Department of Engineering between October 2007 and September 2010. The project was suggested by my research supervisor, Dr Hugh Hunt. I am very grateful to him for his continued support throughout my time at Cambridge as a teacher, a mentor and a friend.

My thanks also go to my advisor Professor Robin Langley for his help and encouragement with the project, especially for his insights and advice while working on the final section of Chapter 4. Finally, I would like to thank all those who supported me over the last three years including my parents, brother and sister-in-law, and my friends here and back home. Without you I would have given up before I even started.

I would like to acknowledge the generous financial support of the Gates Cambridge Trust, Natural Sciences and Engineering Research Council of Canada, the Edmonton Churchill Scholarship, and the Alberta Scholarship Program. I am also grateful to the Department of Engineering and Churchill College for supporting my attendance at numerous conferences.

I declare that except for commonly understood and accepted ideas or where specific reference has been made to the work of others, this dissertation is the result of my own work and includes nothing which is the outcome of work done in collaboration. This dissertation is approximately 45,000 words in length and contains 95 figures.

Simon Jones  
Cambridge  
September 2010

“Traditional scientific method has always been at the very best 20-20 hindsight. It’s good for seeing where you’ve been. It’s good for testing the truth of what you think you know, but it can’t tell you where you ought to go....The solutions all are simple – after you have arrived at them. But they’re simple only when you know already what they are.”

- Robert M. Pirsig

# Abstract

Noise and vibration from underground railways is a documented disturbance to individuals living or working near subways. Much work has been done to understand and simulate the dynamic interactions between the train, track, tunnel and soil resulting in numerical models which can predict ground-borne vibration around the tunnels and at the soil surface. However, all such numerical models rely on simplifying assumptions to make the problems tractable: soil is assumed homogenous, tunnels are assumed long and straight, the soil is assumed to be in perfect contact with the tunnel, etc. This dissertation is concerned with quantifying the uncertainty associated with some of these simplifying assumptions to provide a better estimation of the prediction accuracy when numerical models are used for “real world” applications.

The first section investigates the effect of voids at the tunnel-soil interface. The Pipe-in-Pipe model is extended to allow finite-sized voids at the interface by deriving the discrete transfer functions for the tunnel and soil from the continuous solution. The results suggest that relatively small voids can significantly affect the rms velocity predictions at higher frequencies (100-200Hz) and moderately effect predictions at lower frequencies (15-100Hz). The results are also found to be sensitive to void length and void sector angle.

The second section investigates issues associated with assuming the soil is homogeneous: the effect of inclined soil layers; the effect of a subsiding soil layer; the effect of soil inhomogeneity. The thin-layer method approach is utilized as its semi-analytical formulation allows for accurate predictions with relatively short run times. The results from the three investigations suggest that slight inclination of soil layers and typical levels of soil inhomogeneity can result in significant variation in surface results compared to the homogeneous assumption. The geometric effect of a subsiding soil layer has a less significant effect on surface vibration.

The findings from this study suggest that employing simplifying assumptions for the cases investigated can reasonably result in uncertainty bands of  $\pm 5$ dB. Considering all the simplifying assumptions used in numerical models of ground vibration from underground railways it would not be unreasonable to conclude that the prediction accuracy for such a model may be limited to  $\pm 10$ dB.

# Contents

|          |   |           |
|----------|---|-----------|
| <b>1</b> | <b>Introduction</b>                                     | <b>1</b>  |
| 1.1      | Motivation for Research . . . . .                       | 1         |
| 1.2      | Objectives of the Research . . . . .                    | 2         |
| 1.3      | Outline of the Thesis . . . . .                         | 4         |
| <b>2</b> | <b>Literature Review</b>                                | <b>5</b>  |
| 2.1      | Impact of Vibration . . . . .                           | 5         |
| 2.2      | Vibration Excitation Mechanisms . . . . .               | 8         |
| 2.3      | Simulating Ground Vibration . . . . .                   | 10        |
| 2.3.1    | Basics of Wave Propagation . . . . .                    | 10        |
| 2.3.2    | Analytical Methods . . . . .                            | 13        |
| 2.3.3    | Numerical Methods . . . . .                             | 15        |
| 2.3.3.1  | Finite Difference Method . . . . .                      | 15        |
| 2.3.3.2  | Finite Element Method . . . . .                         | 16        |
| 2.3.3.3  | Boundary Element Method . . . . .                       | 18        |
| 2.3.3.4  | Coupled BE-FE Models . . . . .                          | 19        |
| 2.3.4    | Semi-Analytical Method . . . . .                        | 20        |
| 2.3.4.1  | Thin-Layer Method . . . . .                             | 21        |
| 2.3.4.2  | Pipe-in-Pipe Method . . . . .                           | 21        |
| 2.4      | Uncertainty in Modelling Assumptions . . . . .          | 22        |
| 2.4.1    | Inclined Layers . . . . .                               | 24        |
| 2.4.2    | Soil Subsidence . . . . .                               | 26        |
| 2.4.3    | Soil Inhomogeneity . . . . .                            | 28        |
| 2.5      | Conclusions . . . . .                                   | 30        |
| <b>3</b> | <b>Voides at the Tunnel-Soil Interface</b>              | <b>32</b> |
| 3.1      | Model Description . . . . .                             | 33        |
| 3.1.1    | Overview of PiP Method . . . . .                        | 33        |
| 3.1.2    | Inclusion of Floating-Slab Track in PiP Model . . . . . | 37        |

|          |  |           |
|----------|--|-----------|
| 3.1.3    | Discrete Tunnel-Soil Interface . . . . .                               | 42        |
| 3.1.4    | Including a Void in the Discrete Model . . . . .                       | 46        |
| 3.1.5    | Response due to a Moving Load . . . . .                                | 48        |
| 3.2      | Validation of discrete model against PiP . . . . .                     | 50        |
| 3.3      | Simulating voids using the discrete model . . . . .                    | 55        |
| 3.3.1    | Results for Void Length Sensitivity Study . . . . .                    | 59        |
| 3.3.2    | Results for Void Sector Angle Sensitivity Study . . . . .              | 67        |
| 3.4      | Conclusions . . . . .  | 73        |
| <b>4</b> | <b>The Homogeneous Soil Assumption</b>                                 | <b>75</b> |
| 4.1      | The Thin-Layer Method . . . . .  | 75        |
| 4.1.1    | Semi-infinite region open to the right . . . . .                       | 76        |
| 4.1.2    | Semi-infinite region open to the left . . . . .                        | 83        |
| 4.1.3    | Thin-Layer Method Extension for Layered Media on a Halfspace . . . . . | 85        |
| 4.1.4    | Thin-Layer Method Extension for Hyperelements . . . . .                | 89        |
| 4.1.5    | Constructing a model using the thin-layer method . . . . .             | 94        |
| 4.1.6    | TLM Model Validation for a Surface Load . . . . .                      | 95        |
| 4.1.6.1  | Analytical Solution to a Layered Halfspace . . . . .                   | 96        |
| 4.1.6.2  | Boundary Element Model for a Layered Halfspace . . . . .               | 97        |
| 4.1.6.3  | TLM Model for a Layered Halfspace . . . . .                            | 98        |
| 4.1.6.4  | Model Comparison Results . . . . .                                     | 99        |
| 4.1.7    | TLM Model Validation for Tunnel Loading . . . . .                      | 106       |
| 4.1.7.1  | The Equivalent Internal Source Method . . . . .                        | 106       |
| 4.1.7.2  | Validation Model for Tunnel Loading . . . . .                          | 109       |
| 4.1.7.3  | Results of the Tunnel-Loading Validation Case . . . . .                | 111       |
| 4.1.7.4  | The Effect of Layer Wavespeed . . . . .                                | 115       |
| 4.2      | The Effect of Inclined Soil Layers . . . . .                           | 119       |
| 4.2.1    | Inclined Layer Model . . . . .   | 119       |
| 4.2.2    | Effect of Inclined Layer on Surface Vibration . . . . .                | 121       |
| 4.2.3    | Sensitivity to Inclination Angle . . . . .                             | 125       |
| 4.3      | Subsiding Soil Layers . . . . .  | 131       |
| 4.3.1    | TLM Model of Subsiding Layer . . . . .                                 | 133       |
| 4.3.2    | Surface Response of Subsiding Layer Model . . . . .                    | 135       |
| 4.4      | Inhomogeneous Soils . . . . .  | 138       |
| 4.4.1    | Modelling Local Variation in Soil Properties . . . . .                 | 139       |
| 4.4.2    | Numerical Model of Stochastic Soil Variation . . . . .                 | 143       |
| 4.4.3    | Surface Response of Stochastic Soil Model . . . . .                    | 146       |

---

|          |  |            |
|----------|--|------------|
| 4.5      | Conclusions . . . . .  | 150        |
| <b>5</b> | <b>Conclusions and Further Work</b>  | <b>153</b> |
| 5.1      | Conclusions . . . . .  | 153        |
| 5.2      | Recommendations for Further Work . . . . .                                 | 155        |
| <b>A</b> | <b>Useful Relations and Material Damping</b>                               | <b>157</b> |
| <b>B</b> | <b>Thomas Algorithm</b>  | <b>159</b> |
| <b>C</b> | <b>Green's Functions for a Layered Halfspace</b>                           | <b>161</b> |
| C.1      | Homogeneous Halfspace . . . . .  | 161        |
| C.1.1    | Load acting in the $x$ -direction . . . . .                                | 162        |
| C.1.2    | Load acting in the $z$ -direction . . . . .                                | 163        |
| C.2      | Homogeneous Layer . . . . .  | 163        |
| C.2.1    | Load acting in the $x$ -direction . . . . .                                | 164        |
| C.2.2    | Load acting in the $z$ -direction . . . . .                                | 166        |
| C.3      | Layered Halfspace - Surface Load, Observation at Layer Interface . . . . . | 168        |
| C.4      | Layered Halfspace - Buried Load, Observation at Surface . . . . .          | 169        |
| <b>D</b> | <b>Boundary Element Method</b>   | <b>173</b> |
| D.1      | Fundamental Solution and the Boundary Integral Formulation . . . . .       | 174        |
| D.2      | Numerical Solution . . . . .   | 176        |
| <b>E</b> | <b>The PiP Derivation in 3D</b>  | <b>179</b> |
| E.1      | 3D Cylindrical Shell Equations . . . . .                                   | 179        |
| E.2      | 3D Elastic Continuum Equations . . . . .                                   | 184        |
| E.3      | The Coupled Tunnel-Soil Equations . . . . .                                | 192        |
| <b>F</b> | <b>The PiP Derivation in 2D Plane-Strain</b>                               | <b>195</b> |
| F.1      | Thin-shell and Continuum Equations in 2D Plane-Strain . . . . .            | 196        |
| F.1.1    | The Coupled Tunnel-Soil Equations in 2D Plane-Strain . . . . .             | 200        |
| <b>G</b> | <b>Equivalent internal source method</b>                                   | <b>201</b> |
| G.1      | Fullspace core-in-pipe model . . . . .                                     | 203        |
|          | <b>References</b>  | <b>220</b> |



# List of Figures

|      |   |    |
|------|---|----|
| 2.1  | Deflection bowls created by quasi-static train load . . . . .                         | 8  |
| 2.2  | Examples of wheel and rail discontinuities . . . . .                                  | 9  |
| 2.3  | Depiction of P-wave and SV-wave . . . . .   | 11 |
| 2.4  | Depiction of Rayleigh wave . . . . .  | 11 |
| 2.5  | The use of absorbing boundaries in FEA . . . . .                                      | 17 |
| 2.6  | Example of a coupled BE-FE model . . . . .  | 19 |
| 2.7  | Simplifying assumptions for soil layering . . . . .                                   | 24 |
| 2.8  | Schematic of the major soil horizons . . . . .  | 25 |
| 2.9  | Examples soil stratification . . . . .  | 26 |
| 2.10 | Development of surface subsidence trough due to tunneling . . . . .                   | 27 |
| 2.11 | Schematic of soil inhomogeneity . . . . .   | 28 |
|      |   |    |
| 3.1  | Void at the tunnel-soil interface . . . . .   | 33 |
| 3.2  | Schematic of pipe-in-pipe arrangement . . . . .                                       | 34 |
| 3.3  | Depiction of ring modes . . . . .   | 35 |
| 3.4  | Underground railway cut-away showing floating-slab track . . . . .                    | 37 |
| 3.5  | Floating-slab track on tunnel invert . . . . .  | 38 |
| 3.6  | Total force transmission of floating-slab track . . . . .                             | 42 |
| 3.7  | Circumferential discretization of tunnel . . . . .                                    | 43 |
| 3.8  | Wavenumber parameter convergence testing for free-tunnel model . . . . .              | 46 |
| 3.9  | Schematic of simple vehicle model . . . . .   | 48 |
| 3.10 | Geometric parameters for model and mesh . . . . .                                     | 51 |
| 3.11 | Observation plane centered over the tunnel at height 15m . . . . .                    | 52 |
| 3.12 | Validation of discrete model against PiP at 15Hz . . . . .                            | 53 |
| 3.13 | Validation of discrete model against PiP at 200Hz . . . . .                           | 54 |
| 3.14 | Discrete model response for no void at various third-octave frequency bands . . . . . | 56 |
| 3.15 | Difference between discrete model and PiP response for no void . . . . .              | 57 |
| 3.16 | Schematic showing void at tunnel-soil interface . . . . .                             | 58 |

|      |   |     |
|------|---|-----|
| 3.17 | Close-up schematic of the void showing the void parameters . . . . .  | 59  |
| 3.18 | Response to moving load for VA-3 case . . . . .   | 60  |
| 3.19 | Moving load insertion gain for VA-3 case . . . . .  | 61  |
| 3.20 | Insertion gain for VL-1 . . . . .   | 62  |
| 3.21 | Insertion gain for VL-2 . . . . .   | 63  |
| 3.22 | Insertion gain for VL-3 . . . . .   | 64  |
| 3.23 | Insertion gain for VL-4 . . . . .   | 65  |
| 3.24 | Vertical response of tunnel at 25Hz and 160Hz . . . . .   | 67  |
| 3.25 | Insertion gain for VA-1 . . . . .   | 69  |
| 3.26 | Insertion gain for VA-2 . . . . .   | 70  |
| 3.27 | Insertion gain for VA-3 . . . . .   | 71  |
| 3.28 | Insertion gain for VA-4 . . . . .   | 72  |
| 3.29 | Radial response of tunnel at $x=0$ for 25Hz and 160Hz . . . . .   | 73  |
| 4.1  | Typical layered region (plane-strain) . . . . .   | 77  |
| 4.2  | Matrix addition scheme . . . . .  | 81  |
| 4.3  | Layered region $R$ on a homogeneous halfspace (plane-strain) . . . . .  | 86  |
| 4.4  | Matrix addition scheme including halfspace submatrix . . . . .  | 88  |
| 4.5  | Tunnel in semi-infinite TLM model . . . . .   | 90  |
| 4.6  | Layered finite region on rigid bedrock (plane-strain) . . . . .   | 90  |
| 4.7  | Schematic of a basic TLM model simulating a homogeneous halfspace . . . . .                                   | 94  |
| 4.8  | Matrix addition scheme for thin-layer elements . . . . .  | 95  |
| 4.9  | Validation case schematic . . . . .   | 96  |
| 4.10 | BE model of validation case . . . . .   | 98  |
| 4.11 | TLM model of validation case . . . . .  | 98  |
| 4.12 | Frequency Response Functions (FRF) at the observation point . . . . .   | 100 |
| 4.13 | Horizontal rms velocity along layer interface due to surface load . . . . .                                   | 104 |
| 4.14 | Vertical rms velocity along layer interface due to surface load . . . . .                                     | 105 |
| 4.15 | Depiction of wave energy reflection by halfspace elements due to relatively<br>large incident angle . . . . . | 106 |
| 4.16 | Equivalent internal source arrangement . . . . .  | 107 |
| 4.17 | TLM model with equivalent internal source loading . . . . .   | 108 |
| 4.18 | Validation case for tunnel loading . . . . .  | 109 |
| 4.19 | Horizontal rms velocity along surface due to tunnel load . . . . .  | 112 |
| 4.20 | Vertical rms velocity along surface due to tunnel load . . . . .  | 113 |
| 4.21 | Effect of a horizontal layer's wavespeed on surface vibration . . . . .                                       | 115 |
| 4.22 | Displacement response due to tunnel impulse with horizontal layer . . . . .                                   | 117 |

---

|      |  |     |
|------|--|-----|
| 4.23 | Effect of layer wavespeed on wavefront . . . . .                                 | 118 |
| 4.24 | TLM representation of an inclined layer . . . . .                                | 120 |
| 4.25 | Inclined layer model showing model parameters . . . . .                          | 121 |
| 4.26 | Horizontal rms velocity due to tunnel load ( $3^\circ$ inclined layer) . . . . . | 122 |
| 4.27 | Vertical rms velocity due to tunnel load ( $3^\circ$ inclined layer) . . . . .   | 123 |
| 4.28 | Displacement response due to tunnel impulse with $3^\circ$ inclined layer . . .  | 126 |
| 4.29 | Effect of inclined layer wavespeed on wavefront . . . . .                        | 127 |
| 4.30 | Effect of layer inclination on surface rms velocity . . . . .                    | 128 |
| 4.31 | Depiction of Rayleigh wave energy loss for inclined layer in time-domain .       | 130 |
| 4.32 | Subsidence trough . . . . .  | 132 |
| 4.33 | Schematic of subsiding soil layer model . . . . .                                | 132 |
| 4.34 | Theoretical wave focusing of subsiding layer $\beta_E = 0.25$ . . . . .          | 133 |
| 4.35 | Close-up of subsidence section of TLM model . . . . .                            | 135 |
| 4.36 | Effect of a subsiding layer on horizontal surface rms velocity . . . . .         | 136 |
| 4.37 | Effect of a subsiding layer on vertical surface rms velocity . . . . .           | 137 |
| 4.38 | Parameters of homogeneous randomly varying soil profile . . . . .                | 139 |
| 4.39 | Soil Variation TLM model . . . . .   | 144 |
| 4.40 | Three realizations of soil elastic modulus . . . . .                             | 145 |
| 4.41 | Effect of a soil inhomogeneity on horizontal surface rms velocity . . . . .      | 147 |
| 4.42 | Effect of a soil inhomogeneity on vertical surface rms velocity . . . . .        | 148 |
| 4.43 | Displacement response in halfspace with inhomogeneous elastic modulus            | 151 |
|      |  |     |
| C.1  | Analytic halfspace . . . . .   | 161 |
| C.2  | Analytic solid layer . . . . .   | 164 |
| C.3  | Analytic layered halfspace . . . . .   | 168 |
| C.4  | Analytic layered halfspace - surface load . . . . .                              | 169 |
| C.5  | Analytic layered halfspace - buried load . . . . .                               | 170 |
|      |  |     |
| D.1  | Resultant displacement and traction vectors in fullspace . . . . .               | 175 |
| D.2  | Two-dimensional body divided into constant boundary elements . . . . .           | 176 |
|      |  |     |
| E.1  | The pipe-in-pipe arrangement . . . . .   | 180 |
| E.2  | Coordinate system for three-dimensional cylindrical shell . . . . .              | 181 |
| E.3  | Coordinate system for three-dimensional elastic continuum . . . . .              | 185 |
|      |  |     |
| G.1  | Equivalent internal source arrangement . . . . .                                 | 202 |
| G.2  | The core-in-pipe arrangement . . . . .   | 203 |

# List of Tables

|      |  |     |
|------|--|-----|
| 3.1  | Floating-slab track properties . . . . .                               | 38  |
| 3.2  | Third octave bands as defined by ISO R266 . . . . .                    | 50  |
| 3.3  | Soil model properties . . . . .  | 51  |
| 3.4  | Void parameters . . . . .  | 58  |
| 3.5  | Peak vertical insertion gain for void length study . . . . .           | 66  |
| 3.6  | Peak vertical insertion gain for void sector angle study . . . . .     | 68  |
|      |  |     |
| 4.1  | TLM validation model parameters . . . . .                              | 96  |
| 4.2  | Surface load validation case run times for BE and TLM models . . . . . | 102 |
| 4.3  | Floating-slab track properties . . . . .                               | 108 |
| 4.4  | Tunnel properties for validation case . . . . .                        | 110 |
| 4.5  | Tunnel load validation case run times for BE and TLM models . . . . .  | 111 |
| 4.6  | Inclined layer model properties . . . . .                              | 121 |
| 4.7  | Relative error between TLM and BE for 3° angle . . . . .               | 124 |
| 4.8  | Model properties for subsidence model . . . . .                        | 134 |
| 4.9  | Average soil properties for variability model . . . . .                | 144 |
| 4.10 | Average and peak values for 95% confidence region in dB rms . . . . .  | 149 |

# Chapter 1

## Introduction

The study of ground-borne vibration due to underground railways using numerical models requires a balance of model accuracy and efficiency to produce useful results in a reasonable time-frame. Assumptions made during the modeling process carry inherent uncertainty which is not well understood. This chapter acts to introduce the motivation for studying these uncertainties, to describe the objectives of the current research, and to provide an outline of the chapters comprising this dissertation.

### 1.1 Motivation for Research

Underground railways are proving to be an effective means of transporting large numbers of people in densely populated areas. Urban rail systems are increasingly promoted as developments in tunneling, rail and train technologies allow old lines to be upgraded and new lines to be constructed under existing city infrastructure. However ground-borne vibration from these underground railways is a major source of disturbance for individuals either working or living near subway tunnels, so much so that the European Union has prioritized research into this area.

The CONVURT project<sup>[1]</sup> (CONTRol of Vibrations from Underground Rail Traffic) was established as a grant funded project under the 5<sup>th</sup> Framework of the European

Union Programme for Research, Technological Development and Demonstration and ran from 2000 to 2003. A main goal of the consortium was to create innovative numerical models to predict ground-borne vibration. Although progress was made by the consortium during these three years and has been continued by the participants, there is still much research required to develop accurate models for predicting vibration.

## 1.2 Objectives of the Research

Researchers at the University of Cambridge, a member of the CONVURT consortium, have continued to study and develop numerical models for predicting ground vibration due to underground railways. A key objective of the research group is to develop quick and accurate models which can be run in minutes to give designers meaningful predictions to help streamline the design process. The goal is not to predict absolute vibration levels but to give estimates of the relative difference in ground vibration when attributes of the model are varied (e.g. soil properties, slab properties, tunnel geometry, etc.).

These types of numerical models are becoming accepted in both academic and industrial circles. In the following chapter a review of the literature gives many examples of different models currently in use which have been verified through experiment to varying extent. Unfortunately the numerical predictions and experimental findings often exhibit large differences over the frequency range of interest. This variation between simulation and reality can largely be attributed to simplifying assumptions used to reduce the complexity of the model and deal with unknowns in model parameters. A non-exhaustive list of issues which may require simplification includes:

- can the tunnel be modelled as an infinitely long, straight section or must changes in altitude and direction be included?
- what are the important excitation mechanisms between the train and the tunnel?
- what type of vehicle model is required?

- 
- is the tunnel in continuous contact with the soil or do voids form at the tunnel-soil interface?
  - what elements of the tunnel geometry need to be included in the model?
  - is the soil layered and if so are the layers horizontal, inclined, randomly distributed?
  - what are the soil properties and how do the properties of each major soil layer vary in the horizontal and vertical directions?
  - how does the water table affect ground vibration?
  - is accounting for subsidence or frost-heave important?
  - do other subway tunnels (used or vacant) significantly affect vibration levels?
  - how do building foundations affect vibration propagation?

As shown in the literature review, a common approach to dealing with these issues is to simplify: the tunnel is assumed infinitely long and periodic in the axial direction; the soil is assumed to be a horizontally layered halfspace with homogeneous material properties; additional tunnels and building foundations are neglected; the vehicle is simulated using moving point loads; etc. These sorts of assumptions are necessary to facilitate the development of models in a timely and economic manner which can be run in an acceptable length of time. However, these assumptions introduce inherent uncertainty which must be understood to provide designers with a more realistic measure of model accuracy and allow for more informed decisions when designing for vibration attenuation guidelines and vibration mitigating countermeasures.

The objective of the current research is to quantify the level of vibration prediction uncertainty associated with four simplifying assumptions including:

- assuming the the soil is in continuous contact with the tunnel - what is the effect of a void at the tunnel-soil interface?

- assuming the soil is layered horizontally - what is the effect of inclined soil layers?
- assuming the layers remain horizontal - what is the effect of a soil subsidence trough developing over the tunnel?
- assuming the soil layers are homogeneous - what is the effect of localized soil inhomogeneity?

### 1.3 Outline of the Thesis

The thesis is broken into three main chapters: a literature review of previous work relevant to this research, the development of three-dimensional model to simulate voids at the tunnel-soil interface, and the development of a two-dimensional semi-analytic model to simulate variation in soil homogeneity.

Chapter 2 is a literature review of previous work relating to ground-borne vibration from underground railways. Areas of interest include the impact of vibration on humans, vibration excitation mechanisms associated with rail traffic, and analytic and numerical methods for simulating ground vibration problems.

Chapter 3 investigates the effect of voids at the tunnel-soil interface on ground vibration due to underground railways. A three dimensional model is developed which simulates a railway tunnel with a void at the interface subjected to moving loads. The results for the case with no void are compared to an existing model to validate the new method. The effect of various void geometries are then investigated.

Chapter 4 introduces the thin-layer method as a means of modelling semi-infinite media, complete with element derivations. Predicted vibration for validation cases are compared to the analytical solution and boundary element predictions to verify the method. The chapter finishes with three sections investigating various simplifying assumptions related to soil homogeneity: inclined layers, soil subsidence, soil inhomogeneity.

Overall conclusions and ideas for potential future work are presented in Chapter 5.

# Chapter 2

## Literature Review

This chapter reviews previous work relevant to the current study. Sections include the impact of traffic induced vibration, railway excitation mechanisms, methods of simulating ground vibration, and physical evidence which calls into question the validity of some common simplifying modelling assumptions.

### 2.1 Impact of Vibration

Transportation noise and vibration has become a major source of disturbance and is predicted to worsen with increasing traffic and population densities. Numerous studies over the last thirty years show that inhabitants of urban areas who are subjected to air, road and rail traffic noise report high levels of annoyance and sleep disturbance which negatively impacts quality of life<sup>[28,30,87,102,129]</sup>. Sleep disturbance is considered one of the most serious effects of traffic noise<sup>[11]</sup>; experimental studies have found partial sleep deprivation (i.e. being woken through the night, increasing the time to fall asleep, reduction of hours asleep, etc.) has negative effects on performance and mood<sup>[21]</sup>. Some argue that prolonged exposure to such disturbance could have long-term health implications<sup>[27]</sup>.

More recent studies focus on correlating annoyance and sleep disturbance with quan-

tified noise levels and durations. Öhrström *et al.*<sup>[112]</sup> investigates how annoyance is affected by single and combined sound exposures from road and railway traffic. The findings suggest combined exposures from two sources, road and railway traffic, induce more extensive annoyance than noise from a single source. Furthermore, at sound levels between 51 and 60dB(A) the proportion of people annoyed by railway noise is higher than that annoyed by road traffic; above and below the 51-60dB(A) noise range the levels of annoyance are approximately the same. Griefahn *et al.*<sup>[49]</sup> report a similar finding while assessing the effects of noise emitted from road, rail and air traffic: higher annoyance levels for rail noise when compared to similar levels of aircraft and road traffic noise. These findings challenge earlier studies by Miedema *et al.*<sup>[101,102]</sup> which suggest air traffic causes more disturbance than other forms of traffic noise. This difference in the results could be attributed to the multiple ways people experience railway induced vibrations in the home which are not considered in the study (i.e. air-borne noise, vibratory motion of the floors, and re-radiated noise both in the room and from household objects). An investigation by Öhrström<sup>[111]</sup> suggests that the average level of annoyance was greater for vibration than for noise in houses up to 200 meters from the railway line.

Although airborne noise is largely negated when the trains run underground, vibration generated by the trains is propagated through the tunnel and soil to structures in close proximity to the tunnel<sup>[156]</sup>. The problem frequency range is between 15Hz to 200Hz<sup>[48,156]</sup>; higher frequencies are generally attenuated rapidly with distance along the transmission path through the soil<sup>[71]</sup>. Acceptable sinusoidal vibration levels for various living and working areas are listed in BS 6472<sup>[65]</sup> and depend on many factors such as time of day and building usage; BS ISO 2631<sup>[68]</sup> and BS EN ISO 8041<sup>[66]</sup> provide additional details on effects and measurement of human response to railway vibration. BS ISO 14837 Part 1<sup>[67]</sup> provides guidelines on the essential considerations associated with developing prediction models and shows in outline the stages to be observed for new or modified rail systems. Future parts of BS ISO 14837 are meant to quantify

acceptable vibration levels from underground railways but are unavailable at this time.

Walker and Chan<sup>[156]</sup> find that the degree of annoyance of noise and vibration from underground railways is related to the frequency spectrum, the level of the noise, and the background noise level. The empirical data used in the study shows consistent noise spectrums with broad peaks around 50Hz and/or 80Hz; it was found noise with an 80Hz broad peak is more annoying than with a 50Hz broad peak. A study by Duarte and Filho<sup>[24]</sup> offers a possible explanation to the previous finding. Their paper shows that people are particularly sensitive to low frequency vibrations between 20-40Hz and 50-100Hz as these correspond to the resonant frequencies of the human-head and chest-wall/ocular-globe respectively. Fields<sup>[29]</sup> correlates the level of disturbance from railway noise and vibration with distance from the track. High levels of dissatisfaction are reported for people living or working within 25m of the railway line; levels of annoyance rapidly decrease as the distance to the track increases to 150m, at which point there is uniform low-level complaints. The study also highlights other factors which affect perception of vibration, including time of day, duration of vibration, and whether the railway is visible. Klaboe *et al.*<sup>[80,81,149]</sup> present an extensive study on the Norwegian standard NS8176 for vibration in buildings from road and rail traffic. In the three-part paper they examine the current vibration standard, introduce a single quantity statistical measure to describe the vibration of a building, and present a methodology to standardize socio-vibrational surveys to simplify comparison of data in the future.

Much research has been undertaken to understand the transmission of ground-borne vibrations and to find mitigation methods. At the University of Cambridge, for example, ground-borne vibrations emitted from road traffic, surface railways and underground railways have been studied by Hunt<sup>[59]</sup>, Ng<sup>[107]</sup> and Forrest<sup>[33]</sup>, respectively. Talbot<sup>[142]</sup> discusses the performance of base-isolated buildings and Hussein<sup>[61]</sup> focuses on the effect of isolating the rails from the subway tunnel. Further information regarding ground-borne vibration can be found in the reviews by Hung and Yang<sup>[58]</sup> or Hunt and Hussein<sup>[60]</sup>. A review of vibration excitation mechanisms and methods to simulate

ground-borne vibration can be found in the following sections.

## 2.2 Vibration Excitation Mechanisms

The mechanisms through which moving trains produce ground-borne vibrations were extensively reviewed in a five-part paper over thirty years ago<sup>[37,121,122,126,153]</sup>. Three main mechanisms for the production of vibration are identified for standard rolling stock: quasi-static loading, parametric loading, and general wheel/rail roughness.

Low-frequency vibrations (0-20Hz) arise from the quasi-static load of the train moving along the track<sup>[131]</sup>; the loads at the wheel-rail interface create deflection bowls under each bogie, as shown in Figure 2.1. As the train moves past an observation point, the periodic passing of the deflection bowls produces harmonic excitation.

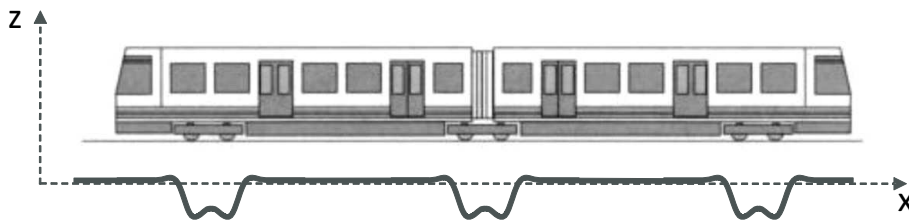


Figure 2.1: Deflection bowls created by quasi-static train load

Parametric excitation can result from a periodic changing of the effective stiffness of the rails and associated supporting structure on which the wheels ride<sup>[94]</sup>. Some track designs use regularly spaced sleepers on a stone ballast to support the rails. The resultant ground stiffness is greater as the wheels pass over a sleeper producing a periodic excitation known as the sleeper-pass frequency. Experimental measurements by Heckl *et al.*<sup>[55]</sup> confirm the importance of this excitation mechanism as results show distinctive peaks in the acceleration spectra at the sleeper-pass frequency. Other excitation mechanisms referred to as parametric excitation include isolated defects such as a wheel flats (Figure 2.2(a)) or badly aligned rail joints (Figure 2.2(b))<sup>[108]</sup>. Every time a wheel passes over a rail discontinuity, or a wheel with a flat spot completes a

revolution, an impact occurs at the wheel rail interface which excites high frequency vibrations. V $\acute{e}$ r *et al.*<sup>[153]</sup> provide an early analytical model to simulate such defects and the resulting levels of vibration. Parametric excitation mechanisms are becoming relatively less important compared to other sources of excitation in underground railways as increased use of continuously-welded track mounted on slabs rather than sleepers and better wheel-maintenance has reduced the amplitude of input energy for these sources.

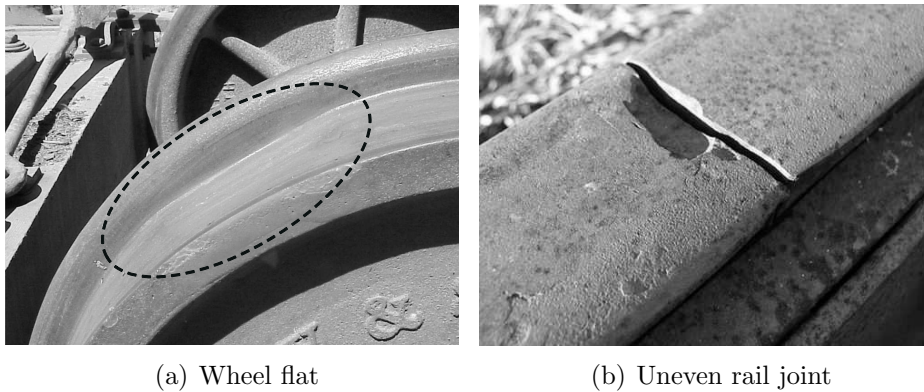


Figure 2.2: Examples of wheel and rail discontinuities

General wheel and rail unevenness or roughness is considered to be the governing excitation mechanism for railway induced vibration<sup>[146]</sup>. Limitations in manufacturing processes result in rails and wheels which are not perfectly smooth or round. This coupled with environmental factors can cause the rails to become pitted or corrugated. The harmonic forces which are developed by this roughness have frequencies which are functions of the rail roughness-wavelength, the wheel circumference and the train velocity. Remington<sup>[121,122]</sup> developed an early theoretical model of rolling noise accounting for the irregularities of the wheel and rail running surface resulting in relative vibrations between the wheel and rail. Thompson<sup>[144]</sup> extended this model which subsequently resulted in the development of TWINS (Track-Wheel Interaction Noise Software)<sup>[145]</sup>. A generally accepted method of modelling track roughness is to assume it is a stationary random process characterized by its power spectral density (PSD) function<sup>[93]</sup>. The random process roughness method is used by Forrest<sup>[33]</sup> and Hussein<sup>[61]</sup> in the Pipe-in-Pipe model to determine the forces at the wheel/rail interface; further review of this method

will be presented in subsequent chapters as it is used in the current study.

## 2.3 Simulating Ground Vibration

The research reviewed in Section 2.1 suggests the greatest source of annoyance caused by underground railways is vibration and re-radiated noise in buildings around the underground tunnels. However, before the vibrational energy enters the buildings it must first propagate through the tunnel wall and the surrounding soil. Numerous models of varying complexity have been developed attempting to simulate wave propagation through a solid. Generally models consider a disturbance in an infinite medium (fullspace) or in a semi-infinite medium (halfspace). The following discussion reviews the common simulation methods including analytical, finite element and boundary element, and semi-analytical.

### 2.3.1 Basics of Wave Propagation

The first significant contributions to the study of ground-borne vibration are attributed to Lord Rayleigh in 1885<sup>[120]</sup> and Lamb in 1904<sup>[88]</sup>. This early work mathematically predicts that a disturbance in an elastic halfspace can be expressed as the superposition of three propagating waves types: dilation waves, equivoluminal waves, and surface waves.

The first two of these are known as body waves and propagate in the bulk medium. The dilation wave (pressure or P-wave) is a longitudinal wave where the particles in the solid move in the same direction as the wavefront. The equivoluminal wave (shear or S-wave) is a transverse wave where the particles move perpendicular to the wave front. A shear wave can be further decomposed into its component in the horizontal plane (SH-waves) and in the vertical plane (SV-waves). See Figure 2.3 for a depiction of these wave types. It should be noted that variation in the bulk medium (i.e. layering) can cause coupling between the P-waves and SV-waves; the SH-waves will remain uncoupled

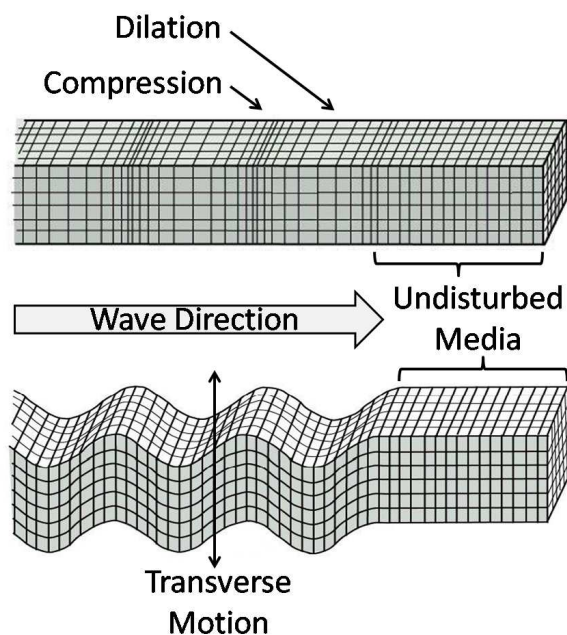


Figure 2.3: Depiction of P-wave (above) and SV-wave (below)

thus wave propagation problems are commonly separated into the P-SV-wave problem and SH-wave problem which can be solved independently.

Surface or Rayleigh waves (R-wave) cause the particles to move elliptically with in-plane longitudinal and transverse components as shown in Figure 2.4. R-waves only propagate along the surface to a depth of approximately one wavelength.

Further work by Love and Stoneley resulted in the discovery of new wave types which bear their names. Love waves propagate on the free surface of a halfspace with particle

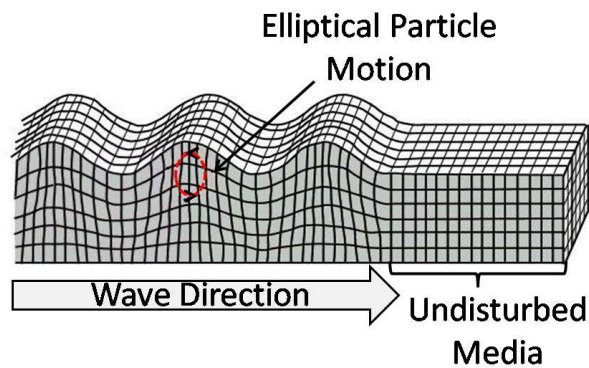


Figure 2.4: Depiction of Rayleigh wave showing elliptic particle motion

motion in the out-of-plane direction. Stoneley waves are similar to surface waves but confined to the vicinity of the interface between layers with different material properties. Further information regarding wave types can be found in Ewing<sup>[26]</sup> or Graff<sup>[47]</sup>.

In ground vibration problems the soil is commonly modelled as an elastodynamic material defined by Lamé constants  $\mu$  and  $\lambda$ ;  $\mu$  is also referred to as the shear modulus  $G$ . As outlined in Appendix A, Lamé constants are related to the elastic modulus  $E$  and Poisson's ratio  $\nu$  as

$$\mu = \frac{E}{2(1 + \nu)} \quad (2.1a)$$

$$\lambda = \frac{E\nu}{(1 + \nu)(1 - 2\nu)}. \quad (2.1b)$$

The P-wave speed ( $c_P$ ) and the S-wave speed ( $c_S$ ) are derived in terms of Lamé constants and density  $\rho$  as

$$c_P = \sqrt{\frac{\lambda + 2\mu}{\rho}} \quad (2.2a)$$

$$c_S = \sqrt{\frac{\mu}{\rho}}. \quad (2.2b)$$

The Rayleigh wave speed,  $c_R$ , cannot be expressed explicitly in these terms but has been shown by Lamb<sup>[88]</sup> to travel slower than the shear wave.

As the waves propagate through the medium their amplitudes decrease both through geometric decay and material damping. Geometric decay, or radiation damping, occurs through the expansion of the wavefront which causes the wave energy to be spread over an ever increasing area. Woods<sup>[160]</sup> details radiation damping for 3D propagating waves due to a surface point load. Near the surface P-waves and S-waves decay inversely as the square of the distance from the disturbance ( $\frac{1}{r^2}$ ) and at depth as the inverse of the distance ( $\frac{1}{r}$ ); Rayleigh waves decay inversely as the square root of the distance from the disturbance ( $\frac{1}{\sqrt{r}}$ ). This decay in wave energy is purely a function of geometry and not the material properties of the medium (i.e. an expanding hemispherical wavefront for body waves and an expanding circular wavefront for surface waves). This theory also

holds for disturbances at depth with the caveat that the radius  $r$  for body wavefronts is measured from the point of disturbance, while the radius of the the surface wavefront is measured from the epicenter of the surface vibration.

Material damping is a function of the material and is related to the dissipation of energy through mechanisms such as friction between soil particles. Two common models for material damping include viscous damping and hysteretic damping: viscous damping is proportional to the relative velocity between particles in the system and is thus rate dependant; hysteretic damping is proportional to the relative displacement of particles and is thus rate independent. Hunt<sup>[59]</sup> provides a thorough review of arguments for and against each damping model. In the current study hysteretic damping is employed because material damping is generally assumed to be rate independent in the low frequency range of soil dynamics problems<sup>[86]</sup>. Damping is included using the correspondence principle<sup>[13,15,31]</sup> which states the frequency response function of a damped system can be obtained from the elastic system by writing the elastic moduli as complex quantities. The complex Lamé constants can be written as<sup>[47]</sup>

$$\lambda^* + 2\mu^* = (\lambda + 2\mu)(1 + 2iD_P) \quad (2.3a)$$

$$\mu^* = \mu(1 + 2iD_S) \quad (2.3b)$$

where  $D_P$  and  $D_S$  are the hysteretic damping ratios for P-waves and S-waves, respectively. These complex constants can be used in Equation 2.2 to determine the complex wave speeds.

### 2.3.2 Analytical Methods

Analytical solutions for the transfer function of a homogeneous elastic halfspace subjected to point-loads and line-loads were first developed by Lamb<sup>[88]</sup>. The solutions are in the form of integral equations and require convolution integration techniques to

solve. For a surface point-load the Rayleigh wave propagates outward from the loading point with a circular wave front while the P-wave and S-wave propagate outward with a hemi-spherical wavefront. For a surface line-load the Rayleigh wave has a linear wave front and the body waves have cylindrical wave fronts. Graff<sup>[47]</sup> provides a thorough review of these solutions and methods which can be used to perform the convolution integration.

Miller and Pursey<sup>[103]</sup> are often cited for publishing the partition of energy between the different wave types in a halfspace subjected to a loaded circular disk: 67% Rayleigh wave, 26% shear wave, 7% pressure wave. This suggests that the bulk of the vibrational disturbance on the surface is due to the Rayleigh wave energy. However, Wolf<sup>[158]</sup> showed that this is only true for low frequency excitation or small disk areas (approaching a point-load). For higher frequencies or larger loading areas the energy imparted to the Rayleigh wave is much less (approximately 10%), with the remainder going into the P-wave and S-wave.

Kausel<sup>[73]</sup> has recently published a compendium of analytical solutions for dynamic response functions resulting from transient sources acting within isotropic, elastic media. The fullspace and halfspace solutions are given for two and three-dimensional problems subject to point-loads, line-loads, torques and pressure-pulses. A significant contribution to this area of research was published by Tadeu and Kausel<sup>[141]</sup> in which they develop the fullspace Greens functions for a harmonic (steady-state) line load whose amplitude varies sinusoidally in the third dimension, typically referred to as a two-and-a-half-dimensional problem; Tadeu later extended this theory for 2.5D halfspace Green's functions<sup>[140]</sup>. The 2.5D halfspace Green's function has been of significant value to numerical-modelling of railway induced vibrations using methods such as boundary-elements<sup>[38]</sup> or the Pipe-in-Pipe model<sup>[62]</sup>; these modelling methods will be discussed further in the following sections.

Limited research is still being done using purely analytical methods for layered media. Gautesen<sup>[39-41]</sup> studies wave scattering in elastic quarterspaces by separating the

problem into symmetric and anti-symmetric regimes which have been Fourier transformed. He has also considered elastic wedges whose angles are greater than  $180^\circ$ <sup>[39]</sup>. Budaev and Bogy<sup>[14]</sup> develop a solution to Rayleigh wave scattering by an infinite wedge using Sommerfeld integrals in the complex plane. Its and Yanovskaya<sup>[69]</sup> use an approach based on the Green's function technique to investigate surface waves in a halfspace composed of two different quarterspaces. In all cases, the equations are too complex to obtain closed-form solutions thus approximate numerical methods are used to solve the governing equations. Also, these techniques are developed for very specific problems and are not flexible enough to be used for general ground vibration problems.

### 2.3.3 Numerical Methods

The complexity of the equations required to solve vibration problems involving layering, foundations or irregular geometries make analytical methods intractable. Approximate numerical methods such as the finite difference (FD) method, finite element (FE) method or the boundary element (BE) method are more commonly used to solve these complex problems.

#### 2.3.3.1 Finite Difference Method

The motivation behind the development of the finite difference method in structural vibrations was largely to overcome the difficulty of finding closed-form solutions to the differential equations of complex continuum problems. Instead, the FD method numerically solves the equations of motion for the continuous structure at specified nodes, replacing the derivatives by finite-difference expressions of the functions. This is different from the finite element method (see Section 2.3.3.2) where the continuous structure is idealized as an assembly of discrete elements.

The finite-difference form of the differential equations governing displacements (or stresses) is applied at each node of the meshed structure, relating the displacements (or

stresses) at the given node and at nodes in its vicinity to the external applied loads. This generally provides a sufficient number of simultaneous equations for the displacements (or stresses) to be determined<sup>[44]</sup>. However, near the boundaries it is necessary to satisfy this finite-difference form for both the equations of motion and the boundary conditions. This can be difficult to achieve at arbitrary boundaries since the FD mesh will restrict the form of differencing which can be carried out<sup>[9]</sup>.

The finite difference method for modelling of viscoelastic solids is thoroughly developed in an academic report by Blanch *et al.*<sup>[12]</sup>. Although the FD method is losing favour in academia, this method has recently been used to study ground vibration due to high-speed trains<sup>[72]</sup> and bridge vibrations due to passing trains<sup>[162]</sup>. The FD method also remains popular in some sectors of industry, for example the FINDWAVE<sup>[143]</sup> package has been used to predict ground vibration levels for the CrossRail line scheduled for development in London, UK.

### 2.3.3.2 Finite Element Method

The finite element method was developed for solving models in differential form<sup>[9]</sup>, a form which allows for simple incorporation of boundary conditions. FE requires the discretization of the entire geometry into small finite-sized elements whose governing equations are known and relatively simple. The displacement solution to a given loading condition for all of the elements is found simultaneously using matrix algebra. FE is well-suited to simulating complex geometries which encompass a finite volume; unfortunately it is impossible to accurately model a semi-infinite space using basic FE theory as the size of the model must be finite by definition<sup>[9]</sup>. Early FE models of semi-infinite media under static loads would use rigid, artificial boundaries “far enough” from the loading location such that the boundaries would not affect the solution. For dynamic simulations this is not possible; the artificial boundaries reflect waves causing erroneous results<sup>[19]</sup>. This prompted research into absorbing boundaries: boundary condition formulations which simulate an infinite elastic layer (see Figure 2.5).

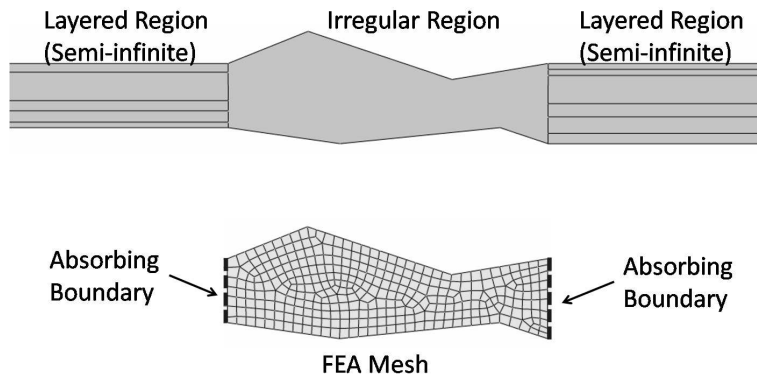


Figure 2.5: The use of absorbing boundaries in FEA to simulate semi-infinite layers

Lysmer and Kuhlemeyer<sup>[97]</sup> were among the first to develop an absorbing boundary, known as “the standard viscous boundary”. Rather than rigidly constraining the artificial boundaries, a series of normal and tangential dashpots are coupled to the boundaries of the 2D model. By carefully selecting the dashpot viscosity the boundaries absorb the P-waves and S-waves, negating wave reflection or other artificial boundary errors. White *et al*<sup>[157]</sup> present a different criteria for selecting the appropriate dashpot values, known as “the unified viscous boundary”, which results in better approximations for certain loading cases.

A second type of absorbing boundary developed by Lysmer *et al.*<sup>[95,96,98]</sup>, based on the theoretical work by Haskell<sup>[54]</sup> and Thomson<sup>[147]</sup>, requires the problem to be transformed into the frequency-wavenumber domain. Separation of variables is used to find a transcendental solution to the wave equation for the semi-infinite layer of soil represented by the absorbing boundary. For layered media, equations are required for each layer and must meet compatibility conditions for adjoining layers. Closed-form solutions can be found for simple cases by contour integration, while numerical solutions are needed for arbitrarily layered soils. Calculation of this type of absorbing boundary, referred to as the stiffness matrix technique, is considered exact as it introducing no further approximation to the model. Drake<sup>[23]</sup> uses FEM coupled with the stiffness matrix technique to determine reflection and transmission factors for Rayleigh waves

in non-horizontally layered media; this requires the full FEM discretization of the non-horizontal section. The stiffness matrix approach has been extended for anisotropic media<sup>[125]</sup>, three-dimensional problems<sup>[128,130]</sup>, and transient analyses<sup>[115]</sup>. An important extension to the stiffness matrix technique, known as the thin-layer method, was developed by Waas<sup>[155]</sup> and will be discussed in Section 2.3.4.1.

### 2.3.3.3 Boundary Element Method

The formulation of the boundary element method's governing equations gives BE a distinct computational advantage over FE when considering infinite or semi-infinite problems. Standard BE uses the boundary integral formulation of the governing equations of motion for a fullspace, which reduces the dimension of the problem by one<sup>[10]</sup>. In other words, the solution to a plane-strain problem can be found by discretizing only the edge, or boundary, of the solid. For the case of a tunnel buried in a halfspace, only the exterior of the tunnel and the surface of the halfspace would need to be discretized; FEM would require meshing a significant portion of the soil around the tunnel and then imposing absorbing boundaries. Since no artificial boundaries are imposed using the boundary element method, no fictitious wave reflections are generated by the model.

Boundary element methods are commonly used for problems concerning structure/soil interactions including railway tunnels<sup>[138]</sup>, piled foundations<sup>[91,159]</sup>, and pile/structure interactions<sup>[142]</sup>. The computational cost of using BEM for homogeneous, isotropic halfspace problems has been significantly reduced by the development of the 2.5D Green's functions for a halfspace<sup>[141]</sup>. Using the halfspace Green's function in the BE formulation results in a model which does not require the discretization of the free surface, only the exterior of buried structure<sup>[6]</sup>. If the soil is inhomogeneous or anisotropic other methods are better suited to accounting for these variations in soil parameters, for instance the thin-layer method.

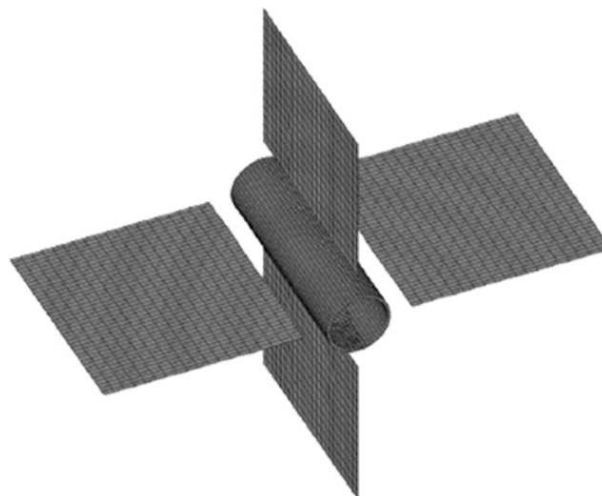


Figure 2.6: Example of a coupled BE-FE model<sup>[50]</sup>; tunnel modelled using FE while response along planes in the soil predicted using BE (reproduced with permission from the author)

### 2.3.3.4 Coupled BE-FE Models

Recently researchers have begun to use coupled BE-FE models to combine the positive attributes from both simulation methods: the ease of modelling complex geometries using FE and the ease of simulating infinite and semi-infinite media using BE. For underground railways the tunnel and associated hardware are generally modelled using finite elements to which a layer of boundary elements are coupled to the exterior of the tunnel to simulate the surrounding media as shown in Figure 2.6. Andersen and Jones<sup>[5]</sup> compare the use of 2D and 3D coupled BE-FE models and show that while 2D models require less computational effort they prove to be only quantitatively useful when simulating structural changes; 3D models can provide better predictions of the absolute vibration levels but require significantly more computational effort.

Continued development into coupled FE-BE models has reduced the computational requirements further. For underground railways it can often be assumed the tunnel and soil are homogeneous along the length of the track, allowing the problem to be transformed into a sequence of 2D models which depend on the wavenumber in the track direction. A 2D coupled FE-BE model is solved for a finite number of wavenumbers and an inverse Fourier transform is performed to compute the three-dimensional spatial

response. This form of simulation is generally referred to as two-and-a-half-dimensional (2.5D) or wavenumber FE-BE modelling. Sheng *et al.*<sup>[132]</sup> present such a model for simulating ground vibration from both surface and underground trains; it is predicted that the 2.5D model requires two-hundred times less computing time than would a similar 3D coupled BE-FE model to produce similar results.

Degrande *et al.*<sup>[16,20]</sup> use the homogeneity along the tunnel in a slightly different manner. The periodicity of the tunnel and the soil is exploited using the Floquet transform, limiting the discretization to a single bounded reference cell of the tunnel modelled using the coupled BE-FE method. The authors state that this is a major advantage compared to the standard 2.5D approach because the use of periodic cells rather than 2D slices allows any type of loading, including point forces, to be more easily simulated. Gupta *et al.* have used this method in a number of published studies including the prediction of vibrations due to underground railways in Beijing<sup>[51]</sup> and the investigation of tunnel and soil parameters on ground vibration<sup>[52]</sup>.

### 2.3.4 Semi-Analytical Method

While finite-element and boundary-element formulations have become more efficient and advances in computer processing have reduced model run-times, it is still common for coupled BE-FE models of underground railways to take tens of hours to compute. If a number of model iterations are required during the design process, these long computational times can make such models economically infeasible. Semi-analytical methods can greatly reduce the computational cost of a model by integrating analytical solutions into the numerical algorithm. Two examples of semi-analytical methods which are used extensively in the current work are the thin-layer method and the Pipe-in-Pipe method.

### 2.3.4.1 Thin-Layer Method

The difficulty associated with solving the transcendental equations of the stiffness matrix technique (see Section 2.3.3.2) resulted in the development of the thin-layer method (TLM) by Waas<sup>[155]</sup>. By discretizing the semi-infinite soil in the vertical direction into a finite number of thin-layers the displacement across each layer can be assumed to vary linearly; this negates the need to use a contour integration over the entire depth of the soil and simplifies the governing equations into a quadratic eigenvalue problem. For the linearity assumption to be valid the thickness of each layer must be small compared to the wavelength of the shear-wave in the layer. The analytical wave equation is used in the horizontal direction which allows layers of any horizontal length (i.e. finite or infinite) to accurately predict harmonic displacement without suffering from the element aspect-ratio restrictions of finite element methods. The method can also be extended to 2.5D space in a similar manner to that used for the BE-FE models described in Section 2.3.3.4.

Kausel, in collaboration with others, has extended the TLM theory to include distributed loads<sup>[77]</sup>, interior dynamic loads<sup>[75]</sup>, static loads in a layered halfspace<sup>[78]</sup>, hyperelements with two vertical boundaries<sup>[76]</sup>, and conversion into the cylindrical coordinate system<sup>[74]</sup>. Further work has also been performed by Andrade who has developed a method to include dynamic loads in a layered halfspace<sup>[7]</sup> and Park who has transformed the coordinate system to allow for inclined boundaries<sup>[116]</sup>.

Further discussion on the thin-layer method can be found in Chapter 4, including a review of the formulation and implementation for predicting ground vibration from underground railways.

### 2.3.4.2 Pipe-in-Pipe Method

Forrest and Hunt<sup>[33-35]</sup> present a computationally efficient, three-dimensional semi-analytical model for calculating soil vibration in a fullspace from underground railways,

known as the Pipe-in-Pipe model (PiP). As the name implies, the PiP model represents the tunnel and soil as concentric, coupled “pipes”. The tunnel pipe is modelled using thin-shell theory while the soil pipe is modelled using elastic continuum theory. The outer radius of the tunnel pipe is equal to the inner radius of the soil pipe, and the outer radius of the soil pipe is infinite to simulate a fullspace.

The coupled governing equations of motion for the tunnel and the surrounding soil are transformed into the frequency, wavenumber, and circumferential ring-mode domains using Discrete Fourier Transforms (DFT). The equations can then be written in matrix form and solve using standard matrix algebra.

The PiP model has been validated against a coupled BE-FE model and shown to have good agreement over the frequency range of interest<sup>[50]</sup> but with a computational cost which is orders of magnitude less than the BE-FE model. The combination of model accuracy and computational efficiency makes PiP a powerful computational tool for calculating vibration from underground railways and for assessing the performance of vibration countermeasures.

Further discussion on the PiP method can be found in Chapter 3, where the formulation is reviewed and extended to account for uncertainty of the bond at the tunnel-soil interface.

## 2.4 Uncertainty in Modelling Assumptions

Review of current literature regarding simulation of vibration from underground railways has revealed a number of different approaches currently in use and/or development. A trait common to all of these simulation methods is the use of simplifying assumptions during the development of the model. A simplifying assumption is defined herein as:

**simplifying assumption** : a means of reducing the complexity of a model (e.g. geometry, material properties, boundary conditions, etc.) under the assumption that this simplification will not significantly affect the results.

A classic example of a simplifying assumption is simulating a railway track as a beam on an elastic foundation. In reality the rail is coupled to individual sleepers at discrete points using mechanical fasteners; the sleepers are supported by gravel ballast which is supported by the earth. To model each connection and each piece of gravel would be extremely time consuming and even then assumptions would need to be made regarding the friction laws governing the interaction between all the elements. It is more reasonable to estimate an overall stiffness and dampening coefficient for the supporting media and assume the rail is continually supported. This allows an efficient model to be developed which can quantitatively predict how changes to the major modelling elements effect the overall response. However, simplifying the model in such a manner inherently introduces uncertainty in the predictions for the situations being modelled.

One area where simplifying assumptions are commonly used when modelling vibrations from underground railways regards the properties and stratification of the soil. The dynamic characteristics of soil are notoriously difficult to measure over an area of interest, more so if the variation with depth is also desired<sup>[59]</sup>. Schevenels *et al.*<sup>[127]</sup> review some of the methods available for *in situ* soil measurements including the spectral analysis of surface waves test (SASW) and the seismic cone penetration test (SCPT). A combination of these measurements allows an estimation of the variation in dynamic shear modulus and material damping with depth. However, the measurements are based on local averages resulting in limited resolution of the soil characteristics. Cone penetration tests can be performed for better resolution but these are only accurate over a small area; coarse global averaging is necessary to extrapolate the findings over larger areas.

It is therefore often assumed during the modelling process that the soil is both homogenous and isotropic (i.e. a uniform halfspace) and is fully bonded to the exterior of the tunnel; if sufficient evidence is available to warrant the extra complexity horizontal layers of homogeneous and isotropic media may be also incorporated (see Figure 2.7 for a schematic representation). These are generally reasonable assumptions due to the

difficulty in obtaining sufficient data to allow accurate modelling of varying layer depths or variation in material properties. Furthermore, using horizontal layering results in a geometrically simple model which reduces the effort involved in modelling and the computational requirements for a solution.

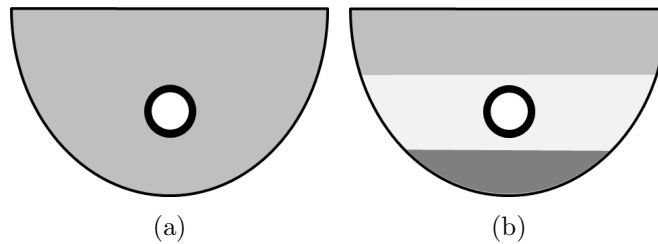


Figure 2.7: Simplifying assumptions commonly used when modelling soil around an underground railway tunnel: (a) homogeneous halfspace; (b) layered halfspace

Although assuming a simplified soil lithology which is fully bonded to the tunnel is convenient, there is little evidence which quantitatively validates these assumptions. Four possible sources of uncertainty associated with these assumptions which will be investigated include the effect of layer inclination, layer subsidence over a tunnel, voids at the tunnel-soil interface, and inhomogeneity of soil properties.

### 2.4.1 Inclined Layers

Natural development and movement of soils results in a stratified lithology. The development of each layer can occur due to two mechanisms: parent material that has not been involved in an erosion cycle (i.e. hard or soft bedrock) is weathered *in situ* forming residual soils, or soils which have already formed through one or more cycles of erosion are moved to a new location (i.e. by ice, wind, water or gravity) known as transported soils<sup>[135]</sup>. This layered soil formation results in the distinct soil horizons shown in Figure 2.8 and outlined below<sup>[4]</sup>.

- H horizon: dominated by undecomposed or partially decomposed organic material at the soil surface, saturated with water for prolonged periods

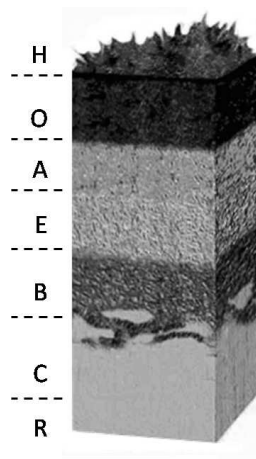


Figure 2.8: Schematic of the major soil horizons (reproduced from the University of Vermont webpage - [www.uvm.edu](http://www.uvm.edu))

- O horizon: dominated by decomposed organic material, not saturated with water for prolonged periods; O layers may be at the surface or at any depth beneath the surface if it has been buried by transported soil
- A horizon: mineral layer formed at the surface or below an O horizon, often formed due to cultivation, pasturing or similar kinds of disturbance
- E horizon: mainly sand and silt due to a loss of silicate clay, iron, aluminium
- B horizon: made up of silicate clay, iron, aluminium, humus, carbonates, gypsum, silica, or combinations thereof
- C horizon: sediments, saprolite and unconsolidated bedrock
- R horizon: hard bedrock underlying the soil

These horizons are often assumed to run parallel with the surface although this is not always the case. Figure 2.9 shows examples of soil lithologies taken from geological and oil/gas surveys. Notice the slight inclination of the layers with respect to adjoining layers; it is not uncommon to have layer inclinations of five degrees. It is unclear how the inclination of a soil layer affects the global vibration response of the soil. This issue is investigated in Section 4.2 where the thin-layer method model is used to quantify

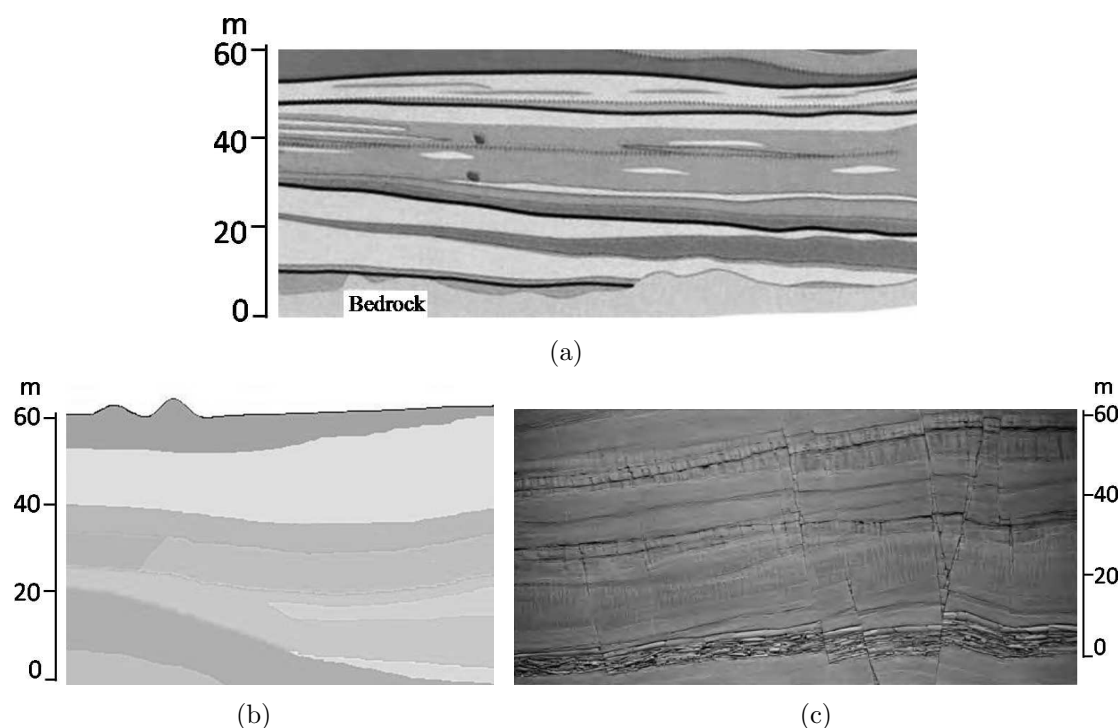


Figure 2.9: Examples soil stratification taken from (a) Texas Bureau of Economic Geology ([www.beg.utexas.edu](http://www.beg.utexas.edu)), (b-c) oil and gas land surveys ([www.republicenergy.com](http://www.republicenergy.com))

the variation in surface response between inclined and horizontally layered halfspaces subjected to vibration from an underground railway.

### 2.4.2 Soil Subsidence

Ground movement associated with the construction of underground railway tunnels is inevitable<sup>[113]</sup>. As the tunneling face progresses forward the lack of support for the overburden causes the ground above the tunnel to subside, as depicted in Figure 2.10.

There are a number of methods which can be employed to help prevent subsidence during construction of the tunnel: compensation grouting, freezing, dewatering, earth pressure balance tunnel-boring machines, etc.<sup>[2]</sup> These methods are all intended to strengthen the soil through which the tunnel is being bored so that the overburden does not cause the open tunnel to deform before the tunnel lining can be installed.

Although compensation methods are improving, they cannot fully negate subsidence during and after the tunneling process. O'Reilly and New<sup>[113]</sup> list a number of vol-

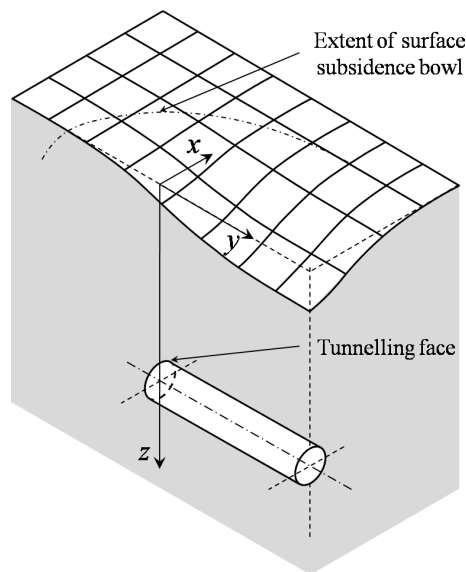


Figure 2.10: Development of surface subsidence trough due to tunneling

ume loss estimations from underground railway sites in the UK ranging from 1.5% to 2.5% (5-8 mm) shortly after construction. A more recent study involving the construction of the Jubilee Line extension in London predicted green-field subsidence levels of 15-20 mm<sup>[85,99]</sup>.

Studies using space radar interferometric techniques show evidence of subsidence levels averaging 10-20 mm/year for underground railways in the UK, Korea, Chile and Greece<sup>[79,82,114]</sup>. The yearly subsidence over the tunnels is attributed to water leakage into the tunnels resulting in a loss of pore pressure in the surrounding soil. A long-term study measuring subsidence in St. James's Park over the Jubilee Line extension show total subsidence (i.e. from construction and long-term settlement) of 60-70 mm after two years<sup>[110]</sup>. It is conceivable that a subsidence trough of 80-100mm could develop over an underground railway tunnel during its lifetime. It is unclear if accounting for subsidence of the soil layers over the tunnel would significantly alter predicted vibration levels compared to a simplified assumption of horizontal layers. The thin-layer method model is used in Section 4.3 to quantify the change in surface vibration when accounting for the geometric soil variation due to subsidence over underground railway tunnels.

A second source of uncertainty which may develop due to subsidence regards the

interface between the tunnel exterior and the surrounding soil. The soil is generally assumed to be in continuous contact with the tunnel (i.e. no voids or gaps at the tunnel-soil interface). Under such large-scale subsidence it is likely that a void will form over a section of the tunnel, disrupting the perfect bond at the interface. Voids may also develop during construction of new buildings in close proximity to the underground tunnels due to pile-driving, excavation, landscaping, etc. The extent of voidage is difficult to quantify but the existence of voids is not in doubt. Chapter 3 introduces a new method which can quantify the change in surface vibration when accounting for voids of various size over an underground railway tunnel subjected to a moving load.

### 2.4.3 Soil Inhomogeneity

The soil in ground vibration simulations is commonly assumed to be homogeneous throughout each layer. In reality the soil properties can vary significantly over relatively short distances (see Figure 2.11 showing the predicted shear modulus variation over a 60m section).

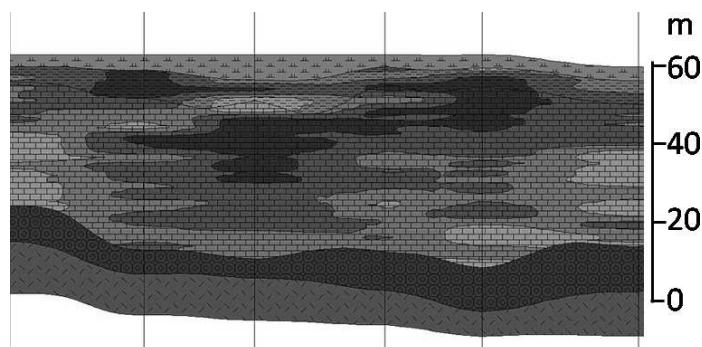


Figure 2.11: Example showing inhomogeneous shear modulus distribution (reproduced from a geological modelling company ([www.rockware.com](http://www.rockware.com)))

Three sources of variability can readily be identified<sup>[150]</sup>: natural inhomogeneity, availability of information and measurement error. Naturally occurring inhomogeneity is caused by factors such as mineral composition, stress history, moisture content, density, etc. The general trends in soil properties (i.e. significant changes in average properties associated with layering) tend to be accounted for in conventional soil models. It is local

variations within those layers that is difficult to distinguish; it is quite impractical to take sufficient soil samples to accurately map local variations in material properties over the area of interest. Soil profiles must be inferred from a limited number of samples. Finally, measurement and testing errors tend to dilute the value of the samples that have been obtained. A practical method to adequately capture the inherent variation in properties involves a probabilistic model employing random field theory.

The theory of random fields has developed over the last century in numerous areas of study dating back to Bachelier's study of economics<sup>[8]</sup> and Einstein's theory of Brownian motion<sup>[25]</sup>. An excellent review of random field theory can be found in the books of Vanmarcke<sup>[151]</sup> and Ghanem and Spanos<sup>[45]</sup>. Use of random field theory for soil variability has been limited to the last forty years. An early method involved first-order perturbation of the governing eigenvalue problems<sup>[17,133]</sup> or finite-element formulations<sup>[53]</sup>. First-order perturbations were found to yield crude approximations to the solution thus second-order perturbation were developed but were dismissed as too computationally expensive for the extended benefits<sup>[105]</sup>. Research into stochastic methods of describing properties as random processes provided more reasonable approximations of response statistics<sup>[134]</sup> and scale of fluctuation<sup>[152]</sup>. The theory of Neumann expansions was also explored for analytical and numerical simulations<sup>[161]</sup>.

A method which has become well-established for numerically simulating soil variability is the stochastic finite element method (SFEM)<sup>[45]</sup>. The SFEM assumes the spatial variation of material properties (i.e. elastic modulus, shear strength, density, etc.) can be expressed via a covariance function (CF). The CF is a measure of the correlation, or similarity, of the value at two different points in the random field. SFEM commonly uses a Karhunen-Loeve (KL) expansion to express the covariance function as a linear combination of deterministic functions with Gaussian-random coefficients<sup>[137]</sup>; this allows the soil variability to be expressed over finite element mesh as the superposition of the average field and the KL-expanded random field governed by the covariance function. The solution to the stochastic system of equations is generally solved using

a Monte Carlo simulation, a Neumann expansion, or a projection of the response on polynomial chaos<sup>[127]</sup>. This method has been used in 1-D and 2-D finite element models to investigate seismic response in soils resting on bedrock<sup>[90,109,163]</sup> and for soil-structure interactions<sup>[46]</sup>.

Schevenels *et al.*<sup>[127]</sup> recently adopted the SFEM method to determine the Green's function for a vertically inhomogeneous soil with random dynamic shear modulus using a hybrid thin-layer method and direct stiffness method; the variation in the horizontal direction was deemed negligible. Published data regarding the spatial variability of soils show that while vertical variability in the soil profile is dominant, horizontal variability is also significant<sup>[56,118,119,136]</sup>. In Section 4.4 the thin-layer method is used to investigate the effect of inhomogeneity in the soil's elastic modulus on surface vibration due to underground railway disturbances; soil variability in both the vertical and horizontal directions is included.

## 2.5 Conclusions

Ground vibration from underground railways is a major source of disturbance for people living and working near subways. Researchers have linked such disturbances to work degradation, sleep disturbance and possible health risks affecting individuals 25m from tunnels and have reported above average annoyance from inhabitants up to 200m from the subways. This public disturbance has spurred the development of ISO standards to quantify acceptable levels of vibration from underground railways and subsequently the development of simulation models to predict ground vibration so as to meet the vibration criteria during the design process.

A number of different modelling methods have been employed to predict ground vibration from underground railways. Analytic Green's functions for homogeneous fullspaces, halfspaces and layers have been developed which allow closed-form solution of geometrically simple problems but lack the flexibility to investigate more complex

---

scenarios. Discrete numerical methods such as finite element and boundary element analysis allow modelling of complex systems but tend to require long computational times. Semi-analytic methods have shown promise as run times tend to be quicker than discrete methods and provide more modelling flexibility than analytic methods while maintaining the accuracy of purely analytic models. However, all such models are based on simplifying assumptions.

Simplifying assumptions, such as assuming the soil is homogeneous, are made to make modelling possible; often limited information of soil properties is available so assumptions must be made from incomplete information. While such assumption make the modelling process tractable there are inherent uncertainties associated with these assumptions which are not well understood. The aim of this dissertation is to quantify some of these uncertainties to give a better understanding of how simplifying assumptions limit prediction accuracy.

# Chapter 3

## Voids at the Tunnel-Soil Interface

A simplifying assumption which is frequently made is that the soil is in continuous contact with the tunnel (ie. no voids or gaps at the tunnel-soil interface). Subsidence and frost-heave have been shown to cause significant tunnel movement<sup>[3,83,123]</sup>; under such large-scale motion it is likely that a void will form over a section of the tunnel disrupting the perfect bond at the tunnel-soil interface, as depicted in Figure 3.1. Voids may also develop during construction of new buildings in close proximity to the underground tunnels due to pile-driving, excavation, landscaping, etc. The extent of voidage is difficult, if not impossible, to quantify but the existence of voids is not in doubt.

A review of the literature suggests there have been no studies predicting the effect of a void at the tunnel-soil interface. The goal of the current investigation is to quantify this effect and determine the level of uncertainty associated with neglecting to include voids in numerical simulations of underground railways. Development of a fully analytical model including a finite sized void arbitrarily located around the tunnel was deemed intractable thus a semi-analytical approach is adopted. The Pipe-in-Pipe (PiP) method is used to determine the discrete transfer functions for both the tunnel and the surrounding soil nodes. The transfer matrices are coupled using continuity and equilibrium conditions. The void is simulated by uncoupling the appropriate tunnel and soil nodes, inhibiting the transfer of forces between the two subsystems over a finite patch.

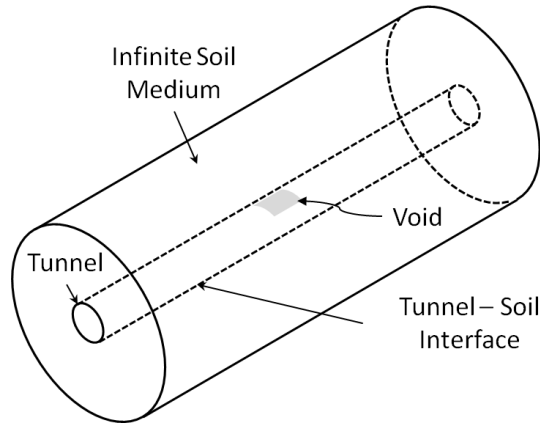


Figure 3.1: Void at the tunnel-soil interface

### 3.1 Model Description

The void model is an extension of the original Pipe-in-Pipe model to allow finite sized voids at the tunnel-soil interface. As introduced in Section 2.3.4.2, the basic PiP method is a computationally efficient, three-dimensional semi-analytical model for calculating soil vibration in a fullspace from underground railways<sup>[33–35,61]</sup>. A brief review of the PiP method is provided below to introduce the reader; further details can be found in Appendix E and in the referenced literature.

#### 3.1.1 Overview of PiP Method

An idealized underground railway tunnel can be thought of as a thin-walled cylinder (i.e. the tunnel) coupled to the inside surface of a thick-walled cylinder (i.e. the surrounding soil), as shown in Figure 3.2. If the outer radius of the thick-walled cylinder is assumed to be infinite ( $R_2$  in Figure 3.2b), this pipe-in-pipe arrangement provides the analytical solution for a buried, circular tunnel in a fullspace.

Forrest<sup>[33]</sup> derives the governing equations of motion for an infinitely long, thin-walled cylinder subjected to a radially-acting point-load as

$$\tilde{\mathbf{U}}_n = \tilde{\mathbf{H}}_{\text{tunnel}} \tilde{\mathbf{P}}_n \quad (3.1)$$

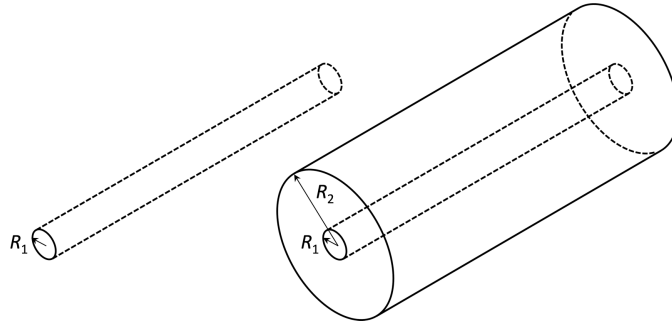


Figure 3.2: Schematic of pipe-in-pipe arrangement: inner pipe representing the tunnel modelled as a thin-walled cylinder (left) and outer pipe representing the soil with outer radius  $R_2 = \infty$  (right)

where  $\tilde{\mathbf{U}}_n$  and  $\tilde{\mathbf{P}}_n$  are the cylindrical displacement and load vectors respectively, in the  $\{Z \theta R\}^T$  directions;  $\tilde{\mathbf{H}}_{\text{tunnel}}$  is a  $3 \times 3$  matrix whose elements are given in Appendix E. The capitalization of the variables indicates the frequency domain ( $\omega$ ), the tilde indicates the wavenumber domain in the axial direction ( $\xi$ ), while the subindex  $n$  refers to the corresponding ring-mode as depicted in Figure 3.3. The first two of these Fourier transforms (i.e. time  $\Rightarrow$  frequency; axial-direction  $\Rightarrow$  axial-wavenumber) are used to convert the equations into a 2.5D frequency-domain problem which greatly simplifies the equations of motion for the current investigation. The transformation from the  $\theta$ - and  $r$ -directions into the ring-mode domain further condenses the equations of motion into the convenient form shown herein.

Similarly, the governing equations of motion for an infinitely long, thick-walled cylinder subjected to a radially-acting point-load is

$$\tilde{\mathbf{U}}_n = \tilde{\mathbf{H}}_{\text{soil}} \tilde{\mathbf{P}}_n \quad (3.2)$$

where the elements of  $\tilde{\mathbf{H}}_{\text{soil}}$  are also given in Appendix E.

Coupling the two cylinders results in the development of reaction forces at the interface; the coupling equations of motion are

$$\tilde{\mathbf{U}}_n^{\text{tunnel}} = \tilde{\mathbf{H}}_{\text{tunnel}} \tilde{\mathbf{F}}_n + \tilde{\mathbf{H}}_{\text{tunnel}} \tilde{\mathbf{R}}_n^{\text{tunnel}} \quad (3.3)$$

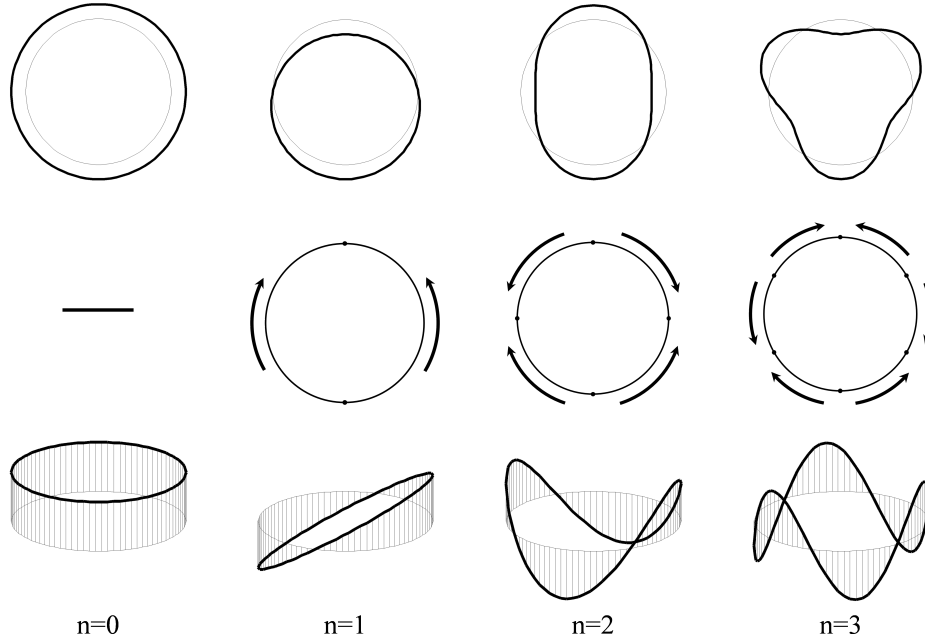


Figure 3.3: Ring-modes  $n=0$  to  $n=3$ : (top) in-plane flexural ring modes corresponding to radial displacement  $\tilde{U}_{Rn}$ ; (middle) in-plane extensional ring modes corresponding to circumferential displacement  $\tilde{U}_{\theta n}$ ; (bottom) out-of-plane flexural ring modes corresponding to axial displacement  $\tilde{U}_{Zn}$

and

$$\tilde{\mathbf{U}}_n^{\text{soil}} = \tilde{\mathbf{H}}_{\text{soil}} \tilde{\mathbf{R}}_n^{\text{soil}} \quad (3.4)$$

where  $\tilde{\mathbf{F}}_n$  is the load applied to the inside of the tunnel and  $\tilde{\mathbf{R}}_n$  is the resultant load between the tunnel and the soil at the cylindrical interface. Continuity of displacements and equilibrium of reaction forces at the interface state

$$\tilde{\mathbf{U}}_n^{\text{tunnel}} = \tilde{\mathbf{U}}_n^{\text{soil}} \equiv \tilde{\mathbf{U}}_n \quad (3.5)$$

$$\tilde{\mathbf{R}}_n^{\text{tunnel}} = -\tilde{\mathbf{R}}_n^{\text{soil}} \quad (3.6)$$

thus the coupled equations of motion for the system can be written as

$$\tilde{\mathbf{U}}_n = \left( \mathbf{I} + \tilde{\mathbf{H}}_{\text{tunnel}} \tilde{\mathbf{H}}_{\text{soil}}^{-1} \right)^{-1} \tilde{\mathbf{H}}_{\text{tunnel}} \tilde{\mathbf{F}}_n. \quad (3.7)$$

It is convenient to recognize that  $\tilde{\mathbf{H}}_{\text{tunnel}} \tilde{\mathbf{F}}_n$  is equivalent to the displacements of the

unconstrained tunnel (i.e. before being coupled to the soil). Let this displacement be referred to as the “original” displacement allowing the equation to be written as

$$\tilde{\mathbf{U}}_n = \left( \mathbf{I} + \tilde{\mathbf{H}}_{\text{tunnel}} \tilde{\mathbf{H}}_{\text{soil}}^{-1} \right)^{-1} \tilde{\mathbf{U}}_n^{\text{orig}}. \quad (3.8)$$

This form of the displacement equation is equivalent to that given by Forrest<sup>[33]</sup>; it is presented in this altered form for use in extending the model to account for voids.

The actual displacements and loads are in general linear combinations of an infinite number of ring-modes. For a radially-acting point-load, the displacements are symmetric about the load with the axial and radial displacements even functions of  $\theta$  and the circumferential displacements an odd function of  $\theta$ . The displacement and load vectors can therefore be written as

$$\begin{Bmatrix} \tilde{U}_Z \\ \tilde{U}_\theta \\ \tilde{U}_R \end{Bmatrix} = \begin{Bmatrix} \tilde{U}_{Z_0} \\ 0 \\ \tilde{U}_{R_0} \end{Bmatrix} + \sum_{n=1}^{\infty} \begin{Bmatrix} \tilde{U}_{Zn} \cos n\theta \\ \tilde{U}_{\theta n} \sin n\theta \\ \tilde{U}_{Rn} \cos n\theta \end{Bmatrix} \quad (3.9)$$

$$\begin{aligned} \tilde{F}_{Zn} &= 0 \\ \tilde{F}_{\theta n} &= 0 \\ \tilde{F}_{Rn} &= \begin{cases} 1/2\pi a, & n = 0 \\ 1/\pi a, & n \geq 1 \end{cases} \end{aligned} \quad (3.10)$$

where  $\theta$  is the radial angle coordinate measured from the location of the point-load. Equation 3.9 is also valid for an axially-acting point-load since  $\tilde{U}_Z$  and  $\tilde{U}_R$  are again even functions of  $\theta$  about the point-load and  $\tilde{U}_\theta$  is an odd function of  $\theta$ .

Hussein<sup>[61]</sup> shows that for a circumferentially-acting point-load the conditions switch, thus

$$\begin{Bmatrix} \tilde{U}_Z \\ \tilde{U}_\theta \\ \tilde{U}_R \end{Bmatrix} = \begin{Bmatrix} 0 \\ \tilde{U}_{\theta_0} \\ 0 \end{Bmatrix} + \sum_{n=1}^{\infty} \begin{Bmatrix} \tilde{U}_{Zn} \sin n\theta \\ \tilde{U}_{\theta n} \cos n\theta \\ \tilde{U}_{Rn} \sin n\theta \end{Bmatrix} \quad (3.11)$$

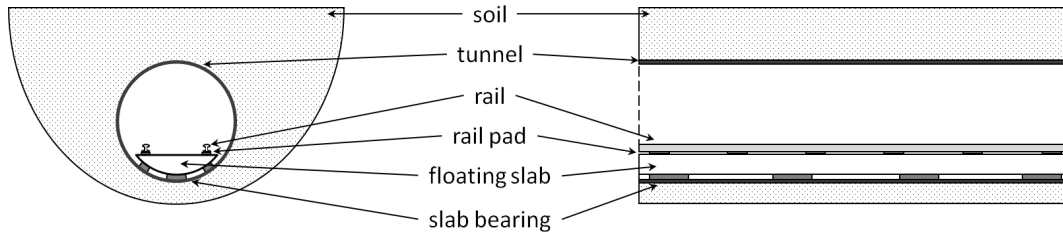


Figure 3.4: Underground railway cut-away showing floating-slab track

and certain elements of the matrices  $\tilde{\mathbf{H}}_{\text{tunnel}}$  and  $\tilde{\mathbf{H}}_{\text{soil}}$  require a change in sign as detailed in Appendix E. The magnitude of a point-load for the axial and circumferential directions is equivalent to that given in Equation 3.10 for the radial direction.

### 3.1.2 Inclusion of Floating-Slab Track in PiP Model

A popular method of installing railway track in underground railways is to use a floating-slab track (FST) system. Rather than employing traditional wooden sleepers and crushed stone ballast, the rails are fastened to a concrete slab which sits on the base of the tunnel invert. To reduce vibration transmission the rails are generally mounted on resilient rubber railpads and the slab on rubber or steel-spring slab bearings as depicted in Figure 3.4.

Forrest and Hussein have thoroughly investigated the modelling of floating-slab track (both continuous and discontinuous) using the PiP method for non-moving and moving loads<sup>[33–35,61,63,64]</sup>. A simple, continuous FST subjected to a quasi-static moving load is included in the current investigation; the more complex systems could be included using the methods derived in the referenced literature.

A schematic of the FST model is shown in Figure 3.5 where it has been simplified to a 2D system; the two rails are assumed to receive identical vertical inputs thus they are combined into a single beam. The rail and slab are modelled as Euler-Bernoulli beams with mass per unit length  $m$  and bending stiffness  $EI$ . The railpads and slab bearings are modelled as continuous layers of elastic support with stiffness per unit length  $k$  and associated loss factor  $\eta$ ; the resulting complex stiffness is given by  $k^* = k(1 + i\eta)$ .

Table 3.1: Floating-slab track properties

| Rail Beam                          | Slab beam                          |
|------------------------------------|------------------------------------|
| $m_{rail} = 120.6 \text{ kg/m}$    | $m_{slab} = 3500 \text{ kg/m}$     |
| $EI_{rail} = 12.9 \text{ MPa m}^4$ | $EI_{slab} = 1430 \text{ MPa m}^4$ |
| Railpad                            | Slab Bearing                       |
| $k_{rail} = 200 \text{ MN/m/m}$    | $k_{slab} = 5 \text{ MN/m/m}$      |
| $\eta_{rail} = 0.3$                | $\eta_{slab} = 0.5$                |

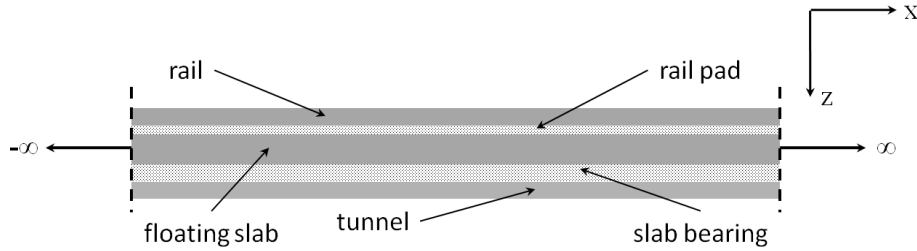


Figure 3.5: Floating-slab track on tunnel invert

The slab-bearing is assumed to only be in contact with the tunnel along the bottom of the invert (i.e. equivalent to a line-load). The FST properties used herein are given in Table 3.1 which approximate UIC60 rails on a standard continuous slab as used by Hussein<sup>[64]</sup>.

The transfer function of the FST assembly is derived as follows. The equation of motion for a Euler-Bernoulli beam is<sup>[47,106]</sup>

$$m \frac{\partial^2 u}{\partial t^2} + EI \frac{\partial^4 u}{\partial x^4} = f(x, t) \quad (3.12)$$

where  $m$  is the mass per unit length,  $E$  is the elastic modulus,  $I$  is the second moment of area, and  $f(x, t)$  is the distribute force per unit length acting on the beam. Assuming the displacements are harmonic in time and space, this can be written in the wavenumber-frequency domain as

$$(EI\xi^4 - m\omega^2) \tilde{U}(\xi, \omega) = \tilde{F}(\xi, \omega) \quad (3.13)$$

thus the transfer function for the beam is

$$\tilde{H}_{\text{beam}}(\xi, \omega) = \frac{1}{(EI\xi^4 - m\omega^2)} \quad (3.14)$$

where  $\omega$  is the frequency and  $\xi$  is the wavenumber in the  $x$ -direction as defined in Figure 3.5.

It is necessary to determine the transfer function for the FST assembly shown in Figure 3.5 giving the displacements at the tunnel due to a load on the rail; this will be used to facilitate loading in the coupled tunnel-soil model. The transfer function for the rail-railpad-slab assembly can be derived by enforcing

- displacement continuity between the rail and railpad
- displacement continuity between the railpad and the slab
- force equilibrium across the railpad.

This results in the coupled equations of motion

$$\begin{Bmatrix} \tilde{U}_{\text{rail}} \\ \tilde{U}_{\text{slab}} \end{Bmatrix} = \begin{Bmatrix} \tilde{H}_{rr} & \tilde{H}_{rs} \\ \tilde{H}_{sr} & \tilde{H}_{ss} \end{Bmatrix} \begin{Bmatrix} \tilde{F}_{\text{rail}} \\ \tilde{F}_{\text{slab}} \end{Bmatrix} \quad (3.15)$$

where

$$\begin{aligned} \tilde{H}_{rr} &= \frac{\tilde{H}_{\text{rail}}(1 + k_{\text{rail}}^* \tilde{H}_{\text{slab}})}{(1 + k_{\text{rail}}^* \tilde{H}_{\text{slab}} + k_{\text{rail}}^* \tilde{H}_{\text{rail}})} \\ \tilde{H}_{rs} &= \frac{k_{\text{rail}}^* \tilde{H}_{\text{rail}} \tilde{H}_{\text{slab}}}{(1 + k_{\text{rail}}^* \tilde{H}_{\text{slab}} + k_{\text{rail}}^* \tilde{H}_{\text{rail}})} = \tilde{H}_{sr} \\ \tilde{H}_{ss} &= \frac{\tilde{H}_{\text{slab}}(1 + k_{\text{rail}}^* \tilde{H}_{\text{rail}})}{(1 + k_{\text{rail}}^* \tilde{H}_{\text{slab}} + k_{\text{rail}}^* \tilde{H}_{\text{rail}})}. \end{aligned} \quad (3.16)$$

This process can be repeated to couple the rail-railpad-slab assembly to the tunnel through the slab-bearing by enforcing

- displacement continuity between the slab and slab-bearing
- displacement continuity between the slab-bearing and the tunnel
- force equilibrium across the slab-bearing.

This results in the FST transfer function matrix

$$\begin{Bmatrix} \tilde{U}_{\text{rail}} \\ \tilde{U}_{\text{tunnel}} \end{Bmatrix} = \begin{Bmatrix} \tilde{H}_{rr} & \tilde{H}_{rt} \\ \tilde{H}_{tr} & \tilde{H}_{tt} \end{Bmatrix} \begin{Bmatrix} \tilde{F}_{\text{rail}} \\ \tilde{F}_{\text{tunnel}} \end{Bmatrix} \quad (3.17)$$

where

$$\begin{aligned} \tilde{H}_{rr} &= \frac{\tilde{H}_{\text{tunnel}}(1 + k_{\text{slab}}^* \tilde{H}_{\text{ss}})}{(1 + k_{\text{slab}}^* \tilde{H}_{\text{ss}} + k_{\text{slab}}^* \tilde{H}_{\text{tunnel}})} \\ \tilde{H}_{rt} &= \frac{k_{\text{slab}}^* \tilde{H}_{rs} \tilde{H}_{\text{tunnel}}}{(1 + k_{\text{slab}}^* \tilde{H}_{\text{ss}} + k_{\text{slab}}^* \tilde{H}_{\text{tunnel}})} = \tilde{H}_{tr} \\ \tilde{H}_{tt} &= \frac{\tilde{H}_{\text{ss}}(1 + k_{\text{slab}}^* \tilde{H}_{\text{tunnel}})}{(1 + k_{\text{slab}}^* \tilde{H}_{\text{ss}} + k_{\text{slab}}^* \tilde{H}_{\text{tunnel}})} \end{aligned} \quad (3.18)$$

and  $\tilde{H}_{\text{tunnel}}$  is the  $RR$  component of  $\tilde{\mathbf{H}}_{\text{tunnel}}$  as defined in Equation 3.1.

Recall Equation 3.8 which gives the coupled tunnel-soil interface displacements as a function of the original free-tunnel displacements

$$\tilde{\mathbf{U}}_n = \left( \mathbf{I} + \tilde{\mathbf{H}}_{\text{tunnel}} \tilde{\mathbf{H}}_{\text{soil}}^{-1} \right)^{-1} \tilde{\mathbf{U}}_n^{\text{orig}}.$$

Equation 3.17 can be used to determine  $\tilde{\mathbf{U}}_n^{\text{orig}}$  by setting  $\tilde{F}_{\text{tunnel}} = 0$  giving

$$\tilde{\mathbf{U}}_n^{\text{orig}} = \tilde{H}_{tr} \tilde{F}_n^{\text{rail}}. \quad (3.19)$$

If the load applied to the rail is assumed to be a point-load in the spatial-domain, the load in the frequency, wavenumber and ring-mode domain is

$$\tilde{F}_n^{\text{rail}} = \begin{cases} 1/2\pi a, & n = 0 \\ 1/\pi a, & n \geq 1 \end{cases} \quad (3.20)$$

as defined in Equation 3.10.

It should be noted that  $\tilde{\mathbf{H}}_{\text{tunnel}}$  in Equation 3.8 is not adjusted to account for the presence of the FST when solving for the coupled tunnel-soil interface displacements. It was found the increased stiffness due to the FST was negligible compared to the concrete tunnel thus was neglected for simplicity; this assumption is supported by Forrest<sup>[33]</sup> and Gupta *et al.*<sup>[52]</sup>.

The isolation properties of the FST assembly can be visualized by computing the total force transmission curve as a function of frequency; force transmission is the ratio of the force acting at the tunnel invert to the input force. The total force transmission can be calculated exactly using a double mass-spring approximation<sup>[33]</sup> using the following equation

$$\frac{F_T}{F_{\text{input}}} = \frac{k_{\text{rail}}^* k_{\text{slab}}^*}{(m_{\text{rail}}\omega^2 - k_{\text{rail}}^*)((m_{\text{slab}}\omega^2 - k_{\text{slab}}^*) - k_{\text{rail}}^* m_{\text{rail}}\omega^2)} \quad (3.21)$$

The frequency response curve for the FST properties listed in Table 3.1 is shown in Figure 3.6. The main peak at 6Hz is governed by the resonance of the slab on the slab bearing while the broad peak around 200Hz is the resonance of the rails on the railpads. These resonances mark the onset of travelling waves in the respective subassemblies. As shown in the figure, the total force transmission drops below unity (i.e. 0dB) above 10Hz and decreases through the frequency range of interest 15-200Hz.

During the derivation of the coupled tunnel-soil displacement equation it is assumed that the tunnel is in continuous contact with the soil, thus the PiP model in its standard form does not allow for discrete sections of the tunnel to be uncoupled from the soil. To investigate the effect of voids around the tunnel the method is extended by discretizing

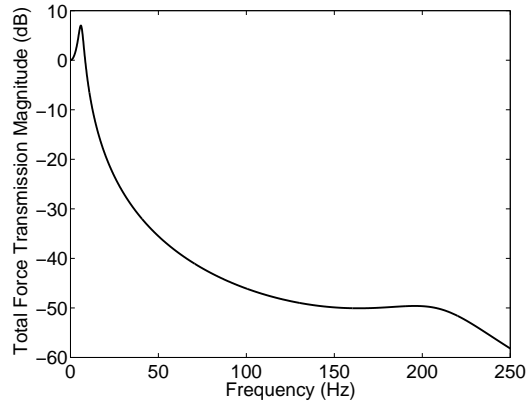


Figure 3.6: Total force transmission of floating-slab track

the tunnel-soil interface.

### 3.1.3 Discrete Tunnel-Soil Interface

To simulate voids using the PiP model the interface is discretized into a number of nodes with their respective transfer functions determined using the continuous solution. Once the global transfer function matrix for the interface is calculated, particular nodes can be uncoupled to simulate the void at the tunnel-soil interface.

Consider an example case shown in Figure 3.7, where the circumference of the tunnel is discretized into 8 nodes. A single unit point-load is applied in the positive radial direction at node 1, causing displacements at all nodes (displacements only depicted at nodes 1 and 3 for clarity). The nodal loading the  $R$ -direction can be written as

$$\tilde{\mathbf{F}} = \begin{bmatrix} 1 & 0 & 0 & 0 & 0 & 0 & 0 & 0 \end{bmatrix}^T. \quad (3.22)$$

The Fourier transform of this force is

$$\tilde{\mathbf{F}}_n = \begin{bmatrix} 1 & 1 & 1 & 1 & 1 & 1 & 1 & 1 \end{bmatrix}^T \quad (3.23)$$

where the subscript  $n$  indicates the ring-mode domain. In the current work the discrete

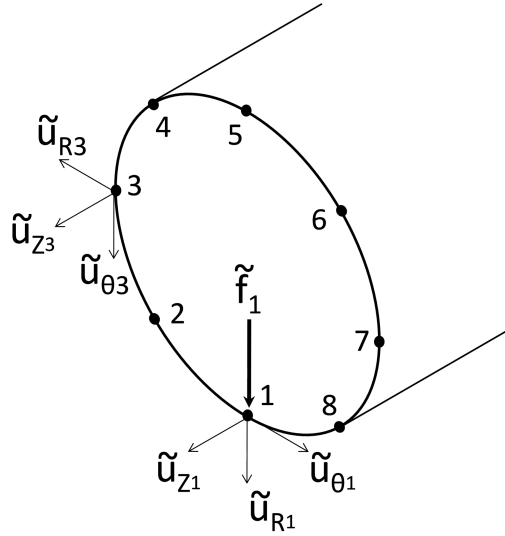


Figure 3.7: Circumferential discretization of tunnel; example tunnel circumference discretized by 8 nodes with a point load applied radially at node 1, showing cylindrical coordinate directions

Fourier transform (DFT) is used to perform the transformations.

The displacements in the ring-mode domain can be calculated for each term in the  $\tilde{\mathbf{F}}_n$  vector using Equation 3.1, resulting in

$$\begin{aligned}
 \tilde{\mathbf{U}}_{Zn} &= \left[ \tilde{U}_{Z_0} \quad \tilde{U}_{Z_1} \quad \tilde{U}_{Z_2} \quad \tilde{U}_{Z_3} \quad \tilde{U}_{Z_4} \quad \tilde{U}_{Z_5} \quad \tilde{U}_{Z_6} \quad \tilde{U}_{Z_7} \right]^T \\
 \tilde{\mathbf{U}}_{\theta n} &= \left[ \tilde{U}_{\theta_0} \quad \tilde{U}_{\theta_1} \quad \tilde{U}_{\theta_2} \quad \tilde{U}_{\theta_3} \quad \tilde{U}_{\theta_4} \quad \tilde{U}_{\theta_5} \quad \tilde{U}_{\theta_6} \quad \tilde{U}_{\theta_7} \right]^T \\
 \tilde{\mathbf{U}}_{Rn} &= \left[ \tilde{U}_{R_0} \quad \tilde{U}_{R_1} \quad \tilde{U}_{R_2} \quad \tilde{U}_{R_3} \quad \tilde{U}_{R_4} \quad \tilde{U}_{R_5} \quad \tilde{U}_{R_6} \quad \tilde{U}_{R_7} \right]^T.
 \end{aligned} \tag{3.24}$$

Since the circumference of the cylinder is discretized into a finite number of points ( $N_{\text{ring}}$ ), the Nyquist criterion restricts the largest ring mode to  $N_{\text{ring}}/2$ . Furthermore, Equation 3.9 states that  $\tilde{\mathbf{U}}_{Zn}$  and  $\tilde{\mathbf{U}}_{Rn}$  are even functions and  $\tilde{\mathbf{U}}_{\theta n}$  is an odd function. Therefore the ring-mode coefficients are symmetric and anti-symmetric respectively. The ring-mode coefficients are written in standard inverse DFT (IDFT) input notation

as follows

$$\begin{aligned}\tilde{\mathbf{U}}_{Zn} &= \left[ \tilde{U}_{Z_0} \quad \tilde{U}_{Z_1} \quad \tilde{U}_{Z_2} \quad \tilde{U}_{Z_3} \quad \tilde{U}_{Z_4} \quad \tilde{U}_{Z_3} \quad \tilde{U}_{Z_2} \quad \tilde{U}_{Z_1} \right]^T \\ \tilde{\mathbf{U}}_{\theta n} &= \left[ 0 \quad -i\tilde{U}_{\theta_1} \quad -i\tilde{U}_{\theta_2} \quad -i\tilde{U}_{\theta_3} \quad 0 \quad i\tilde{U}_{\theta_3} \quad i\tilde{U}_{\theta_2} \quad i\tilde{U}_{\theta_1} \right]^T \\ \tilde{\mathbf{U}}_{Rn} &= \left[ \tilde{U}_{R_0} \quad \tilde{U}_{R_1} \quad \tilde{U}_{R_2} \quad \tilde{U}_{R_3} \quad \tilde{U}_{R_4} \quad \tilde{U}_{R_3} \quad \tilde{U}_{R_2} \quad \tilde{U}_{R_1} \right]^T.\end{aligned}\quad (3.25)$$

Performing the IDFT results in a set of transfer function terms

$$\begin{aligned}\tilde{\mathbf{H}}_{Z_i R_1} \\ \tilde{\mathbf{H}}_{\theta_i R_1} \\ \tilde{\mathbf{H}}_{R_i R_1}\end{aligned}\quad (3.26)$$

where each term represents the displacement ( $Z$ ,  $\theta$ , or  $R$ ) of the  $i$ th node due to a radial point-load at node 1. This process is repeated to determine the transfer functions at every node due to loads acting in all three directions.

The transfer function terms can be arranged in matrix form as follows

$$\begin{Bmatrix} \tilde{\mathbf{U}}_Z \\ \tilde{\mathbf{U}}_\theta \\ \tilde{\mathbf{U}}_R \end{Bmatrix} = \begin{bmatrix} \tilde{\mathbf{H}}_{Z_i Z_j} & \tilde{\mathbf{H}}_{Z_i \theta_j} & \tilde{\mathbf{H}}_{Z_i R_j} \\ \tilde{\mathbf{H}}_{\theta_i Z_j} & \tilde{\mathbf{H}}_{\theta_i \theta_j} & \tilde{\mathbf{H}}_{\theta_i R_j} \\ \tilde{\mathbf{H}}_{R_i Z_j} & \tilde{\mathbf{H}}_{R_i \theta_j} & \tilde{\mathbf{H}}_{R_i R_j} \end{bmatrix}_\xi \begin{Bmatrix} \tilde{\mathbf{F}}_Z \\ \tilde{\mathbf{F}}_\theta \\ \tilde{\mathbf{F}}_R \end{Bmatrix} = \tilde{\mathbf{H}}\tilde{\mathbf{F}}\quad (3.27)$$

which describes, for a given wavenumber  $\xi$ , the displacements at all nodes due to an arbitrary load applied with frequency  $\omega$ . An IDFT is used to transform the set of transfer functions into the spatial domain,  $\mathbf{H}_{\text{tunnel}}$  and  $\mathbf{H}_{\text{soil}}$ , thus the coupled equations of motion for the tunnel-soil system can be written in the spatial domain as

$$\mathbf{U} = (\mathbf{I} + \mathbf{H}_{\text{tunnel}}\mathbf{H}_{\text{soil}}^{-1})^{-1} \mathbf{U}^{\text{orig}}.\quad (3.28)$$

The wavenumber sampling and maximum values must be selected to ensure the

discretization is sufficient to capture details at localized peaks as well as the far-field disturbance of traveling waves. The results from a convergence study investigating the effect of wavenumber properties on the response of a free-tunnel are shown in Figure 3.8. The tunnel is subjected to a radially-acting unit point load at  $x=0$  and the radial displacement response in the spatial domain along the base of the tunnel is plotted to determine convergence.

Figure 3.8(a) shows the response at 15Hz; at this low frequency the wavelengths are relatively long thus fine discretization in the wavenumber domain is required to capture the corresponding small wavenumbers. As the number of samples between  $-2\pi\frac{1}{m} < \xi < 2\pi\frac{1}{m}$  is increased the solution tends towards the converged solution at  $N=2^{14}$  samples. At higher frequencies the wavelengths are relatively short thus the maximum wavenumber must be increased to capture the localized peaks. Figure 3.8(b) shows convergence of the solution at  $\xi_{max} = 2\pi\frac{1}{m}$ .

These wavenumber parameters ( $N=2^{14}$  and  $\xi_{max} = 2\pi\frac{1}{m}$ ) were found to be sufficient to capture the response in the free-tunnel when the FST assembly is included and subjected to a point load on the rail, as well as for the free-soil model subjected to a point load. As such they are used throughout the remainder of the investigation. Note that these parameters result in a total model length of  $-4096m < x < 4096m$  with  $\Delta x = 0.5m$  according to the conversions

$$\xi_{max} = \frac{2\pi}{2\Delta x} \quad (3.29)$$

and

$$\Delta\xi = \frac{2\pi}{x_{max}}. \quad (3.30)$$

This discretized spatial formulation of PiP allows nonuniform interaction between the tunnel and surrounding soil making it possible to simulate variable stiffness between the tunnel and soil, such as a void at the tunnel-soil interface.

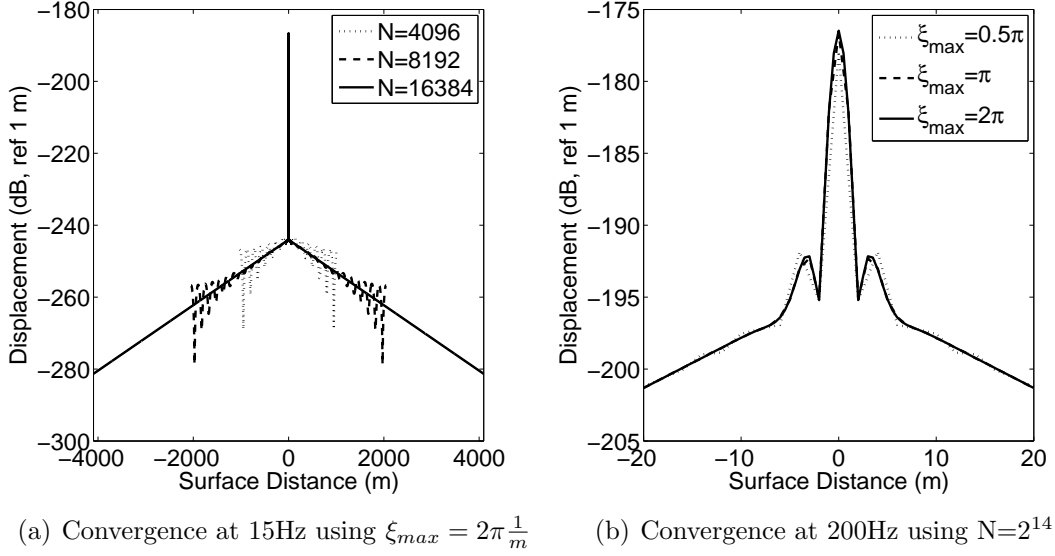


Figure 3.8: Wavenumber parameter convergence testing for free-tunnel model subjected to a radial point load at  $x=0$

### 3.1.4 Including a Void in the Discrete Model

To simulate a void at the tunnel-soil interface, individual matching nodes on the tunnel and soil cylinders can be uncoupled. This allows the displacements of the two subsystems to differ at the void location while preventing any transfer of force between the tunnel and the soil. The degrees of freedom for both the tunnel and the soil are rearranged to group the coupled and uncoupled nodes

$$\begin{Bmatrix} \mathbf{U}_c \\ \mathbf{U}_u \end{Bmatrix} = \begin{bmatrix} \mathbf{H}_{cc} & \mathbf{H}_{cu} \\ \mathbf{H}_{uc} & \mathbf{H}_{uu} \end{bmatrix} \begin{Bmatrix} \mathbf{F}_c \\ \mathbf{F}_u \end{Bmatrix} \quad (3.31)$$

where the subscripts  $c$  and  $u$  refer to the coupled and uncoupled degrees of freedom, respectively. Rewriting the continuity equations (Equations 3.3 and 3.4) for the displacement of the coupled nodes gives

$$\mathbf{U}_{\text{tunnel}_c} = \mathbf{H}_{\text{tunnel}_{cc}} \mathbf{F}_c + \mathbf{H}_{\text{tunnel}_{cu}} \mathbf{F}_u + \mathbf{H}_{\text{tunnel}_{cc}} \mathbf{R}_{\text{tunnel}_c} + \mathbf{H}_{\text{tunnel}_{cu}} \mathbf{R}_{\text{tunnel}_u} \quad (3.32)$$

$$\mathbf{U}_{\text{soil}_c} = \mathbf{H}_{\text{soil}_{cc}} \mathbf{R}_{\text{soil}_c} + \mathbf{H}_{\text{soil}_{cu}} \mathbf{R}_{\text{soil}_u} \quad (3.33)$$

where displacement continuity and force equilibrium requires

$$\mathbf{U}_{\text{tunnel}_c} = \mathbf{U}_{\text{soil}_c} \quad (3.34a)$$

$$\mathbf{R}_{\text{tunnel}_c} = -\mathbf{R}_{\text{soil}_c} \quad (3.34b)$$

$$\mathbf{R}_{\text{tunnel}_u} = -\mathbf{R}_{\text{soil}_u}. \quad (3.34c)$$

Assuming that no internal forces will be applied to the uncoupled nodes (i.e.  $\mathbf{F}_u = \mathbf{0}$ ) and recalling that no resultant interface forces develop at these uncoupled nodes (i.e.  $\mathbf{R}_u = \mathbf{0}$ ), Equations 3.32 and 3.33 can be combined as

$$\mathbf{U}_c = (\mathbf{I} + \mathbf{H}_{\text{tunnel}_{cc}} \mathbf{H}_{\text{soil}_{cc}}^{-1})^{-1} \mathbf{H}_{\text{tunnel}_{cc}} \mathbf{F}_c. \quad (3.35)$$

Noting that  $\mathbf{H}_{\text{tunnel}_{cc}} \mathbf{F}_c = \mathbf{U}_c^{\text{orig}}$  Equation 3.35 can be written as

$$\mathbf{U}_c = (\mathbf{I} + \mathbf{H}_{\text{tunnel}_{cc}} \mathbf{H}_{\text{soil}_{cc}}^{-1})^{-1} \mathbf{U}_c^{\text{orig}} \quad (3.36)$$

which describes the displacement at the coupled degrees of freedom for the tunnel-soil model as a function of the original free-tunnel displacements at the coupled nodes. Equation 3.36 is in a useful form to perform parametric studies of void parameters.  $\mathbf{H}_{\text{tunnel}}$  and  $\mathbf{H}_{\text{soil}}$  are the same for each case and need only be partitioned to include the appropriate nodes.  $\mathbf{U}_c^{\text{orig}}$  can be calculated relatively quickly and easily using the IDFT of Equation 3.19; as  $\mathbf{U}_c^{\text{orig}}$  is only a function of the FST and tunnel parameters it is the same for all void cases. This allows for more efficient calculation when investigating numerous void parameters.

The resultant interface loads can be back-calculated from  $\mathbf{U}_c$  using

$$\mathbf{H}_{\text{soil}_{cc}}^{-1} \mathbf{U}_c = \mathbf{R}_c \quad (3.37)$$

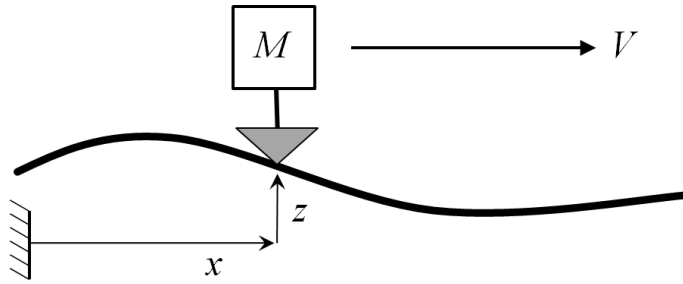


Figure 3.9: Schematic of simple vehicle model

and  $\mathbf{R}_u = \mathbf{0}$ . After rearranging the nodes back to the original order this resultant interface load vector can be used to determine the soil response at any desired radius  $R$  using

$$\mathbf{U}_R = \mathbf{H}_{\text{soil}_R} \mathbf{R}_{\text{interface}} \quad (3.38)$$

where  $\mathbf{H}_{\text{soil}_R}$  is derived in a similar way to the original soil transfer function as described in Appendix E. This formulation is also efficient for parametric studies of void parameters;  $\mathbf{H}_{\text{soil}_R}$  is the same for all void cases thus  $\mathbf{U}_R$  can be calculated quickly for any case after the initial determination of the transfer function matrix.

This form of the solution can predict ground vibrations at any radius due to a dynamic load applied to the rail on the FST assembly at a fixed location. It is now useful to consider moving loads.

### 3.1.5 Response due to a Moving Load

Amongst many others, Hussein and Hunt<sup>[63]</sup> show that a predominant loading mechanism on the tunnel invert is due to rail-roughness at the wheel-rail interface. For the purposes of the current investigation this loading mechanism is simplified to a single, moving point-load acting on the rail surface. The load is calculated using a single degree-of-freedom model of a 500kg mass moving at constant speed along a rough rail (Figure 3.9) as

$$F(x) = Ma(x) = -M\omega^2 z(x). \quad (3.39)$$

The rail-roughness profile is randomly distributed thus the theory of random vibrations<sup>[106]</sup> must be used to predict the resultant soil response. As the velocity of the moving load is much less than the shear-wave speed of the surrounding soil a quasi-stationary approximation of a non-stationary random vibration can be used<sup>[89]</sup>. This implies that the Doppler effect of the moving load is negligible so the load at any given point in time can be assumed a stationary random process (i.e. the mean, mean square and standard deviation are all independent of time).

Frederich<sup>[36]</sup> provides an empirical formula for the single-sided rail-roughness spectrum based on track measurements. The average rail-roughness is calculated as follows

$$S_{\delta}(\omega) = \frac{a}{v \left( b + \frac{\omega}{2\pi v} \right)^3} \quad (3.40)$$

where  $v$  is the load velocity (m/s),  $\omega$  is the forcing frequency (rad/s), and  $a$  and  $b$  are constants describing the rail unevenness ( $1.31 \times 10^{-2} \text{ mm}^2/\text{m}^2$  and  $2.94 \times 10^{-2} \text{ /m}$ , respectively<sup>1</sup>). Using Equation 3.39 and standard random vibration theory<sup>[106]</sup>, the force spectrum magnitude can be written as

$$S_f(\omega) = |m\omega^2|^2 S_{\delta}(\omega). \quad (3.41)$$

The discrete void model is used to determine the transfer function ( $H_{ij}$ ) describing the displacement at an arbitrary point  $r_i$  in the surrounding soil for a point load applied to the rail at  $x_j$ . The velocity spectrum magnitude at this arbitrary point is given by

$$S_v(\omega) = |(i\omega)H_{ij}|^2 S_f(\omega). \quad (3.42)$$

This velocity spectrum can be used to provide a measure of the mean-square velocity

---

<sup>1</sup>An error was found after compilation of the results: the magnitude of the single-sided rail-roughness was mistakenly multiplied by two resulting in  $a = 2.62 \times 10^{-2} \text{ mm}^2/\text{m}^2$ . According to Equation 3.43 this resulted in an increase of all absolute rms frequency band predictions by  $20\log_{10}\sqrt{2} \cong 3 \text{ dB}$  but does not affect insertion gain results.

Table 3.2: Third octave bands as defined by ISO R266

| Reference name (Hz) | Frequency band (Hz) |
|---------------------|---------------------|
| 20                  | 17.8 - 22.4         |
| 25                  | 22.4 - 28.2         |
| 31.5                | 28.2-35.5           |
| 40                  | 35.5 - 44.7         |
| 50                  | 44.7 - 56.2         |
| 63                  | 56.2 - 70.8         |
| 80                  | 70.8 - 89.1         |
| 100                 | 89.1 - 112          |
| 125                 | 112 - 141           |
| 160                 | 141 - 178           |
| 200                 | 178 - 224           |

over a frequency band using the following property

$$E[v^2]_{\omega_1 \rightarrow \omega_2} = \int_{\omega_1}^{\omega_2} S_v(\omega) d\omega. \quad (3.43)$$

The rms velocity over the frequency band is simply the square-root of Equation 3.43. Note this derivation of the  $\omega_1 \rightarrow \omega_2$  frequency band rms velocity is equivalent to having a perfect band filter which eliminates all input frequencies outside the band of interest. Although this is an idealized value it is still a useful measure of the vibration levels at different frequency bands. The vertical rms velocities are determined in third-octave frequency bands according to Table 3.2.

The final step is to consider the slow variation of the rms particle velocity as the load travels along the length of the tunnel. This is best shown through the example detailed in Section 3.3. First it is sensible to validate the discrete model of a tunnel in continuous contact with the soil against PiP.

## 3.2 Validation of discrete model against PiP

A schematic of the 3D tunnel-soil interface used in the semi-analytical model is shown in Figure 3.10; Table 3.3 lists the set of sample material properties used in the simulation

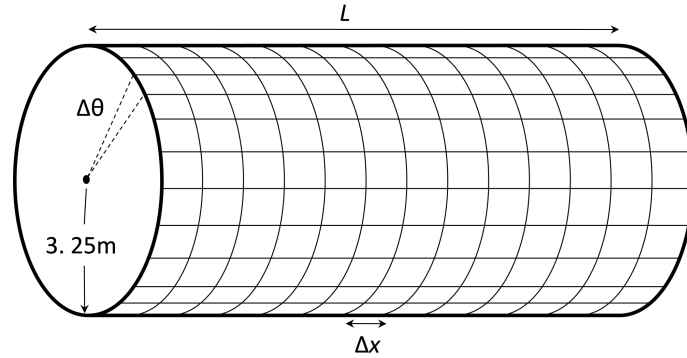


Figure 3.10: Geometric parameters for model and mesh

Table 3.3: Soil model properties

|                                      | <b>Tunnel</b>  | <b>Soil</b>      |
|--------------------------------------|----------------|------------------|
| Elastic modulus (GPa)                | $50(1 + 0.1i)$ | $0.55(1 + 0.1i)$ |
| Density ( $\text{kg} / \text{m}^3$ ) | 2500           | 2000             |
| Poisson's ratio                      | 0.3            | 0.44             |
| P-wave speed (m/s)                   | 5200           | 950              |
| S-wave speed (m/s)                   | 2800           | 310              |

of a 0.25m thick concrete tunnel and surrounding soil. The vertical particle velocities are calculated for a  $30\text{m} \times 30\text{m}$  observation plane 15m above the center of the tunnel as depicted in Figure 3.11.

Recall from Section 3.1.3 that the free-tunnel and free-soil models were deemed to converge in the wavenumber domain for  $N=2^{14}$  and  $\xi_{\max} = 2\pi$ . This is equivalent to a total model length of  $-4096\text{m} < x < 4096\text{m}$  with  $\Delta x = 0.5\text{m}$ . If, for example, 32 nodes are used around the circumference of the interface with 3 degrees of freedom each, this would result in a total of more than 1.5 million degrees of freedom; this is an impractical number of DOF's for a model which is intended for parametric studies with short computational times. When the tunnel is coupled to the soil model the system damping is greatly increased due to geometric decay and material damping in the soil. The hypothesis is that much less of the model in the axial direction will be required as the travelling waves will quickly decay.

To test this hypothesis a convergence test is performed to ensure that the spatial

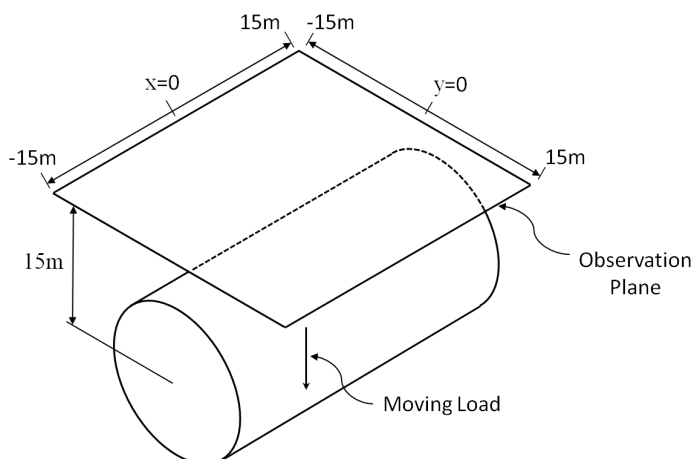


Figure 3.11: Observation plane centered over the tunnel at height 15m

parameters of the tunnel-soil interface are sufficient to adequately represent the continuous bond at this interface. A harmonic load is applied to the rail at  $x = 0$  at 15Hz and 200Hz (i.e. the limits of the frequency range of interest) and the displacement response is calculated along four horizontal lines 15 meters above the tunnel extending perpendicular to the tunnel axis as depicted in Figures 3.12 and 3.13. The effect of circumferential nodal density (nodes/circumference or  $N/C$ ) and the half length of the model ( $x_{max}$ ) are illustrated in the figures. Three representative sets of parameters are shown in comparison to the continuous PiP solution. The results are deemed to converge when refining the parameters results in less than a 1% relative difference at any  $x$ -location from the previous case; convergence was found to occur using 32 nodes per circumference with  $x_{max} = 40\text{m}$ . As shown in Figures 3.12 and 3.13 these model parameters result in predictions which agree well with the continuous PiP solution at the given locations and frequencies. The maximum difference between the two model predictions is 0.1dB which occurs at  $y=15\text{m}$  and 15Hz (Figure 3.12(d)).

The vertical rms particle velocities over the observation plane are predicted by the void-free discrete model using  $N/C = 32$  and  $x_{max} = 40\text{m}$ . The results for the 25Hz, 50Hz, 100z and 160Hz third-octave frequency bands are shown in Figure 3.14 as a representative sample of the results; results are plotted in dB(rms, ref 1 m/s) when the moving load is at  $x=0$ . These results are compared to the PiP prediction in Figure 3.15

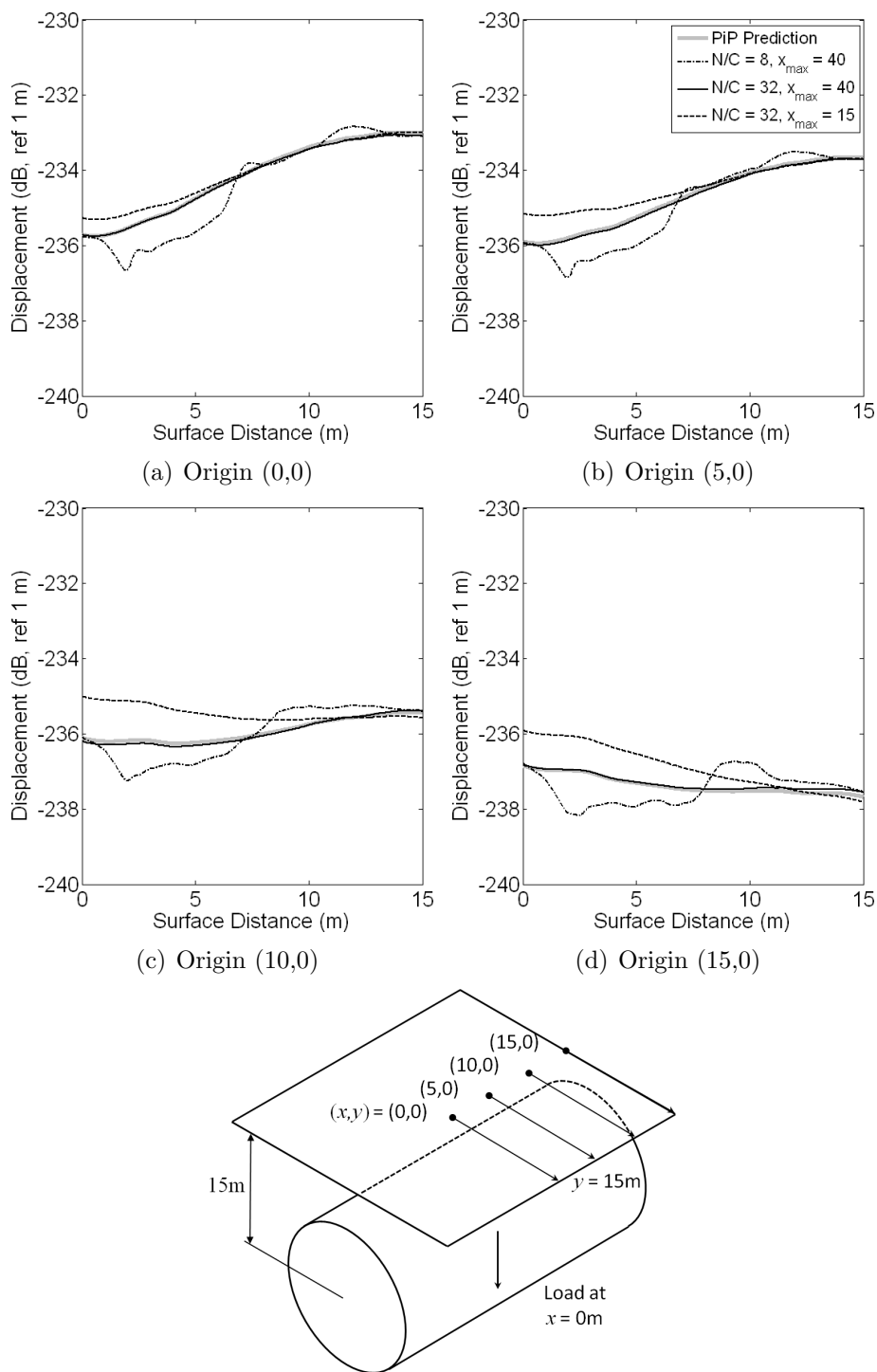


Figure 3.12: Validation of discrete model against PiP at 15Hz; three test cases shown for varying node density around the tunnel circumference ( $N/C$ ) and axial length ( $x_{max}$ )

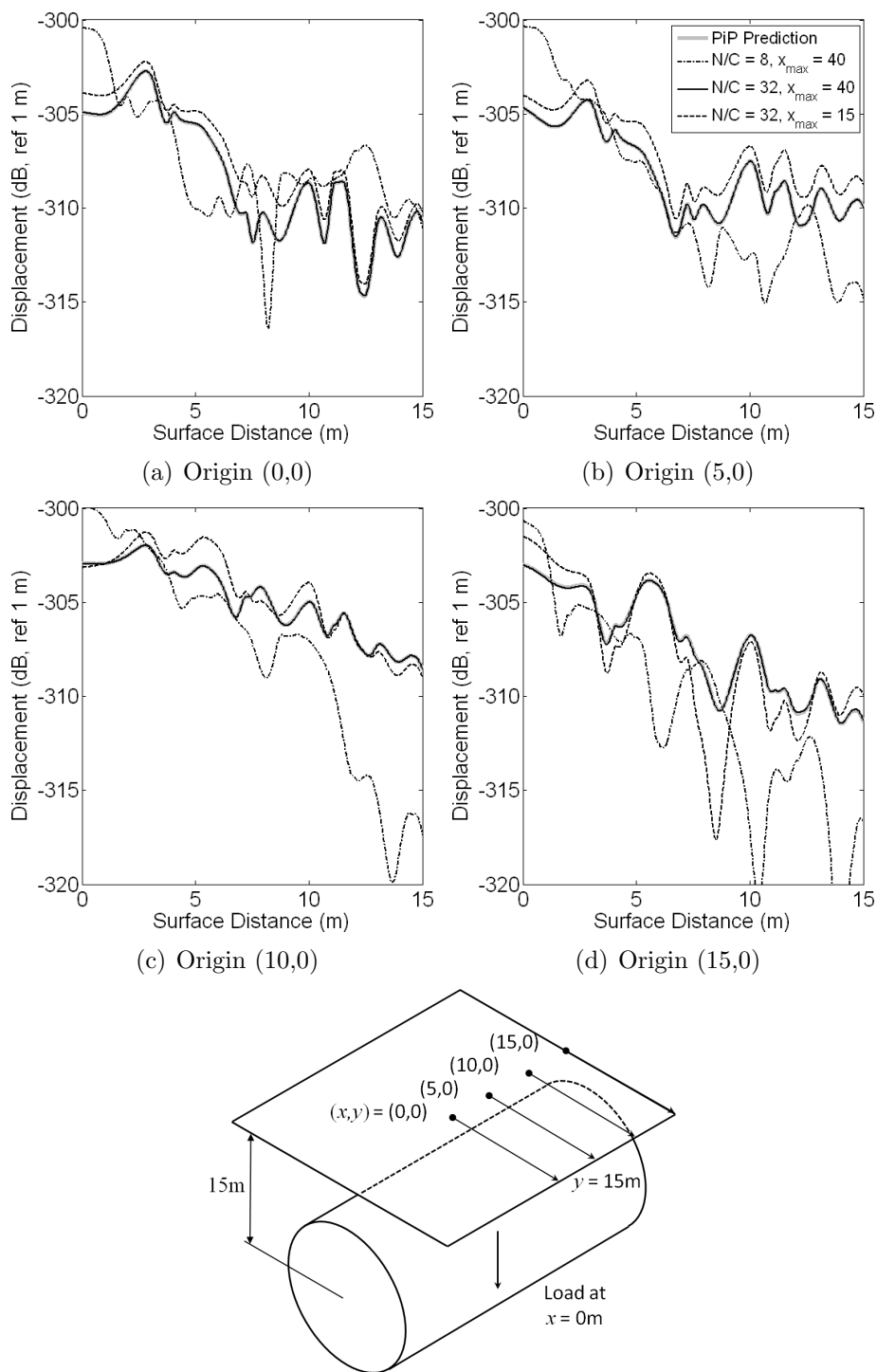


Figure 3.13: Validation of discrete model against PiP at 200Hz; three test cases shown for varying node density around the tunnel circumference ( $N/C$ ) and axial length ( $x_{max}$ )

where the difference between the two models are plotted in dB for the same four frequency bands; a positive difference signifies the discrete model predicts larger values than PiP.

The results from the two models show good agreement at all frequency bands. The maximum difference is (+0.9,-0.7)dB occurring at the 25Hz frequency band shown in Figure 3.15(a); differences at higher frequency bands are significantly lower ( $< 0.1$ dB). The larger error at the low frequency band is attributed to the truncation of the longest wavelengths by the reduced model length  $x_{max} = 40$ m, hence the areas of greatest error occur at large  $x$ -values rather than at the center of the model. This relatively small difference between two different numerical models suggest the discrete model is valid for a continuously coupled tunnel-soil interface. The final section considers the same tunnel-soil parameters but with the inclusion of a void.

### 3.3 Simulating voids using the discrete model

To quantify the effect of a void on vertical response compared to a continuously bonded model a number of different void configurations are investigated; Table 3.4 lists the void parameters. A schematic showing the tunnel, observation plane, moving load and void placement is presented in Figure 3.16 with a schematic showing the void parameters in Figure 3.17. For all cases the void is centered on the top of the tunnel at  $(x,y) = (0,0)$  in the observation plane.

As an example of the response due to a moving load, the discrete model is used to predict the vertical particle velocity response for the case of a  $4\text{m} \times 90.0^\circ$  void (VA-3) subjected to a moving point-load oscillating at 100Hz. The nine figures presented in Figure 3.18 represent the response as the load position (LP) moves from left to right through the tunnel ( $-12\text{m} \rightarrow 12\text{m}$  in 3m intervals). When the load is relatively far from the void (LP1 - LP2) the response is symmetric in both the  $x$  and  $y$  directions and seemingly unaffected by the presence of the void. As the load approaches the void

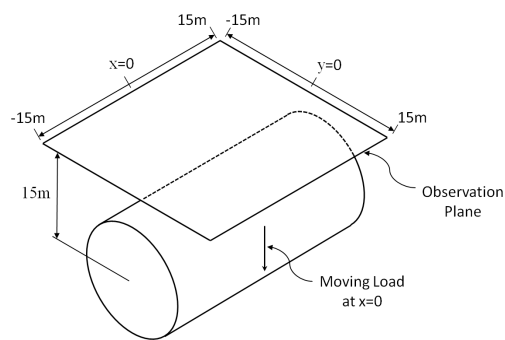
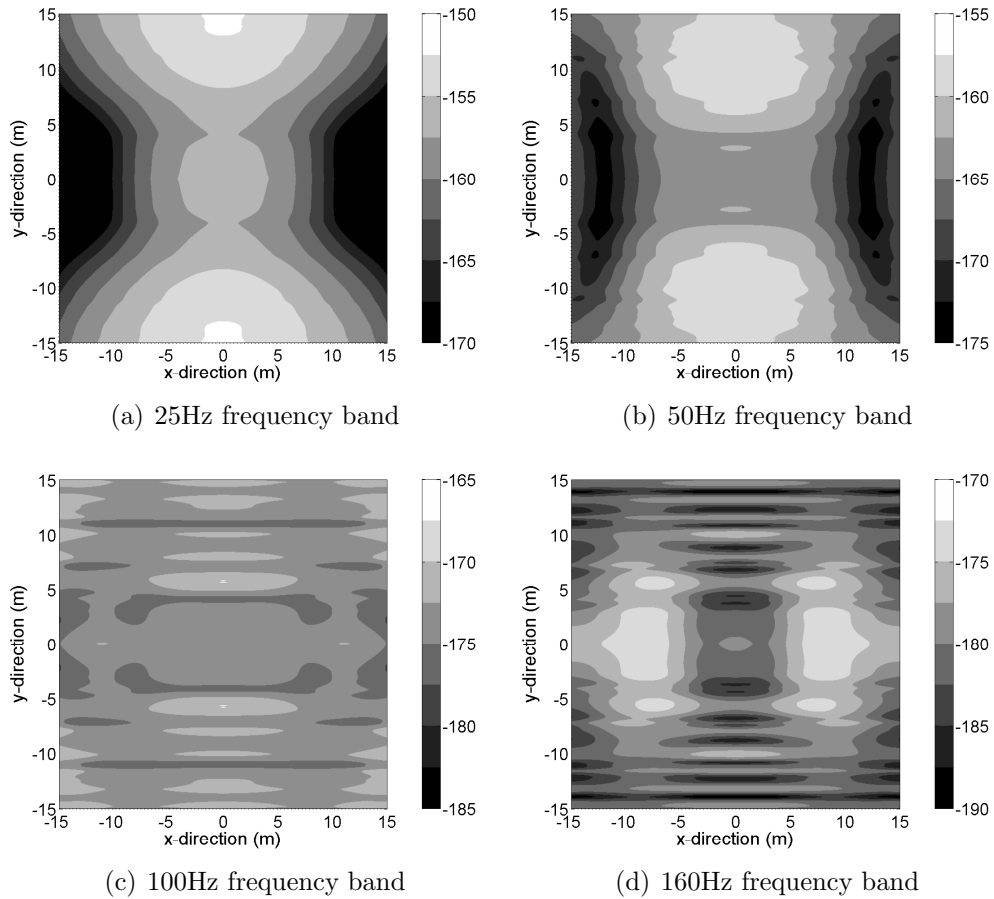


Figure 3.14: Discrete model response for no void at 25Hz, 50Hz, 100Hz and 160Hz third-octave frequency bands; response in rms velocity (dB, ref 1 m/s)



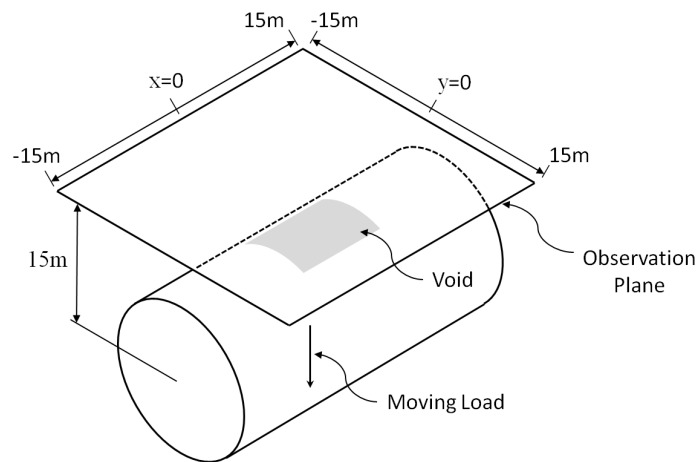


Figure 3.16: Schematic showing void at tunnel-soil interface and observation plane centered over the tunnel at height 15m

Table 3.4: Void parameters - sensitivity to void length (VL) and void sector angle (VA)

| Case | Void Sector Angle ( $^{\circ}$ ) | Void Length (m) |
|------|----------------------------------|-----------------|
| VL-1 | 67.5                             | 2               |
| VL-2 | 67.5                             | 4               |
| VL-3 | 67.5                             | 6               |
| VL-4 | 67.5                             | 8               |
| VA-1 | 45.0                             | 4               |
| VA-2 | 67.5                             | 4               |
| VA-3 | 90.0                             | 4               |
| VA-4 | 112.5                            | 4               |

location the response around the void location begins to change, as seen in the loss of  $x$ -direction symmetry developing at LP3. This void effect remains visible through LP7 until the load is again sufficiently far away such that the void has little effect on the predicted particle velocity.

To better illustrate the effect of the void the insertion gain is calculated for the same case as shown in Figure 3.19. Insertion gain is defined as the difference of the results for the void model (in dB) and the continuously coupled discrete model (in dB) at the same observation points and is reported in dB(rms, ref 1 m/s); a positive insertion gain signifies an increase in rms particle velocity due to the presence of a void at the tunnel-soil interface. The benefit of using the insertion gain method is seen at LP1

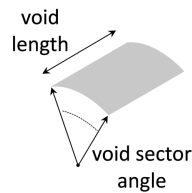


Figure 3.17: Close-up schematic of the void showing the void parameters

where a void-effect is visible even when the moving load is relatively far from the void location (compare to LP1 in Figure 3.18 where there is little evidence of disturbance due to the void). There is a distinctive “wake-effect” which causes small areas of velocity reduction by up to approximately 2.3dB, as well as a wave energy localization behind the tunnel causing an increase of approximately 3.1dB. The effect of the void increases as the moving load approaches the void location. The average insertion gain over the observation plane reaches a maximum when the load is directly under the void (LP5) with areas of (-3.4,+4.2)dB in the near-field of the void.

This case study suggests the void has a significant effect when the load is directly under the void as well as a moderate effect when the load is relatively far from the void. As the average IG value reaches a maximum when the load is directly under the void, results for the void sensitivity studies will be presented for this load location only. It should be noted that the wake-effect is present in all cases when the load is reasonably far from the void location. The results for the two sensitivity studies are presented in the following subsections: void length sensitivity and void sector angle sensitivity.

### 3.3.1 Results for Void Length Sensitivity Study

The effect of void length on vertical rms velocity response at different third-octave frequency bands is investigated for a  $67.5^\circ$  sector angle using four void lengths: 2, 4, 6 and 8m (see Table 3.4). The observation plane responses are presented in Figures 3.20 to 3.23.

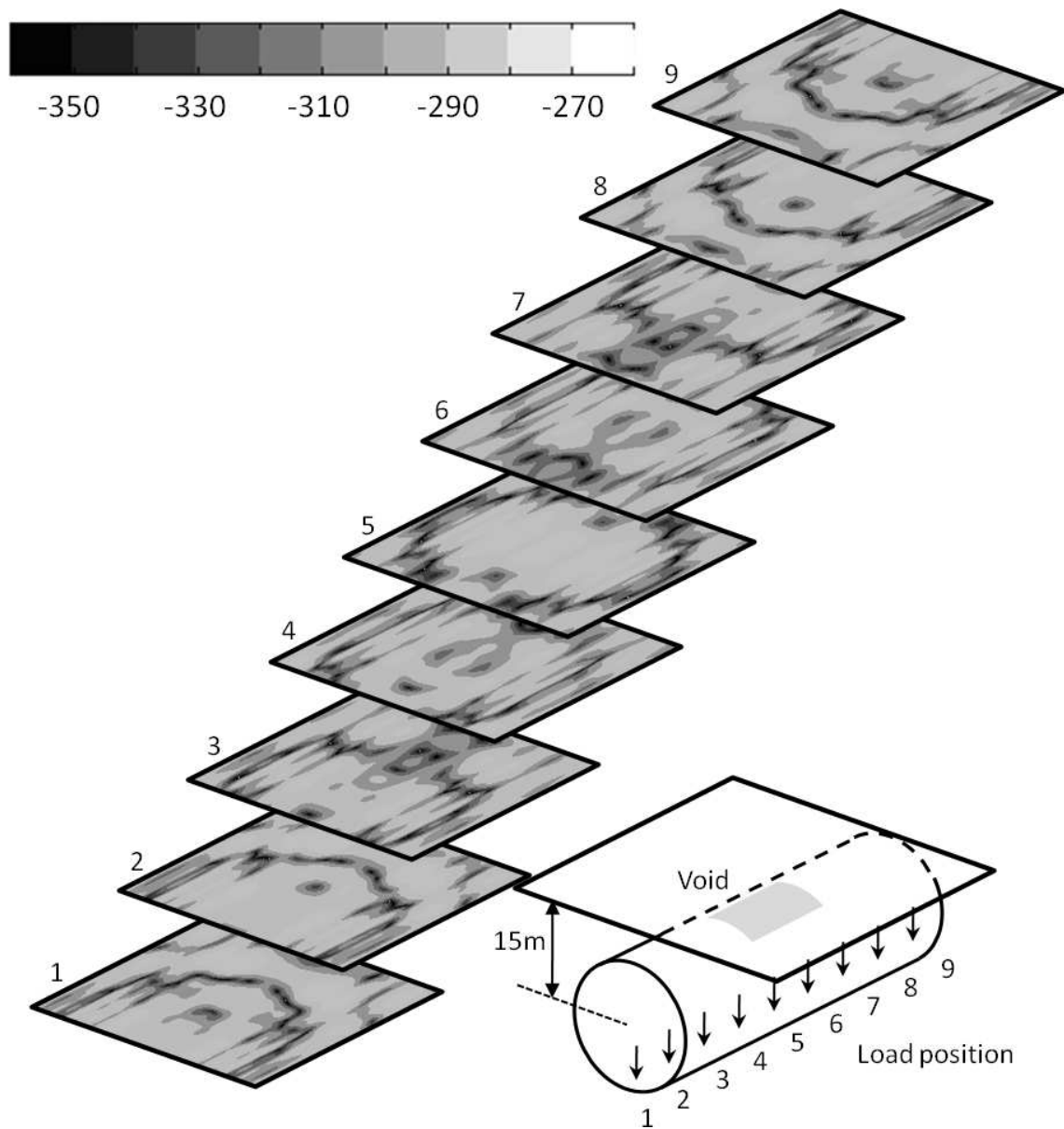


Figure 3.18: Particle velocity response in dB(rms, ref 1 m/s) for case VA-3 at  $h = 10\text{m}$  as load moves along tunnel invert

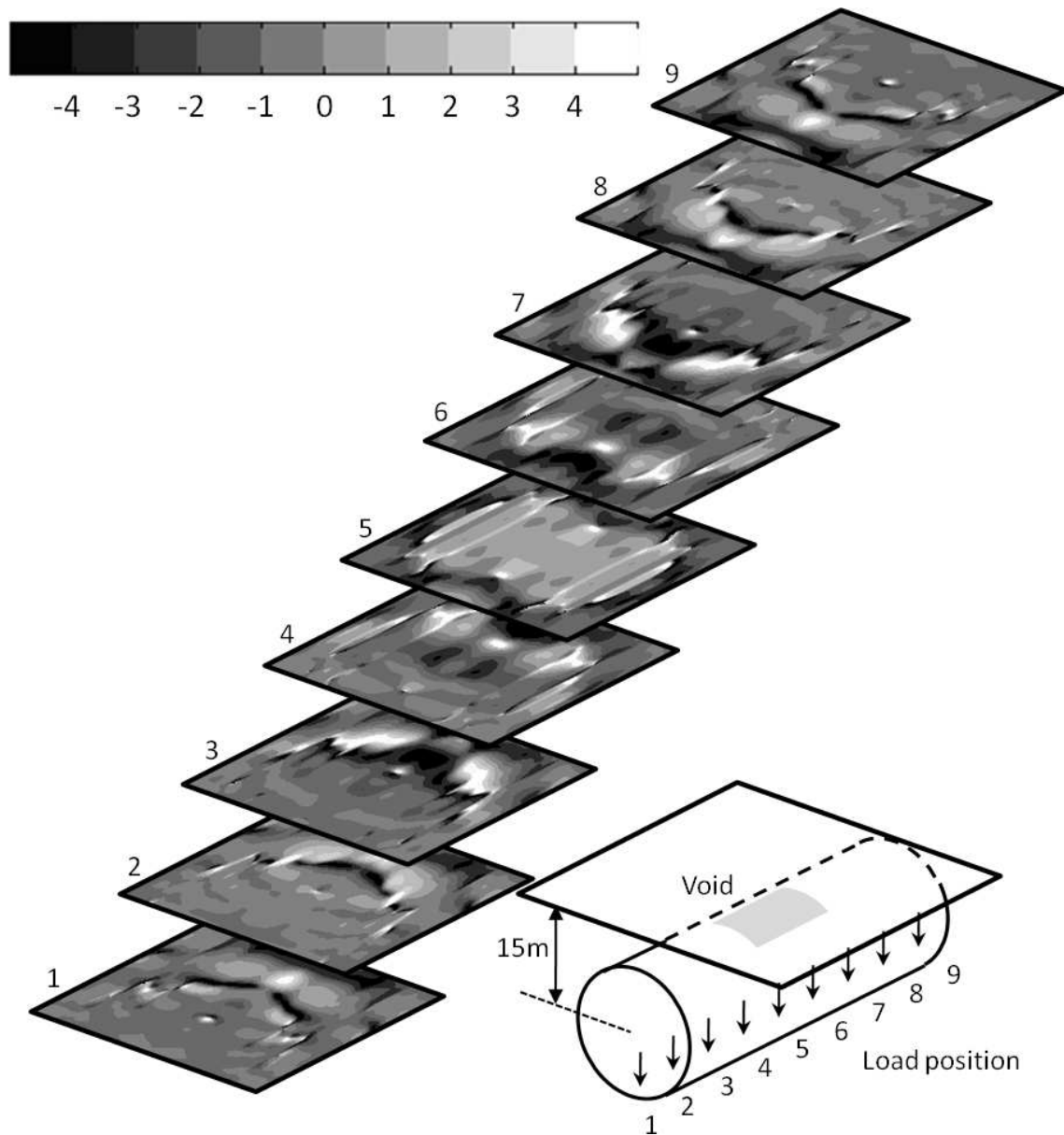


Figure 3.19: Insertion gain response in dB(rms, ref 1 m/s) for case VA-3 at  $h = 15\text{m}$  as load moves along the tunnel invert; the highest levels of insertion gain occur at load point 5, when the load is directly under the void location

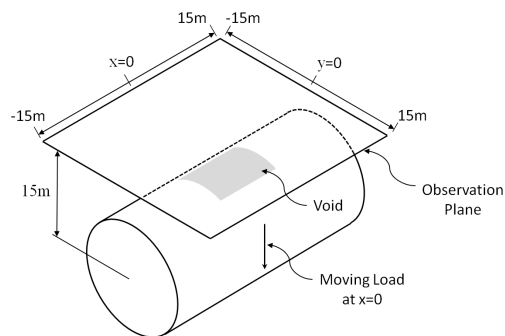
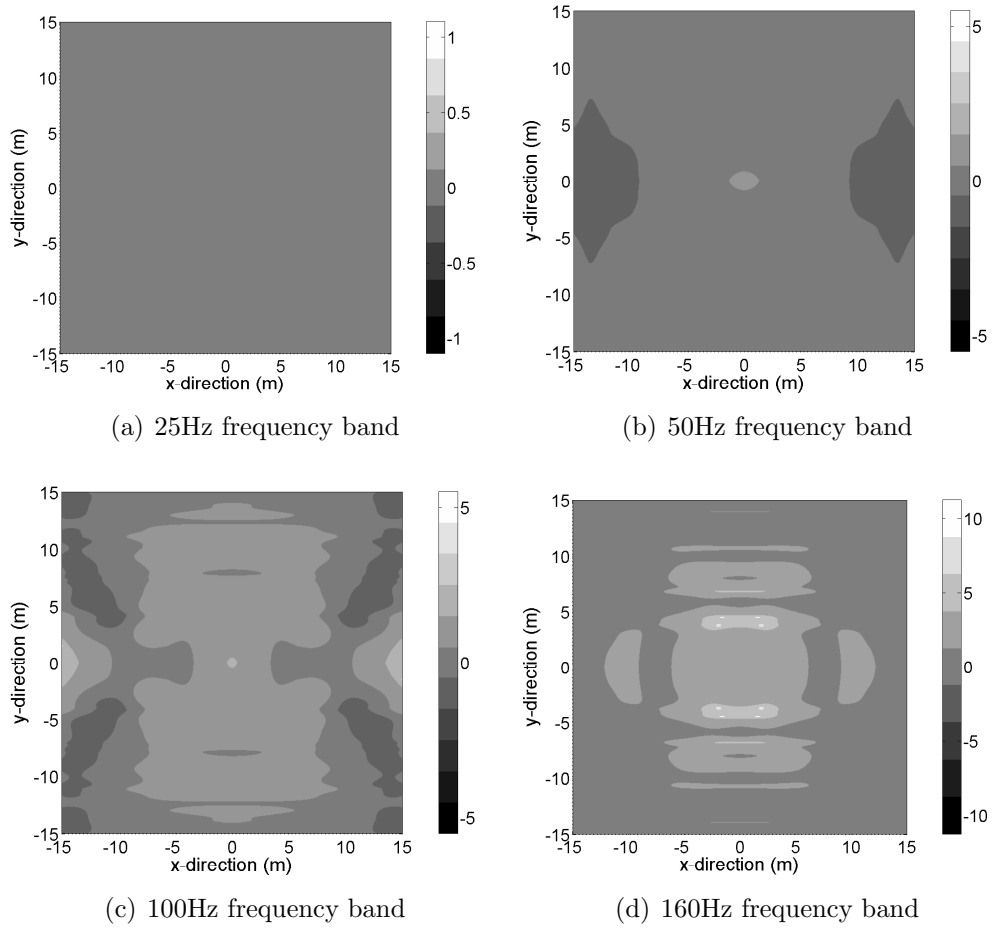


Figure 3.20: Insertion gain response in dB(rms, ref 1 m/s) for case VL-1 ( $2\text{m} \times 67.5^\circ$ ) at four representative third-octave frequency bands; moving load at  $x=0$

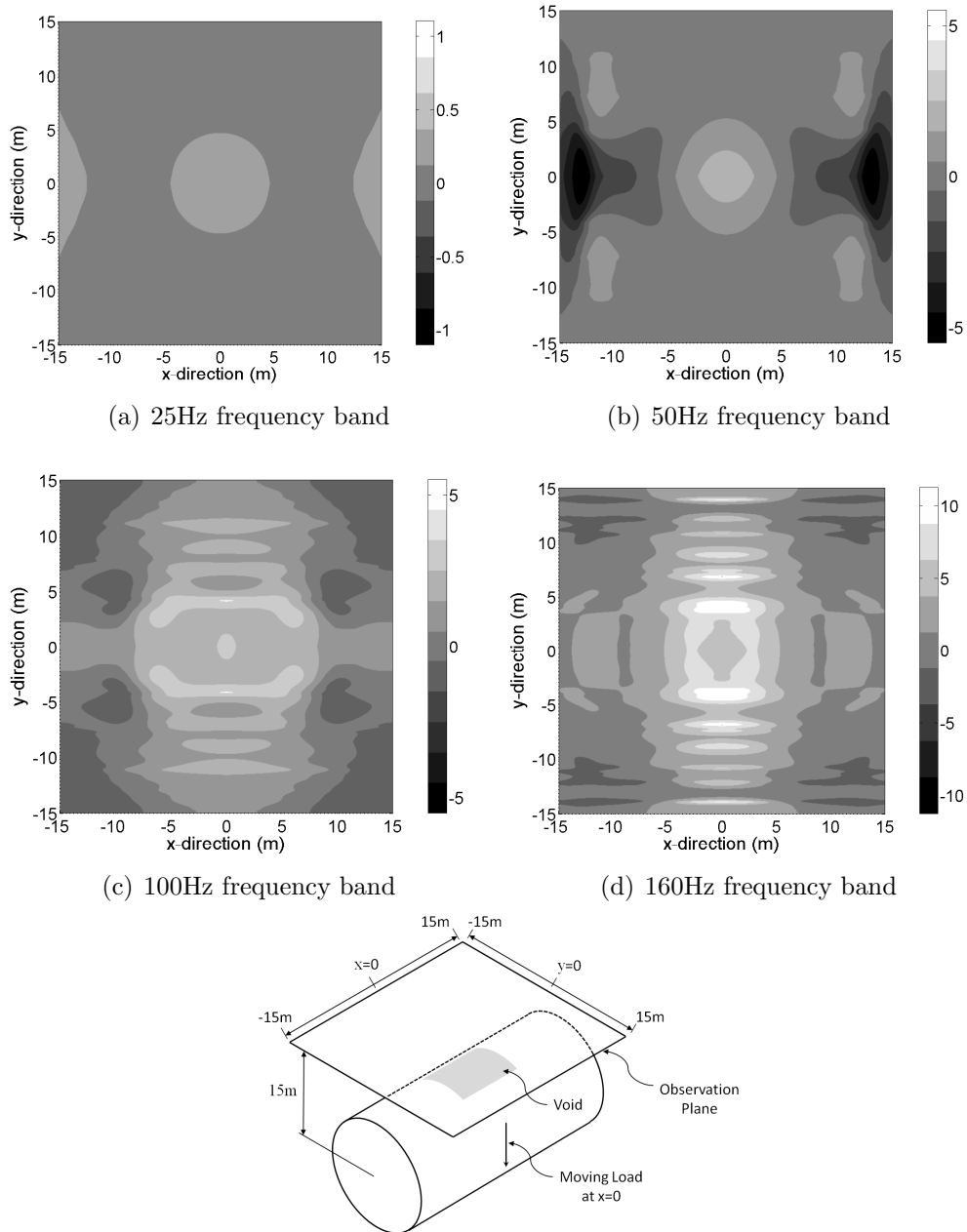


Figure 3.21: Insertion gain response in dB(rms, ref 1 m/s) for case VL-2 ( $4\text{m} \times 67.5^\circ$ ) at four representative third-octave frequency bands; moving load at  $x=0$

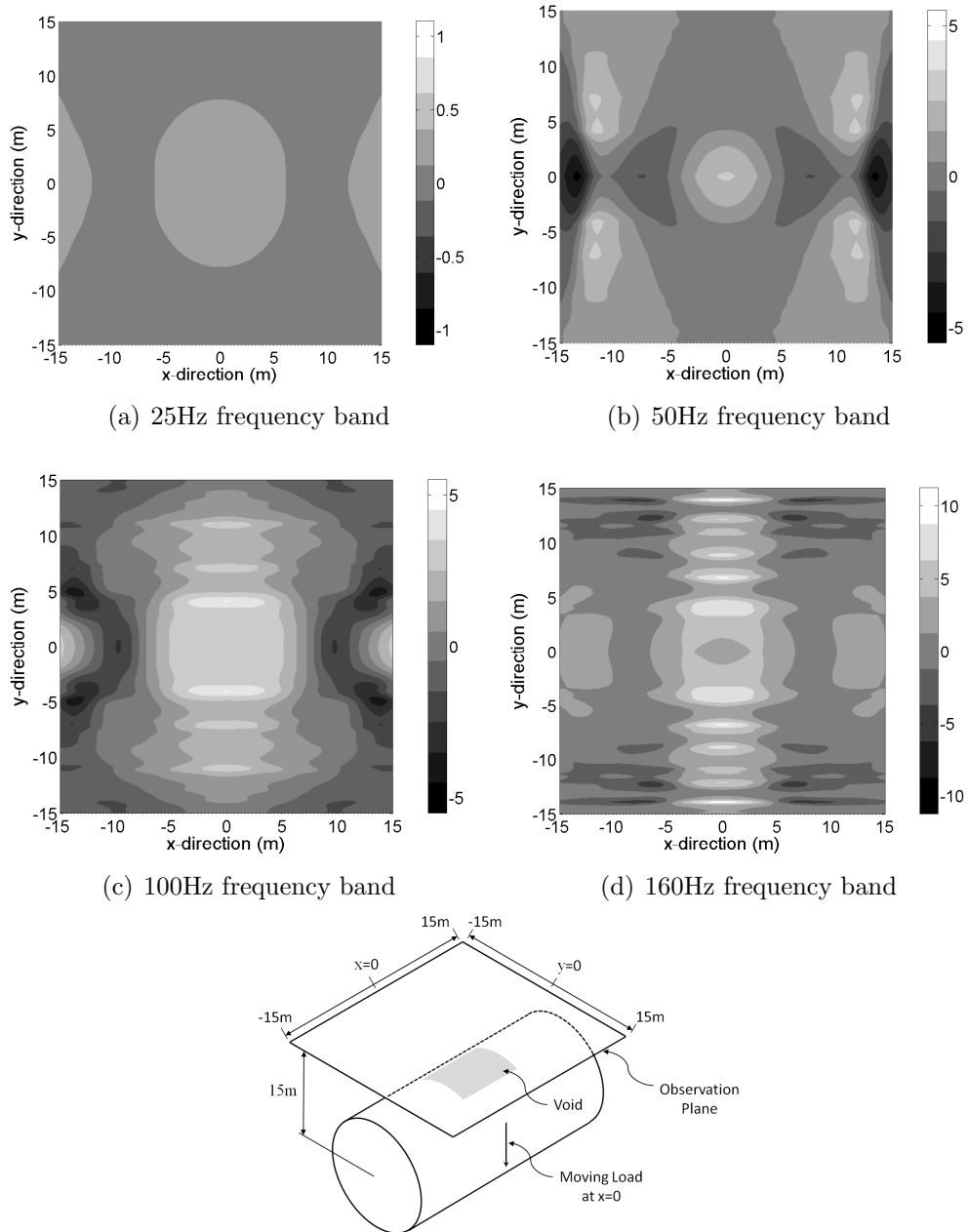


Figure 3.22: Insertion gain response in dB(rms, ref 1 m/s) for case VL-3 ( $6\text{m} \times 67.5^\circ$ ) at four representative third-octave frequency bands; moving load at  $x=0$

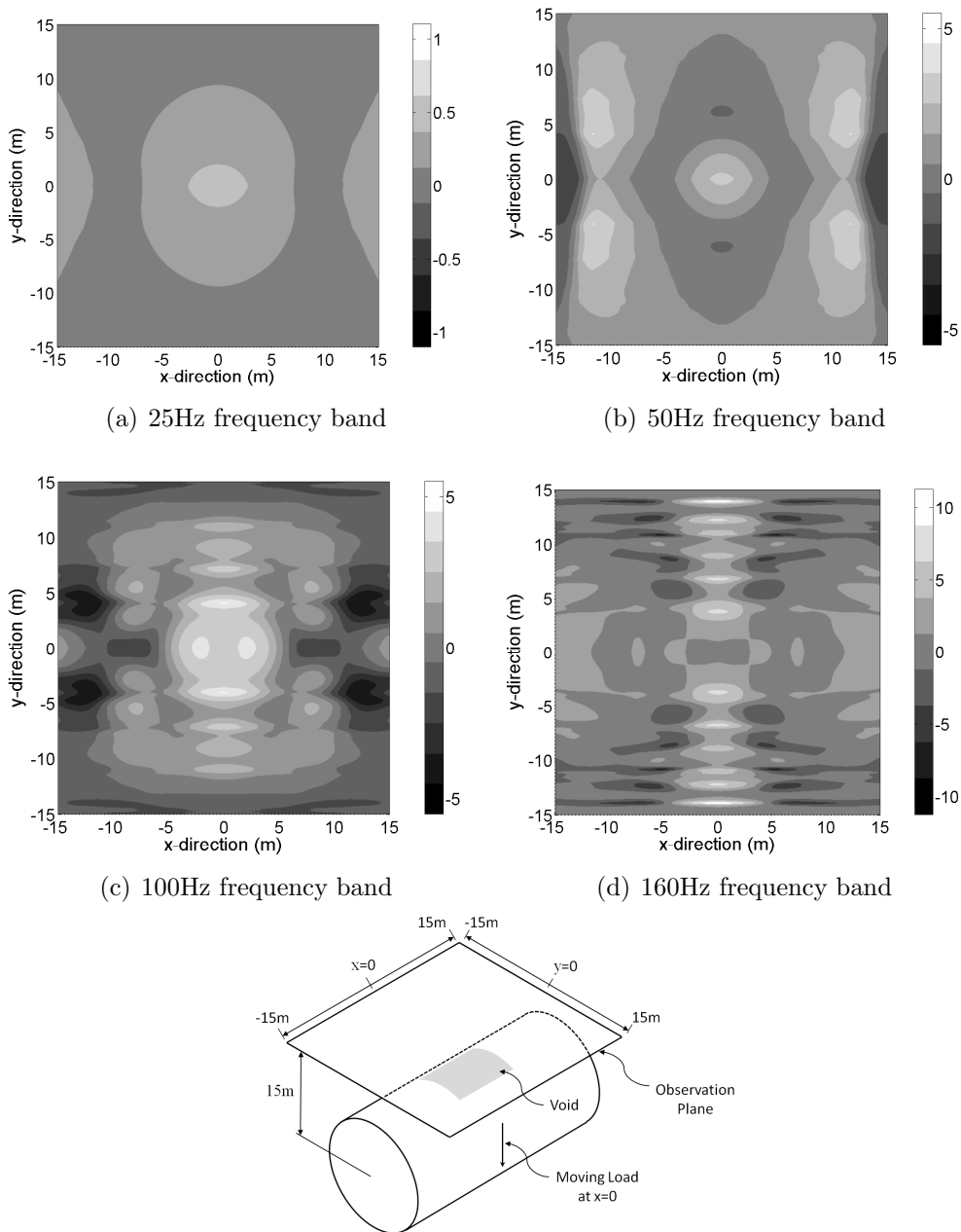


Figure 3.23: Insertion gain response in dB(rms, ref 1 m/s) for case VL-4 ( $8\text{m} \times 67.5^\circ$ ) at four representative third-octave frequency bands; moving load at  $x=0$

Table 3.5: Peak vertical insertion gain (IG) for void length sensitivity study at 25Hz, 50Hz, 100Hz and 160Hz frequency bands measured in dB(rms, ref 1 m/s)

| Case | 25Hz        | 50Hz        | 100Hz       | 160Hz       |
|------|-------------|-------------|-------------|-------------|
| VL-1 | (-0.0,+0.1) | (-0.3,+0.5) | (-1.3,+1.5) | (-0.9,+3.3) |
| VL-2 | (-0.0,+0.2) | (-1.7,+2.0) | (-0.9,+2.7) | (-3.4,+8.5) |
| VL-3 | (-0.0,+0.4) | (-2.2,+2.6) | (-1.4,+3.4) | (-5.2,+8.3) |
| VL-4 | (-0.0,+0.4) | (-1.5,+2.8) | (-3.4,+3.9) | (-5.6,+8.1) |

A trend common in all frequency bands is the IG magnitude increases as the length of the void is increased. For example, the peak IG values at the 100Hz frequency band increase from (-1.3,+1.5)dB for case VL-1 to (-3.4,+3.9)dB for case VL-4. Table 3.5 lists the peak insertion gains for the four cases at the frequency bands listed. Furthermore, the density of increased IG values increases with void length; only small areas of insertion gain with magnitude greater than 1dB are visible in the 50Hz frequency band for case VL-1 while the bulk of the observation plane has IG magnitudes greater than 1dB for case VL-4 with substantial areas of 2dB or more.

This variation in response with void length is attributed to how the vibration energy is transformed into pressure and shear-waves when a void is present at the tunnel-soil interface. Since there is no force transmission at the void site, motion of the tunnel at this location will not directly result in wave propagation. Figure 3.24 shows the vertical response of the tunnel for a void-free case at 25Hz and 160Hz. The average wavelength at 25Hz is approximately 13m while at 160Hz it is approximately 5m. For case VL-1 the void is only 2m long which is relatively small compared to the 25Hz wavelength thus it has little effect on the response at the observation plane (Figure 3.20(a)); the bulk of the wavelength bridges the void. At 160Hz the void length is more substantial relative to the wavelength thus it has a greater effect (Figure 3.20(d)); the void accounts for almost half a wavelength thus a significant amount of energy is not transmitted to the soil above the tunnel resulting in peak IG values of (-0.9,+3.3)dB. The lack of force transmission at the void results in higher interface forces elsewhere around the tunnel thus energy localization in the wavefronts occurs relative to the void-free case. This

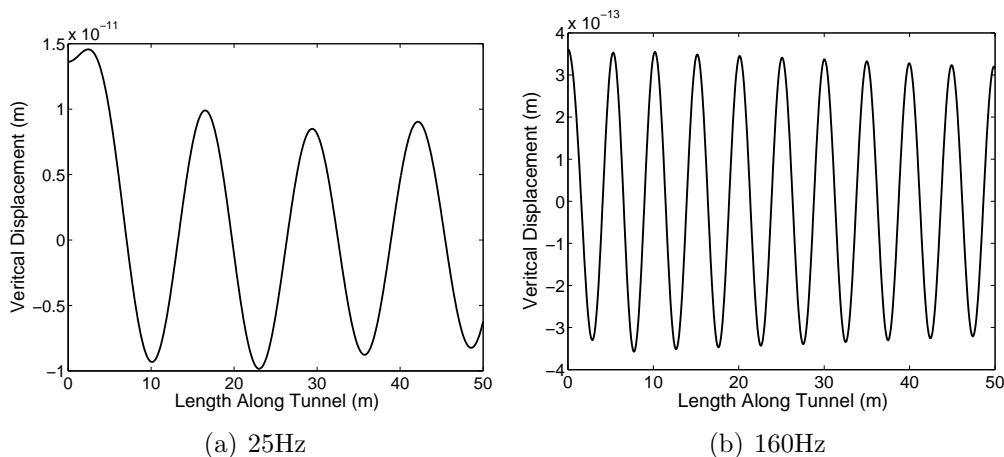


Figure 3.24: Vertical response of tunnel at 25Hz and 160Hz

explains why the void causes IG losses at some locations (no force transmission across the void) and IG increases at others (energy localization to other areas of the tunnel-soil interface). However, as the void length is relatively small compared to the wavelengths the effect is mainly constrained to the near-field response (i.e. the area over the void).

For case VL-4 the void length is 8m; this is a substantial amount of the low frequency wavelength thus the insertion gain is more significant than in the VL-1 case. However, the IG is still less than 1dB which is relatively small and within the error range of the model (see Section 3.2). The 8m void is large compared to the 160Hz wavelength thus a large amount of vibrational energy is not transmitted through the top of the tunnel-soil interface compared to the void-free case. The result is peak insertion gains of (-5.6,+8.1)dB. This is a significant change compared to the void-free case. Also the effect of the void extends further into the far-field of the observation plane as a significant amount of vibrational energy has to be redistributed around the tunnel-soil interface due to the length of the void.

### 3.3.2 Results for Void Sector Angle Sensitivity Study

The effect of void sector angle on vertical rms velocity response at different third-octave frequency bands is investigated for a 4m void length using four void sector angles: 45°,

Table 3.6: Peak vertical insertion gain (IG) for void sector angle sensitivity study at 25Hz, 50Hz, 100Hz and 160Hz frequency bands measured in dB(rms, ref 1 m/s)

| Case | 25Hz        | 50Hz        | 100Hz       | 160Hz        |
|------|-------------|-------------|-------------|--------------|
| VA-1 | (-0.0,+0.1) | (-0.6,+0.9) | (-0.7,+2.2) | (-1.9,+7.3)  |
| VA-2 | (-0.0,+0.2) | (-1.7,+2.0) | (-0.9,+2.7) | (-3.4,+8.5)  |
| VA-3 | (-0.0,+0.5) | (-2.8,+2.4) | (-1.0,+3.1) | (-3.2,+9.8)  |
| VA-4 | (-0.1,+0.9) | (-3.4,+2.6) | (-1.0,+3.4) | (-2.0,+10.9) |

67.5°, 90° and 112.5° (see Table 3.4). The observation plane responses are presented in Figures 3.25 to 3.28.

Again a common trend in all frequency bands is the increase in IG magnitude as the sector angle of the void is increased. For example, the peak IG values at the 100Hz frequency band increase from (-0.7,+2.2)dB for case VA-1 to (-1.0,+3.4)dB for case VA-4. Table 3.6 lists the peak insertion gains for the four cases at the given frequency bands. However, unlike the void length study, the density of insertion gain over the observation plane does not largely depend void sector angle, especially in the higher frequency bands. The 160Hz frequency band response tends to grow in magnitude as the void angle is increased (Figures 3.25(d) to 3.28(d)) while the distribution remains relatively constant.

This response is again attributed to the disruption of force transmission between the tunnel and the soil at the void location, but in the case of the void sector angle the response around the circumference of the tunnel is deemed to be the governing factor. Figure 3.29 shows the radial response of the tunnel at  $x=0$  for a void-free case at 25Hz and 160Hz. The average circumferential wavelength at 25Hz is approximately 360° while at 160Hz it is approximately 50°.

For case VA-1 the void sector angle is 45° which is relatively small compared to the wavelength at 25Hz. In a similar fashion to the VL-1 case, the wavelength bridges the void which essentially negates its presence. At 160Hz the void angle is basically the same as the circumferential wavelength thus a large portion of the vibration energy is not transmitted through the top of the tunnel-soil interface resulting in significant

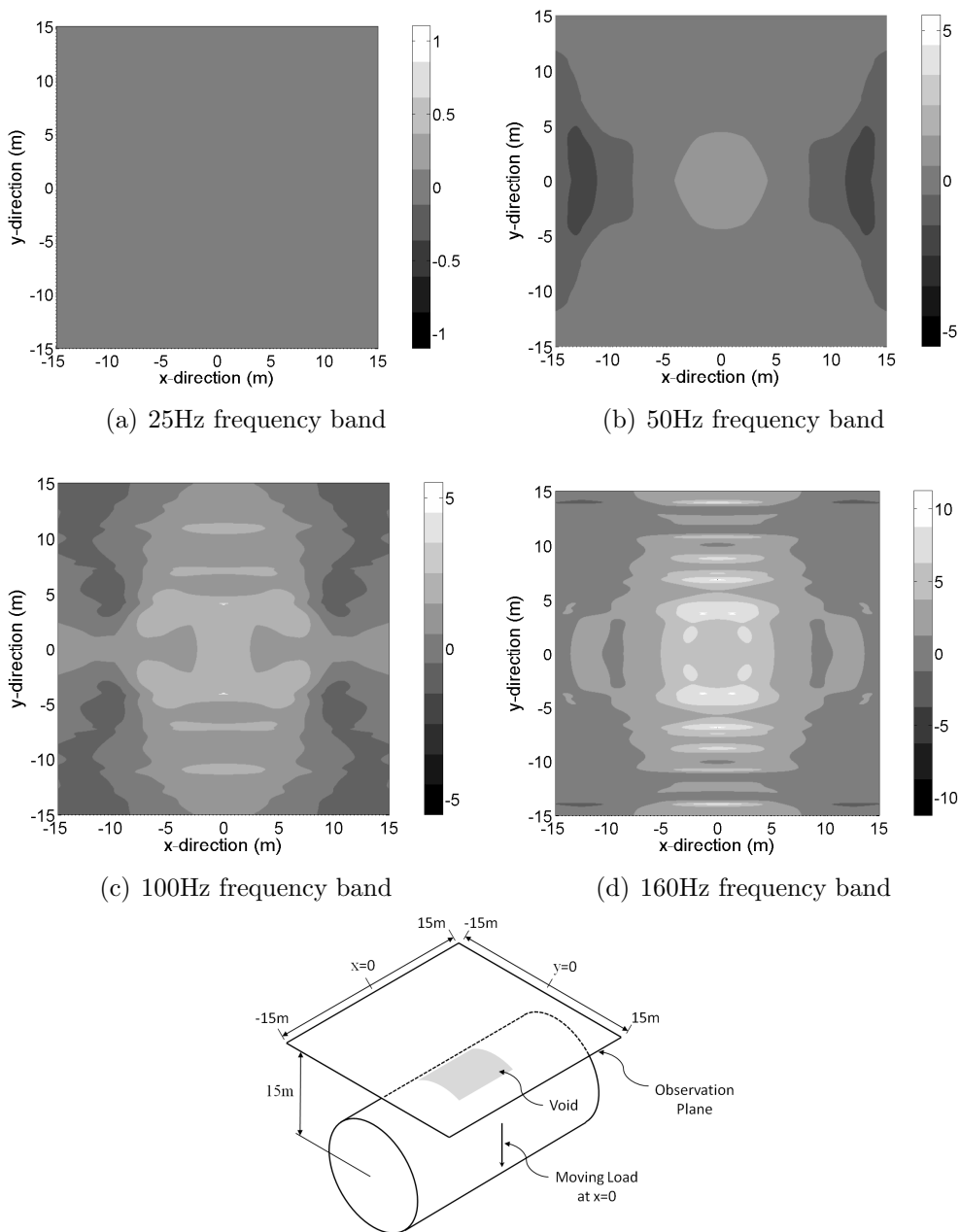


Figure 3.25: Insertion gain response in dB(rms, ref 1 m/s) for case VA-1 ( $4\text{m} \times 45^\circ$ ) at four representative third-octave frequency bands; moving load at  $x=0$

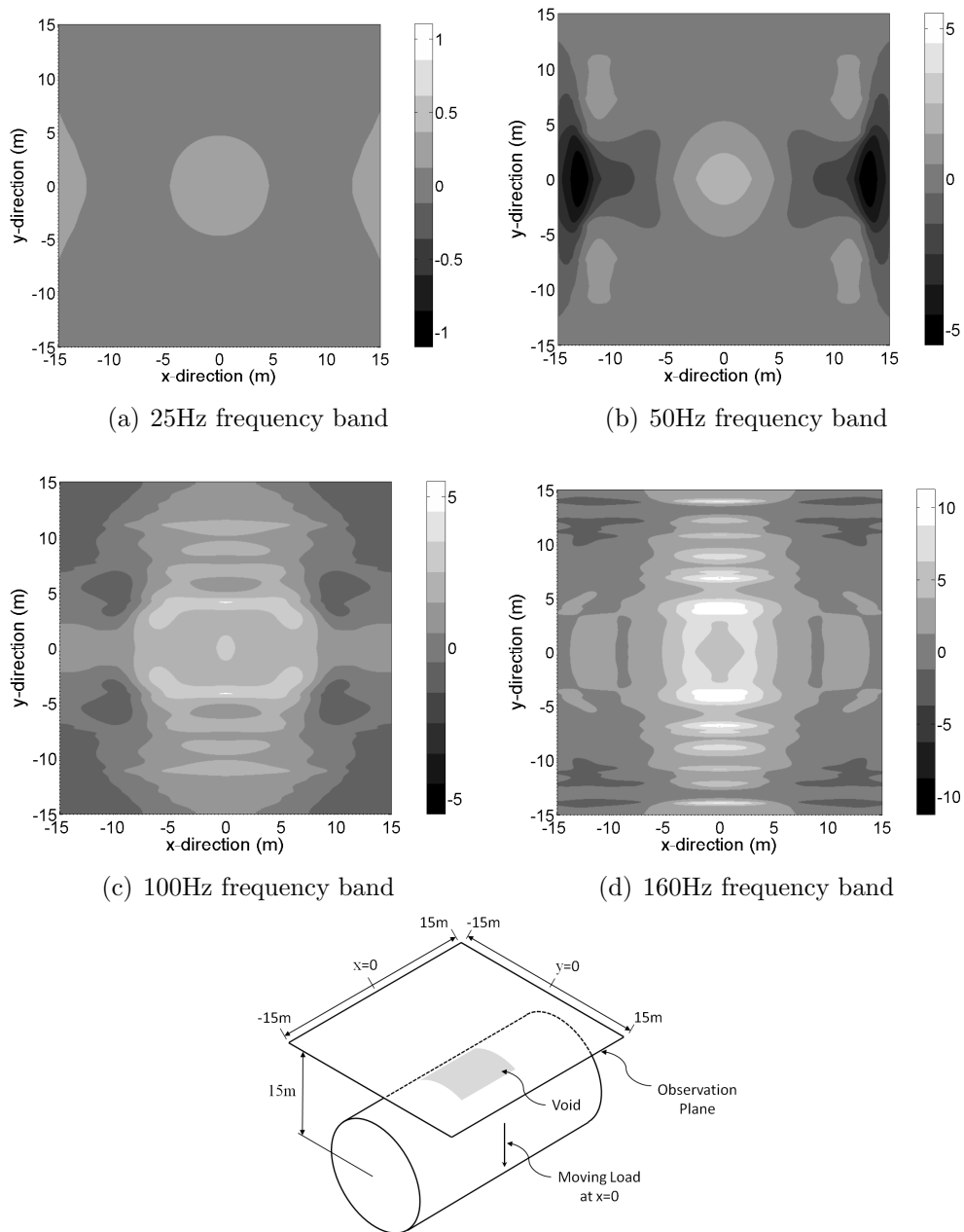


Figure 3.26: Insertion gain response in dB(rms, ref 1 m/s) for case VA-2 ( $4\text{m} \times 67.5^\circ$ ) at four representative third-octave frequency bands; moving load at  $x=0$

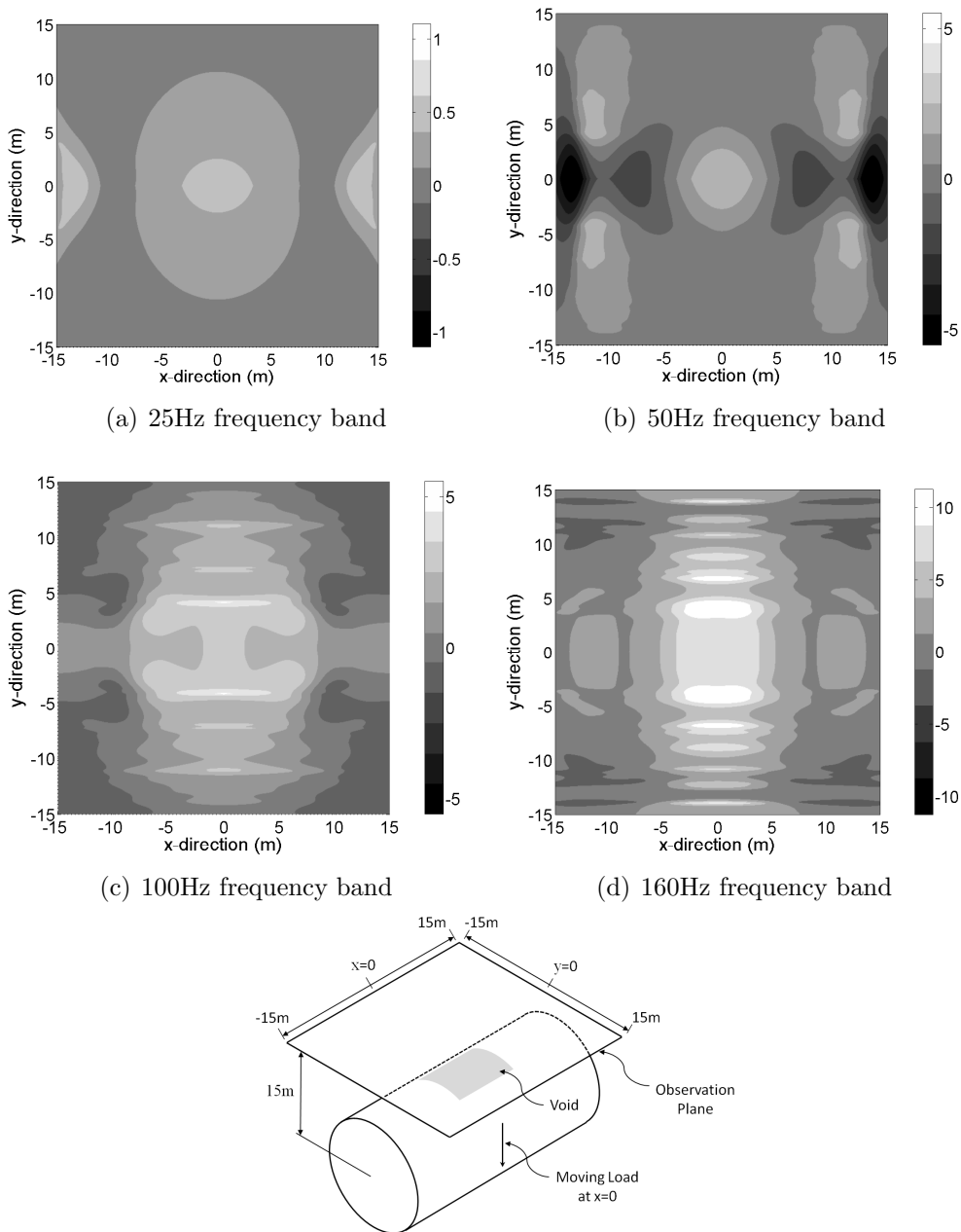


Figure 3.27: Insertion gain response in dB(rms, ref 1 m/s) for case VA-3 ( $4\text{m} \times 90^\circ$ ) at four representative third-octave frequency bands; moving load at  $x=0$

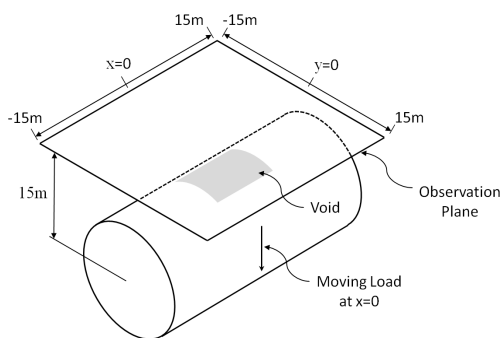
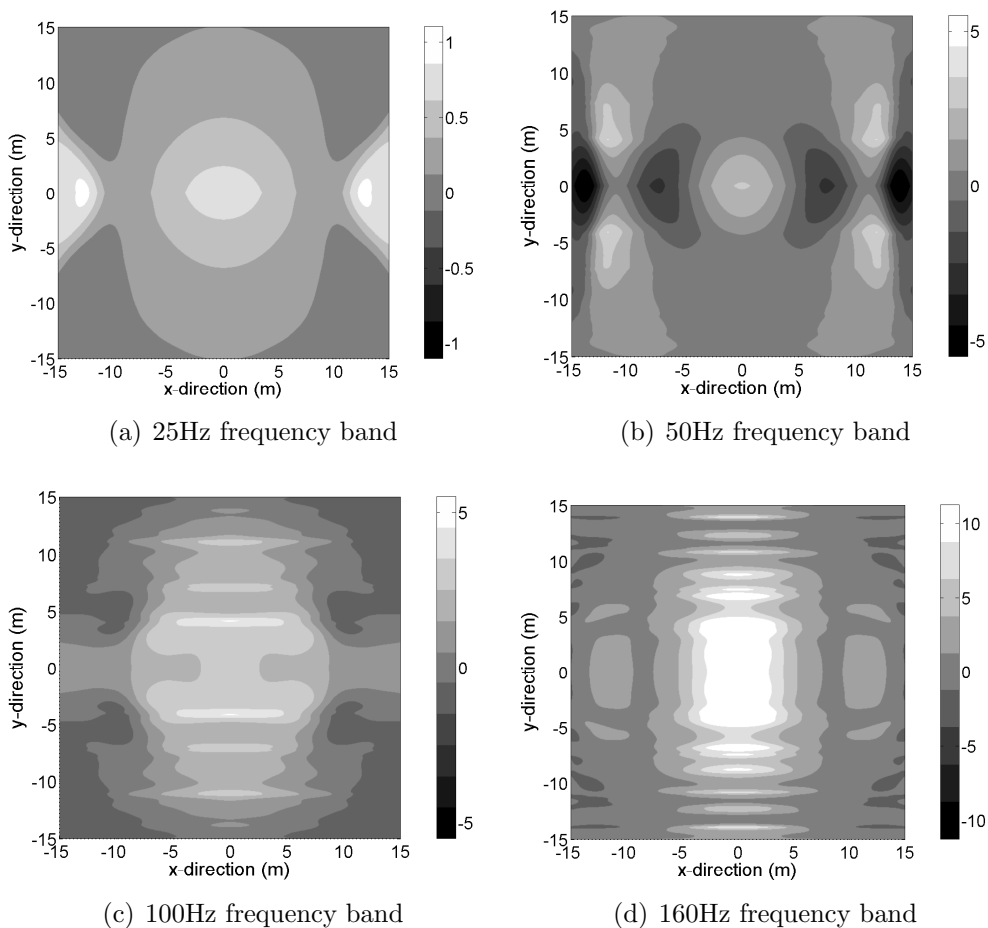


Figure 3.28: Insertion gain response in dB(rms, ref 1 m/s) for case VA-4 ( $4\text{m} \times 112.5^\circ$ ) at four representative third-octave frequency bands; moving load at  $x=0$

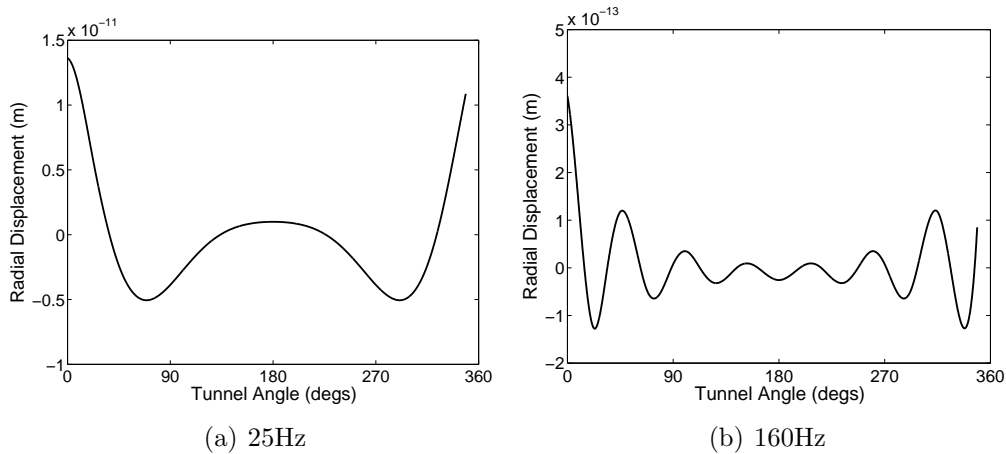


Figure 3.29: Radial response of tunnel at  $x=0$  for 25Hz and 160Hz

insertion gains with peak values of  $(-1.9, +7.3)$ dB.

By case VA-4 the void sector angle is  $112.5^\circ$  which is a significant void for all frequency bands. As in the void length study, the void has little effect on observation plane response for the 25Hz frequency band ( $< 1$ dB) even at this large void angle; the insertion gain at higher frequency bands is significant, reaching a peak of  $(-2.0, +10.9)$ dB for the 160Hz frequency band.

### 3.4 Conclusions

A semi-analytical model is developed to investigate the effect of voids around an underground railway tunnel on ground vibration. The method derives the discrete transfer functions for the tunnel and soil from the Pipe-in-Pipe continuous solution. The void is simulated by uncoupling the appropriate nodes to prevent the transfer of force between the tunnel and the soil. A number of void geometries are investigated to determine how sensitive the vertical response of the soil is to changes in void size. The results from this investigation show that relatively small voids ( $4\text{m} \times 90^\circ$ ) can significantly affect the rms velocity predictions at higher frequencies (peak insertion gain:  $(-3.4, +8.5)$ dB for 160Hz frequency band) while they have less effect at lower frequencies (peak insertion gain:  $(-1.7, +2.0)$ dB for 50Hz frequency band). The sensitivity to void length and void

---

sector angle was also investigated and results suggest that rms velocity predictions are sensitive to both parameters. The findings from this study suggest that the uncertainty associated with assuming a perfect bond at the tunnel-soil interface in an area with known voidage can reasonably reach  $\pm 5\text{dB}$  for frequencies between 100-200Hz and thus should be considered in the design process.

# Chapter 4

## The Homogeneous Soil Assumption

Arguably the most important component to any ground vibration simulation is the definition of the soil domain. Both the material properties assigned to the soil (i.e. stiffness, damping, homogeneous vs. inhomogeneous, etc.) and the defined geometry (i.e. fullspace vs. halfspace, layering, inclusions, voids, etc.) have a significant effect on the final prediction of the model. However, it is common in the literature reviewed to find the soil is often greatly simplified as a homogeneous halfspace or a horizontally layered halfspace. This chapter attempts to quantify the amount of uncertainty that may be introduced into a simulation when such simplifying assumptions are employed for the three cases discussed in Chapter 2: inclined soil layering (Section 2.4.1), subsiding soil layers (Section 2.4.2), and soil inhomogeneity (Section 2.4.3). To investigate these cases a semi-analytical model employing the thin-layer method (TLM) is developed which is shown to be both accurate and computationally efficient.

### 4.1 The Thin-Layer Method

The thin-layer method (TLM) is a semi-analytical approach to solving ground vibration problems in a halfspace. The semi-infinite soil is discretized in the vertical direction into a finite number of thin-layers where the displacement across each layer is assumed

to vary linearly. The analytical wave equation is used in the horizontal direction which allows layers of any horizontal length (i.e. finite or infinite) to accurately predict harmonic displacement without suffering from the element aspect-ratio restrictions of the finite element method. The TLM model is comprised of three element types which are described in the following sections: semi-infinite elements, halfspace elements and hyperelements. For verification a TLM model of a surface load on a halfspace and tunnel loading in a halfspace are validated against analytical and boundary element methods.

The thin-layer method is derived herein for a plane-strain problem. This approach is selected because the model will be used to determine relative differences between different soil assumptions; Andersen and Jones have shown plane-strain models to be acceptable for this type of comparison<sup>[5]</sup>. The TLM model could be extended to 2.5D in a manner similar to those discussed in Section 2.3.3.4 but was deemed unnecessary for the current investigation.

#### 4.1.1 Semi-infinite region open to the right

The Navier equation governing motion for homogeneous, isotropic, linear elastic bodies, is given by Graff<sup>[47]</sup> as

$$\mu \nabla^2 \mathbf{u} + (\lambda + \mu) \nabla \nabla \cdot \mathbf{u} + \rho \mathbf{b} = \rho \ddot{\mathbf{u}} \quad (4.1)$$

where  $\mathbf{u}$  is the displacement vector in the x, y, and z-directions,  $\mu$  and  $\lambda$  are Lamé's constants of the solid,  $\rho$  is the density of the solid, and  $\mathbf{b}$  is the body load vector. Consider the layered soil system depicted in Figure 4.1. The layer interfaces represent discontinuities in material properties in the vertical direction or artificial discretization necessary to meet the formulation requirements outlined below. Using the Cartesian coordinate system depicted in the figure and assuming plane-strain conditions and harmonic motion with no body loads, Equation 4.1 can be written for each layer as

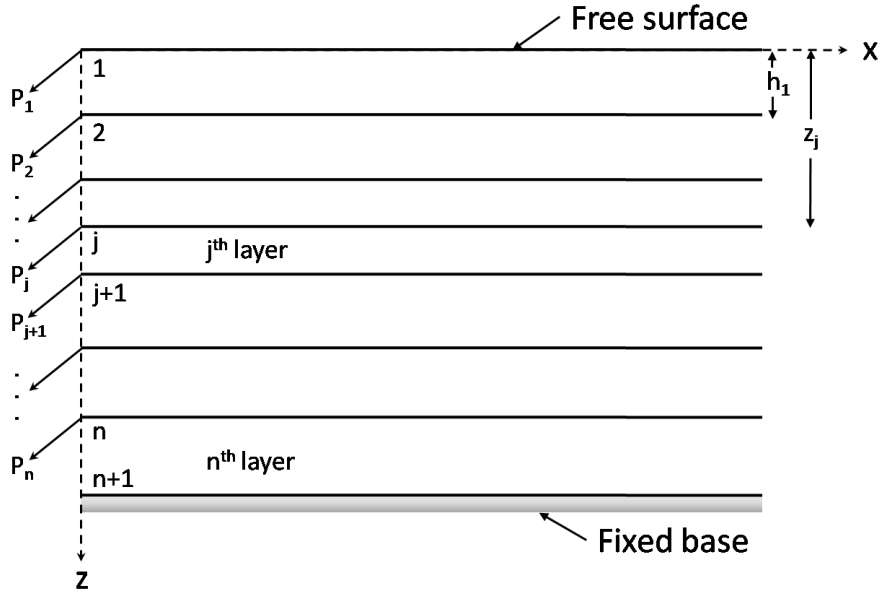


Figure 4.1: Typical layered region (plane-strain)

$$G_j \left( \frac{\partial^2 u_x}{\partial x^2} + \frac{\partial^2 u_x}{\partial z^2} \right) + (\lambda_j + G_j) \left( \frac{\partial^2 u_x}{\partial x^2} + \frac{\partial^2 u_z}{\partial x \partial z} \right) + \rho_j \omega^2 u_x = 0 \quad (4.2a)$$

$$G_j \left( \frac{\partial^2 u_z}{\partial x^2} + \frac{\partial^2 u_z}{\partial z^2} \right) + (\lambda_j + G_j) \left( \frac{\partial^2 u_x}{\partial x \partial z} + \frac{\partial^2 u_z}{\partial z^2} \right) + \rho_j \omega^2 u_z = 0. \quad (4.2b)$$

Equations 4.2a and 4.2b are coupled, governing motion in the  $x$ - $z$  plane. Only in-plane loading conditions will be considered thus the solution will be independent of  $y$ . The plane-strain condition  $\varepsilon_{zz} = 0$  and rigid constraint at the base in Figure 4.1 prevents any motion in the  $y$ -direction.

The dynamic displacement of any point in the  $x$ - $z$  plane is assumed harmonic and described as

$$u_x = q_x(x, z)e^{i\omega t} \quad (4.3a)$$

$$u_z = q_z(x, z)e^{i\omega t}. \quad (4.3b)$$

Assuming separation of variables

$$q_x(x, z) = u(z)g(x) \quad (4.4a)$$

$$q_z(x, z) = w(z)g(x) \quad (4.4b)$$

leads to the coupled ordinary differential equations

$$(k^2(\lambda_j + 2G_j) - \omega^2\rho_j) u - G_j \frac{d^2u}{dz^2} + ik(\lambda_j + G_j) \frac{dw}{dz} = 0 \quad (4.5a)$$

$$(k^2G_j - \omega^2\rho_j) w - (\lambda_j + 2G_j) \frac{d^2w}{dz^2} + ik(\lambda_j + G_j) \frac{du}{dz} = 0 \quad (4.5b)$$

for each of the  $n$  layers,  $j = 1, 2, \dots, n$  and the differential equation

$$\frac{d^2g}{dx^2} + k^2g = 0. \quad (4.6)$$

A solution to Equation 4.6 is

$$g(x) = e^{-ikx} \quad (4.7)$$

thus the displacements in the layered region can be expressed as

$$u_x = u(z)e^{(i\omega t - ikx)} \quad (4.8a)$$

$$u_z = w(z)e^{(i\omega t - ikx)}. \quad (4.8b)$$

The mode shapes  $u(z)$  and  $w(z)$  are determined by Equations 4.5 and by satisfying the continuity of stress and strain at the layer interfaces, zero stress at the free surface and zero displacement at the base. This problem consists of  $2n$  simultaneous equations with coefficients containing the eigenvalue  $k^2$  in the argument of the transcendental functions. Solving these equations analytically for even a simple halfspace is quite difficult; layered regions generally require numerical searching methods to find a solution.

Waas<sup>[155]</sup> suggested treating the layered region as a continuum in the horizontal direction but to discretize in the vertical direction by assuming that  $u(z)$  and  $w(z)$  in Equations 4.8 vary linearly within each layer. Using a virtual work method Equation 4.5 may be written in matrix notation as

$$(\mathbf{A}k^2 + i\mathbf{B}k + \mathbf{C}) \mathbf{v} = 0 \quad (4.9a)$$

where

$$\mathbf{C} = \mathbf{G} - \omega^2\mathbf{M}. \quad (4.9b)$$

The vector  $\mathbf{v}$  contains the displacements  $v_j$  in the  $x$ -direction ( $j = 1, 3, \dots, 2n - 1$ ) and  $z$ -direction ( $j = 2, 4, \dots, 2n$ ) for the  $n$  layers. The  $2n \times 2n$  matrices  $\mathbf{A}$ ,  $\mathbf{B}$ ,  $\mathbf{G}$  and  $\mathbf{M}$  consist of the contributions from the  $n$  individual layers and are assembled using standard FE stiffness matrix addition as depicted in Figure 4.2 (the frequency  $\omega$  is a given parameter). The submatrices used to construct Equation 4.9 are given in Equations 4.10.

$$\mathbf{A}_j = \frac{h_j}{6} \begin{bmatrix} 2(2G_j + \lambda_j) & 0 & (2G_j + \lambda_j) & 0 \\ 0 & 2G_j & 0 & G_j \\ (2G_j + \lambda_j) & 0 & 2(2G_j + \lambda_j) & 0 \\ 0 & G_j & 0 & 2G_j \end{bmatrix} \quad (4.10a)$$

$$\mathbf{B}_j = \frac{1}{2} \begin{bmatrix} 0 & (G_j - \lambda_j) & 0 & (G_j + \lambda_j) \\ -(G_j - \lambda_j) & 0 & (G_j + \lambda_j) & 0 \\ 0 & -(G_j + \lambda_j) & 0 & -(G_j - \lambda_j) \\ -(G_j + \lambda_j) & 0 & (G_j - \lambda_j) & 0 \end{bmatrix} \quad (4.10b)$$

$$\mathbf{G}_j = \frac{1}{h_j} \begin{bmatrix} G_j & 0 & -G_j & 0 \\ 0 & (2G_j + \lambda_j) & 0 & -(2G_j + \lambda_j) \\ -G_j & 0 & G_j & 0 \\ 0 & -(2G_j + \lambda_j) & 0 & (2G_j + \lambda_j) \end{bmatrix} \quad (4.10c)$$

$$\mathbf{M}_j = \frac{\rho_j h_j}{6} \begin{bmatrix} 2 & 0 & 1 & 0 \\ 0 & 2 & 0 & 1 \\ 1 & 0 & 2 & 0 \\ 0 & 1 & 0 & 2 \end{bmatrix} \quad (4.10d)$$

For any given frequency, Equation 4.9a has a non-trivial solution  $\mathbf{v}$  if and only if

$$|\mathbf{A}k^2 + i\mathbf{B}k + \mathbf{C}| = 0. \quad (4.11)$$

This results in a quadratic-eigenvalue problem in  $k$ , where  $k$  defines the possible wave

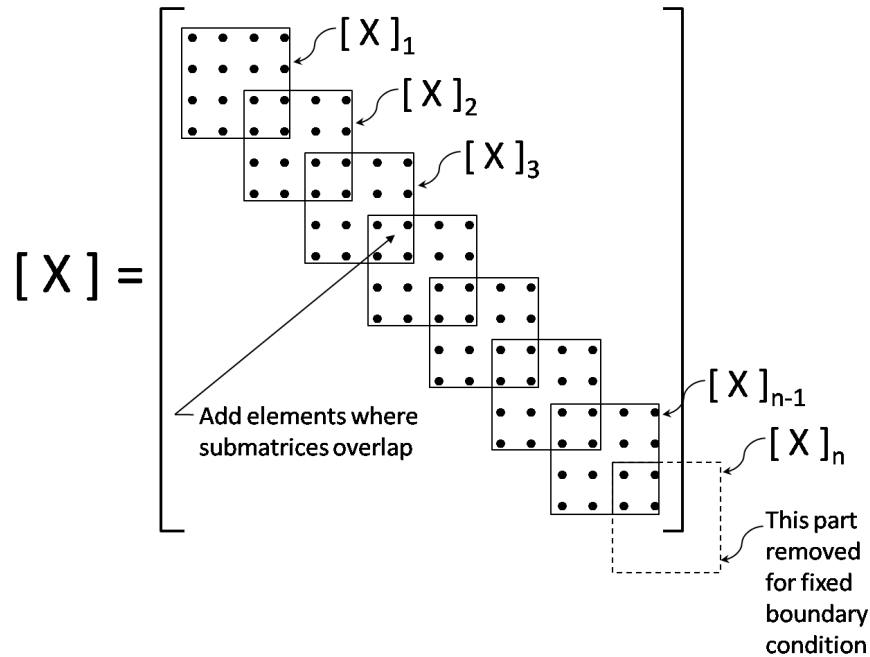


Figure 4.2: Matrix addition scheme

numbers for the layered region and can have eigenvalues which are

- complex: a wave travelling in the  $x$ -direction with decaying or increasing amplitude depending on the sign of the imaginary part
- purely real: a wave travelling in the  $x$ -direction with constant magnitude
- purely complex: a stationary wave varying exponentially in the  $x$ -direction
- null (i.e.  $k=0$ ): one-dimensional standing wave.

Simulations in this study always contain soil damping which will attenuate the waves thus purely real and null eigenvalues will not occur. In general, the solution will consist of  $4n$  eigenvalues:  $2n$  solutions with positive imaginary parts representing waves travelling in the negative  $x$ -direction with decaying magnitude, and  $2n$  solutions with negative imaginary parts representing waves travelling in the positive  $x$ -direction with decaying magnitude. For the example depicted in Figure 4.1 only waves travelling away from the vertical boundary at  $x=0$  are necessary (i.e. the waves travel into the semi-infinite

medium without reflection). As such only the eigenvalues with negative imaginary parts are retained for the solution to this  $2n$  degree-of-freedom problem.

The displacements in the layered region can be written as a modal summation of selected wave numbers  $k_s$  as follows

$$\mathbf{u} = \sum_{s=1}^{2n} \alpha_s \mathbf{v}_s e^{(i\omega t - ik_s x)} \quad (4.12)$$

where  $\alpha_s$  are the mode shape participation factors which can be determined using the system boundary conditions and  $\mathbf{v}_s$  are the associated mode shapes. Comparing Equation 4.12 to 4.8, the displacements of the nodal points at the boundary  $x = 0$  can be written

$$\mathbf{u}^R(z) = \sum_{s=1}^{2n} \alpha_s \mathbf{v}_s = \mathbf{V} \boldsymbol{\alpha}. \quad (4.13)$$

The matrix  $\mathbf{V}$  is the  $2n \times 2n$  modal matrix containing the mode shapes (columnwise), while  $\mathbf{u}^R(z)$  and  $\boldsymbol{\alpha}$  are column vectors of size  $2n$ . The superscript  $R$  in  $\mathbf{u}^R$  signifies the solution is for a semi-infinite layer open to the right.

Using the stress and strain compatibility conditions at  $x = 0$  for all layers, the total force acting at each node can be written as<sup>[155]</sup>

$$\mathbf{P}^R(z) = (i\mathbf{A}\mathbf{V}\mathbf{K} + \mathbf{D}\mathbf{V}) \boldsymbol{\alpha} \quad (4.14)$$

in which  $\mathbf{P}^R(z)$  is a  $2n$  column vector containing the nodal forces,  $\mathbf{K}$  is a diagonal matrix containing the wave numbers  $k_s$ ,  $s = 1, 2, \dots, 2n$ , and  $\mathbf{D}$  is a  $2n \times 2n$  matrix constructed as before using the submatrix

$$\mathbf{D}_j = \frac{1}{2} \begin{bmatrix} 0 & \lambda_j & 0 & -\lambda_j \\ G_j & 0 & -G_j & 0 \\ 0 & \lambda_j & 0 & -\lambda_j \\ G_j & 0 & -G_j & 0 \end{bmatrix}. \quad (4.15)$$

Substitution of Equation 4.13 into 4.14 gives

$$\mathbf{P}^R = \mathbf{R}\mathbf{u}^R \quad (4.16)$$

where

$$\mathbf{R} = i\mathbf{A}\mathbf{V}\mathbf{K}\mathbf{V}^{-1} + \mathbf{D}. \quad (4.17)$$

The  $2n \times 2n$  matrix  $\mathbf{R}$  is the modal dynamic stiffness matrix of the semi-infinite layered region (open to the right) for the nodes located along the boundary  $x = 0$ .

The displacement at each layer interface for any value of  $x$  can be found by combining Equations 4.12 and 4.13

$$\mathbf{u}(x, z) = \mathbf{V}\mathbf{E}\mathbf{V}^{-1}\mathbf{u}^R e^{i\omega t} \quad (4.18a)$$

where

$$\mathbf{E} = \text{diag} [e^{-ik_s x}] \quad s = 1, 2, \dots, 2n. \quad (4.18b)$$

A major assumption used in deriving the thin-layer method is the parameter linearity in the vertical direction of each element (see Equation 4.9). For this assumption to be valid the height of each element must be small compared to the shear-wavelength of the solid. The effect of element thickness on predicted vibration is investigated in Section 4.1.6 during the TLM model validation to determine an appropriate discretization.

### 4.1.2 Semi-infinite region open to the left

The method for determining the dynamic stiffness matrix for a layered region open to the left  $\mathbf{L}$  is analogous to that of the right region. Assuming the layer properties are equivalent, the only difference between the two regions is their positions with respect to the coordinate system shown in Figure 4.1. Thus the dynamic stiffness matrix of a

semi-infinite region open to the left  $\mathbf{L}$  may be computed from Equation 4.17 by changing the sign on all the coefficients relating horizontal forces to vertical displacements or vice-versa, or simply

$$\mathbf{L} = \mathbf{TRT} \quad (4.19)$$

where

$$\mathbf{T} = \begin{bmatrix} -1 & & & & 0 \\ & 1 & & & \\ & & \ddots & & \\ & & & -1 & \\ 0 & & & & 1 \end{bmatrix}. \quad (4.20)$$

The dynamic stiffness matrix for the left region can also be derived by considering leftward propagating waves. The structure of the quadratic eigenvalue problem Equation 4.11 is such that if  $k$  is an eigenvalue with corresponding eigenvector  $\mathbf{v}$ , where

$$\mathbf{v}^T = (v_1, v_2, v_3, v_4, \dots, v_{2n-1}, v_{2n}) \quad (4.21)$$

then  $-k$  is also an eigenvalue with corresponding eigenvector

$$\tilde{\mathbf{v}}^T = (-v_1, v_2, -v_3, v_4, \dots, -v_{2n-1}, v_{2n}). \quad (4.22)$$

which is obtained from  $\mathbf{v}$  by changing the sign of the horizontal components of the modeshape (i.e.  $\tilde{\mathbf{v}} = \mathbf{T}\mathbf{v}$ )<sup>[155]</sup>. This new set of eigenvalues and eigenvectors are in fact the other  $2n$  solutions to the quadratic eigenvalue problem (Equation 4.11) describing waves travelling in the negative  $x$ -direction which were discarded in Section 4.1.1. For the remainder of this work all parameters marked with a tilde ( $\sim$ ) will be associated with waves travelling in the negative  $x$ -direction.

The dynamic stiffness matrix for the left region constructed using these new eigen-

vectors is

$$\mathbf{L} = i\mathbf{A}\tilde{\mathbf{V}}\mathbf{K}\tilde{\mathbf{V}}^{-1} - \mathbf{D} \quad (4.23)$$

and the displacement at any value of  $x$  is found using

$$\mathbf{u}(x, z) = \tilde{\mathbf{V}}\tilde{\mathbf{E}}\tilde{\mathbf{V}}^{-1}\mathbf{u}^L e^{i\omega t} \quad (4.24a)$$

where

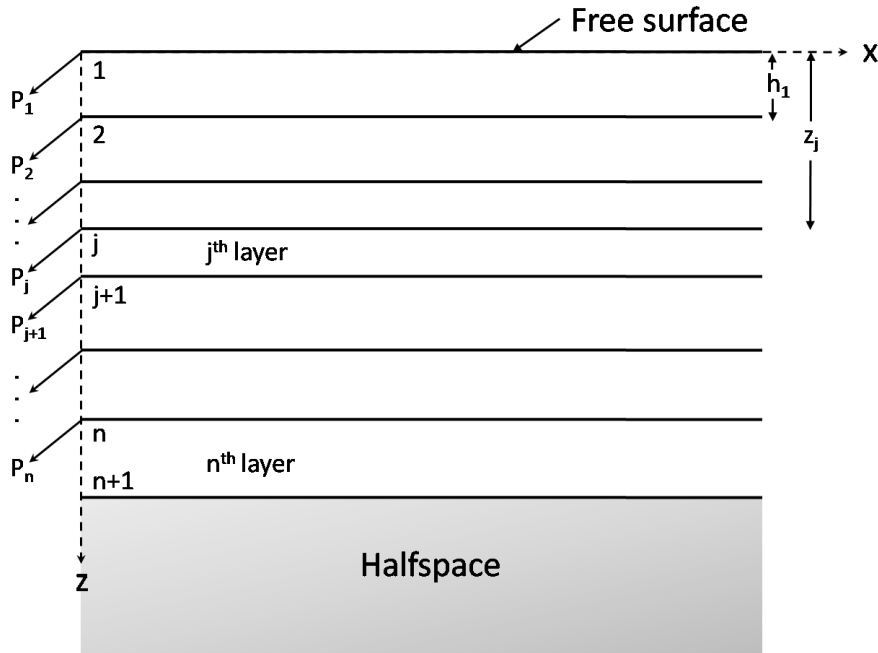
$$\tilde{\mathbf{E}} = \text{diag} \left[ e^{-i\tilde{k}_s x} \right] \quad s = 1, 2, \dots, 2n.. \quad (4.24b)$$

Note that up to this point the eigenvectors  $\mathbf{V}$  and  $\tilde{\mathbf{V}}$  have not been normalized. This is acceptable since all derivations using the eigenvectors (i.e. deriving  $\mathbf{R}$ ,  $\mathbf{L}$ ,  $\mathbf{u}$ , etc.) require premultiplication of the eigenvector matrix and postmultiplication by its inverse which negates any scaling factor. If desired the eigenvectors can be normalized using the standard eigenvector orthogonality condition<sup>[155]</sup>.

### 4.1.3 Thin-Layer Method Extension for Layered Media on a Halfspace

The TLM derivation outlined above uses a fixed base boundary condition simulating rigid bedrock. Although this is a useful formulation, some ground vibration problems require the ability to investigate the response of layered media resting on a halfspace. To use the thin-layer method with a halfspace an absorbing boundary on the base of the vertically-finite TLM domain is necessary such that a vertically-infinite domain can be simulated, as depicted in Figure 4.3.

The exact impedance matrix relating the tractions and displacements on the surface of a homogeneous halfspace (i.e. the “perfect” absorbing boundary) is derived by Kausel

Figure 4.3: Layered region  $R$  on a homogeneous halfspace (plane-strain)

and Roësset<sup>[77]</sup> as

$$\mathbf{K} = 2kG \left( \frac{1-s^2}{2(1-rs)} \begin{bmatrix} r & -1 \\ -1 & s \end{bmatrix} \begin{bmatrix} 0 & -1 \\ -1 & 0 \end{bmatrix} \right) \quad (4.25a)$$

$$r = \sqrt{1 - \frac{\omega^2}{k^2 c_p^2}} \quad (4.25b)$$

$$s = \sqrt{1 - \frac{\omega^2}{k^2 c_s^2}} \quad (4.25c)$$

where  $k$  is the horizontal wave number,  $\omega$  is the frequency, and  $c_s$  and  $c_p$  are the wave velocities of the shear and pressure waves respectively; this formulation is derived using the “stiffness matrix approach”. The impedance matrix in its current form does not lend itself to implementation into the thin-layer method approach as it would result in a transcendental equation in  $k$ .

Kausel later demonstrated<sup>[57]</sup> that the elastic wave equation for a halfspace in plane strain can be approximated by expanding Equation 4.25a using a Taylor series about

$k = 0$  and retaining the first three terms

$$\mathbf{K} = i\omega\rho c_p \begin{bmatrix} \gamma & 0 \\ 0 & 1 \end{bmatrix} + \frac{G(1-2\gamma)k}{\gamma} \begin{bmatrix} 0 & -1 \\ -1 & 0 \end{bmatrix} + \frac{iGc_s k^2}{2\omega\gamma^3} \begin{bmatrix} \gamma^3 - 2\gamma & 0 \\ 0 & i - 2\gamma \end{bmatrix} \quad (4.26)$$

where  $\gamma$  is the ratio of shear to pressure wave speed  $\frac{c_s}{c_p}$ . Andrade<sup>[7]</sup> extended this idea to be used with the thin-layer method resulting in the derivation of the halfspace element.

Consider the layered region resting on a homogeneous halfspace depicted in Figure 4.3. The layered region is discretized in the vertical direction into thin layers; the halfspace is not discretized. Displacements are again assumed to vary linearly across each thin layer resulting in the quadratic eigenvalue problem

$$(\mathbf{A}k^2 + i\mathbf{B}k + \mathbf{C}) \mathbf{v} = 0 \quad (4.27a)$$

where

$$\mathbf{C} = \mathbf{G} - \omega^2\mathbf{M} \quad (4.27b)$$

which is the same as before (see Equation 4.9). The matrices  $\mathbf{A}$ ,  $\mathbf{B}$  and  $\mathbf{C}$  are formed using the same submatrices defined in Equations 4.10 with one exception: rather than neglecting the last two rows and columns of the  $n^{\text{th}}$  layer the entire  $[X]_n$  submatrix is used and the halfspace submatrix is added to the final two degrees-of-freedom as depicted in Figure 4.4. The size of each matrix is thus increased by two degrees-of-freedom compared to the rigid bedrock case ( $(2n+2) \times (2n+2)$ ) to account for the horizontal and vertical displacements of the halfspace surface. The halfspace submatrices are given below

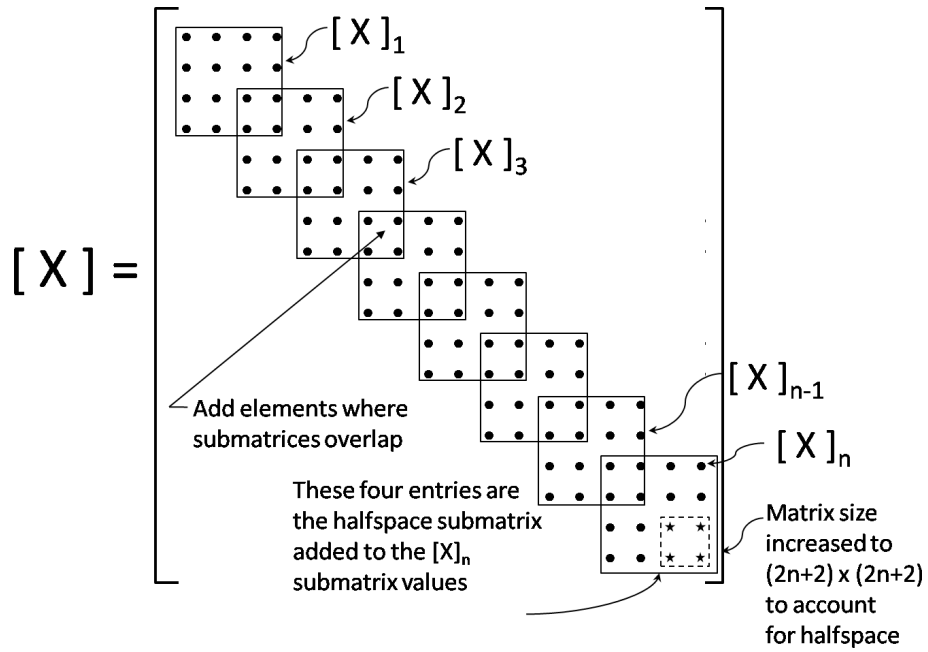


Figure 4.4: Matrix addition scheme including halfspace submatrix

$$\mathbf{A}^{hs} = \frac{iGc_s}{2\omega\gamma^3} \begin{bmatrix} (\gamma - 2)\gamma^2 & 0 \\ 0 & (1 - 2\gamma) \end{bmatrix} \quad (4.28a)$$

$$\mathbf{B}^{hs} = \frac{G(1 - 2\gamma)}{\gamma} \begin{bmatrix} 0 & -1 \\ 1 & 0 \end{bmatrix} \quad (4.28b)$$

$$\mathbf{C}^{hs} = i\omega\rho \begin{bmatrix} c_s & 0 \\ 0 & c_p \end{bmatrix} \quad (4.28c)$$

$$\mathbf{D}^{hs} = \frac{G(1 - 2\gamma)}{\gamma} \begin{bmatrix} 0 & 1 \\ -1 & 0 \end{bmatrix}. \quad (4.28d)$$

Using the stress and strain compatibility conditions at  $x = 0$  for all layers as before,

the dynamic stiffness matrix for the semi-infinite layered region on a halfspace (open to the right) can be written as

$$\mathbf{R} = i\mathbf{A}\mathbf{V}\mathbf{K}\mathbf{V}^{-1} + \mathbf{D} \quad (4.29)$$

where  $\mathbf{R}$  is now  $(2n + 2) \times (2n + 2)$ . The derivation for the dynamic stiffness matrix of the left region  $\mathbf{L}$  in Section 4.1.2 also remains valid when used with the extended halfspace matrices.

As in the semi-infinite derivation, a major assumption is used in the derivation of the halfspace element. The Taylor expansion about  $k = 0$  (see Equation 4.26) assumes that the incoming wave fronts are parallel to the surface of the halfspace. For this assumption to be valid the halfspace elements must be reasonably far from external sources such that the curvature of the wavefronts is relatively large. The effect of halfspace element placement on predicted vibration is investigated in Section 4.1.6 during the TLM model validation to determine an appropriate model depth.

#### 4.1.4 Thin-Layer Method Extension for Hyperelements

The TLM semi-infinite elements and halfspace elements provide a computationally efficient means of simulating a horizontally layered halfspace. A major limitation is how external loading can be applied to the system. As shown in Figure 4.5, the TLM halfspace only has nodes along the vertical seam between the semi-infinite regions to which external loads can be applied. This does not allow accurate coupling of structures such as an underground railway tunnel where the external surface of the tunnel must be coupled to the surrounding soil. Furthermore, it would not be possible to easily consider soil inhomogeneity such as inclined layers, subsiding soil layers and random soil properties using semi-infinite elements. A finite length TLM element is necessary for such examples.

Kausel and Roësset<sup>[76]</sup> derived the formulation for a TLM hyperelement (i.e. an element of finite length) by accounting for waves traveling in both directions through the layer due to nodal loading at both edges of the element. Consider the finite section of

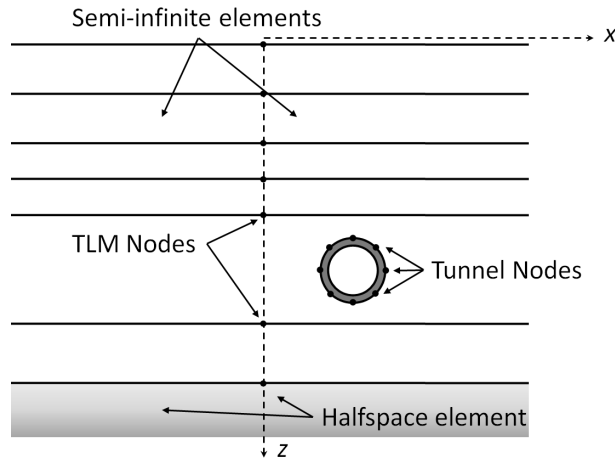


Figure 4.5: Example of an underground tunnel in a thin-layer model meshed with semi-infinite elements; the nodes along the semi-infinite seam do not match up with the exterior nodes of the tunnel

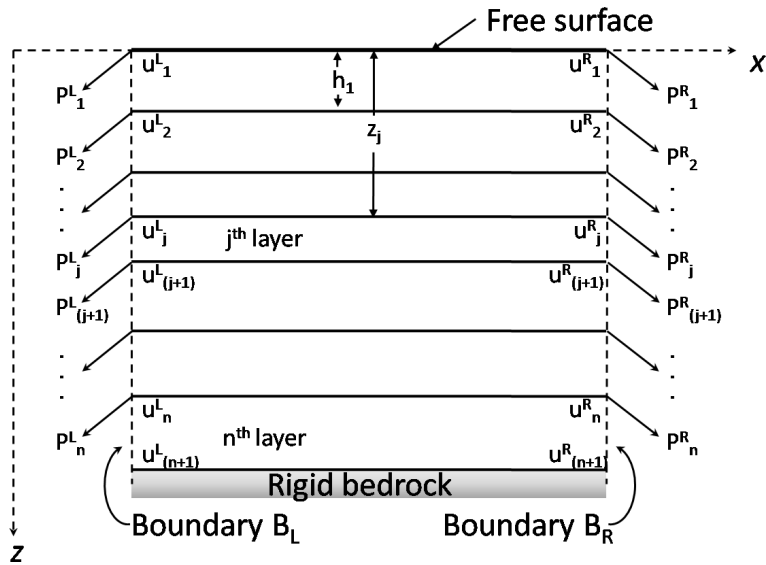


Figure 4.6: Layered finite region on rigid bedrock (plane-strain)

horizontally layered stratum resting on rigid bedrock as shown in Figure 4.6. Harmonic loads  $\mathbf{P}_L$  and  $\mathbf{P}_R$  are applied along the boundaries  $B_L$  and  $B_R$  at frequency  $\omega$ . As with the standard thin-layer method, the thickness of each thin layer is defined by  $h_j$ . The intersection of the layer boundaries with the vertical boundaries defines two sets of  $n$  nodes where each node has  $x$  and  $z$  degrees of freedom ( $\mathbf{u}_L$  and  $\mathbf{u}_R$ ).

The derivation of the quadratic eigenvalue problem used for the semi-infinite elements still holds (Equations 4.1 to 4.11); recall the governing equation of motion for the layered

region

$$(\mathbf{A}k^2 + i\mathbf{B}k + \mathbf{C}) \mathbf{v} = 0. \quad (4.30)$$

As before, the solution to this eigenvalue problem consists of  $4n$  eigenvalues:  $2n$  solutions  $k_s$  with negative imaginary parts and associated eigenvectors  $v_s$  corresponding to waves propagating in the positive  $x$ -direction and  $2n$  solutions  $\tilde{k}_s$  with positive imaginary parts and associated eigenvectors  $\tilde{v}_s$  corresponding to waves propagating in the negative  $x$ -direction ( $s = 1, 2, \dots, 2n$ ).

Recall that in matrix form the eigenvalues and eigenvectors describing waves travelling in the positive  $x$ -directions are termed  $\mathbf{K}$  and  $\mathbf{V}$ , respectively;  $\mathbf{K}$  is a  $2n \times 2n$  diagonal matrix comprised of  $k_s$  values and  $\mathbf{V}$  is a  $2n \times 2n$  matrix containing the eigenvectors columnwise. The eigenvalues and eigenvectors for waves travelling in the negative  $x$ -directions are termed  $\tilde{\mathbf{K}}$  and  $\tilde{\mathbf{V}}$ , where

$$\tilde{\mathbf{K}} = -\mathbf{K} \quad (4.31a)$$

and

$$\tilde{\mathbf{V}} = \mathbf{TV}. \quad (4.31b)$$

To determine the nodal displacements at the vertical boundaries, the contributions from both sets of boundary loads must be superimposed. Consider the nodal displacements on the left boundary of Figure 4.6. Equation 4.12 describes the contribution due to the left boundary loads  $\mathbf{P}^L$  whilst a combination of Equations 4.12 and 4.18 describe the contribution due to the right boundary loads  $\mathbf{P}^R$

$$\mathbf{u}^L = \mathbf{V}\boldsymbol{\alpha}^L + \tilde{\mathbf{V}}\tilde{\mathbf{E}}_L\boldsymbol{\alpha}^R \quad (4.32a)$$

where

$$\tilde{\mathbf{E}}_L = \text{diag} \left[ e^{-i\tilde{k}_s(-L)} \right] \quad (4.32b)$$

in which  $L$  is the distance between the lateral boundaries  $B_L$  and  $B_R$ , and  $\boldsymbol{\alpha}^L$  and  $\boldsymbol{\alpha}^R$  are the modal participation factors corresponding to waves travelling in the positive and negative  $x$ -directions, respectively. Note that  $\tilde{\mathbf{V}}$  is used for the  $\mathbf{P}^R$  contribution since the waves must travel in the negative  $x$ -direction to reach the  $B_L$  boundary. Similarly, the nodal displacements on the right boundary are

$$\mathbf{u}^R = \mathbf{V}\mathbf{E}_L\boldsymbol{\alpha}^L + \tilde{\mathbf{V}}\boldsymbol{\alpha}^R \quad (4.33a)$$

where

$$\mathbf{E}_L = \text{diag} [e^{-ik_s L}] \quad (4.33b)$$

Note that  $\tilde{k}_s = -k_s$ , thus  $\mathbf{E}_L = \tilde{\mathbf{E}}_L$ . Combining Equations 4.32 and 4.33 results in the coupled equations

$$\begin{Bmatrix} \mathbf{u}^L \\ \mathbf{u}^R \end{Bmatrix} = \begin{bmatrix} \mathbf{V} & \tilde{\mathbf{V}}\mathbf{E}_L \\ \mathbf{V}\mathbf{E}_L & \tilde{\mathbf{V}} \end{bmatrix} \begin{Bmatrix} \boldsymbol{\alpha}^L \\ \boldsymbol{\alpha}^R \end{Bmatrix}. \quad (4.34)$$

The stress and strain compatibility conditions at the two vertical boundaries are imposed as before (see Equation 4.14), resulting in the governing equation

$$\begin{Bmatrix} \mathbf{P}^L \\ \mathbf{P}^R \end{Bmatrix} = \begin{bmatrix} \mathbf{A}\mathbf{V}\mathbf{K} + \mathbf{D}\mathbf{V} & -(\mathbf{A}\tilde{\mathbf{V}}\mathbf{K} - \mathbf{D}\tilde{\mathbf{V}})\mathbf{E}_L \\ -(\mathbf{A}\mathbf{V}\mathbf{K} + \mathbf{D}\mathbf{V})\mathbf{E}_L & \mathbf{A}\tilde{\mathbf{V}}\mathbf{K} - \mathbf{D}\tilde{\mathbf{V}} \end{bmatrix} \begin{Bmatrix} \boldsymbol{\alpha}^L \\ \boldsymbol{\alpha}^R \end{Bmatrix}. \quad (4.35)$$

After some algebra it is possible to show that combining Equations 4.34 and 4.35 results in<sup>[76]</sup>

$$\begin{Bmatrix} \mathbf{P}^L \\ \mathbf{P}^R \end{Bmatrix} = \mathbf{S}_{hyper} \begin{Bmatrix} \mathbf{u}^L \\ \mathbf{u}^R \end{Bmatrix} \quad (4.36a)$$

where

$$\mathbf{S}_{hyper} = \begin{bmatrix} \mathbf{R}_1 & \mathbf{R}_2 \\ \tilde{\mathbf{R}}_2 & \tilde{\mathbf{R}}_1 \end{bmatrix} \quad (4.36b)$$

and

$$\mathbf{R}_1 = (\mathbf{R} + \mathbf{L}) \left( \mathbf{I} - \tilde{\mathbf{J}}\mathbf{J} \right)^{-1} - \mathbf{L} \quad (4.36c)$$

$$\mathbf{R}_2 = -(\mathbf{R}_1 + \mathbf{L})\tilde{\mathbf{J}} \quad (4.36d)$$

$$\tilde{\mathbf{R}}_1 = \mathbf{T}\mathbf{R}_1\mathbf{T} \quad (4.36e)$$

$$\tilde{\mathbf{R}}_2 = \mathbf{T}\mathbf{R}_2\mathbf{T} \quad (4.36f)$$

$$\mathbf{J} = \mathbf{V}\mathbf{E}_L\mathbf{V}^{-1} \quad (4.36g)$$

$$\tilde{\mathbf{J}} = \mathbf{T}\mathbf{J}\mathbf{T} \quad (4.36h)$$

$$\mathbf{I} = \text{the identity matrix.} \quad (4.36i)$$

Note these equations all hold true when the halfspace elements are added in the submatrices as described in Section 4.1.3.

The displacement at an arbitrary point  $x$  within the hyperelement can be found using the contributions from the nodal displacements acquired above. Designate the distance between the boundaries at which the displacements are desired by  $\zeta = x - x_L$  and furthermore

$$\mathbf{E}_\zeta = \text{diag} \left[ e^{-ik_s\zeta} \right] \quad (4.37a)$$

$$\mathbf{E}_{L-\zeta} = \text{diag} \left[ e^{-ik_s(L-\zeta)} \right]. \quad (4.37b)$$

The displacement at  $\zeta$  is then a superposition of the contributions from both boundaries

$$\mathbf{u}_\zeta = \mathbf{V}\mathbf{E}_\zeta\boldsymbol{\alpha}^L + \tilde{\mathbf{V}}\mathbf{E}_{L-\zeta}\boldsymbol{\alpha}^R. \quad (4.38)$$

Combining Equations 4.38 with 4.34 and 4.35 results in<sup>[76]</sup>

$$\mathbf{u}_\zeta = \begin{bmatrix} \mathbf{J}_\zeta & \tilde{\mathbf{J}}_{L-\zeta} \end{bmatrix} \begin{bmatrix} \mathbf{I} & -\tilde{\mathbf{J}} \\ -\mathbf{J} & \mathbf{I} \end{bmatrix} \begin{bmatrix} \left( \mathbf{I} - \tilde{\mathbf{J}}\mathbf{J} \right)^{-1} & \mathbf{0} \\ \mathbf{0} & \left( \mathbf{I} - \mathbf{J}\tilde{\mathbf{J}} \right)^{-1} \end{bmatrix} \begin{bmatrix} \mathbf{u}^L \\ \mathbf{u}^R \end{bmatrix} \quad (4.39a)$$

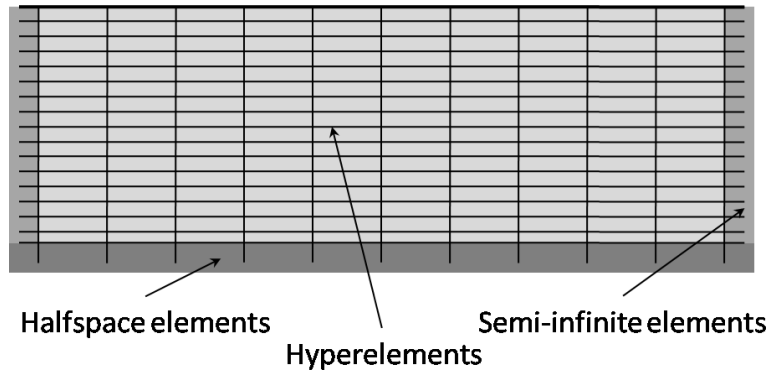


Figure 4.7: Schematic of a basic TLM model simulating a homogeneous halfspace

where

$$\mathbf{J}_\zeta = \mathbf{V}\mathbf{E}_\zeta\mathbf{V}^{-1} \quad (4.39b)$$

$$\mathbf{J}_{L-\zeta} = \mathbf{V}\mathbf{E}_{L-\zeta}\mathbf{V}^{-1} \quad (4.39c)$$

$$\tilde{\mathbf{J}}_{L-\zeta} = \mathbf{T}\mathbf{J}_{L-\zeta}\mathbf{T}. \quad (4.39d)$$

#### 4.1.5 Constructing a model using the thin-layer method

The four previous sections detail the derivation of the dynamic stiffness matrices for semi-infinite elements, halfspace elements and hyperelements. Constructing a model using these elements is a simple case of standard FE addition. Consider the basic model of a halfspace shown in Figure 4.7 built up of two semi-infinite regions, a half-space region and ten columns of hyperelements. The resulting total system dynamic stiffness matrix is block-tridiagonal as shown in Figure 4.8, where each submatrix  $\mathbf{S}_{hyper}^m$  is the stiffness matrix for the  $m$ th column of hyperelements including the halfspace element; the outer most quadrants also include the stiffness of the semi-infinite element regions.

The total system of coupled equations is thus

$$\mathbf{P} = \mathbf{S}_{total}\mathbf{u} \quad (4.40)$$

where  $\mathbf{P}$  is a vector describing the externally applied nodal loads and  $\mathbf{u}$  is a vector

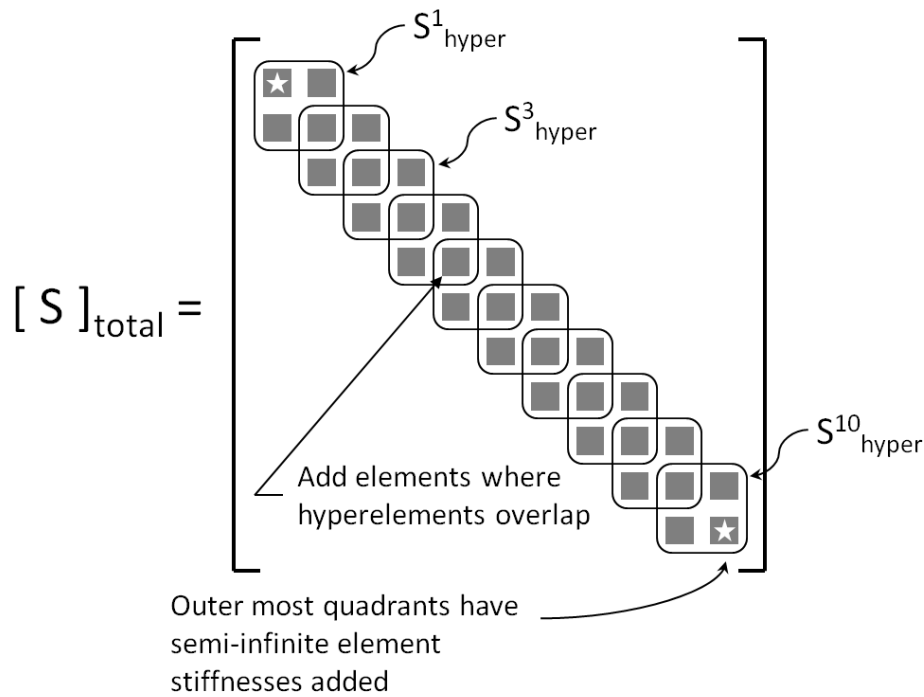


Figure 4.8: Matrix addition scheme for thin-layer elements

describing the nodal displacements. This is a standard system of equations and can be solved using matrix inversion, although this is computationally expensive. A more efficient approach is to use a Thomas algorithm<sup>[18]</sup> which utilizes the block-tridiagonal nature of the stiffness matrix to perform a simplified Gaussian elimination; a description of the Thomas algorithm is provided in Appendix B. The benefit of the algorithm is that it only requires the inversion of a few of the quadrants of the submatrices, which are orders of magnitude smaller than the total stiffness matrix, making the solution significantly less computationally expensive.

#### 4.1.6 TLM Model Validation for a Surface Load

Before the TLM model is used to investigate soil uncertainty it is necessary to validate the modelling approach; the test case is a horizontally layered halfspace subjected to a surface line load as depicted in Figure 4.9. The layer has thickness  $h$  and material properties defined by elastic modulus  $E_1$ , Poisson's ratio  $\nu_1$ , density  $\rho_1$ , dilation damping coefficient  $D_{P_1}$  and shear damping coefficient  $D_{S_1}$ ; the halfspace has properties  $E_2$ ,

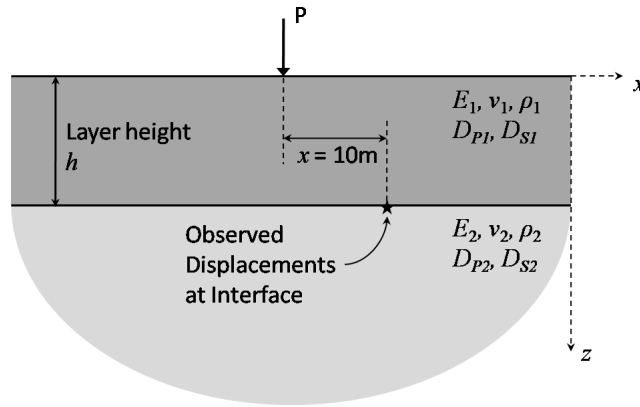


Figure 4.9: Validation case of harmonic unit load on surface with displacement observation point at the layer interface and  $x = 10\text{m}$

Table 4.1: TLM validation model parameters

| Layer                          | Halfspace                       |
|--------------------------------|---------------------------------|
| $E_1 = 550 \text{ MPa}$        | $E_2 = [0.25, 1, 4] \times E_1$ |
| $\nu_1 = 0.44$                 | $\nu_2 = \nu_1$                 |
| $\rho_1 = 2000 \text{ kg/m}^3$ | $\rho_2 = \rho_1$               |
| $D_{P_1} = 0.05$               | $D_{P_2} = D_{P_1}$             |
| $D_{S_1} = 0.05$               | $D_{S_2} = D_{S_1}$             |

$\nu_2$ ,  $\rho_2$ ,  $D_{P_2}$ ,  $D_{S_2}$ . Table 4.1 gives the material properties used in the validation case. The displacements are observed at the interface layer 10m horizontally from the applied load. The predicted ground vibration at the observation point is compared using the TLM method, the analytical solution for a horizontally layered halfspace, and a boundary-element (BE) model between 15-200Hz (using 5Hz frequency steps). The following subsections provide specifics regarding the three models used in the validation comparison.

#### 4.1.6.1 Analytical Solution to a Layered Halfspace

The analytical frequency response functions (FRF's) for a line-load on the surface of a horizontally layered, plane strain halfspace is derived by coupling the Green's functions for a homogeneous halfspace<sup>[140]</sup> and a homogeneous layer<sup>[139]</sup>; details of this derivation

can be found in Appendix C. The final equation of motion for the validation case is

$$\mathbf{u}_B = (\mathbf{I} + \mathbf{H}_{BB}\mathbf{G}_{BB}^{-1})^{-1} \mathbf{H}_{BA}\mathbf{P} \quad (4.41)$$

where  $\mathbf{u}_B(k_n, \omega)$  is the displacement vector at the layer interface in the wavenumber ( $k_n$ ) and frequency ( $\omega$ ) domains, while  $\mathbf{P}$  is the forcing vector applied at the surface. The entries to the individual transfer function matrices (i.e.  $\mathbf{H}_{BA}, \mathbf{H}_{BB}, \mathbf{G}_{BB}$ ) are rather convoluted so for brevity they will not be reproduced here; see Appendix C.3 for details.

An inverse direct Fourier transform (iDFT) is used to determine the spatial response at the layer interface in the  $x$ -direction using 4096 samples between  $\pm 4\pi$  resulting in a spatial resolution of 0.25m between  $x = \pm 512\text{m}$  ( $x = 0$  is directly below the surface load). Convergence testing was done to ensure this resolution was sufficient to capture the sharp gradients in the near-field response at the highest test frequency (200Hz) while also extending out far enough that the response had decayed to zero before truncation at the lowest test frequency (15Hz).

#### 4.1.6.2 Boundary Element Model for a Layered Halfspace

As mentioned in Chapter 2, boundary element (BE) modelling is an accepted method of simulating ground vibration problems in semi-infinite domains. The BE model used herein is derived using the method outlined in Appendix D.

A schematic of the validation case BE model is given in Figure 4.10. As shown, only the soil surface and layer interface are discretized using an element length of 0.2m. This element size was selected such that the eight elements per shear-wavelength requirement<sup>[20]</sup> was maintained at the highest test frequency (200Hz). Except for the node at which the unit line load is applied, a zero-traction boundary condition is applied to the soil surface (i.e. free-surface condition). Force equilibrium and displacement continuity is enforced between the two regions at the layer interface.

The boundary element model is included in the validation test not to verify the

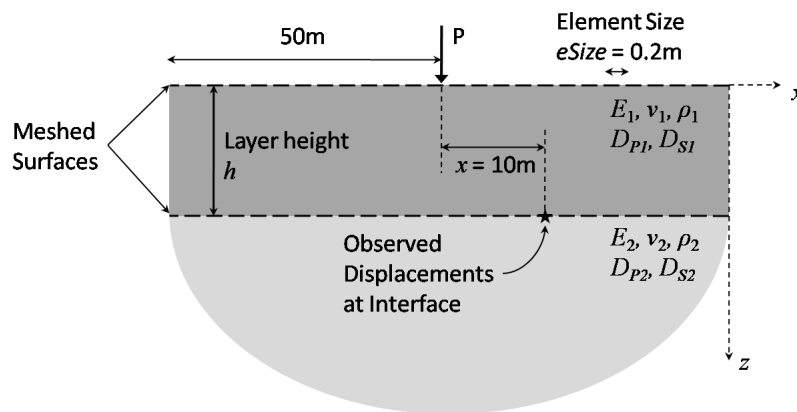


Figure 4.10: BE model of validation case: harmonic unit load on surface with displacement observation point at the layer interface and  $x = 10\text{m}$

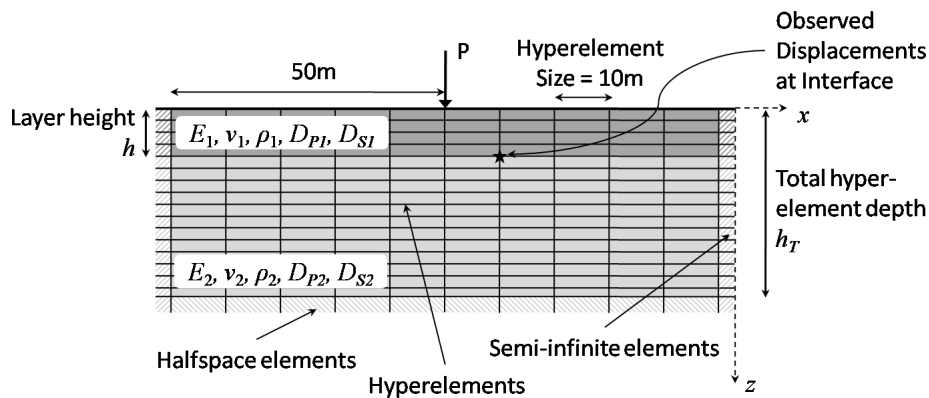


Figure 4.11: TLM model of validation case: harmonic unit load on surface with displacement observation point at the layer interface and  $x = 10\text{m}$

TLM model but to validate the BE model itself against the analytical solution. The BE model predictions will later be used as a benchmark for the TLM model predictions in Section 4.2 for inclined layers.

#### 4.1.6.3 TLM Model for a Layered Halfspace

The TLM model used for the validation test is shown in Figure 4.11. Ten columns of 10m long hyperelements are enclosed by semi-infinite regions on either side and halfspace elements at the base.

As mentioned in Sections 4.1.1 and 4.1.3, two important assumptions were made in deriving the thin-layer method: the height of the thin-layer elements must be small compared to the shear-wavelength and the halfspace elements must be reasonably far

from external loading such that the radius of the wavefronts will be large. Therefore, the vertical discretization  $\Delta h$  and total hyperelement depth  $h_T$  are varied to determine suitable values at which the TLM model has converged to the analytical solution. At each test frequency, the vertical discretization is updated such that

$$\Delta h = \frac{\gamma_s}{\Delta_\gamma} \quad (4.42)$$

where  $\gamma_s$  is the shear-wavelength at the current frequency and  $\Delta_\gamma$  is varied between 4 and 20. Also, the total depth is updated such that

$$h_T = \gamma_s h_\gamma \quad (4.43)$$

where  $h_\gamma$  is varied between 1 and 10.

#### 4.1.6.4 Model Comparison Results

The ground displacements at the observation point ( $x = 10, z = 5$ ) are displayed in Figure 4.12 as frequency response functions (FRF's) between 15-200Hz for a vertical surface load. The results from the three models include FRF's in the  $x$ -direction ( $H_{xz}$ ) and  $z$ -direction ( $H_{zz}$ ) for the three layer cases where  $E_1 = \beta_E E_2$  and  $\beta_E = [4, 1, 0.25]$ . Three representative curves from the TLM parametric study are included to illustrate how the variables  $\Delta_\gamma$  and  $h_\gamma$  affect the predicted response.

In all cases the boundary element model produces acceptable results; the deviation from the analytical solution is never more than 0.6dB (ref 1m/N). The results from the TLM parametric study show how important it is to adhere to the requirements of the method assumptions. When a reasonably shallow and coarse vertical discretization are used ( $\Delta_\gamma = 6, h_\gamma = 1$ ) the results differ significantly from the analytical solution, especially when the layer stiffness is equal to or less than the halfspace stiffness (see Figures 4.12(c) to 4.12(f)). As the total depth and discretization is increased the results

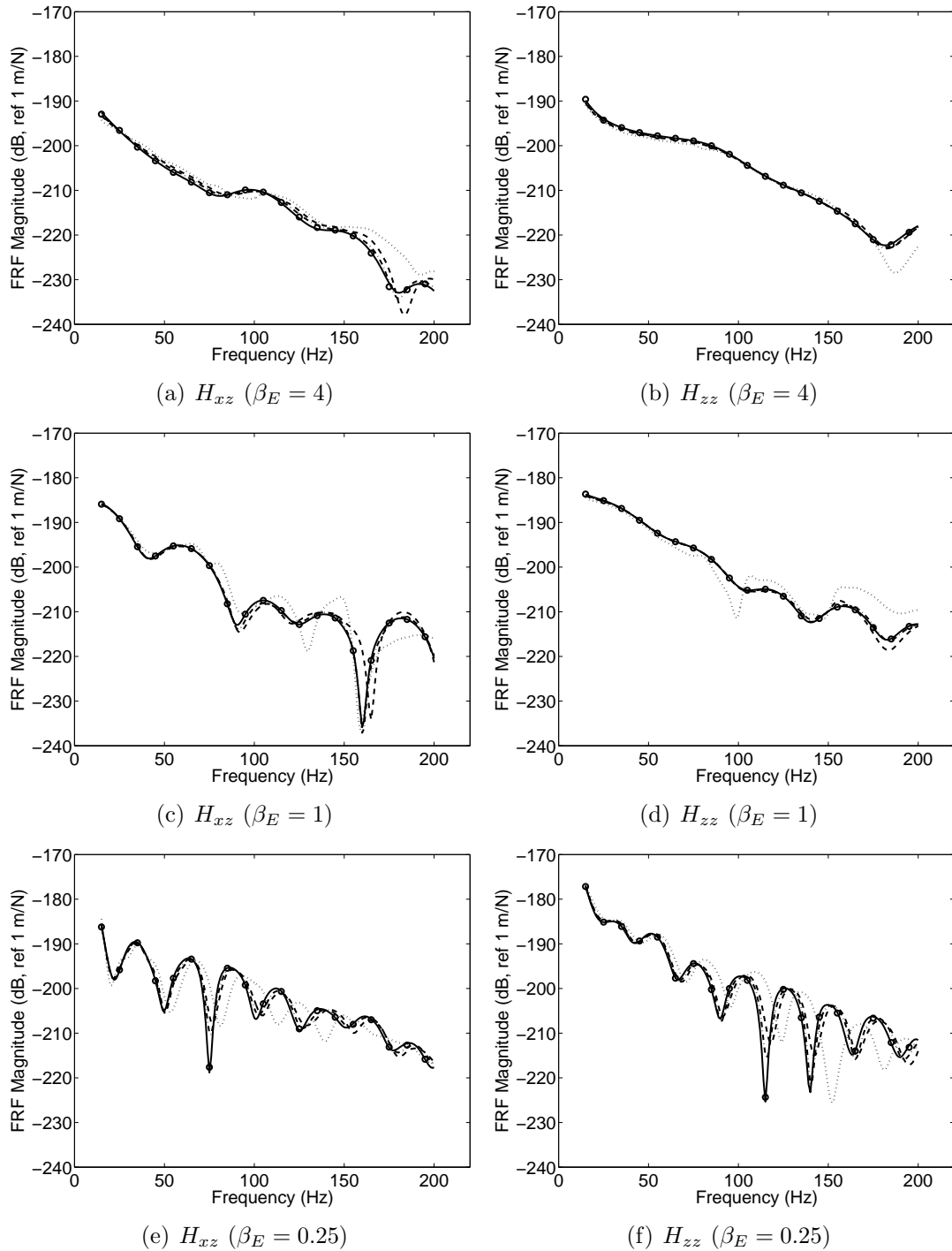


Figure 4.12: Frequency Response Functions (FRF) at the observation point; response in  $x$ -direction ( $H_{xz}$ ) and  $z$ -direction ( $H_{zz}$ ) due to vertical surface load (solid - analytical solution; circle - BE solution; dotted -  $[\Delta_\gamma = 6, h_\gamma = 1]$ ; dashed -  $[\Delta_\gamma = 11, h_\gamma = 3]$ ; dash-dotted -  $[\Delta_\gamma = 16, h_\gamma = 5]$ )

converge towards the analytical solution. The case of  $\Delta_\gamma = 11$ ,  $h_\gamma = 3$  produce results similar to the analytical solution but still have areas of discrepancy (i.e. between 150-200Hz in Figures 4.12(a) and 4.12(c)).

The parametric study of the TLM model was deemed to converge when increasing the discretization coefficient  $\Delta_\gamma$  or total depth coefficient  $h_\gamma$  resulted in a relative difference of less than 1% for  $H_{zz}$  over the frequency range. The convergent parameters are  $\Delta_\gamma = 16$ ,  $h_\gamma = 5$ . As depicted in Figure 4.12, the TLM results using these parameters are consistent with the analytical results; the maximum deviation is 1.6dB. This deviation is predominantly due to a 10Hz frequency shift in Figure 4.12(f) at higher frequencies; if this shift is neglected the maximum deviation between the models is 0.8dB. The frequency shift is attributed to the truncation assumption used in the halfspace element; if the total depth of the model is further increased the frequency shift slowly diminishes but results in a significant increase in computational requirements.

The computational times for the BE model and TLM model using  $\Delta_\gamma = 16$ ,  $h_\gamma = 5$  are given in Table 4.2 for  $\beta_E = 1$ . The TLM method is significantly quicker than the BE model while producing results with comparable error relative to the analytical solution. The compromise between this level of error and maintaining quick run times is deemed acceptable for the TLM model. These parameters are used for all TLM models throughout the rest of the investigation. It should be noted that run times for the TLM model differ depending on the layer properties while the BE model run-times do not. For example, the total time for the TLM  $\beta_E = 0.25$  case is 463 seconds due to the increased discretization necessary to capture the shorter wavelengths in the upper layer; however, this is still approximately 7 times quicker than the BE model.

The response along the length of the layer interface is also investigated to determine if the models are consistent with the analytical solution along the boundary rather than just a single point. To facilitate illustration of the results, the vibrational response is depicted as rms velocity for the 25Hz, 50Hz, 100Hz and 160Hz third-octave frequency bands (see Table 3.2 in Section 3.1.5 for a list of the frequency bands). The frequency

Table 4.2: Surface load validation case run times for BE and TLM models using  $\beta_E = 1$ 

|                                   | Boundary Element Model | Thin-Layer Method |
|-----------------------------------|------------------------|-------------------|
| Average time per frequency step   | 83.1 sec               | 4.6 sec           |
| Minimum time for a frequency step | 81.6 sec               | 3.0 sec           |
| Maximum time for a frequency step | 85.3 sec               | 5.6 sec           |
| Total time                        | 3158 sec               | 175 sec           |

band rms velocity is calculated for a white-noise input (i.e. unit harmonic vertical load at all frequencies between 15-200Hz) using the method of random vibrations outlined in Section 3.1.5. For white-noise input this simplifies to

$$v_{rms}(x) = 2 \int_{\omega_1}^{\omega_2} |(i\omega)H_{ij}|^2 d\omega. \quad (4.44)$$

where  $v_{rms}(x)$  is the  $\omega_1 \rightarrow \omega_2$  frequency band rms velocity at a given surface location  $x$ , and  $H_{ij}$  is the transfer function describing displacement at location  $x_i$  due to a load at location  $x_j$ .

The rms velocities along the layer interface are displayed in Figures 4.13 and 4.14, respectively. The presented results from the three models include velocities in the  $x$ -direction (horizontal) and  $z$ -direction (vertical) for  $\beta_E = [4, 1, 0.25]$ . The rms velocity results show good agreement between the three models. The maximum rms velocity difference between the analytical response and the BE model is: 3.4dB in the horizontal direction for the 25Hz frequency band; 1.1dB in the vertical direction for the 25Hz frequency band. The peak error occurs at distances greater than 40m from the load site and diminishes at higher frequency bands. Recall the surface discretization only extends to 50m either side of the load in the BEM model; past this point the BE formulation assumes the medium is a fullspace. This discontinuity can cause reflection of surface waves which account for the discrepancy compared to the analytical solution. Between 0-42m, the peak rms velocity error is less than 0.5dB. Overall the BE model is

deemed to adequately reproduce the velocity profile along the interface layer compared to the analytical solution.

The maximum rms velocity difference between the analytical response and the TLM model is: 4.2dB in the horizontal direction for the 160Hz frequency band; 5.3dB in the vertical direction for the 160Hz frequency band. Again, the maximum error occurs at relatively large  $x$ -distances; however, unlike the BE model this discrepancy occurs at higher band frequencies. There are no artificial boundaries to cause reflections in the TLM model thus it is not a result of truncating low frequency wavelength. This error is attributed to the imperfect halfspace elements. The halfspace element formulation assumes the incoming wavefield has planar wavefronts parallel to the surface of the halfspace (see Section 4.1.3). Thus if the incident angle of the incoming wavefield is relatively far from perpendicular there will be a reflection of some energy as shown in Figure 4.15. Increasing the total depth of the model would decrease this effect since the wavefront radius would be larger (i.e. decreased incident angle) and less energy would reach the elements for reflection due to damping and geometric decay. However, the small amount of error produced using  $h_\gamma = 5$  is again deemed an acceptable compromise between accuracy and computational requirements.

In conclusion, the thin-layer method is used to simulate a horizontally layered halfspace subjected to a vertical surface line load and found to accurately predict the displacement response and rms velocity at the layer interface over a frequency range of 15-200Hz. Optimal parameters of 16 elements per minimum shear-wavelength ( $\Delta_\gamma = 16$ ) and a total model depth of 5 wavelengths before halfspace elements ( $h_\gamma = 5$ ) are derived from a parametric analysis. Implementing the TLM model with these parameters produces similar results to the analytic solution for run times of approximately 5 seconds per frequency step. The boundary element model is also shown to accurately predict the response of the layered halfspace, although computational times are significantly greater than the TLM model. In the next section tunnel loading will be introduced to the three models to complete the validation process.

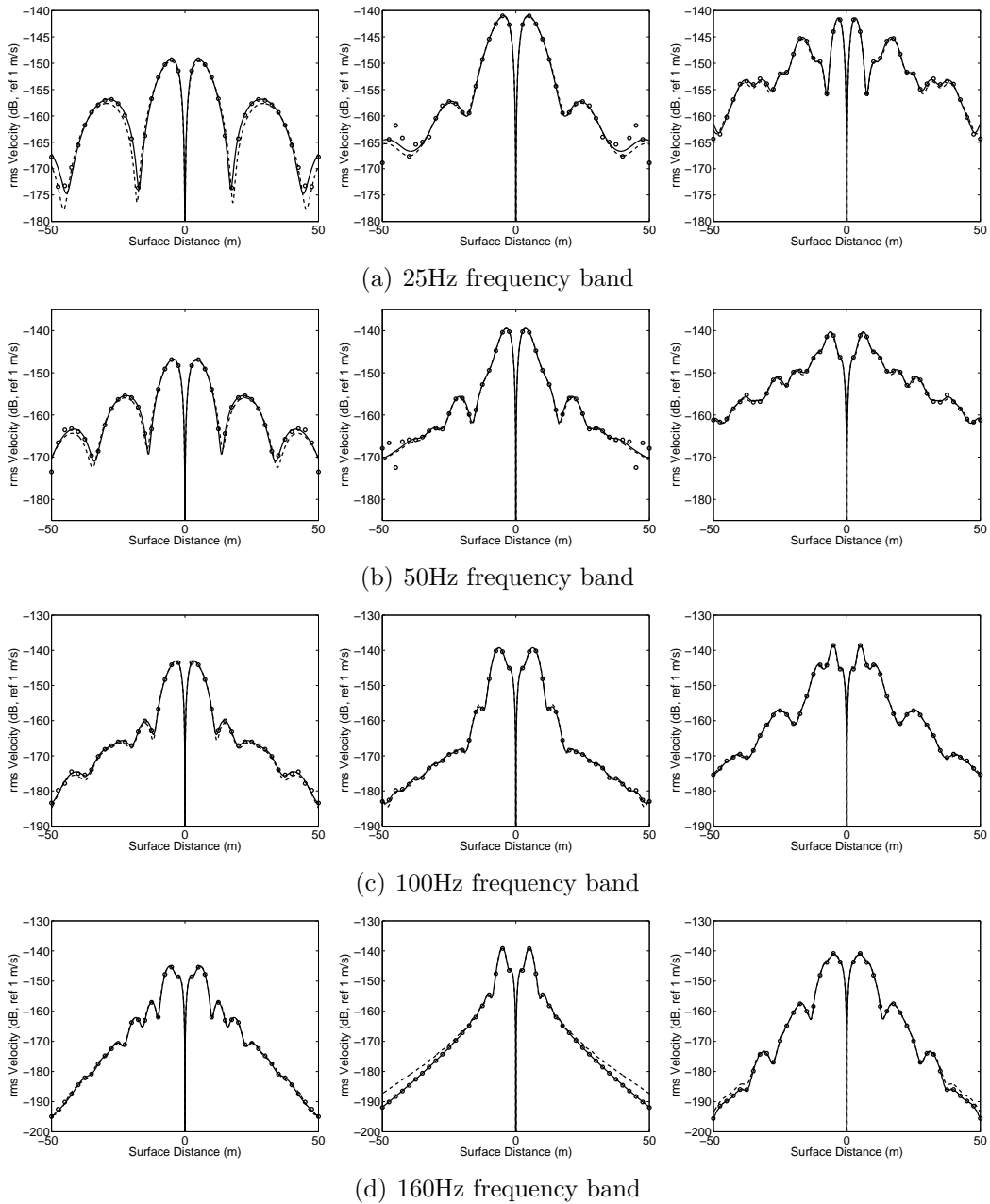


Figure 4.13: Horizontal rms velocity along layer interface located at a depth of 5m at four frequency bands (left -  $\beta_E = 4$ ; center -  $\beta_E = 1$ ; right -  $\beta_E = 0.25$ ); response due to vertical surface load at  $x = 0$  (solid - analytical solution; circle - BE solution; dashed - TLM solution)

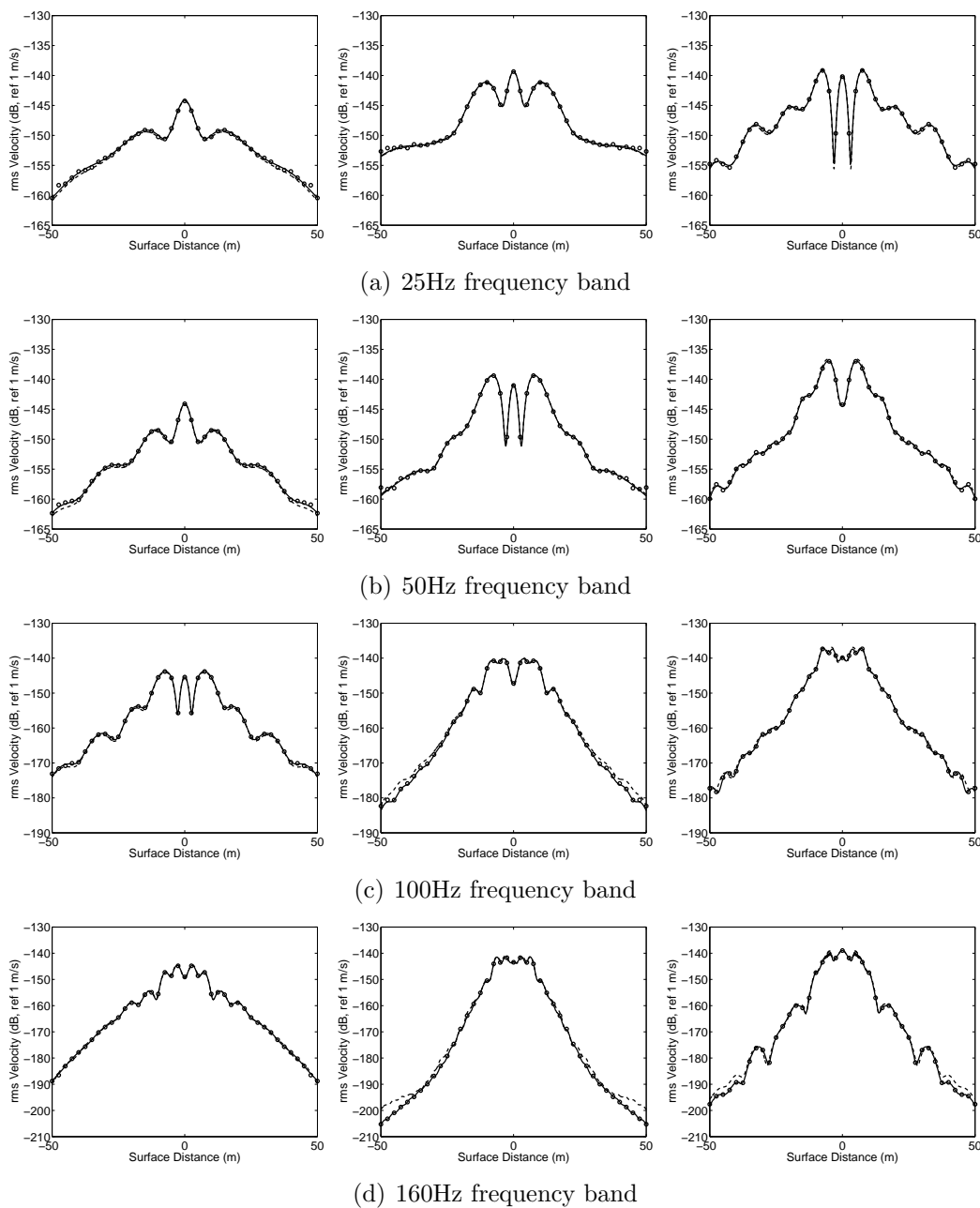


Figure 4.14: Vertical rms velocity along layer interface located at a depth of 5m at four frequency bands (left -  $\beta_E = 4$ ; center -  $\beta_E = 1$ ; right -  $\beta_E = 0.25$ ); response due to vertical surface load at  $x = 0$  (solid - analytical solution; circle - BE solution; dashed - TLM solution)

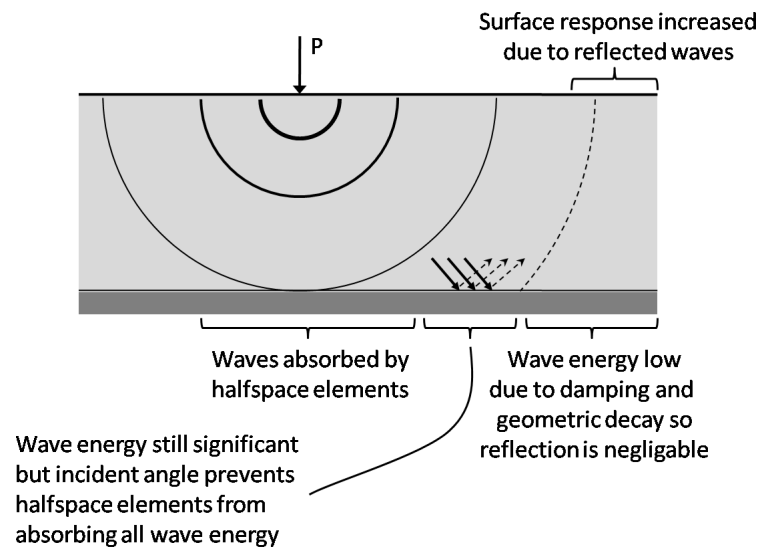


Figure 4.15: Depiction of wave energy reflection by halfspace elements due to relatively large incident angle

### 4.1.7 TLM Model Validation for Tunnel Loading

The thin-layer method has been shown to accurately predict displacements in a layered halfspace when subjected to a surface load. Simulating rail-loading from a tunnel buried in the halfspace presents new challenges: force transmission from rails to tunnel must be calculated, the stiffness of the tunnel must be included, non-uniform loading around the tunnel must be captured, etc. Rather than incorporating a numerical model of the tunnel and associated rail hardware into the TLM model, an equivalent internal source method is used which simulates the presence of the tunnel through discrete line loads in the halfspace.

#### 4.1.7.1 The Equivalent Internal Source Method

The equivalent internal source method (EIS) negates the need to include an actual tunnel in the model by instead simulating the presence of a tunnel in a fullspace using a number of discrete line loads. The line loads have specific magnitude and directions so as to produce equivalent displacement and stress fields as would an actual tunnel with an internal train load (see Figure 4.16). The benefit of this method is no inclusion is required in the halfspace which reduces modelling complexity.

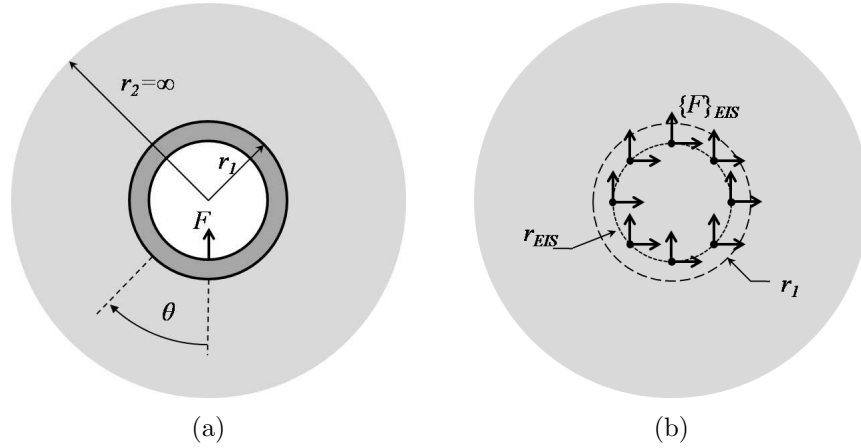


Figure 4.16: Schematic of the PiP arrangement (left) and equivalent internal source arrangement (right) to simulate a tunnel buried in a fullspace under plane-strain loading.

The derivation of the EIS method in plane-strain is detailed in Appendix G using the Pipe-in-Pipe (PiP) method detailed in Chapter 3 and Appendix F. First the standard PiP prediction is performed to calculate the displacement and stress fields at the tunnel-soil interface. Next a Core-in-Pipe (CiP) model (i.e. solid cylinder coupled inside a cylinder of infinite radius) is constructed to simulate the fullspace without a tunnel; the core radius must be smaller than the tunnel radius (i.e.  $r_{EIS} < r_1$ ). By forcing the solution of the CiP model to equal the PiP model at  $r_1$  it is possible to back-calculate the necessary loading at  $r_{EIS}$  as

$$\mathbf{F}_{EIS} = ([\mathbf{T}_\infty]_{r_{EIS}} - [\mathbf{T}_0]_{r_{EIS}} [\mathbf{U}_0]_{r_{EIS}}^{-1} [\mathbf{U}_\infty]_{r_{EIS}}) [\mathbf{U}_\infty]_{r_1}^{-1} [\mathbf{U}_n]^{PiP} \quad (4.45)$$

where  $\mathbf{F}_{EIS}$  is the loading at  $r_{EIS}$  in the ring-mode-wavenumber-frequency domain,  $\mathbf{U}_n^{PiP}$  is the displacement at  $r_1$  calculated using PiP, and  $\mathbf{T}_0$ ,  $\mathbf{U}_0$ ,  $\mathbf{T}_\infty$  and  $\mathbf{U}_\infty$  are matrices describing the inner and outer cylinders, respectively (see Appendix G). The magnitude and direction of the discrete line loads required to reproduce the tunnel loading in the spatial domain can be calculated using a standard IDFT.

The plane-strain equivalent (i.e.  $\xi = 0$ ) of the float-slab-track (FST) arrangement used in Chapter 3 is employed to determine the force transmission to the tunnel invert due to a unit line load applied to the rail surface. The plane-strain rail and slab pa-

Table 4.3: Floating-slab track properties

|                                 |                                |
|---------------------------------|--------------------------------|
| <b>Rail Beam</b>                | <b>Slab beam</b>               |
| $m_{rail} = 120.6 \text{ kg/m}$ | $m_{slab} = 3500 \text{ kg/m}$ |
| <b>Railpad</b>                  | <b>Slab Bearing</b>            |
| $k_{rail} = 200 \text{ MN/m/m}$ | $k_{slab} = 5 \text{ MN/m/m}$  |
| $\eta_{rail} = 0.3$             | $\eta_{slab} = 0.5$            |

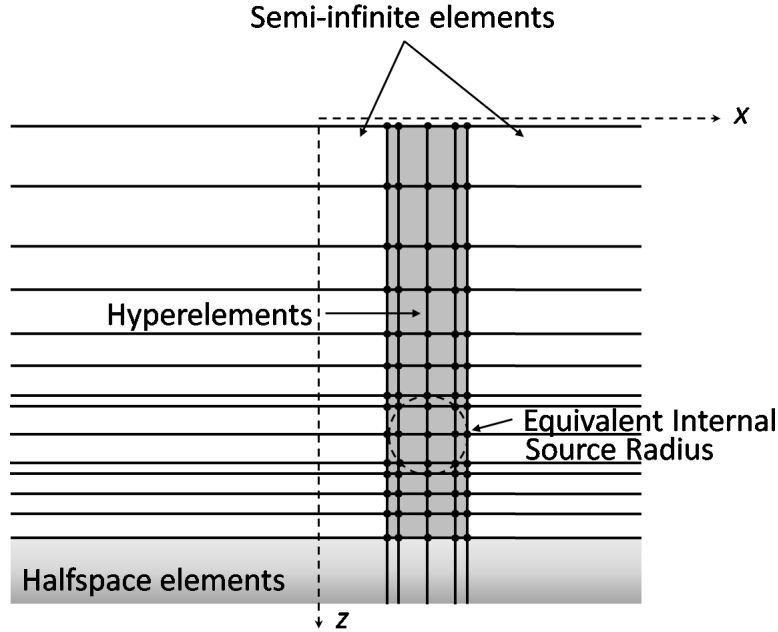


Figure 4.17: Modified TLM model incorporating a set of nodes for equivalent internal source (EIS) loading

Parameters are listed again in Table 4.3 with the force transmission function given below where the complex stiffness is given by  $k^* = k(1 + i\eta)$  (see Section 3.1.2 for more details on the derivation).

$$\frac{F_T}{F_{input}} = \frac{k_{rail}^* k_{slab}^*}{(m_{rail}\omega^2 - k_{rail}^*)((m_{slab}\omega^2 - k_{slab}^*) - k_{rail}^* m_{rail}\omega^2)} \quad (4.46)$$

Tunnel loading is incorporated into the thin-layer model using the equivalent internal source method by refining the hyperelement mesh to ensure nodes at the EIS radius as shown in Figure 4.17.

Although the EIS method is derived in a fullspace, it is assumed that the equivalent internal sources can be used in a halfspace without introducing significant error. This

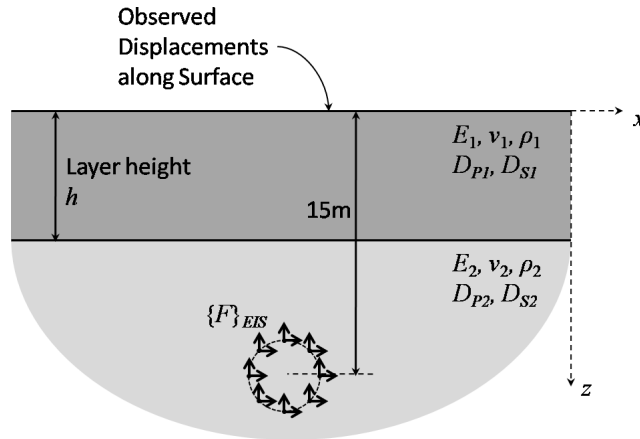


Figure 4.18: Validation case for tunnel loading

assumption requires the EIS loading to be reasonably far from layer boundaries or free-surfaces so that wave energy reflected back toward the tunnel by the boundaries is small compared to the source (i.e. approximating a fullspace)<sup>[61]</sup>. In the current investigation a wave-path separation of at least 3 tunnel diameters is maintained between the tunnel and a layer boundary; the wave-path is defined as the distance an outgoing wave would travel before returning to the tunnel. The 20m wave-path is approximately the size of the longest expected shear-wavelength (22m at 15Hz); at this low frequency there will be little material damping over that distance but geometric decay will significantly reduce the wave-energy of the reflected wave compared to the original. At higher frequencies material damping will play a more significant role in reducing reflected wave energy returning to the tunnel. Due to these mechanisms the assumption is deemed acceptable.

#### 4.1.7.2 Validation Model for Tunnel Loading

The tunnel-loading validation case is shown schematically in Figure 4.18 for the same material properties used in the previous validation case (see Table 4.1). The equivalent internal source method is used to simulate a tunnel with the properties listed in Table 4.4 subjected to a vertical, harmonic, unit lineload acting on the rail of the FST assembly. A total of 32 discrete lineloads are used at a radius  $r_{EIS} = 3m$  centered at  $x = 0m$ ,  $z = 15m$ .

Table 4.4: Tunnel properties for validation case

| Parameter                    | Value                  |
|------------------------------|------------------------|
| Outer radius                 | 3.25 m                 |
| Inner radius                 | 3.00 m                 |
| Elastic modulus              | 50 GPa                 |
| Poisson's ratio              | 0.3                    |
| Density                      | 2500 kg/m <sup>3</sup> |
| Dilational damping ( $D_P$ ) | 0.05                   |
| Shear damping ( $D_S$ )      | 0.05                   |

The BE and TLM model predictions at the surface of the layered halfspace are compared to the analytical solution using rms velocities at the 25Hz, 50Hz, 100Hz and 160Hz frequency bands. The analytical solution is derived by superimposing the surface displacements developed by each of the EIS line loads; the transfer function for the displacement at the surface due to a buried line load is derived in Appendix C as

$$\mathbf{u}_A = \mathbf{H}_{AB} (\mathbf{H}_{BB} + \mathbf{G}_{BB})^{-1} \mathbf{G}_{BO} \mathbf{P} \quad (4.47)$$

where  $\mathbf{u}_A$  is the surface displacement in the wavenumber-frequency domain,  $\mathbf{P}$  is the loading vector, and  $\mathbf{H}_{ij}$  and  $\mathbf{G}_{ij}$  are transfer function for the layer and halfspace respectively.

The boundary element model uses the same element properties and lengths as defined in the previous validation case. For this case a ring of 32 EIS loads with  $r_{EIS} = 3\text{m}$  at a depth of 15m is included to simulate the tunnel loading. Convergence testing showed an unacceptable level of deviation from the analytical solution when a total model width of 100m is used; the reflection of wave energy at the artificial surface boundaries discussed in Section 4.1.6.4 is more pronounced in the tunnel loading case. The total width of the model is increased to 200m for the remaining investigations so that the bulk of the wave energy will have decayed before reaching the boundary of the BE surface.

The TLM model also uses the same properties and element sizes as in the previous validation case; however further hyperelement mesh refinement is necessary to ensure

Table 4.5: Tunnel load validation case run times for BE and TLM models using  $\beta_E = 1$ 

|                                   | Boundary Element Model | Thin-Layer Method |
|-----------------------------------|------------------------|-------------------|
| Average time per frequency step   | 438 sec                | 56 sec            |
| Minimum time for a frequency step | 406 sec                | 11 sec            |
| Maximum time for a frequency step | 541 sec                | 132 sec           |
| Total time                        | 16643 sec              | 2150 sec          |

a node at each of the 32 EIS locations. The total depth of the model before halfspace elements is determined using  $h_\gamma = 5$  below the lowest EIS line load:

$$h_T = z_{0_{tunnel}} + r_{EIS} + \gamma_s h_\gamma. \quad (4.48)$$

#### 4.1.7.3 Results of the Tunnel-Loading Validation Case

The surface frequency band rms velocities predicted by the three models are presented in Figures 4.19 and 4.20. The presented results include velocities in the  $x$ -direction (horizontal) and  $z$ -direction (vertical) for  $\beta_E = [4, 1, 0.25]$ .

As shown in the figures, both the BE and TLM models predict surface rms velocities which are similar to the analytical solution; the maximum difference between the the TLM and analytic models is 0.8dB in the horizontal direction for the 100Hz frequency band and 0.6dB in the vertical direction for the 160Hz frequency band. For the BE to analytic model comparison the maximum error is 1.2dB in horizontal direction for the 160Hz frequency band and 1.0dB in the vertical direction for the 100Hz frequency band. Changes in layer properties do not appear to have a correlated effect on the prediction accuracy of the models; the results match well for all  $\beta_E$  values. The increase in total width of the BE model to 200m appears to have rectified the artificial wave reflection and the consequent deviation from the analytical solution as was seen in the surface load case.

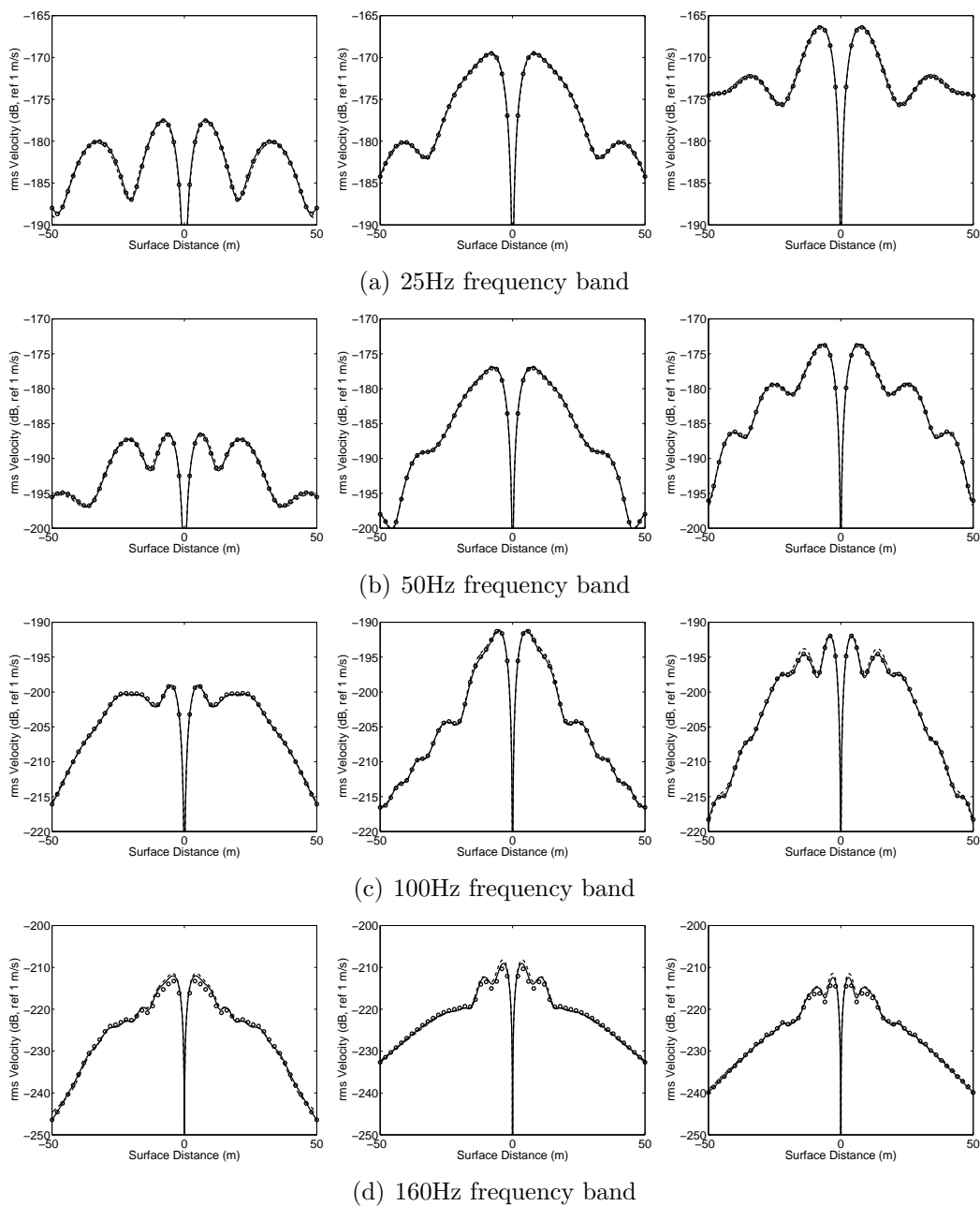


Figure 4.19: Horizontal rms velocity along surface with 5m layer at four frequency bands (left -  $\beta_E = 4$ ; center -  $\beta_E = 1$ ; right -  $\beta_E = 0.25$ ); response due to vertical line load applied to the rail in a 6.5m OD tunnel with centroid at (0,15) (solid - analytical solution; circle - BE solution; dashed - TLM solution)

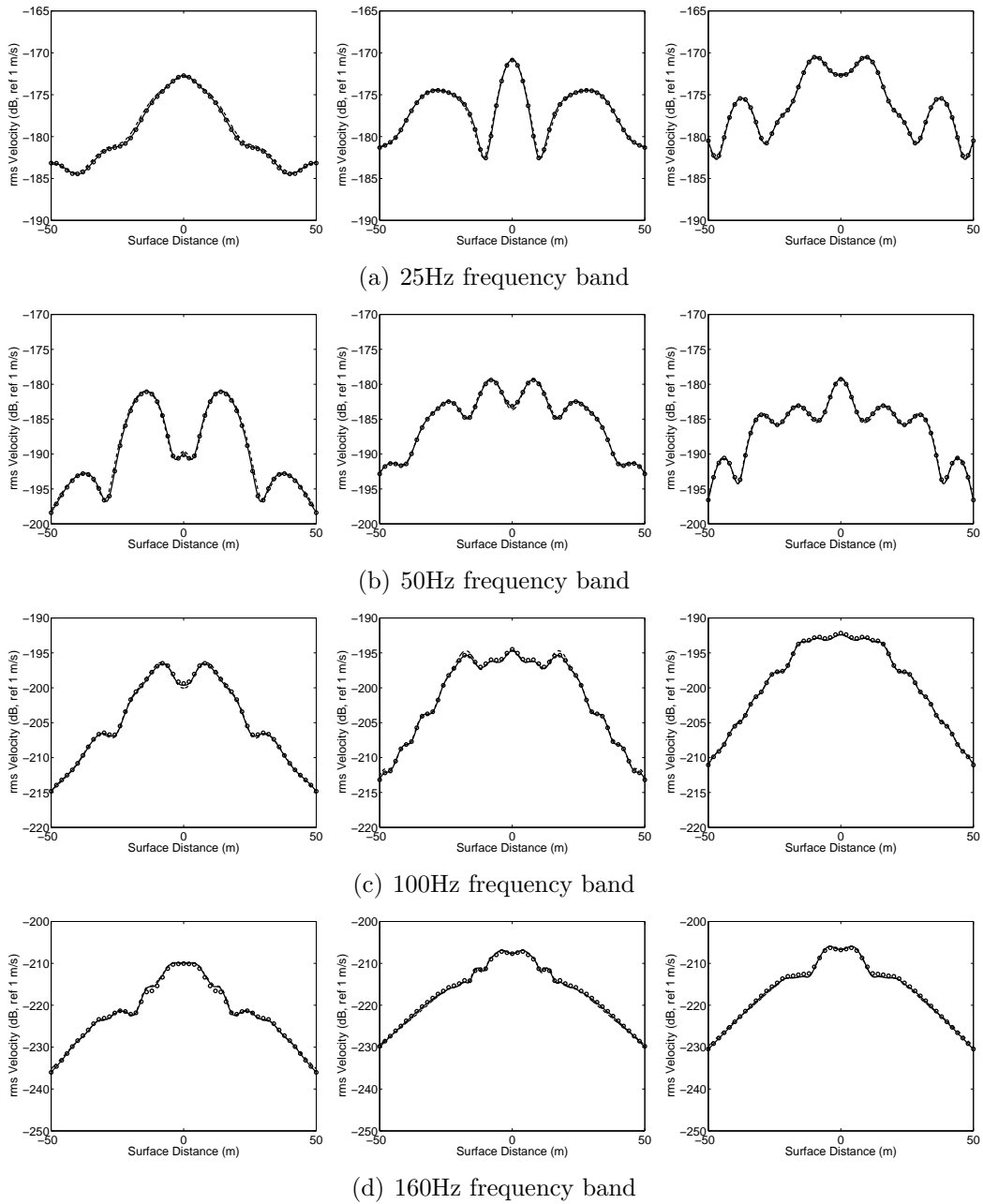


Figure 4.20: Vertical rms velocity along surface with 5m layer at four frequency bands (left -  $\beta_E = 4$ ; center -  $\beta_E = 1$ ; right -  $\beta_E = 0.25$ ); response due to vertical line load applied to the rail in a 6.5m OD tunnel with centroid at (0,15) (solid - analytical solution; circle - BE solution; dashed - TLM solution)

The computational times for the BE and TLM models are listed in Table 4.5. Comparing these times to those of the surface load case (see Table 4.2) it is obvious the TLM model takes longer when predicting vibration due to tunnel loading; however the TLM model is still significantly faster than the BE method on average. The increased computational time in the TLM model is attributed to two factors: the need to model more of the soil and an increase in the number of hyperelement columns necessary to mesh the EIS ring. In the surface load case the total depth before the halfspace elements is defined in Equation 4.43 as  $h_T = \gamma_s h_\gamma$  whereas for tunnel loading the depth must be increased (Equation 4.48:  $h_T = z_{0_{tunnel}} + r_{EIS} + \gamma_s h_\gamma$ ) to ensure there is at least  $h_\gamma$  wavelengths of soil modelled below every load. Consider the 200Hz frequency step for  $\beta_E = 1$  where  $\gamma_s = 1.55\text{m}$ . According to Equation 4.42 the necessary element heights are 0.1m. This equates to a total model depth of 7.75m for the surface load case requiring 78 elements per column of hyperelements/semi-infinite elements, and 25.75m for the tunnel loading case requiring 258 elements per column. Furthermore, in order to mesh the EIS ring 16 more columns of hyperelements are required to create nodes for the 32 equally spaced line loads around the circumference. The combination of these two factors increase the number of elements in the model from approximately 900 to 7200. This order of magnitude increase in elements explains the order of magnitude increase in computational time.

It should also be noted that the computation time using the BE method was found to decrease linearly with frequency; this is attributed to improved matrix conditioning in the BE formulation at higher frequencies allowing for faster matrix inversions. Conversely the TLM computation time increases quadratically as the frequency increases. This is due to the constant amount of soil that must be modelled (i.e.  $z_{0_{tunnel}} + r_{EIS}$ ) with elements which decrease in height as the frequency increases. Therefore the average computation time per frequency step will decrease for the TLM model if the upper limit of the frequency range is reduced, whereas it will increase for the BE method.

In conclusion, the thin-layer method is used to simulate a horizontally layered half-

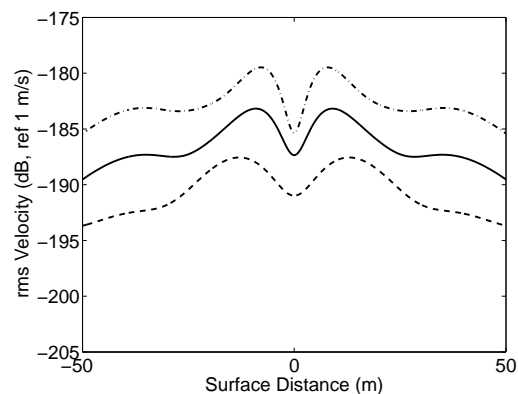


Figure 4.21: The effect of layer wavespeed on rms velocity along surface of a halfspace with a 5m thick horizontal layer; response magnitude due to vertical line load applied to the rail in a 6.5m OD tunnel with centroid at (0, 15) (solid -  $\beta_E = 1$ ; dashed -  $\beta_E = 4$ ; dash-dotted -  $\beta_E = 0.25$ )

space with a buried tunnel subjected to a vertical lineload acting on the FST rail. The model accurately predicts the frequency band rms velocities at the surface of the halfspace when compared to the analytical solution. The TLM parameters of 16 elements per minimum shear-wavelength and a total model depth of 5 wavelengths below the deepest lineload proved acceptable for the simulation. The boundary element model is also shown to accurately predict the response of the layered halfspace once the total model width was increased to 200m, although computational time is again significantly greater than the TLM model.

#### 4.1.7.4 The Effect of Layer Wavespeed

The results presented in Figures 4.19 and 4.20 show an interesting effect on surface vibration as the layer wavespeed is varied by changing the elastic modulus. Increasing the wavespeed (i.e. increasing the elastic modulus) causes a decrease in surface rms over the 100m interval above the tunnel. For ease of comparison the magnitude of the rms response for the three  $\beta_E$  cases are calculated for the 15-200Hz frequency range and are plotted in Figure 4.21.

To aid in the visualization of the mechanisms behind this effect it is most convenient to consider the response to the white-noise harmonic input in the time-domain (i.e. a

unit impulsive line load). Considering the response to an impulse results in the development of a single set of pressure, shear and Rayleigh waves which propagate through the domain making reflection and refraction of the waves easier to visualize and interpret. The response in the frequency-domain exhibits similar reflection/refraction mechanisms as the time-domain solution; however the frequency-domain response is more difficult to interpret visually as there are many wavefronts interacting with the model boundaries which confuses the interpretation.

The time response is calculated by taking the inverse Fourier transform (iDFT) of the frequency domain response for white noise between 0-500Hz using 1Hz sampling; frequencies above 500Hz are neglected as the frequency response function amplitudes are negligible compared to the 100-200Hz region. Figure 4.22 shows the displacement magnitude of the soil surrounding the tunnel for the three  $\beta_E$  cases at a number of time instants between 7.4ms and 74ms. These figures show that the interaction of both the pressure and shear wavefronts at the surface cause significantly more surface displacement for the  $\beta_E = 0.25$  case than for the  $\beta_E = 4$  case.

Shortly after the impulse (i.e. 7.4ms) the responses from the three cases are identical; this is expected as the wavefronts have not reached the interface between the halfspace and layer. At 12.6ms the pressure wavefronts have entered the layer. The law of refraction, or Snell's law, states that the ratios of the angles of incidence and refraction for waves passing through a boundary between two different media are equivalent to the ratio of the media wavespeeds<sup>[47]</sup>. The predicted response of a cylindrical wavefront moving into a medium with a faster wavespeed would be an increase in wavelength and decrease in radius of curvature (Figure 4.23(a);  $\beta_E = 4$ ), while the wavelength would decrease and radius of curvature increase for a wavefront passing into a medium with slower wavespeed (Figure 4.23(b);  $\beta_E = 0.25$ ). This response is visible in the TLM predictions shown in Figure 4.23(c) and Figure 4.23(d) as the P-wave crosses the layer interface at time  $t = 12.6$ ms. Recall from Chapter 2 that pressure and shear waves decay inversely with the radius of curvature in a bulk medium, thus the energy loss

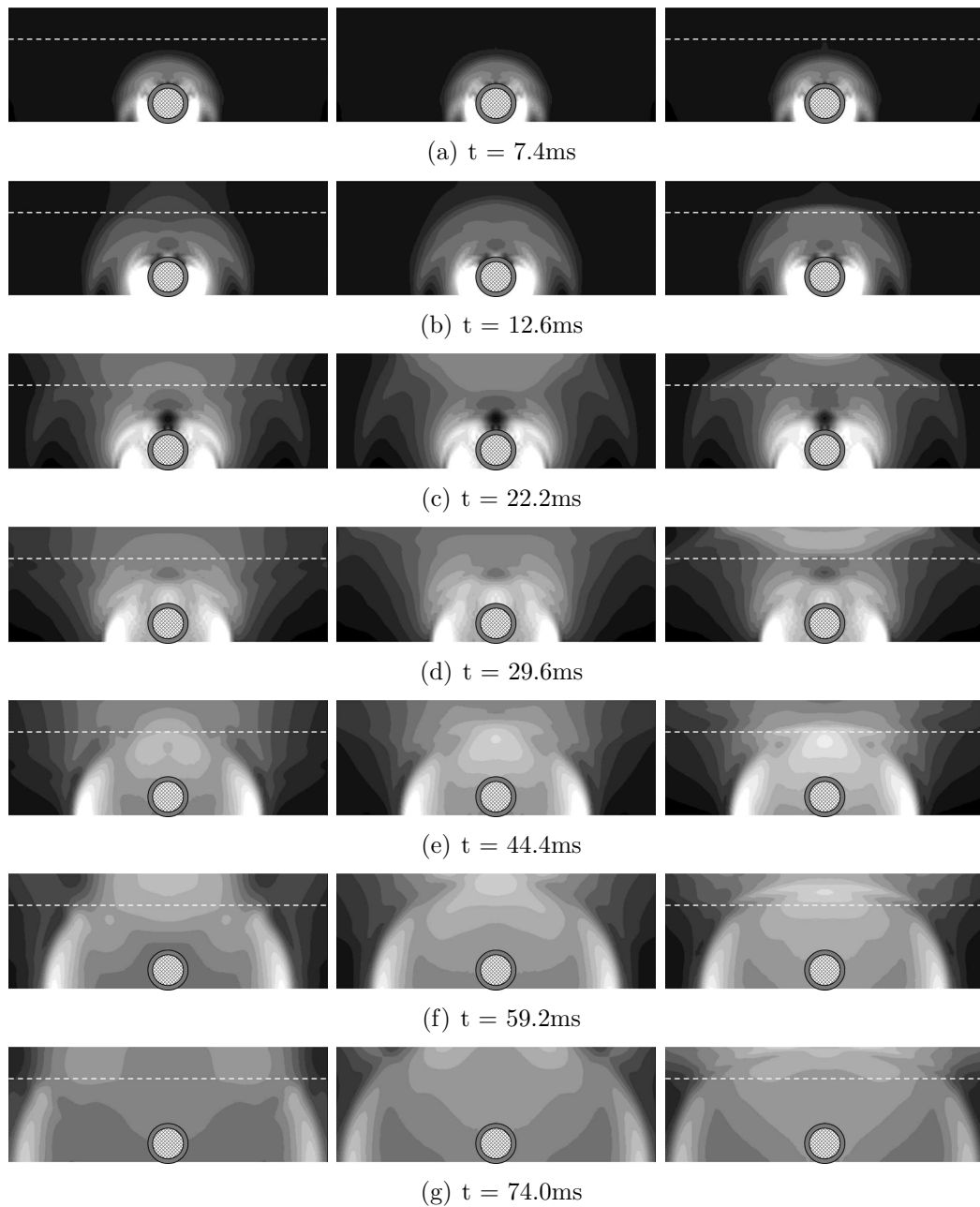


Figure 4.22: Displacement response in the layered validation case halfspace:  $\beta_E = 4$  on the left;  $\beta_E = 1$  in the center;  $\beta_E = 0.25$  on the right. Black indicates no soil motion while white indicates relatively large displacements; dashed line shows location of layer interface, ring shows location of tunnel

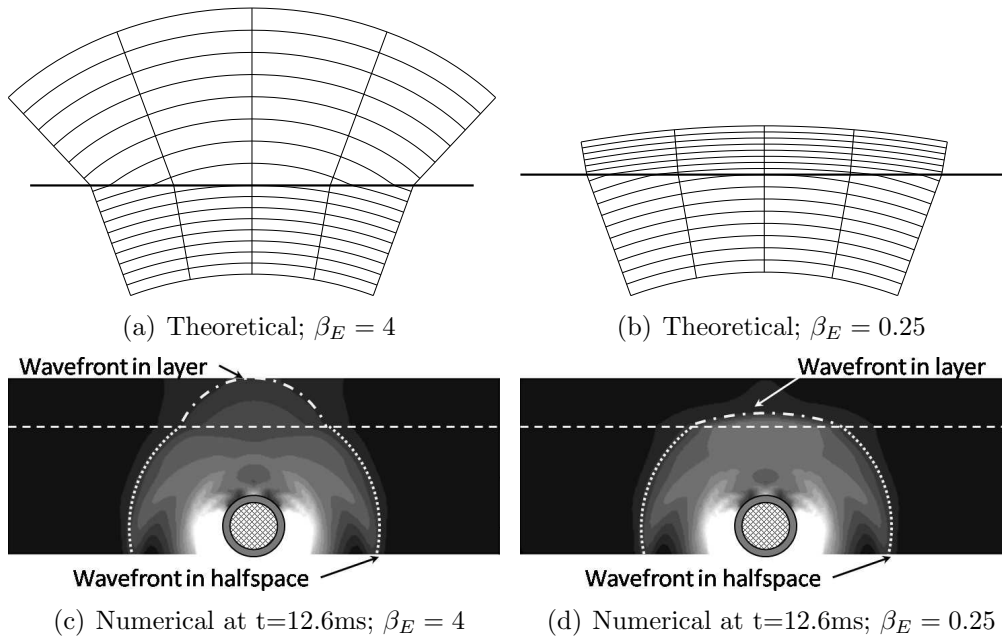


Figure 4.23: The effect of layer wavespeed on the radius of curvature of incoming wavefronts: top - theoretical predictions from Snell's law of refraction including five direction normals to visualize the refraction angle; bottom - TLM predictions at  $t=12.6\text{ms}$  where radius decreases for  $\beta_E = 4$  case and increases for  $\beta_E = 0.25$  case as expected

as a wavefront propagates from the layer interface to the surface is proportional to  $\left(\frac{1}{r_1} - \frac{1}{r_1 + 5}\right)$  where  $r_1$  is the radius of curvature at the interface and the layer is 5m thick. The radius of curvature of the wavefront in the  $\beta_E = 4$  case is smaller than in the  $\beta_E = 0.25$  case thus the energy loss must be greater for  $\beta_E = 4$  according to the equation above. This increase in geometric decay for a layer with higher wavespeed partially explains the decrease of rms velocity for the  $\beta_E = 4$  case.

Continuing on in Figure 4.22, after 22.2ms the pressure wave has just begun to reflect off the surface for the  $\beta_E = 0.25$  case, while in the other two cases the pressure wavefront has already passed back over the layer interface into the halfspace. At 29.6ms the superposition of the reflected pressure wave with the incoming wave energy is visible in the  $\beta_E = 0.25$  case as the large area of light grey near the surface; the reflected wavefront has already exited the layer in the  $\beta_E = 4$  thus there is little superposition of energy. The shear wavefront has entered the layer at 59.2ms; the figures show how the wave energy is concentrated over a smaller area in the  $\beta_E = 0.25$  case due to the

decrease in wavespeed while the wavefront is spread out in the  $\beta_E = 4$  case. Finally, at 74ms the concentration of shear wave energy is seen in the  $\beta_E = 0.25$  case as large displacements (light grey), while the energy has quickly propagated away in the  $\beta_E = 4$  case resulting in much smaller displacements. This superposition of the concentrated wavefront reflecting off the surface in the  $\beta_E = 0.25$  case is the other contributing factor attributed to the increase in rms velocity as the layer stiffness decreases.

For these model parameters, the results suggest that neglecting to include a single layer when modelling wave propagation through a solid medium can result in surface rms velocity inaccuracies of  $\pm 5$ dB. This should be taken into account when stating the prediction accuracy of a model simulating “real” soils using a homogeneous halfspace.

## 4.2 The Effect of Inclined Soil Layers

Soil layering is a natural process resulting from soil development and movement. Soil models often assume that layers run parallel to the surface for simplicity; uniform layers are geometrically simple to include in a numerical model, they can be described analytically or meshed with simple elements, and often model developers do not have sufficient empirical data to create a realistic soil lithology. However, as discussed in Chapter 2 soil layering is commonly inclined at angles of up to  $5^\circ$ . It is unclear how the inclination of a soil layer affects the vibration response at the surface due to disturbances from underground railways. The TLM model is employed to quantify the level of uncertainty associated with neglecting to include layer inclination in ground vibration models.

### 4.2.1 Inclined Layer Model

A single layer inclined on a halfspace is used to investigate the effect of layer inclination on surface vibration, as depicted in Figure 4.24(a). As the hyperelement geometry is rectangular it is not possible to simulate the exact interface between the layer and the halfspace; instead the inclined interface is approximated in step-wise fashion as shown

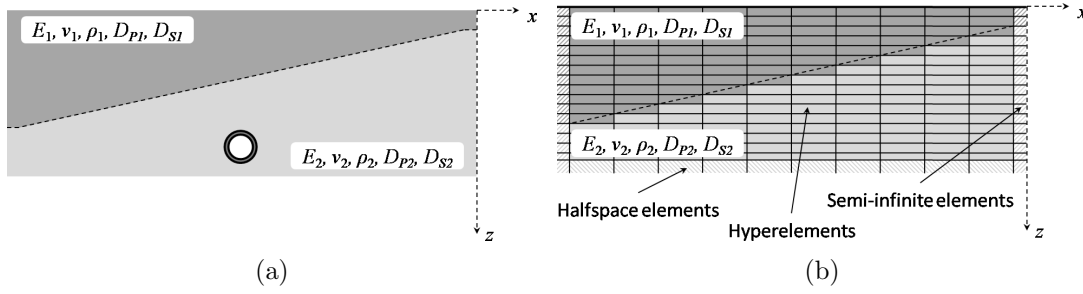


Figure 4.24: TLM representation of an inclined layer on a halfspace using step-wise increments in hyperelement material properties

in Figure 4.24(b). The inclined boundary is meshed using 10m wide hyperelement steps which results in step heights of less than 1m for angles  $\leq 5^\circ$ . This is deemed an acceptable approximation relative to the sizes of the layer and halfspace model in general. To verify this assumption the TLM model for a layer inclined at  $3^\circ$  will be compared to a BE model with a smooth interface between the layer and the halfspace.

It should be noted that some work has been reported on creating semi-infinite elements with non-vertical side-boundaries<sup>[116]</sup>. These “zigzag” elements use a coordinate transform which describes the elements in a non-orthogonal system resulting in additional terms in the elemental submatrices. The use of these elements was considered for the current investigation but they were found to be numerically unstable at small inclination angles (i.e. less than  $20^\circ$ ). As the investigation is concerned with inclination angle less than  $5^\circ$  the zigzag elements were deemed unacceptable for use in this simulation.

The parameters for the inclined layer model are shown schematically in Figure 4.25 with material properties listed in Table 4.6. Tunnel loading is simulated using the equivalent internal source method for the 6.5m OD concrete tunnel with floating-slab track subjected to a unit harmonic lineload at the rail as used in the validation case (see Section 3.1.2 for FST properties); the EIS ring is 3m in radius with a centroid at  $x=0$ ,  $z=15$ m.

The TLM model is constructed in the same manner as the tunnel-loading validation case. The main difference is the material properties are varied so as to create the inclined

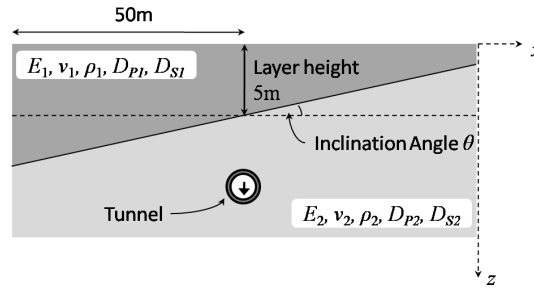


Figure 4.25: Inclined layer model showing model parameters

Table 4.6: Inclined layer model properties

|                             | Tunnel | Halfspace | Layer                   |
|-----------------------------|--------|-----------|-------------------------|
| $E$ (GPa)                   | 50     | 0.55      | $[0.25, 4] \times 0.55$ |
| $\rho$ (kg/m <sup>3</sup> ) | 2500   | 2000      | 2000                    |
| $\nu$                       | 0.3    | 0.44      | 0.44                    |
| $D_P$                       | 0.05   | 0.05      | 0.05                    |
| $D_S$                       | 0.05   | 0.05      | 0.05                    |

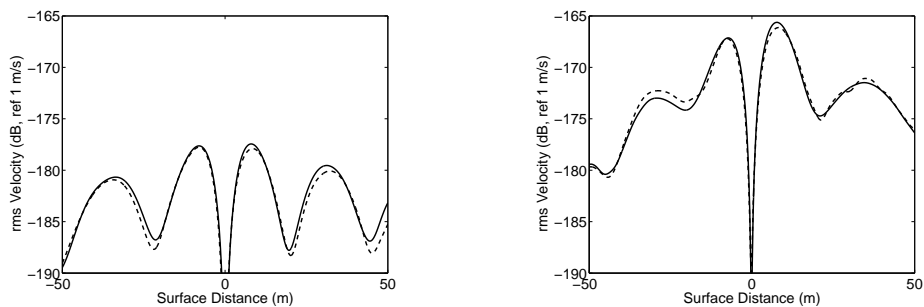
layer in a step-wise fashion. The model has element heights which are varied to ensure at least 16 elements per smallest shear wavelength in either region (i.e.  $\Delta_\gamma = 16$ ) and has five shear wavelengths of material included below the deepest EIS load (i.e.  $h_\gamma = 5$ ). Inclination angles of  $\theta = [1^\circ, 3^\circ, 5^\circ]$  are simulated using the TLM method.

The boundary element model retains the parameters from the tunnel-loading validation case (i.e. 200m total width, 0.2m element length, 32 elements around the  $r_{EIS} = 3\text{m}$  ring). The interface between the layer and the halfspace is linear from  $-100\text{m} \leq x \leq 100\text{m}$ . Only the results from the  $\theta = 3^\circ$  inclination angle case are reported in comparison with the TLM predictions.

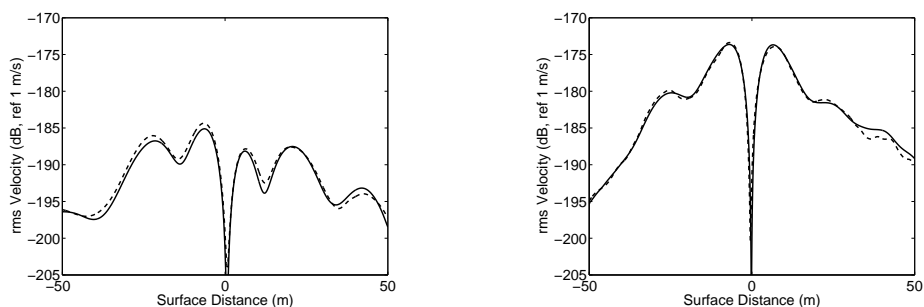
### 4.2.2 Effect of Inclined Layer on Surface Vibration

The predicted surface rms velocity for the TLM and BE models simulating a layer inclined at  $3^\circ$  are presented in Figures 4.26 and 4.27 for the 25Hz, 50Hz, 100Hz and 160Hz frequency bands. The presented results include velocities in the  $x$ -direction (horizontal) and  $z$ -direction (vertical) for  $\beta_E = [4, 0.25]$ .

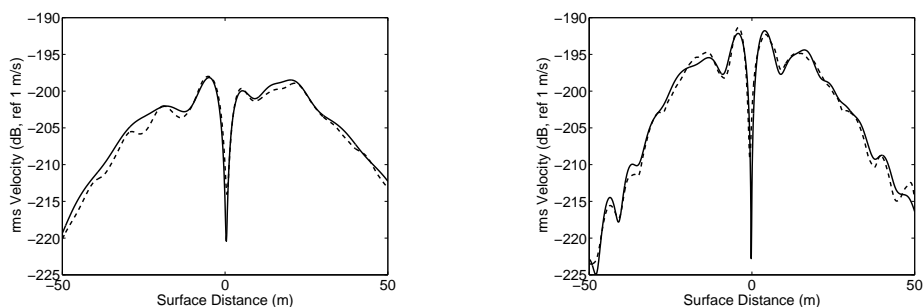
As shown in the figures the results for the two models show good agreement over the



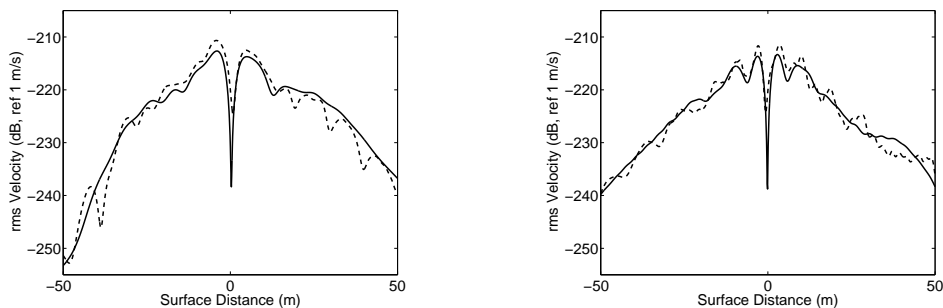
(a) 25Hz frequency band



(b) 50Hz frequency band

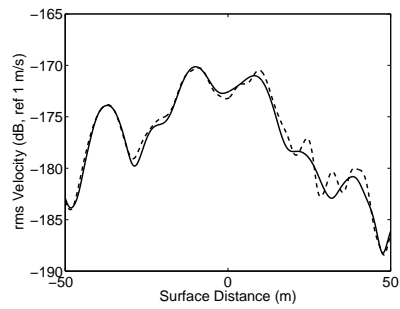
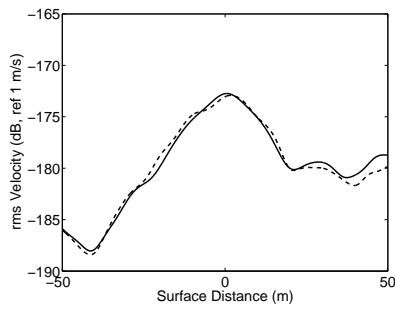


(c) 100Hz frequency band

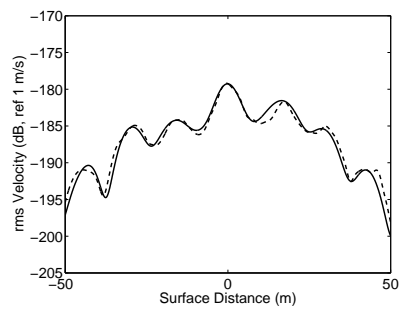
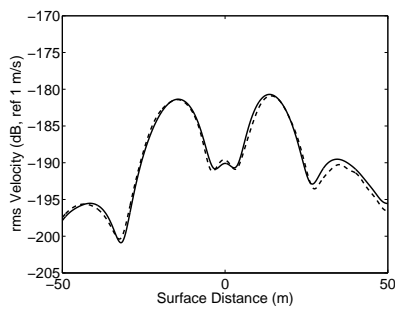


(d) 160Hz frequency band

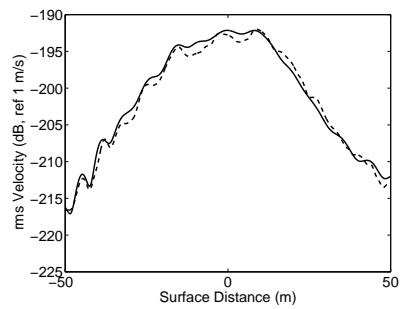
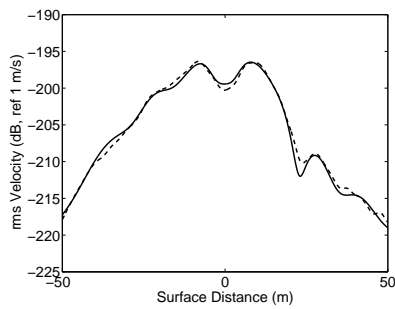
Figure 4.26: Horizontal rms velocity along surface of a halfspace with a layer 5m deep at  $x = 0$  inclined at  $3^\circ$  (left -  $\beta_E = 4$ ; right  $\beta_E = 0.25$ ); response due to vertical line load applied to the rail in a 6.5m OD tunnel with centroid at (0, 15) (solid - BE solution; dashed - TLM solution)



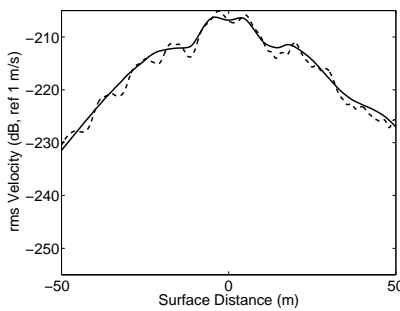
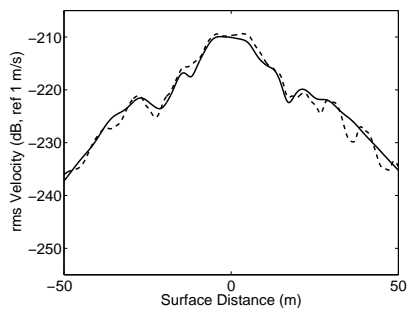
(a) 25Hz frequency band



(b) 50Hz frequency band



(c) 100Hz frequency band



(d) 160Hz frequency band

Figure 4.27: Vertical rms velocity along surface of a halfspace with a layer 5m deep at  $x = 0$  inclined at  $3^\circ$  (left -  $\beta_E = 4$ ; right  $\beta_E = 0.25$ ); response due to vertical line load applied to the rail in a 6.5m OD tunnel with centroid at (0, 15) (solid - BE solution; dashed - TLM solution)

Table 4.7: Relative error between TLM and BE model predictions for  $3^\circ$  inclination angle in dB rms

| Frequency Band | $\beta_E = 4$ |       | $\beta_E = 0.25$ |       |
|----------------|---------------|-------|------------------|-------|
|                | $v_x$         | $v_z$ | $v_x$            | $v_z$ |
| 25Hz           | 1.9           | 1.4   | 0.8              | 1.7   |
| 50Hz           | 0.9           | 1.3   | 1.3              | 2.1   |
| 100Hz          | 2.1           | 1.0   | 1.9              | 2.0   |
| 160Hz          | 5.7           | 4.1   | 3.1              | 2.6   |

100m span when  $\theta = 3^\circ$  at all frequency bands; the maximum rms differences are listed in Table 4.7 for both the stiffer layer ( $\beta_E = 4$ ) and softer layer ( $\beta_E = 0.25$ ). A distinct characteristic of the TLM model response accounts for the main source of discrepancy between the TLM and BE predictions: periodic fluctuations around the BE prediction. To explain this discrepancy one must first consider how the inclined layer affects wave propagation.

The ground vibration time-response for the inclined layer case is presented in Figure 4.28; the time-response is again calculated using an iDFT for frequencies between 0-500Hz. The response is similar to the horizontally layered cases but examination of the plots show the response is no-longer symmetric in the  $x$ -direction. The predicted vertical rms velocities (Figure 4.27) for the  $\beta_E = 4$  case show larger amplitudes for  $x > 0$ , while displacement amplitudes for the  $\beta_E = 0.25$  case are larger over  $x < 0$ ; this response is most notable at lower frequencies. Consider how the law of refraction would affect the pressure-wave. The pressure wave is symmetric about the  $x$ -axis with the bulk of the wave energy centered over the tunnel as shown previously in the horizontally layered time-response plots; this is due to the vertical loading condition applied to the tunnel which results in tunnel motion predominantly in the vertical direction (i.e. compression at the top and bottom of the tunnel, shear on the sides). The law of refraction predicts that as the center of the wave passes through the interface layer it will be refracted to the right for stiffer layers (Figure 4.29(a);  $\beta_E = 4$ ) and to the left for softer layers (Figure 4.29(b);  $\beta_E = 0.25$ ). This response is visible in Figures 4.29(c) and 4.29(d) as predicted by the TLM model. This refraction is responsible for the relative increase in

surface velocities over  $x > 0$  for the  $\beta_E = 4$  case and over  $x < 0$  for the  $\beta_E = 0.25$  case.

The periodically fluctuating discrepancy between the BE and TLM results is attributed to the multiple refracting surfaces of the step-wise interface of the TLM model. The fluctuations visible in Figure 4.27(d) have a period of approximately 10m which corresponds to the width of the hyperelement columns. The step-wise boundary segments the incoming wave-field into numerous wavefronts at various angles. The superposition of these refracted wavefronts with themselves and the reflected waves off the surface cause periodic localizations of energy compared to the predicted response through the smooth boundary of the BE model. However, the mean response matches well with the BE model prediction.

In conclusion, the TLM model simulating an inclined layer interface using the step-wise approximation is deemed sufficiently accurate in predicting the surface rms velocity compared to the BE model. Errors between the models are attributed to the step-wise discretization of the interface causing localization of wave energy. The peak error between the TLM and BE models is generally below 2dB for low and mid-frequency bands; error at higher frequency bands is shown to peak at approximately 5dB however the trend of the results still matches well with the BE solution. In the next section the TLM model is used to investigate the sensitivity of surface vibration to inclination angle.

### 4.2.3 Sensitivity to Inclination Angle

To aid in comparison of the predicted surface vibrations at varying layer inclination angles, the results are presented as the dB difference between the inclined and horizontal layer results. For lack of a better term, this difference will be referred to as insertion gain (IG). A positive IG signifies an increase in surface vibration due to layer inclination compared to a horizontal layer of equivalent material, whereas a negative IG signifies a decrease in vibration. The predicted surface rms velocity insertion gains calculated for

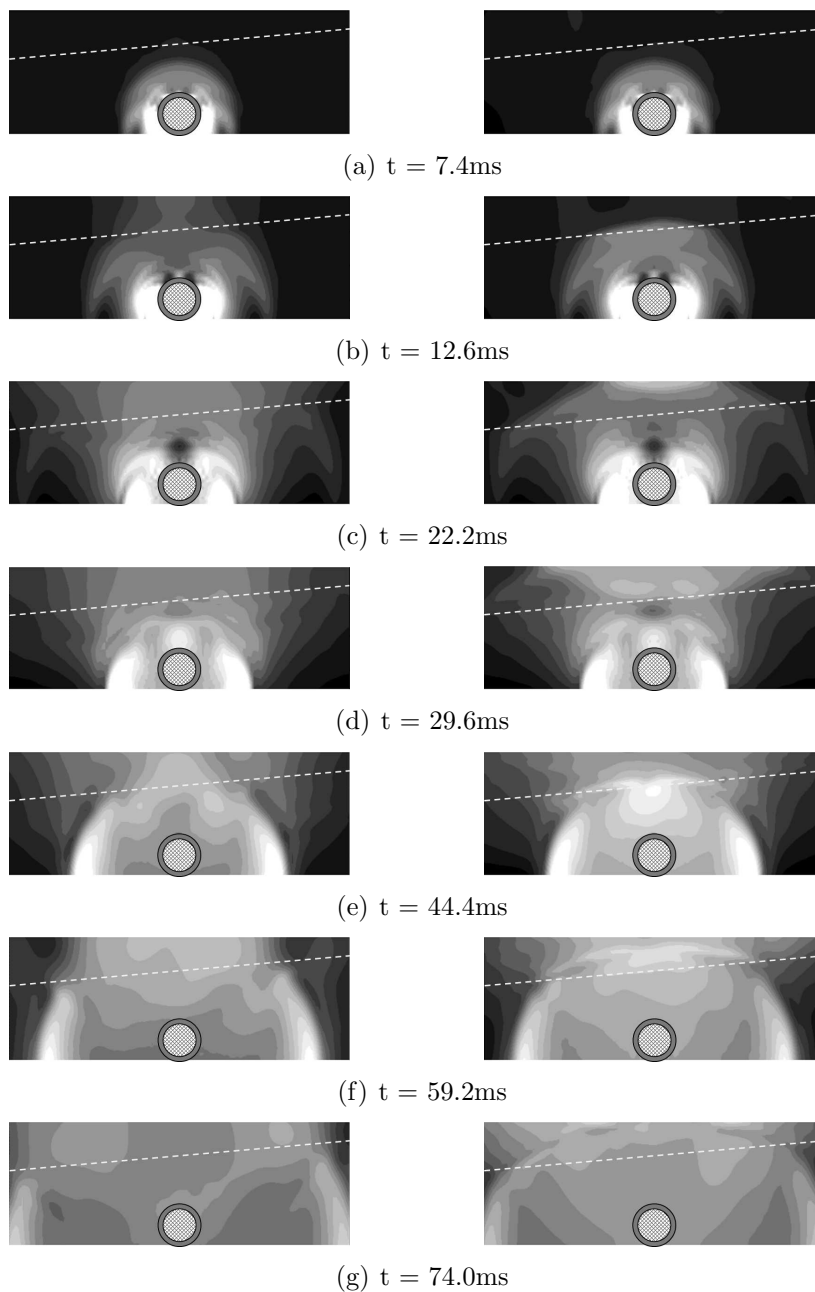


Figure 4.28: Displacement response in the  $3^\circ$  inclined layered case:  $\beta_E = 4$  on the left;  $\beta_E = 0.25$  on the right. Black indicates no soil motion while white indicates relatively large displacements; dashed line shows location of layer interface, ring shows location of tunnel.

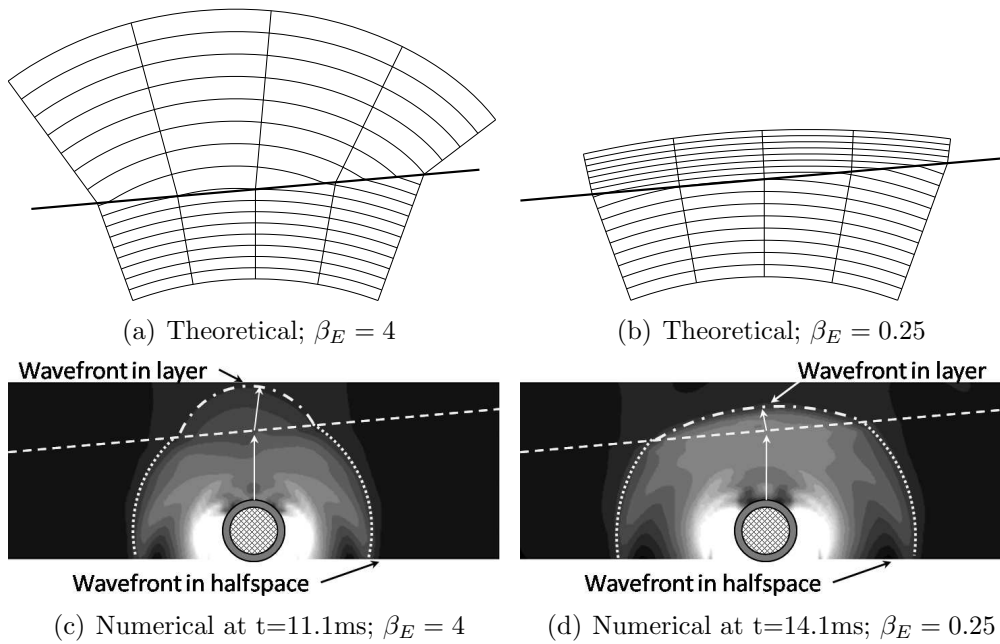


Figure 4.29: The effect of layer wavespeed on the radius of curvature of incoming wavefronts through an inclined layer: top - theoretical predictions from Snell's law of refraction including five direction normals to visualize the refraction angle; bottom - TLM predictions where wavefront refracts to the right for  $\beta_E = 4$  case at  $t=11.1\text{ms}$  and refracts to the left for  $\beta_E = 0.25$  case at  $t=14.1\text{ms}$

the 15-200Hz frequency range are presented in Figure 4.30. The presented results include velocities in the  $x$ -direction (horizontal) and  $z$ -direction (vertical) for  $\beta_E = [4, 0.25]$  at inclination angles of  $1^\circ$ ,  $3^\circ$ , and  $5^\circ$ . The rms velocity for the 15-200Hz range is displayed instead of various frequency band rms plots to simplify the visualization of the results in a concise argument.

The central spike in IG for all the  $v_x$  cases may be deceiving so must be explained. Recall from Figure 4.26 that the  $v_x$  response for a horizontal layer is zero at  $x = 0\text{m}$ ; the response is symmetric across the  $x$ -axis which is a result of the  $x$ -symmetric material properties of the soil and the vertical load applied to the base of the tunnel. For the inclined layer cases the soil properties are no longer  $x$ -symmetric thus the  $v_x$  response at  $x = 0\text{m}$  is no longer zero. The location of minimum velocity is actually shifted slightly left or right depending on the soil properties. When the dB insertion gain is calculated this shift in the minimum results in what appears to be a large difference between the two models. In reality the relative difference in magnitude is very small compared to the

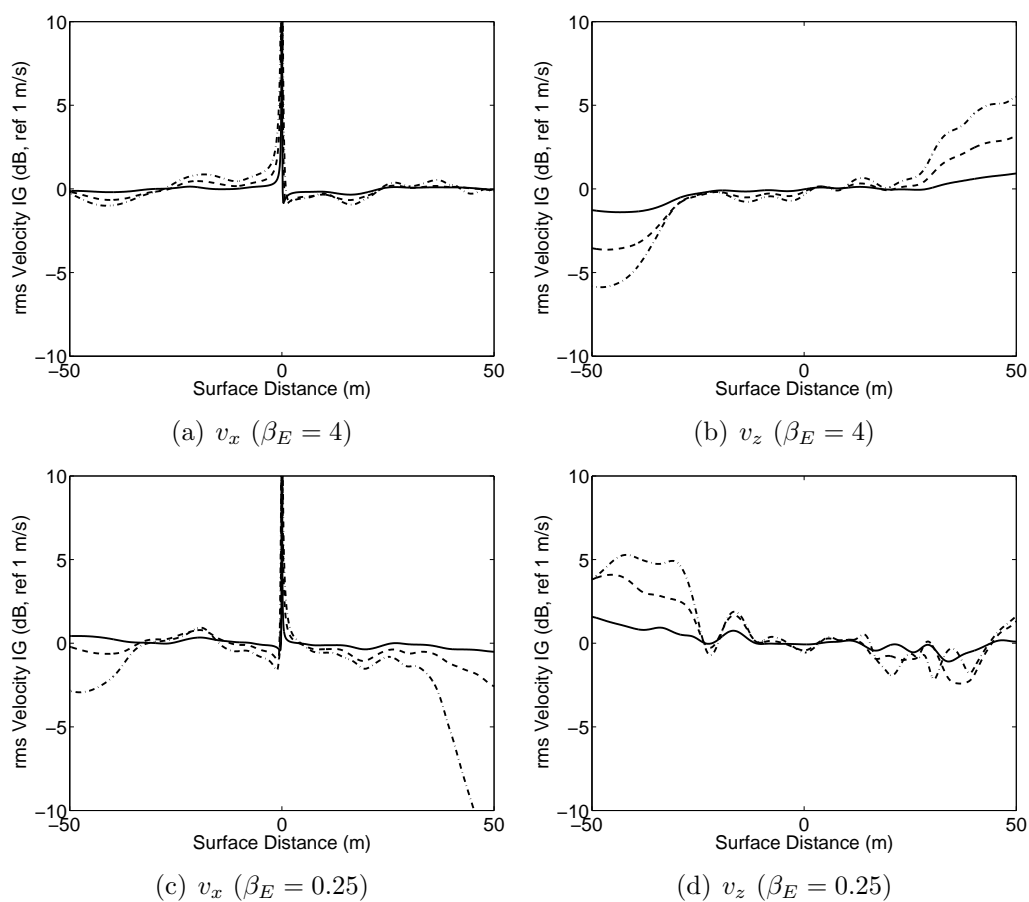


Figure 4.30: rms velocity along surface of a halfspace with a layer 5m deep at  $x = 0$  inclined at various angles; response in  $x$ -direction ( $v_x$ ) and  $z$ -direction ( $v_z$ ) due to vertical line load applied to the rail in a 6.5m OD tunnel with centroid at (0, 15) (solid -  $1^\circ$  inclination; dashed -  $3^\circ$  inclination; dash-dotted -  $5^\circ$  inclination)

response at  $x > 10\text{m}$  thus the spike at  $x = 0\text{m}$  is not of great concern when considering how the surface vibration differs with layer inclination angle.

The deflection of wave energy due to the refraction of the inclined layer interface, as described in Section 4.2.2, is apparent in Figures 4.30(b) and 4.30(d). There is a distinct upward slope to the  $v_z$  rms velocity IG for the  $\beta_E = 4$  case resulting from the refraction of wave energy to the right, whereas there is a downward slope to the IG for the  $\beta_E = 0.25$  case. For the  $1^\circ$  case this results in only approximately  $\pm 1\text{dB}$  rms but for a  $5^\circ$  inclination angle the insertion gain reaches  $6\text{dB}$  rms for vertical the  $\beta_E = 4$  and  $7\text{dB}$  rms for  $\beta_E = 0.25$ .

The refraction-effect is less noticeable in the  $v_x$  plots, where the maximum insertion gain is  $2\text{ dB}$  rms for the  $\beta_E = 4$  case with a  $5^\circ$  inclination angle. This is because the horizontal surface movement is dominated by Rayleigh waves. Rayleigh waves are formed from the interaction of P-waves and S-waves with the surface thus are also affected by the refraction effect of the inclined layer interface; however the deflection of energy by the inclined layer essentially just moves the epicenter of the Rayleigh waves left or right. Since wave energy decays much slower in Rayleigh waves than in bulk waves ( $\frac{1}{\sqrt{r}}$  vs  $\frac{1}{r^2}$ ) the relative difference in the Rayleigh waves across the surface for different inclination angles is significantly less than P- or S-waves. This is true for the  $\beta_E = 0.25$  case as well, except there two additional effects which cause a decrease in IG at  $x < -30\text{m}$  and a sharp change in gradient at  $x > 40\text{m}$  for the  $5^\circ$  inclination case seen in Figure 4.30(c).

The negative IG over  $x < -30\text{m}$  in the  $\beta_E = 0.25$  case is attributed to the refraction of shear-waves by the layer interface in the negative  $x$ -direction. As mentioned previously, the vertical load applied to the base of the tunnel invert results in  $x$ -symmetric wave formation which is predominantly P-waves over and under the tunnel and S-waves at the sides of the tunnel as visible in Figure 4.22. The bulk of the P-wave energy strikes the surface with an incident angle almost perpendicular to the surface, thus is mostly responsible for vertical surface motion. The bulk of the S-wave energy reaches

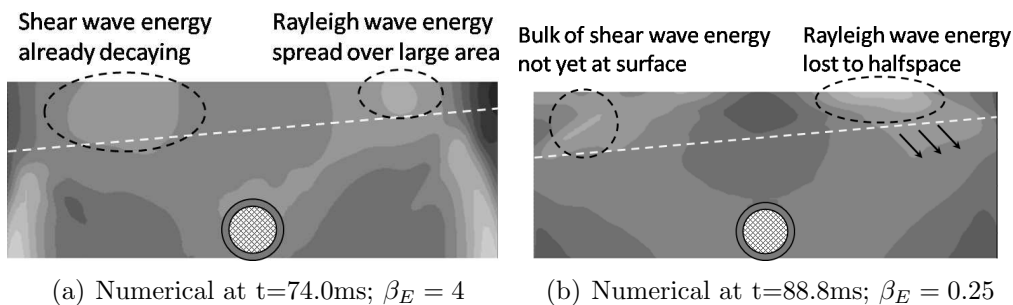


Figure 4.31: Depiction of Rayleigh wave energy loss for inclined layer in time-domain

the surface at  $|x| > 25\text{m}$  at a steep incident angle (see Figures 4.22(f) and 4.22(g)) thus is responsible for a significant component of the horizontal response over those areas. The inclined layer for the  $\beta_E = 0.25$  case causes the S-waves to refract to the left in a similar manner to the P-wave description in Section 4.2.2. This causes the bulk of the S-wave energy which would reach the surface at  $x < -30\text{m}$  to be shifted further in the negative  $x$ -direction (see Figure 4.31(b)) resulting in the relative decrease seen in Figure 4.30(c), most noticeably for the  $5^\circ$  inclination case.

The sharp change in gradient at  $x > 40\text{m}$  for the  $5^\circ$  inclination case seen in Figure 4.30(c) is attributed to a disruption of the Rayleigh wave. For the  $\beta_E = 0.25$  case the Rayleigh wave energy is localized over a small area due to the relatively small Rayleigh wavelength. For an inclination of  $5^\circ$ , the layer thickness for the TLM model is only  $1.5\text{m}$  for  $40\text{m} < x < 50\text{m}$  and  $0.6$  for  $x > 50\text{m}$ . This is shallow enough to interfere with the base of the Rayleigh wave as it passes through this zone; some wave energy is passed into the halfspace and propagated away from the surface. This results in the decrease in  $v_x$  rms velocity for  $x > 40\text{m}$  in the  $5^\circ$  inclination  $\beta_E = 0.25$  case. This is not as evident in the  $\beta_E = 4$  case because the energy associated with the Rayleigh wave in this case is spread over a larger area (see Figure 4.28(f)). A loss of some wave energy at the base of the Rayleigh wavefront has a less significant effect on the surface than in the  $\beta_E = 0.25$  case.

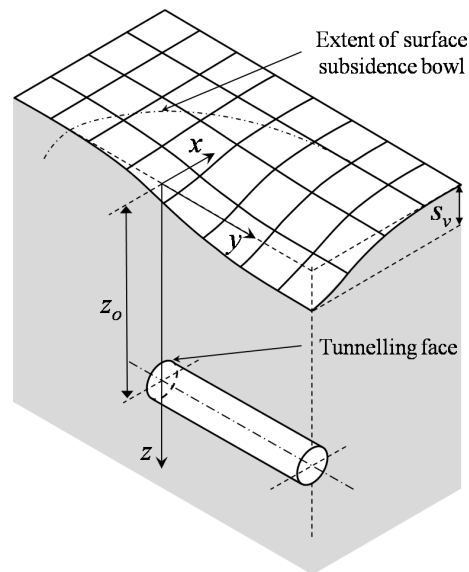
In conclusion the thin layer method is used to simulate wave propagation through an inclined soil layer to determine the effect on surface vibration. The inclined layer

is modelled using step-wise variation in the hyperelement properties. The rms velocity response predicted using the TLM model are compared to BE results for a layer inclined at  $3^\circ$  and found to match well at a number of frequency bands. The sensitivity of surface vibrations to inclination angle is also investigated and the results suggest that small inclination angles of  $5^\circ$  or less can cause significant variation in rms response. This variation is attributed to the refraction on wave energy by the inclined layer.

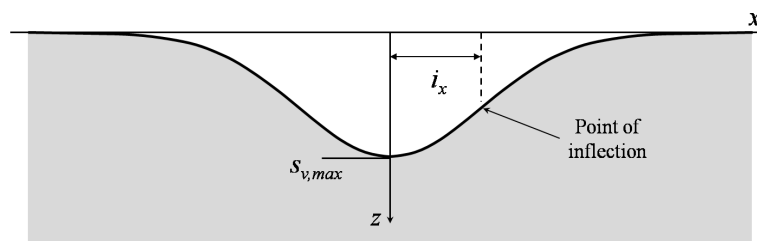
### 4.3 Subsiding Soil Layers

As discussed in Section 2.4.2, ground movement associated with the construction of underground railway tunnels is inevitable<sup>[113]</sup>. Progression of the tunnelling face reduces support for the overburden resulting in subsidence above the tunnel as depicted in Figure 4.32. Even using modern tunnelling techniques to support the overburden, recent studies show tunnelling-related subsidence at levels of 15-20 mm<sup>[85,99]</sup>. The overburden often continues to subside as water leakage into the tunnel results in a loss of pore pressure in the surrounding soil. A long-term study measuring subsidence in St. James's Park over the Jubilee Line extension show total subsidence of 60-70 mm after two years<sup>[110]</sup> (i.e. from construction and long-term settlement). It is conceivable that a 100mm deep subsidence trough could develop over an underground railway tunnel during its lifetime.

The concern is this subsidence could have a lensing effect above the tunnel focusing the wave-energy over a relatively small area. Consider the example case displayed in Figure 4.33. If the layer has a wavespeed slower than that of the halfspace (i.e.  $\beta_E = 0.25$ ), the law of refraction predicts the wave-field presented in Figure 4.34. Note how the wavefront normals converge towards an area directly above the tunnel; this may result in a substantial increase in surface particle velocity. If the layer were stiffer than the halfspace (i.e.  $\beta_E = 4$ ) the wave energy would be refracted away from the area above the tunnel and could potentially create a vibration shadow area on the surface. The



(a) Three-dimensional representation of subsidence trough due to tunnelling



(b) Plane-strain representation of subsidence trough

Figure 4.32: Subsidence trough

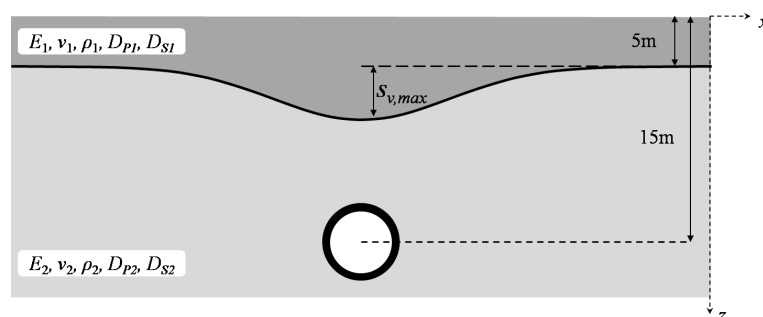


Figure 4.33: Schematic of subsiding soil layer model

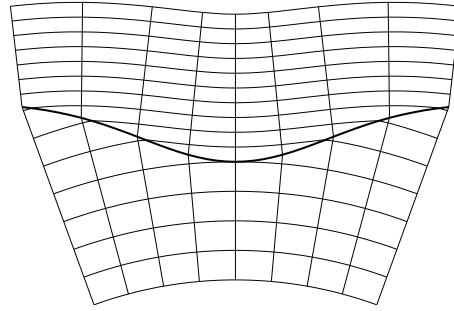


Figure 4.34: Theoretical wave focusing of subsiding layer  $\beta_E = 0.25$

TLM model is used to simulate a subsiding layer above an underground railway tunnel to quantify the effect on surface vibration.

#### 4.3.1 TLM Model of Subsiding Layer

The plane-strain example case considered herein is shown in Figure 4.33. The model consists of a subsiding layer with a 5m nominal depth atop a halfspace. The geometry of the subsidence trough can be described by a Gaussian error function<sup>[113,117]</sup> given by

$$f(x) = S_{v,max} e^{\left( \frac{-(x - x_o)^2}{2(i_x)^2} \right)} \quad (4.49a)$$

where

$$i_x = 0.5(z_0 - z) \quad (4.49b)$$

and  $x$  and  $z$  describe the location of interest for the subsidence estimation,  $x_0$  and  $z_0$  are the location of the centreline of the tunnel,  $S_{v,max}$  is the depth of the trough at height  $z$  and  $x = 0$ , and  $i_x$  is the distance from the centre of the trough to the point of inflections (see Figure 4.32(b)).

A number of trough depths  $S_{v,max}$  listed below are investigated based on the reported subsidence levels for modern UK underground tunnels. The soil layer elastic modulus

Table 4.8: Model properties for subsidence model

|                             | Tunnel | Halfspace | Layer                   |
|-----------------------------|--------|-----------|-------------------------|
| $E$ (GPa)                   | 50     | 0.55      | $[0.25, 4] \times 0.55$ |
| $\rho$ (kg/m <sup>3</sup> ) | 2500   | 2000      | 2000                    |
| $\nu$                       | 0.3    | 0.44      | 0.44                    |
| $D_P$                       | 0.05   | 0.05      | 0.05                    |
| $D_S$                       | 0.05   | 0.05      | 0.05                    |

coefficient  $\beta_E$  is also varied to determine the effect on surface vibration.

$$S_{v,max} = [0, 30, 60, 100]\text{mm} \quad \beta_E = [4, 0.25]$$

The subsidence trough is simulated using step-wise variations of the hyperelement properties in a similar manner to the inclined soil layer. Due to the small scale of the subsidence trough, the width of the hyperelements are reduced to 5m to better represent the changing slope of the trough. The height of the hyperelements are reduced over the subsidence region to ensure a maximum step-height of 1/5 of  $S_{v,max}$ . The surface of the soil is assumed horizontal to simulate a freshly landscaped building site above a pre-existing tunnel.

The equivalent internal source model is again used to simulate loading from a 6.5m OD, 6.0m ID concrete tunnel subjected to a unit harmonic line load acting on the rail of the floating slab track assembly; the EIS ring is 3m in radius with a centroid at  $x=0$ ,  $z=15\text{m}$ . The model has element heights which are varied to ensure at least 16 elements per smallest shear wavelength in either region (i.e.  $\Delta_\gamma = 16$ ) and has five shear wavelengths of material included below the deepest EIS load (i.e.  $h_\gamma = 5$ ). The properties associated with the model are listed in Table 4.8. A schematic of the TLM model with  $S_{v,max}=100\text{mm}$  is shown in Figure 4.35; the dashed line represents the curve defined by Equation 4.49a.

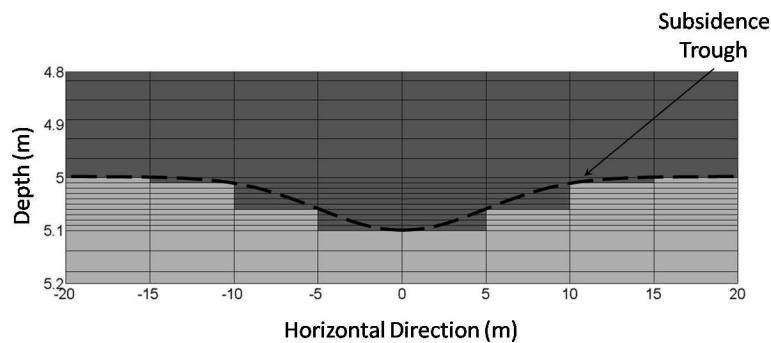


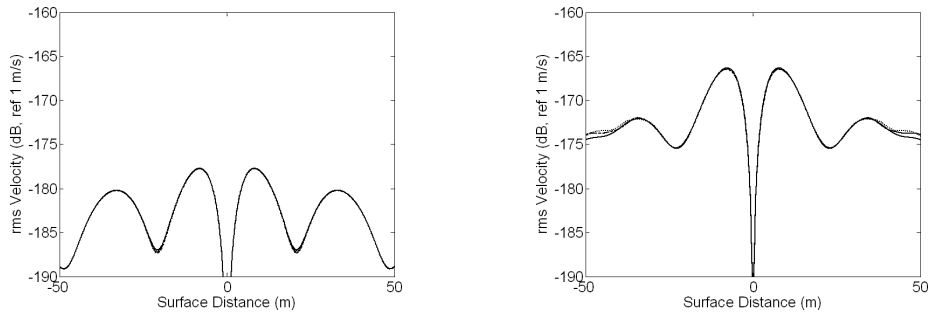
Figure 4.35: Close-up of subsidence section of TLM model

### 4.3.2 Surface Response of Subsiding Layer Model

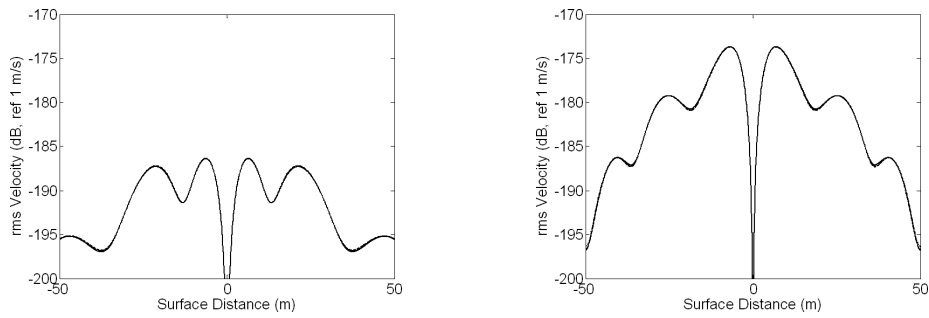
The predicted surface rms velocities for the subsiding layer TLM model are presented in Figures 4.36 and 4.37 for the 25Hz, 50Hz, 100Hz and 160Hz frequency bands. The presented results include velocities in the  $x$ -direction (horizontal) and  $z$ -direction (vertical) for  $\beta_E = [4, 0.25]$ .

The surface particle velocities predicted by the TLM model are relatively insensitive to varying levels of layer subsidence for the range investigated. The rms response curves for the four cases  $S_{v,max} = [0, 30, 60, 100]$ mm practically lie atop one another. The vertical rms response is magnified for the  $\beta = 4$  and  $\beta = 0.25$  cases in Figures 4.37(c) and 4.37(d), respectively. At this magnification it is possible to distinguish a separation in the results, although the total spread is only approximately 0.2dB for the  $\beta = 4$  case and 0.5dB for the  $\beta = 0.25$  case.

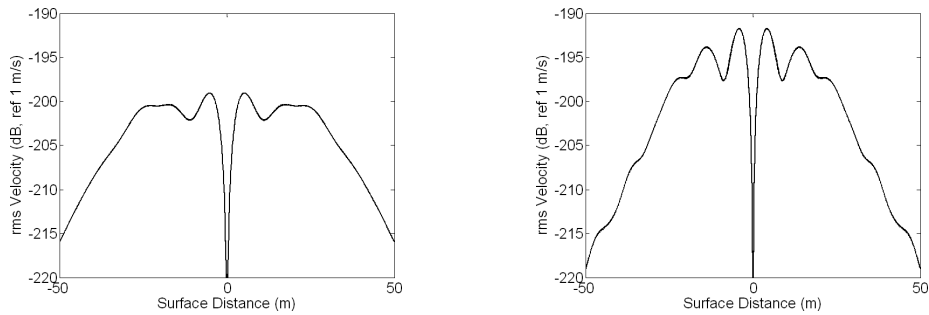
As predicted earlier in this section, the refraction of wave energy varies the surface response above the tunnel (see Figure 4.34). The  $\beta_E = 4$  results in Figure 4.37 show a decrease in vertical response as the level of subsidence increases in the stiffer layer, creating a vibration shadow area above the tunnel. The results for  $\beta_E = 0.25$  in Figure 4.37 show a wave energy focusing effect in the softer layer above the tunnel as the response increases with the level of subsidence. The response above the tunnel in the horizontal direction does not appear to be significantly affected by the variation in subsidence levels. As discussed in Section 4.2.3, the horizontal surface response is dominated



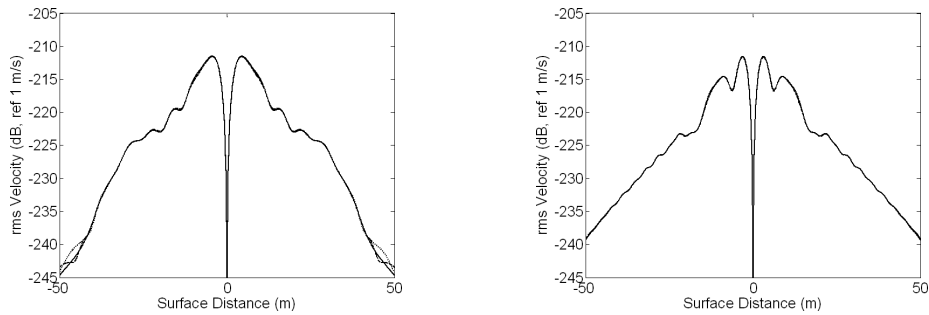
(a) 25Hz frequency band



(b) 50Hz frequency band

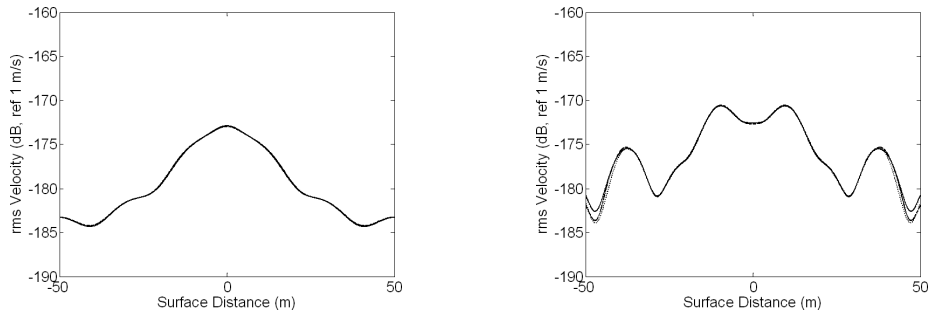


(c) 100Hz frequency band

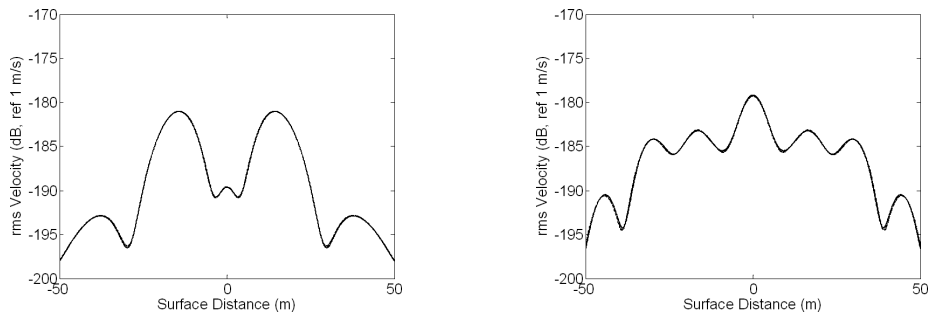


(d) 160Hz frequency band

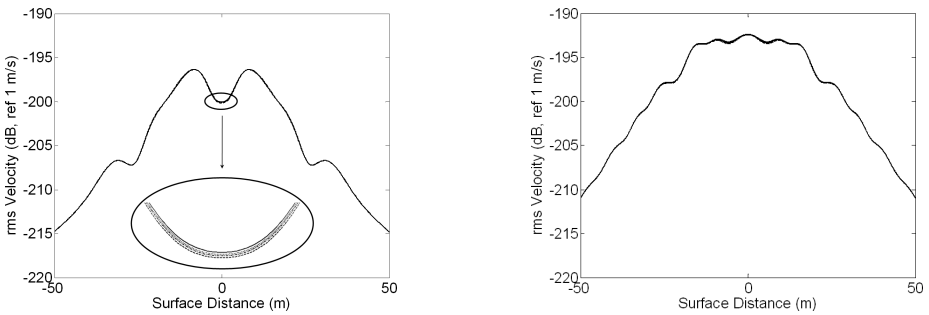
Figure 4.36: Horizontal rms velocity along surface with a subsiding layer at four frequency bands (left -  $\beta_E = 4$ ; right  $\beta_E = 0.25$ ); response in  $x$ -direction ( $v_x$ ) due to vertical line load applied to the rail in a 6.5m OD tunnel with centroid at (0, 15) (solid -  $S_{v,max} = 0\text{mm}$ ; dotted -  $S_{v,max} = 30\text{mm}$ ; dash-dotted -  $S_{v,max} = 60\text{mm}$ ; dashed =  $S_{v,max} = 100\text{mm}$ )



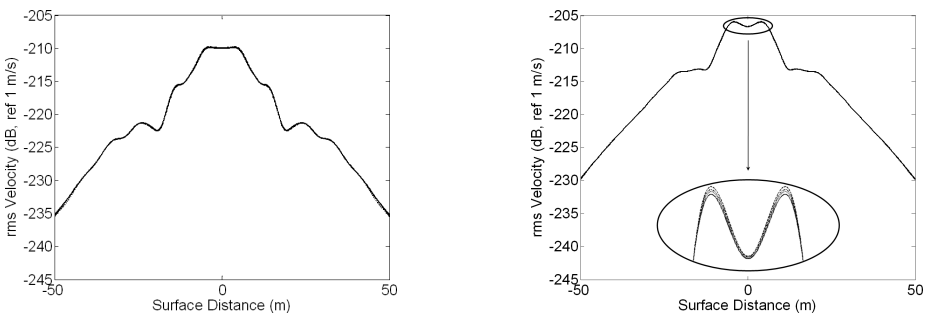
(a) 25Hz frequency band



(b) 50Hz frequency band



(c) 100Hz frequency band



(d) 160Hz frequency band

Figure 4.37: Vertical rms velocity along surface with a subsiding layer at four frequency bands (left -  $\beta_E = 4$ ; right  $\beta_E = 0.25$ ); response in  $z$ -direction ( $v_z$ ) due to vertical line load applied to the rail in a 6.5m OD tunnel with centroid at (0, 15) (solid -  $S_{v,max} = 0$ mm; dotted -  $S_{v,max} = 30$ mm; dash-dotted -  $S_{v,max} = 60$ mm; dashed =  $S_{v,max} = 100$ mm)

by Rayleigh and S-waves which are relatively weak above the tunnel compared to the P-wave; these waves reach significant levels on the surface further away from the tunnel once the bulk of the S-wave energy interacts with the surface. As the subsidence trough only varies the model geometry over a small area above the tunnel the propagation of the S-wave is not significantly affected by changes to  $S_{v,max}$ , thus horizontal surface vibration is similar for all cases under investigation.

In conclusion the TLM model is used to investigate the effect of layer subsidence over an underground railway. The subsidence bowl is modelled using step-wise variation in the hyperelements to simulate a maximum deflection of 100mm in the layer. The hypothesized lensing effect of a subsiding softer layer is visible in the predicted response but the magnitude of variation from a horizontal layer is relatively small at approximately 0.5dB.

## 4.4 Inhomogeneous Soils

Assuming homogeneous soil layering is the standard approach for simulating global trends in soil properties (e.g. a shift from a sandy layer to a layer of clay). Localized soil variability throughout the layer can also produce significant variation in material properties, though this variability is rarely included in ground vibration simulations. It is impractical to take sufficient soil samples to accurately map local variations in material properties over the area of interest thus soil profiles must be inferred from a limited number of samples. For simplicity the properties of each layer are normally assumed homogeneous with average value.

The purpose of this section is to quantify the effect on surface vibration when accounting for localized inhomogeneity in layered soil models. A probabilistic model employing random field theory coupled with the thin-layer method model is used to capture the inherent variation in soil properties. Variation in both the vertical and horizontal directions are included.

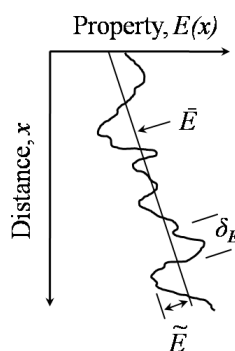


Figure 4.38: Parameters of homogeneous randomly varying soil profile

#### 4.4.1 Modelling Local Variation in Soil Properties

In a conventional soil model the layer properties are idealized by a set of average values; the fluctuation about these values are neglected. This implies that the layers are homogeneous. In a probabilistic soil profile at least one soil property is assumed to vary about the mean and is treated as a random function. While a number of soil properties will vary locally throughout the layer, only the effect of varying the elastic modulus will be investigated herein.

Figure 4.38 displays how three parameters are required for a one-dimensional stochastic description of variability  $E(x)$ :

- $\bar{E}$  - the average value over the area of interest
- $\tilde{E}$  - the standard deviation of the function; a measure of the degree to which actual values of  $E$  deviate from the mean  $\bar{E}$
- $\delta_E$  - the scale of fluctuation; the distance within which the soil property  $E(x)$  shows relatively strong correlation from point to point (i.e. two points that lie within  $\delta_E$  are likely to be both above or below the average)

The dimensionless coefficient of variation (CoV) may also be reported instead of the standard deviation where  $\text{CoV} = \tilde{E}/\bar{E}$ .

The spatial variation  $E(x)$  can be decomposed into its mean value  $\bar{E}(x)$  and a fluc-

tuating component  $\Delta E(x)$  which accounts for the variation over the  $x$ -direction.

$$E(x) = \bar{E}(x) + \Delta E(x) \quad (4.50)$$

An accepted means of quantifying variability in soil is to assume the property of interest is a homogeneous random function<sup>[45,151]</sup>. The function  $\Delta E(x)$  is considered statistically homogeneous if the mean and variance between two points  $x_1$  and  $x_2$  remain unchanged when these points are translated (but not rotated) in the parameter space (i.e. the statistics depend only on the relative, not absolute, locations of the points). For this case the random variation is described by the covariance function  $C(x, \xi)$  which is a measure of the correlation, or similarity, of the value at two different points  $x$  and  $\xi$  in the one-dimensional random function. By definition the covariance function is bounded, symmetric and positive definite<sup>[137]</sup>, thus it can be spectrally decomposed into its eigenfunctions as

$$C(x, \xi) = \sum_{n=0}^{\infty} \lambda_n \phi_n(x) \phi_n(\xi) \quad (4.51)$$

where  $\lambda_n$  and  $\phi_n$  are the eigenvalues and eigenfunctions of the covariance kernel, respectively. Eigenfunctions are similar to eigenvectors only they are continuous rather than discrete and are the solutions to the integral equation

$$\int_L C(x, \xi) \phi_n(x) d\xi = \lambda_n \phi_n(x). \quad (4.52)$$

According to Loeve<sup>[92]</sup> the eigenfunctions form a complete set and can be used to expand the covariance function in a Fourier-type series using orthogonal decomposition; this is known as the Karhunen-Loeve (KL) Expansion<sup>[45]</sup>. The result of this expansion is the random process  $E(x)$  can be written as

$$E(x) = \bar{E}(x) + \Delta E(x) = \bar{E}(x) + \tilde{E}(x) \sum_{n=0}^{\infty} b_n \sqrt{\lambda_n} \phi_n(x). \quad (4.53)$$

If  $E(x)$  is assumed to be a Gaussian process, the series can be shown to converge<sup>[92]</sup> and the coefficient vector  $\mathbf{b}$  is a set of uncorrelated Gaussian random variables with zero mean and mean-square equal to unity.

The exponential covariance kernel, extensively used in geophysics modelling<sup>[137]</sup>, is used herein to simulate the random soil properties. The covariance kernel in the  $x$ -direction is defined as

$$C(x, \xi) = e^{-c|x-\xi|} \quad (4.54)$$

where  $x$  and  $\xi$  are the value at two different points in the one-dimensional random function, and  $c$  is related to the scale of fluctuation<sup>[150]</sup> as  $c = \frac{2}{\delta_E}$ . The eigenfunctions are determined using Equation 4.52 over the interval  $[-a, +a]$  as

$$\phi_n(x) = \frac{\cos(\omega_n x)}{\sqrt{a + \frac{\sin(2\omega_n a)}{2\omega_n}}} \quad (4.55a)$$

for  $n$  odd and

$$\phi_n^*(x) = \frac{\sin(\omega_n^* x)}{\sqrt{a - \frac{\sin(2\omega_n^* a)}{2\omega_n^*}}} \quad (4.55b)$$

for  $n$  even.

The corresponding eigenvalues are

$$\lambda_n = \frac{2c}{\omega_n^2 + c^2} \quad (4.56a)$$

and

$$\lambda_n^* = \frac{2c}{\omega_n^{*2} + c^2} \quad (4.56b)$$

where  $\omega_n$  and  $\omega_n^*$  are the solutions to the transcendental equations

$$c - \omega \tan(\omega a) = 0 \quad (4.57a)$$

and

$$\omega^* + c \tan(\omega^* a) = 0. \quad (4.57b)$$

As cited in Section 2.4.3, published data regarding the spatial variability of soils show that both vertical and horizontal soil variability is significant<sup>[56,118,119,136]</sup>, thus a two-dimensional stochastic description of variability  $E(x, z)$  is required. The scale of fluctuation in the vertical direction is generally smaller than the horizontal, which implies the random field is not statistically isotropic; a statistically isotropic field is one where the mean and variance between two points  $(x_1, z_1)$  and  $(x_2, z_2)$  remain unchanged when these points are either translated or rotated in the parameter space<sup>[45,151]</sup>. Vanmarcke states that in modelling spatial random variation in geology it is appropriate to assume a separable correlation for the horizontal and vertical variation<sup>[151]</sup> (i.e. the 2-D variance function can be expressed as the product of two 1-D variance functions). This results in

$$C(x, \xi, z, \chi) = C(x, \xi) \cdot C(z, \chi) \quad (4.58a)$$

thus

$$\begin{aligned} E(x, z) &= \bar{E}(x, z) + \Delta E(x, z) \\ &= \bar{E}(x, z) + \tilde{E}(x, z) \sum_{n=0}^{\infty} \sum_{m=0}^{\infty} b_{nm} \sqrt{\lambda_n \gamma_m} \phi_n(x) \varphi_m(z) \end{aligned} \quad (4.58b)$$

where  $\lambda_n$  and  $\gamma_m$  are the eigenvalues and  $\phi_n(x)$  and  $\varphi_m(z)$  are the eigenfunctions of the horizontal and vertical covariance kernels  $C(x, \xi)$  and  $C(z, \chi)$ , respectively. The exponential covariance kernel detailed in Equations 4.54 to 4.57 is used for both the vertical and horizontal functions. Again,  $E(x, z)$  is assumed to be a Gaussian process thus the coefficient array  $\mathbf{b}$  is a set of uncorrelated Gaussian random variables with zero mean and mean-square equal to unity. Note that the average elastic modulus and

standard deviation there of are assumed constant over the modelling area thus

$$\bar{E}(x, z) = \bar{E} \quad (4.59)$$

$$\tilde{E}(x, z) = \tilde{E}. \quad (4.60)$$

It is impractical to compute an infinite number of KL-expansion modes  $n$  and  $m$ , thus the expansion must be truncated. For low frequency ranges (i.e. 15Hz-200Hz) only a relatively small number of KL-expansion modes are necessary to adequately represent the covariance function<sup>[45]</sup>. Schevenels *et al.*<sup>[127]</sup> show that for a triple-layered halfspace increasing the mode-count from 15 to 100 has negligible affect on the results for frequencies up to 200Hz. Ten KL-expansion modes will be used in each of the directions of expansion for the model herein; inclusion of higher modes was found to have no significant affect on the solutions for the model described in the next section.

When using the KL-expansion in a discrete system such as stochastic-FE or TLM models, Vanmarcke states that it is necessary to consider the spatial average and standard deviation over the element. This is required because each element is given a single value for the variable field; the larger the element the more fluctuations of  $E$  tend to be cancelled by spatial averaging. The standard deviation used in Equation 4.58 should include a scaling factor if the dimensions of the element are larger than the scale of fluctuation<sup>[150]</sup>. As outlined in the following sections, all elements used in the current TLM model have dimensions which are less than the scales of fluctuation, thus the scaling factor is unnecessary.

#### 4.4.2 Numerical Model of Stochastic Soil Variation

The stochastic soil variation model is shown in Figure 4.39 with average properties given in Table 4.9. The equivalent internal source model is again used to simulate loading from a 6.5m OD, 6.0m ID concrete tunnel subjected to a unit harmonic lineload at the rail of the FST assembly; the EIS ring is 3m in radius with a centroid at  $x=0$ ,  $z=15$ m.

Table 4.9: Average soil properties for variability model

|                             | Tunnel | Halfspace | Layer                      |
|-----------------------------|--------|-----------|----------------------------|
| $E$ (GPa)                   | 50     | 0.55      | $[0.25, 1, 4] \times 0.55$ |
| $\rho$ (kg/m <sup>3</sup> ) | 2500   | 2000      | 2000                       |
| $\nu$                       | 0.3    | 0.44      | 0.44                       |
| $D_P$                       | 0.05   | 0.05      | 0.05                       |
| $D_S$                       | 0.05   | 0.05      | 0.05                       |

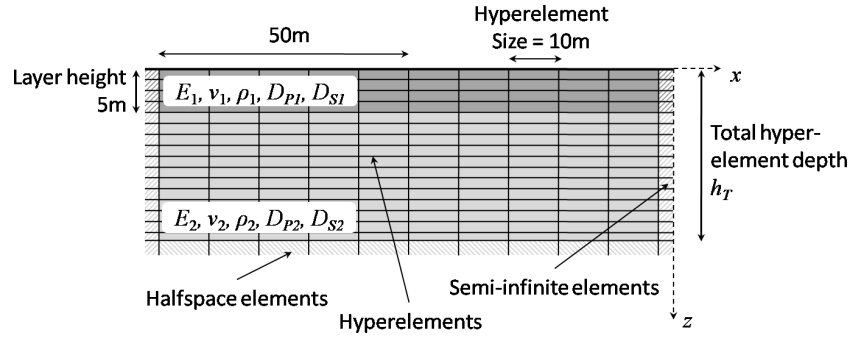


Figure 4.39: Soil Variation TLM model

The model has element heights which are varied to ensure at least 16 elements per smallest shear wavelength in either region (i.e.  $\Delta_\gamma = 16$ ) and has five shear wavelengths of material included below the deepest EIS load (i.e.  $h_\gamma = 5$ ).

The local variation in elastic modulus is governed by the KL-expansion method as described in Section 4.4.1. Determining the scale of fluctuation and standard deviation of the elastic modulus of the soil is difficult; there is limited knowledge of the variability of this soil property. The few references which list values for elastic modulus variability give a wide range of coefficient of variability (CoV) and scale of fluctuation ( $\delta$ ) values<sup>[56,70,127]</sup>: CoV = 15-50%;  $\delta_x = 1.5\text{m}-50\text{m}$ ;  $\delta_z = 1\text{m}-10\text{m}$ . Jaksa *et al.*<sup>[70]</sup> suggest that the scale of fluctuation for undrained shear strength is similar to that of elastic modulus. Extensive literature reviews by Phoon *et al.*<sup>[118]</sup> and Huber *et al.*<sup>[56]</sup> provide the following ranges for scales of fluctuation for undrained shear strength of clays:  $\delta_x = 20\text{m}-60\text{m}$ ;  $\delta_z = 0.8\text{m}-6.1\text{m}$ . These values agree well with those listed for elastic modulus variability, thus average values from these ranges are used for the cur-

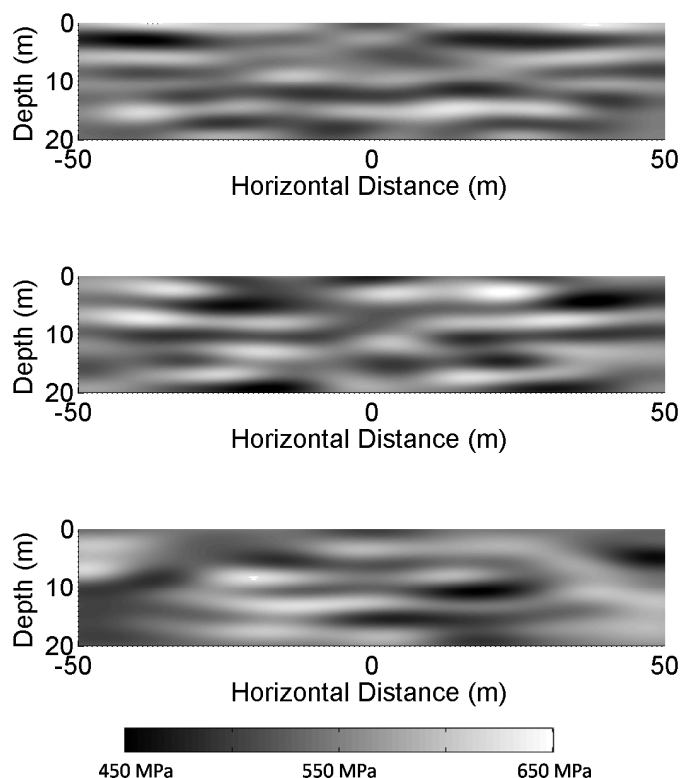


Figure 4.40: Three realizations of soil elastic modulus as determined using a KL-expansion with  $\tilde{E} = 0.30\bar{E}$ ,  $\delta_x = 40\text{m}$ ,  $\delta_z = 2.5\text{m}$

rent investigation

$$\tilde{E} = 0.30\bar{E} \quad \delta_x = 40\text{m} \quad \delta_z = 2.5\text{m}.$$

Three realizations of the elastic modulus variability as determined by the KL-expansion are shown in Figure 4.40. The realization show how there is greater variability in the  $z$ -direction than the  $x$ -direction due to the respective scales of fluctuation. The coefficient of variability  $\tilde{E} = 0.30\bar{E}$  results in the elastic modulus ranging from 450-650MPa. A total of 50 realizations are used in the investigation.

It has been assumed that the equivalent internal source method is still valid for a medium with varying elastic modulus. This is assumed because the variation is smooth and the scale of fluctuation in the vertical direction is the same order of magnitude as the diameter of the EIS ring. The actual displacement and stress field at the tunnel-soil

interface in the stochastic soil would differ slightly from that predicted by the EIS; neglecting this difference is deemed an acceptable compromise for maintaining the benefits of the EIS method.

### 4.4.3 Surface Response of Stochastic Soil Model

The predicted surface rms velocities for the stochastic soil TLM model are presented in Figures 4.41 and 4.42 for the 25Hz, 50Hz, 100Hz and 160Hz frequency bands. The presented results include velocities in the  $x$ -direction (horizontal) and  $z$ -direction (vertical) for  $\beta_E = [4, 1, 0.25]$ . The results for the 50 realizations of soil variability are plotted as a 95% confidence region (grey region) with the mean predicted response plotted as a solid line. The confidence region describes the interval over which 95% of the responses from the 50 realizations can be found.

As shown in the figures, the effect of soil inhomogeneity depends on excitation frequency for all  $\beta_E$  values; Table 4.10 lists average and peak values for the 95% confidence interval in both horizontal and vertical response. The interval is relatively small around the mean rms velocity for the 25Hz frequency band (average values  $< 1.5$ dB) but increase to significant deviation from the mean at higher band frequencies (average values of approximately 5dB with peaks close to 10dB). The relatively small confidence region at low frequencies is attributed to the relatively long wavelengths compared to the scale of fluctuation in the soil. At 15Hz the average shear wavelength is approximately 22m which is an order of magnitude greater than the scale of fluctuation in the vertical direction  $\delta_z = 2.5$ m. These large wavelengths essentially “average out” the localized soil variation. At higher frequencies the wavelengths are of the same order of magnitude as the scale of fluctuation; at 130Hz the shear wavelength for average soil properties is approximately 2.5m. At these wavelengths the local variation in elastic modulus cause significant refraction of wave energy in the manner described in Sections 4.1.7.4 and 4.2.2. The random variation in soil properties causes the diversion of wave energy by

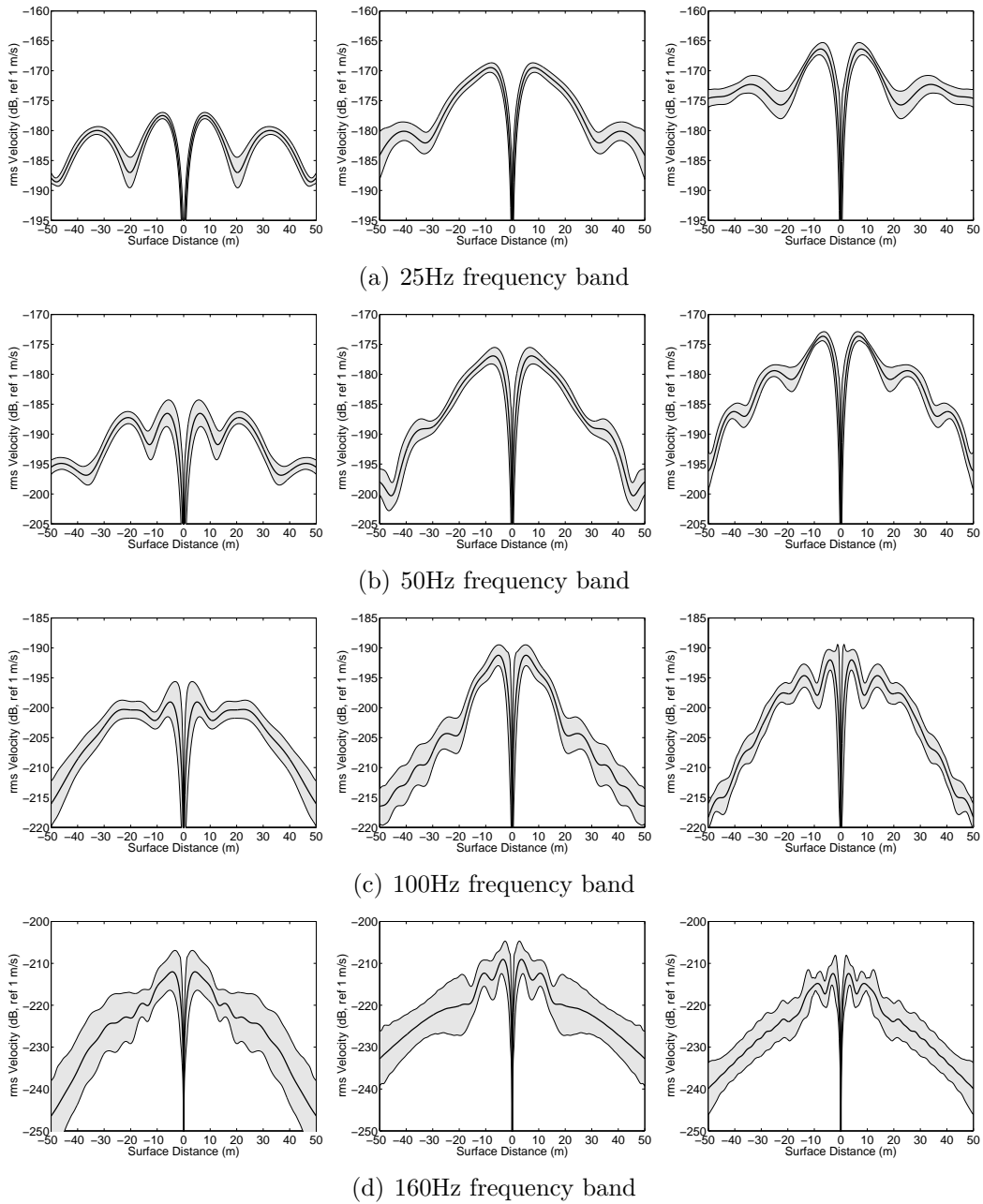


Figure 4.41: Horizontal rms velocity along surface of a halfspace with inhomogeneous soil properties (left -  $\beta_E = 4$ ; center -  $\beta_E = 1$ ; right -  $\beta_E = 0.25$ ); response due to vertical line load applied to the rail in a 6.5m OD tunnel with centroid at (0, 15) (solid - mean response; grey area - 95% confidence interval)

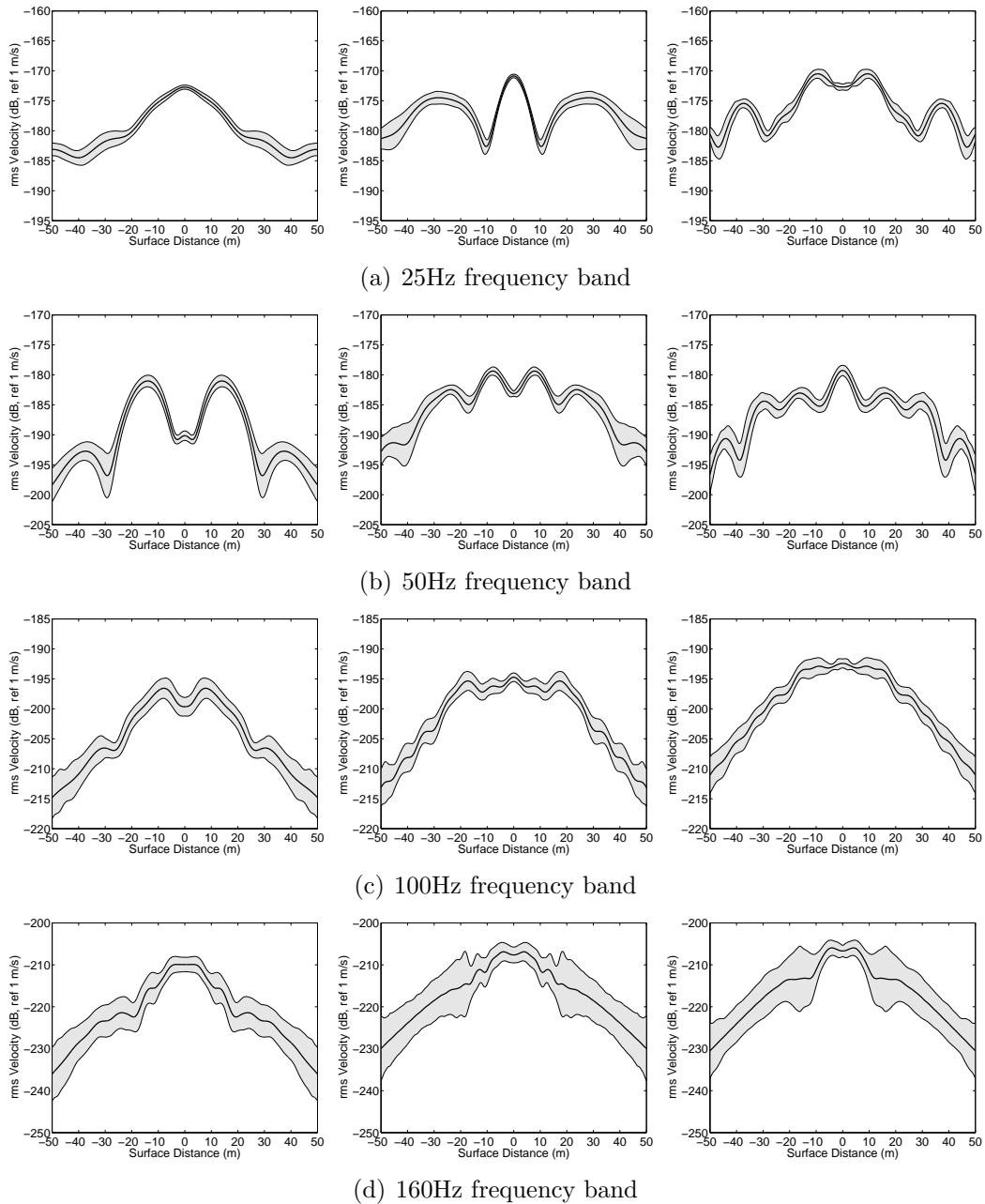


Figure 4.42: Vertical rms velocity along surface of a halfspace with inhomogeneous soil properties (left -  $\beta_E = 4$ ; center -  $\beta_E = 1$ ; right -  $\beta_E = 0.25$ ); response due to vertical line load applied to the rail in a 6.5m OD tunnel with centroid at (0, 15) (solid - mean response; grey area - 95% confidence interval)

Table 4.10: Average and peak values for 95% confidence region in dB rms

| Frequency Band | $\beta_E = 4$ |          | $\beta_E = 1$ |          | $\beta_E = 0.25$ |          |
|----------------|---------------|----------|---------------|----------|------------------|----------|
|                | $v_x$         | $v_z$    | $v_x$         | $v_z$    | $v_x$            | $v_z$    |
| 25Hz           | 1.5, 2.3      | 1.2, 2.3 | 1.5, 4.0      | 1.3, 2.4 | 1.1, 2.6         | 1.0, 1.5 |
| 50Hz           | 1.4, 3.2      | 1.7, 3.7 | 1.6, 3.1      | 1.6, 3.6 | 1.5, 2.8         | 1.7, 3.7 |
| 100Hz          | 2.0, 3.1      | 1.7, 3.0 | 2.6, 3.6      | 1.8, 3.4 | 2.1, 3.8         | 2.1, 3.5 |
| 160Hz          | 4.1, 6.2      | 4.9, 7.8 | 5.1, 7.3      | 5.0, 7.8 | 6.2, 9.4         | 4.0, 6.7 |

localized refraction resulting in relatively large variations in surface response.

Note that while the confidence regions are symmetric about  $x = 0$  this does not imply the surface response for any given realization of the soil will also be symmetric. In general each realization has non-symmetric surface response due to the non-symmetric soil properties as defined by the stochastic KL-expansion of the covariance function. The confidence intervals are symmetric due to the relatively large number of realizations used to populate the interval implying the confidence interval has converged (i.e. including further realizations would not significant alter the confidence region only further populate the current region).

This non-symmetric behaviour can also be seen by plotting the response in the time domain. The wave propagation from three realizations are shown in Figure 4.43: a homogeneous halfspace on the left and two inhomogeneous halfspaces in the center and on the right. As before, the homogenous halfspace has symmetric wave propagation across  $x = 0$ . The inhomogeneous halfspaces cause energy to be refracted and diverted relative to the homogenous case causing energy localization. For instance, at  $t=12.6\text{ms}$  both inhomogeneous realizations show pressure waves which have been diverted slightly to the right; at  $74.0\text{ms}$  the two realizations have localized displacement on either side of center.

An interesting note is that both realizations shown appear to have softer regions above the tunnel, relative to the mean elastic modulus. This can be seen by the reduced wave speed where the pressure wave has just reached the surface at  $22.2\text{ms}$  in the inhomogeneous cases while it has already reflected in the homogenous case. Also, the shear

wave is just starting to interact with the surface at 74.0ms while in the homogeneous case the Rayleigh waves have already developed (i.e. the two areas of light grey at approximately  $x = \pm 10\text{m}$ ).

In conclusion, the thin layer method model is used to investigate the effect of soil inhomogeneity on surface vibration. The elastic modulus of the soil is modelled stochastically using a KL-expansion to smoothly vary the properties in both the vertical and horizontal directions. Fifty realizations of the inhomogeneous soil are used to predict the 95% confidence region around the mean response for  $\beta_E = [4, 1, 0.25]$ . The results suggest that variation in the surface response is dependant on the band frequency. At lower frequencies the effect of local variation in elastic modulus has a small effect of approximately 1.5dB on average, while at higher frequency bands the effect is significant with a 5dB average and peak values up to 10dB.

## 4.5 Conclusions

The thin-layer method is introduced as an efficient semi-analytical means of simulating ground vibration due to underground railways. The elements use the analytical wave equation to describe vibration in the horizontal direction while assuming displacements in the vertical direction can be described using a linear shape-function. This allows elements of any length to be used (finite or infinite) without suffering from aspect-ratio requirements common in other discrete methods such as finite element analysis. Optimal parameters of 16 elements per minimum shear-wavelength and a total model depth of five wavelengths before halfspace elements are determined from a parametric analysis. The model accurately predicts the frequency band rms velocities at the surface of a halfspace due to excitation from an underground railway over a frequency range of 15-200Hz when compared to both an analytical and boundary element solution. The equivalent internal source method is used to simulate loading from the underground railway using 32 discrete line-loads.

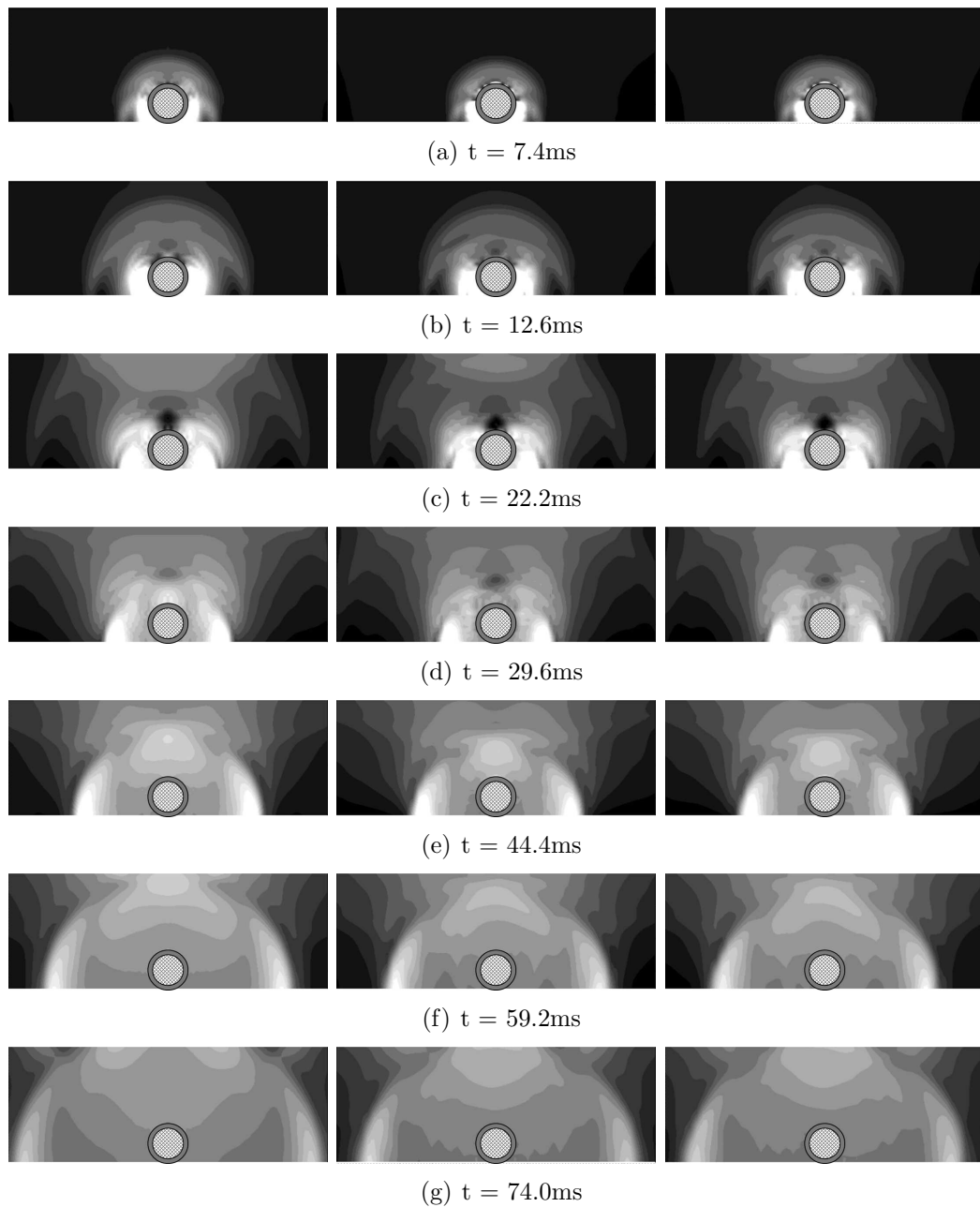


Figure 4.43: Displacement response in halfspace with inhomogeneous elastic modulus: homogenous halfspace on the left; first realization of  $\tilde{E} = 0.30\bar{E}$  in the center; second realization of  $\tilde{E} = 0.30\bar{E}$  on the right. Black indicates no soil motion while white indicates relatively large displacements; ring shows location of tunnel

The TLM model is used to simulate an inclined layer interface using a step-wise approximation and is deemed sufficiently accurate in predicting the surface rms velocity compared to the BE model. Errors between the models are attributed to the step-wise discretization of the interface causing localization of wave energy. The peak error between the TLM and BE models is generally below 2dB for low and mid-frequency bands and the trend of the results match well with the BE solution. The sensitivity of surface vibrations to inclination angle is also investigated and the results suggest that small inclination angles of  $5^\circ$  or less can cause significant variation in rms response of approximately 5dB. This variation is attributed to the refraction on wave energy by the inclined layer.

The model is also used to investigate the effect of layer subsidence over an underground railway. The subsidence bowl is modelled using step-wise variation in the hyperelements to simulate a maximum deflection of 100mm in the layer. The hypothesized lensing effect of a subsiding soft layer is visible in the predicted response but the variation from a horizontal layer is relatively small at approximately 0.5dB.

Finally, the thin-layer method is used to investigate the effect of soil inhomogeneity on surface vibration. The elastic modulus of the soil is modelled stochastically using a KL-expansion to smoothly vary the properties in both the vertical and horizontal directions. Results suggest that local soil inhomogeneity can result in 95% confidence intervals with 5dB averages and peak values up to 10dB.

# Chapter 5

## Conclusions and Further Work

This chapter summaries the conclusions drawn from the work described in the previous chapters and suggests areas where further work may be achieved.

### 5.1 Conclusions

Noise and vibration from underground railways is a documented disturbance to individuals living or working near subways. Researchers have linked such disturbances to work degradation, sleep disturbance and possible health risks affecting individuals 25m from tunnels and have reported above average annoyance from inhabitants up to 200m from the subways. This public disturbance has spurred the development of ISO standards to quantify acceptable levels of vibration from underground railways and subsequently the development of simulation models to predict ground vibration so as to meet the vibration criteria during the design process.

Much work has been done developing these numerical models to understand and simulate the dynamic interactions between the train, track, tunnel and soil. However, all such numerical models rely on simplifying assumptions to make the problems trackable: soil is assumed homogenous, tunnels are assumed long and straight, the soil is assumed to be in perfect contact with the tunnel, etc. The aim of this dissertation is to quantify some

of these uncertainties to give a better understanding of how simplifying assumptions limit prediction accuracy.

The first section investigates the effect of voids at the tunnel-soil interface on ground vibration due to underground railways. The Pipe-in-Pipe model is extended to allow finite-sized voids at the interface by deriving the discrete transfer functions for the tunnel and soil from the continuous solution; voids are simulated by uncoupling the appropriate nodes at the interface to prevent force transfer between the two subsystems. The formulation presented is efficient as the tunnel and soil transfer function matrices are only calculated once and reused for any void geometry. The results suggest that relatively small voids can significantly affect the rms velocity predictions at higher frequencies ( $>5\text{dB}$  at 100-200Hz) and moderately effect predictions at lower frequencies ( $\sim 2\text{dB}$  at 15-100Hz). The results are also found to be sensitive to void length and void sector angle.

The second section investigates issues associated with assuming the soil is homogeneous: the effect of inclined soil layers; the effect of a subsiding soil layer; the effect of soil inhomogeneity. The thin-layer method approach is utilized as its semi-analytical formulation allows for accurate predictions with relatively short run times. The inclusion of an inclined layer at  $5^\circ$  or less is shown to affect the surface rms velocity predictions by up to 5dB; the extent and location of this variation is found to be dependent on layer properties and inclination angle. The geometric effect of a subsiding soil layer is found to have less significant effect on surface vibration ( $\sim 0.5\text{dB}$ ). Finally, accounting for localized inhomogeneity of a halfspace is found to result in significant variation in surface results compared to the homogeneous assumption; at higher frequencies the 95% confidence intervals are predicted to average 5dB with peak values of around 10dB.

The findings from this study suggest that employing simplifying assumptions for the cases investigated can reasonably result in uncertainty bands of  $\pm 5\text{dB}$ . Considering all the simplifying assumptions used in numerical models of ground vibration from underground railways it would not be unreasonable to conclude that the prediction accuracy

for such a model may be limited to  $\pm 10$ dB.

## 5.2 Recommendations for Further Work

The thin-layer method presented in this dissertation is derived as a 2D plane-strain model. While it was deemed unnecessary to use a 2.5D or 3D model for the studies it would be interesting to compare the plane-strain results with those from a 2.5D model to verify this assumption. Through recent discussion with Kausel, the author has learnt that Kausel and one of his students have recently finished a derivation of the thin-layer method in 2.5D and plan to publish the results in the next year. The formulation is reported to be efficient and should allow calculation of 2.5D predictions in similar run-times to the 2D formulation.

The TLM model has the potential to be more efficient if a means of simulating the underground railway tunnel could be found which does not require dense meshing of the hyperelements so as to have a node at 32 locations around the tunnel circumference. There is potential that substructuring techniques<sup>[9]</sup> may be employed to create a super-hyperelement which contains all the equivalent internal sources. The external nodes of said super-hyperelement (i.e. the master degrees of freedom) could be coupled to the standard TLM model, while the internal nodes (i.e. the dense mesh required for the EIS ring) are condensed and only used if the predicted motion within the super-hyperelement is required.

Both the TLM and discrete-void model could be used to perform a more comprehensive study of the effect of simplifying assumptions by considering different material properties of the soil, tunnel, floating-slab-track, etc. It may be beneficial to non-dimensionalize the results with respect to governing properties (i.e. wave-speed of the soil). A more complete set of geometrical properties could also be considered including different layer depths, tunnel sizes, tunnel depths, etc.

The models presented also have the potential to be used to investigate further sim-

plifying assumptions. For example, the TLM model could be used to study the effect of water-table height on surface vibration due to underground railways. This could be done simply by varying the material properties at the appropriate depth to simulate a saturated soil (i.e. Poisson's ratio = 0.5; density and stiffness adjusted to saturated values). The discrete-void model could be used to investigate the effect of cavities occurring below the tunnel. The bulk of the wave-energy exits through the base of the tunnel invert<sup>[61]</sup> thus a cavity under the tunnel may also have a significant effect on ground vibration.

# Appendix A

## Useful Relations and Material Damping

The material properties of a solid may be defined using a number of different variables (i.e. Lamé constants, elastic modulus, etc.). Below is a list of conversions of some common properties into a standard set of variables

$$\lambda = \frac{E\nu}{(1 + \nu)(1 - 2\nu)} \quad (\text{A.1a})$$

$$\mu = \frac{E}{2(1 + \nu)} \quad (\text{A.1b})$$

$$G = \mu \quad (\text{A.1c})$$

where  $\lambda$  and  $\mu$  are Lamé constants,  $G$  is the shear modulus,  $E$  is the elastic modulus,  $\nu$  is Poisson's ratio, and  $\rho$  is density.

Wave velocities are defined as

$$c_1 = \left( \frac{\lambda + 2\mu}{\rho} \right)^{1/2} \quad \text{P-wave velocity} \quad (\text{A.2a})$$

$$c_2 = \left( \frac{\mu}{\rho} \right)^{1/2} \quad \text{S-wave velocity.} \quad (\text{A.2b})$$

In soil dynamics, material damping is usually assumed to be rate independent in the low frequency range of interest for this research. Under this assumption material damping of a soil can be simulated using the correspondence principle<sup>[124]</sup> which states that a viscoelastic material can be modelled in the frequency domain as an equivalent elastic material with modified elastic constants (i.e. complex material properties). A convenient means of applying damping is

$$\lambda^* + 2\mu^* = (\lambda + 2\mu)(1 + 2iD_P) \quad (\text{A.3a})$$

$$\mu^* = \mu(1 + 2iD_S) \quad (\text{A.3b})$$

where  $D_p$  and  $D_s$  represent the material damping ratio for the pressure waves and the shear waves, respectively.

# Appendix B

## Thomas Algorithm

The Thomas Algorithm, also known as the tridiagonal matrix algorithm, is a simplified form of Gaussian elimination that can be used to solve both scalar-tridiagonal and block-tridiagonal systems of equations<sup>[18]</sup>. A block-tridiagonal system for  $n$  submatrices may be written as

$$\begin{bmatrix} \mathbf{b}_1 & \mathbf{c}_1 & & & 0 \\ \mathbf{a}_2 & \mathbf{b}_2 & \mathbf{c}_2 & & \\ & \mathbf{a}_3 & \mathbf{b}_3 & \ddots & \\ & & \ddots & \ddots & \mathbf{c}_{n-1} \\ 0 & & & \mathbf{a}_n & \mathbf{b}_n \end{bmatrix} \begin{Bmatrix} \mathbf{u}_1 \\ \mathbf{u}_2 \\ \mathbf{u}_3 \\ \vdots \\ \mathbf{u}_n \end{Bmatrix} = \begin{Bmatrix} \mathbf{f}_1 \\ \mathbf{f}_2 \\ \mathbf{f}_3 \\ \vdots \\ \mathbf{f}_n \end{Bmatrix}. \quad (\text{B.1})$$

where each submatrix  $\mathbf{a}_i$ ,  $\mathbf{b}_i$ ,  $\mathbf{c}_i$  is  $m \times m$ , and each displacement vector  $\mathbf{u}_i$  and forcing vector  $\mathbf{f}_i$  has  $m$  elements for  $i = 1, 2, \dots, n$ .

The first step in the solution requires a forward sweep to define new coefficients  $\mathbf{c}_i^{\mathbf{x}}$  and  $\mathbf{f}_i^{\mathbf{x}}$  as

$$\mathbf{c}_i^{\mathbf{x}} = \begin{cases} \mathbf{b}_1^{-1} \mathbf{c}_1 & ; i = 1 \\ (\mathbf{b}_i - \mathbf{a}_i \mathbf{c}_{i-1}^{\mathbf{x}})^{-1} \mathbf{c}_i & ; i = 2, 3, \dots, (n-1) \end{cases} \quad (\text{B.2})$$

and

$$\mathbf{d}_i^{\mathbf{x}} = \begin{cases} \mathbf{b}_1^{-1} \mathbf{d}_1 & ; i = 1 \\ (\mathbf{b}_i - \mathbf{a}_i \mathbf{c}_{i-1}^{\mathbf{x}})^{-1} (\mathbf{d}_i - \mathbf{a}_i \mathbf{d}_{i-1}^{\mathbf{x}}) & ; i = 2, 3, \dots, n \end{cases} \quad (\text{B.3})$$

followed by a back substitution

$$\begin{aligned} \mathbf{u}_n &= \mathbf{d}_i^{\mathbf{x}} \\ \mathbf{u}_i &= \mathbf{d}_i^{\mathbf{x}} - \mathbf{c}_i^{\mathbf{x}} \mathbf{u}_{i+1} \quad ; \quad i = (n-1), (n-2), \dots, 1. \end{aligned} \tag{B.4}$$

# Appendix C

## Green's Functions for a Layered Halfspace in Plane Strain

### C.1 Homogeneous Halfspace

The plane strain halfspace frequency response functions (FRF's) detailed here are derived from the Green's functions for a two-and-a-half dimensional elastodynamic halfspace given by Tadeu<sup>[140]</sup>. The plane strain condition is a particular case of the general functions where the wavenumber in the  $y$ -direction  $k_y$  is set to zero (i.e. a line load). It should be noted that the coordinate system has been changed from that used by Tadeu in order to match the coordinate system defined in Figure C.1.

The FRF's are given in wavenumber-frequency domain  $(k_n, \omega)$  for ease of computa-

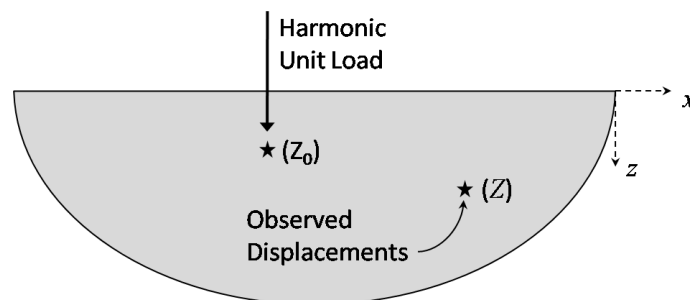


Figure C.1: Analytical halfspace where displacements are observed at a depth  $z$  due to a harmonic line-load at a depth  $z_0$

tion;  $k_n$  is the wavenumber from the  $x$ -direction. As detailed in Figure 4.7, the load is applied at  $(x_0, z_0)$  and displacements are observed at  $(x, z)$ .

### C.1.1 Load acting in the $x$ -direction

For a line-load applied in the  $x$ -direction, the FRF's for displacement in the  $x$ -direction ( $H_{xx}^{half}$ ) and in the  $z$ -direction ( $H_{zx}^{half}$ ) are as follows

$$H_{xx}^{half}(z, z_0, k_n, \omega) = \frac{1}{2\rho\omega^2} \left[ \frac{-ik_n^2}{\nu_n} (E_b + A_n^x E_{b0}) - i\gamma_n (E_c + C_n^x E_{c0}) \right] \quad (C.1)$$

$$H_{zx}^{half}(z, z_0, k_n, \omega) = \frac{ik_n}{2\rho\omega^2} [(\pm E_b + A_n^x E_{b0}) - (\pm E_c + C_n^x E_{c0})] \text{ for } z \gtrless z_0 \quad (C.2)$$

where

$$\begin{bmatrix} -2k_n^2 & 0 & k_n^2 - \gamma_n^2 \\ -2 & 1 & 1 \\ \frac{-k_s^2}{\nu_n} + 2\frac{k_n^2}{\nu_n} & 0 & 2\gamma_n \end{bmatrix} \begin{Bmatrix} A_n^x \\ B_n^x \\ C_n^x \end{Bmatrix} = \begin{Bmatrix} -2k_n^2 E_{b1} + (2k_n^2 - k_s^2) E_{c1} \\ -2E_{b1} + 2E_{c1} \\ \left(\frac{k_s^2}{\nu_n} - 2\frac{k_n^2}{\nu_n}\right) E_{b1} - 2\gamma_n E_{c1} \end{Bmatrix} \quad (C.3)$$

and

$$E_b = e^{-i\nu_n|z-z_0|} \quad E_{b0} = e^{-i\nu_n z} \quad E_{b1} = e^{-i\nu_n z_0} \quad (C.4a)$$

$$E_c = e^{-i\gamma_n|z-z_0|} \quad E_{c0} = e^{-i\gamma_n z} \quad E_{c1} = e^{-i\gamma_n z_0} \quad (C.4b)$$

$$\nu_n = \sqrt{k_p^2 - k_n^2} \quad \gamma_n = \sqrt{k_s^2 - k_n^2} \quad k_p = \frac{\omega}{C_p} \quad k_s = \frac{\omega}{C_s}. \quad (C.5)$$

The pressure wave-speed  $C_p$  and shear wave-speed  $C_s$  are calculated from the halfspace material properties as defined earlier.

### C.1.2 Load acting in the $z$ -direction

For a line-load applied in the  $z$ -direction, the FRF's for displacement in the  $x$ -direction ( $H_{xz}^{half}$ ) and in the  $z$ -direction ( $H_{zz}^{half}$ ) are as follows

$$H_{xz}^{half}(z, z_0, k_n, \omega) = \frac{ik_n}{2\rho\omega^2} [(\pm E_b + A_n^z E_{b0}) - (\pm E_c + B_n^z E_{c0})] \text{ for } z \geq z_0 \quad (\text{C.6})$$

$$H_{zz}^{half}(z, z_0, k_n, \omega) = \frac{1}{2\rho\omega^2} \left[ -i\nu_n (E_b + A_n^z E_{b0}) - \frac{ik_n^2}{\gamma_n} (E_c + B_n^z E_{c0}) \right] \quad (\text{C.7})$$

where

$$\begin{bmatrix} -2\nu_n & \frac{-k_n^2}{\gamma_n} + \gamma_n & 0 \\ -2\nu_n & \frac{-k_n^2}{\gamma_n} & \gamma_n \\ (-k_s^2 + 2k_n^2) & -2k_n^2 & 0 \end{bmatrix} \begin{Bmatrix} A_n^z \\ B_n^z \\ C_n^z \end{Bmatrix} = \begin{Bmatrix} 2\nu_n E_{b1} + \left( \frac{k_n^2}{\gamma_n} - \gamma_n \right) E_{c1} \\ 2\nu_n E_{b1} + \left( \frac{k_n^2}{\gamma_n} - \gamma_n \right) E_{c1} \\ (-k_s^2 + 2k_n^2) E_{b1} - 2k_n^2 E_{c1} \end{Bmatrix} \quad (\text{C.8})$$

with the other variables are defined in Section C.1.1.

## C.2 Homogeneous Layer

The frequency response functions (FRF's) for a free homogeneous layer of thickness  $h$  are also derived by Tadeu<sup>[139]</sup>. The plane strain condition is detailed below by setting the wavenumber in the  $y$ -direction  $k_y$  to zero. It should be noted again that the coordinate system has been changed from that used by Tadeu in order to match the coordinate system defined in Figure C.2.

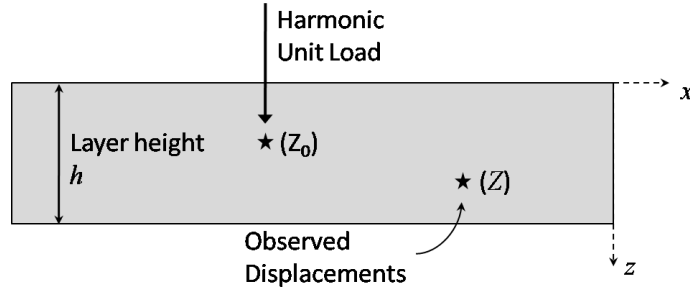


Figure C.2: Analytical solid layer where displacements are observed at a depth  $z$  due to a harmonic line-load at a depth  $z_0$

### C.2.1 Load acting in the $x$ -direction

For a line-load applied in the  $x$ -direction, the FRF's for displacement in the  $x$ -direction

( $H_{xx}^{layer}$ ) and in the  $z$ -direction ( $H_{zx}^{layer}$ ) are as follows

$$H_{xx}^{layer}(z, z_0, k_n, \omega) = \frac{1}{2\rho\omega^2} \left[ \frac{-ik_n^2}{\nu_n} (E_b + A_n^x E_{b0} + D_n^x E_{b0}^h) - i\gamma_n (E_c + C_n^x E_{c0} + F_n^x E_{c0}^h) \right] \quad (C.9)$$

$$H_{zx}^{layer}(z, z_0, k_n, \omega) = \frac{ik_n}{2\rho\omega^2} [(\pm E_b + A_n^x E_{b0} - D_n^x E_{b0}^h) - (\pm E_c + C_n^x E_{c0} - F_n^x E_{c0}^h)] \text{ for } z \geq z_0 \quad (C.10)$$

where

$$[\mathbf{r}] \left\{ \begin{array}{c} A_n^x \\ B_n^x \\ C_n^x \\ D_n^x \\ E_n^x \\ F_n^x \end{array} \right\} = [\mathbf{s}] \quad (C.11)$$

and

$$\begin{aligned}
r_{11} &= -2k_n^2 & r_{12} &= 0 & r_{13} &= k_n^2 - \gamma_n^2 \\
r_{14} &= -r_{11}E_b^h & r_{15} &= 0 & r_{16} &= -r_{13}E_c^h \\
r_{21} &= -2 & r_{22} &= 1 & r_{23} &= 1 \\
r_{24} &= -r_{21}E_b^h & r_{25} &= -r_{22}E_c^h & r_{26} &= -r_{23}E_c^h \\
r_{31} &= \frac{-ks^2}{\nu_n} + \frac{2k_n^2}{\nu_n} & r_{32} &= 0 & r_{33} &= 2\gamma_n \\
r_{34} &= r_{31}E_b^h & r_{35} &= 0 & r_{36} &= r_{33}E_c^h \\
r_{41} &= r_{11}E_b^h & r_{42} &= 0 & r_{43} &= r_{13}E_c^h \\
r_{44} &= -r_{11} & r_{45} &= 0 & r_{46} &= -r_{13} \\
r_{51} &= r_{21}E_b^h & r_{52} &= r_{22}E_c^h & r_{53} &= r_{23}E_c^h \\
r_{54} &= -r_{21} & r_{55} &= -r_{22} & r_{56} &= -r_{23} \\
r_{61} &= r_{31}E_b^h & r_{62} &= 0 & r_{63} &= r_{33}E_c^h \\
r_{64} &= r_{31} & r_{65} &= 0 & r_{66} &= r_{33}
\end{aligned} \tag{C.12a}$$

$$\begin{aligned}
s_1 &= -2k_n^2 E_{b1} + (-k_s^2 + 2k_n^2) E_{c1} \\
s_2 &= -2E_{b1} + 2E_{c1} \\
s_3 &= \left( \frac{k_s^2}{\nu_n} - \frac{2k_n^2}{\nu_n} \right) E_{b1} - 2\gamma_n E_{c1} \\
s_4 &= 2k_n^2 E_{b1}^h - (-k_s^2 + 2k_n^2) E_{c1}^h \\
s_5 &= 2E_{b1}^h - 2E_{c1}^h \\
s_6 &= \left( \frac{k_s^2}{\nu_n} - \frac{2k_n^2}{\nu_n} \right) E_{b1}^h - 2\gamma_n E_{c1}^h
\end{aligned} \tag{C.12b}$$

$$E_b^h = e^{-i\nu_n h} \quad E_{b0}^h = e^{-i\nu_n |z-h|} \quad E_{b1}^h = e^{-i\nu_n |h-z_0|} \quad (\text{C.13a})$$

$$E_c^h = e^{-i\gamma_n h} \quad E_{c0}^h = e^{-i\gamma_n |z-h|} \quad E_{c1}^h = e^{-i\gamma_n |h-z_0|} \quad (\text{C.13b})$$

### C.2.2 Load acting in the $z$ -direction

For a line-load applied in the  $z$ -direction, the FRF's for displacement in the  $x$ -direction ( $H_{xz}^{layer}$ ) and in the  $z$ -direction ( $H_{zz}^{layer}$ ) are as follows

$$H_{xz}^{layer}(z, z_0, k_n, \omega) = \frac{ik_n}{2\rho\omega^2} [(\pm E_b + A_n^z E_{b0} - D_n^z E_{b0}^h) - (\pm E_c + B_n^z E_{c0} - E_n^z E_{c0}^h)] \text{ for } z \geq z_0 \quad (\text{C.14})$$

$$H_{zz}^{layer}(z, z_0, k_n, \omega) = \frac{1}{2\rho\omega^2} \left[ -i\nu_n (E_b + A_n^z E_{b0} + D_n^z E_{b0}^h) - \frac{ik_n^2}{\gamma_n} (E_c + B_n^z E_{c0} + E_n^z E_{c0}^h) \right] \quad (\text{C.15})$$

where

$$[\mathbf{r}] \left\{ \begin{array}{c} A_n^x \\ B_n^x \\ C_n^x \\ D_n^x \\ E_n^x \\ F_n^x \end{array} \right\} = [\mathbf{s}] \quad (\text{C.16})$$

and

$$\begin{aligned}
r_{11} &= -2\nu_n & r_{12} &= \frac{-kn^2}{\gamma_n} + \gamma_n & r_{13} &= 0 \\
r_{14} &= r_{11}E_b^h & r_{15} &= r_{12}E_c^h & r_{16} &= 0 \\
r_{21} &= -2\nu_n & r_{22} &= \frac{-kn^2}{\gamma_n} & r_{23} &= \gamma_n \\
r_{24} &= r_{21}E_b^h & r_{25} &= r_{22}E_c^h & r_{26} &= r_{23}E_c^h \\
r_{31} &= -ks^2 + 2kn^2 & r_{32} &= -2kn^2 & r_{33} &= 0 \\
r_{34} &= -r_{31}E_b^h & r_{35} &= -r_{32}E_c^h & r_{36} &= 0 \\
r_{41} &= r_{11}E_b^h & r_{42} &= r_{12}E_c^h & r_{43} &= 0 \\
r_{44} &= r_{11} & r_{45} &= r_{12} & r_{46} &= 0 \\
r_{51} &= r_{21}E_b^h & r_{52} &= r_{22}E_c^h & r_{53} &= r_{23}E_c^h \\
r_{54} &= r_{21} & r_{55} &= r_{22} & r_{56} &= r_{23} \\
r_{61} &= r_{31}E_b^h & r_{62} &= r_{32}E_c^h & r_{63} &= 0 \\
r_{64} &= -r_{31} & r_{65} &= -r_{32} & r_{66} &= 0
\end{aligned} \tag{C.17a}$$

$$\begin{aligned}
s_1 &= 2\nu_n E_{b1} + \left( \frac{k_n^2}{\gamma_n} - \gamma_n \right) E_{c1} \\
s_2 &= 2\nu_n E_{b1} + \left( \frac{k_n^2}{\gamma_n} - \gamma_n \right) E_{c1} \\
s_3 &= (-k_s^2 + 2k_n^2) E_{b1} - 2k_n^2 E_{c1} \\
s_4 &= 2\nu_n E_{b1}^h + \left( \frac{k_n^2}{\gamma_n} - \gamma_n \right) E_{c1}^h \\
s_5 &= 2\nu_n E_{b1}^h + \left( \frac{k_n^2}{\gamma_n} - \gamma_n \right) E_{c1}^h \\
s_6 &= (k_s^2 - 2k_n^2) E_{b1}^h + 2k_n^2 E_{c1}^h
\end{aligned} \tag{C.17b}$$

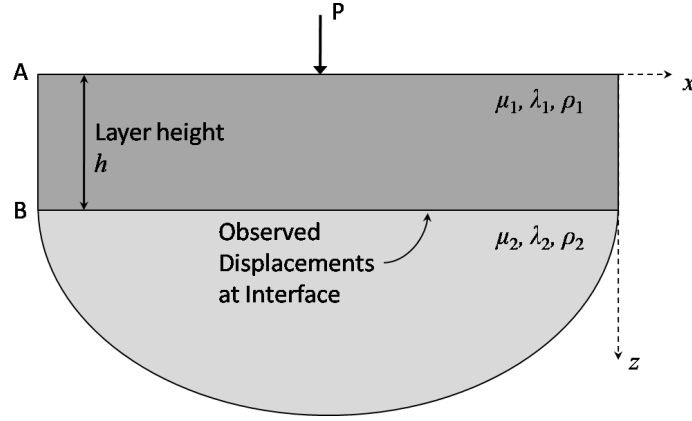


Figure C.3: Analytical layered halfspace where displacements are observed at layer interface (B) due to a harmonic line-load  $\mathbf{P}$  applied at the surface (A)

### C.3 Layered Halfspace - Surface Load, Observation at Layer Interface

The analytical Green's function for a horizontally layered halfspace can be derived from the Green's functions detailed above. Consider the TLM verification example depicted in Figure C.3. A harmonic line-load is applied on the surface and the displacement at the layer interface is observed.

If the systems are separated as depicted in Figure C.4, the equations of motions for a given wavenumber  $k_n$  and frequency  $\omega$  can be written as follows

$$\begin{Bmatrix} \mathbf{u}_A \\ \mathbf{u}_{B1} \end{Bmatrix} = \begin{bmatrix} \mathbf{H}_{AA} & \mathbf{H}_{AB} \\ \mathbf{H}_{BA} & \mathbf{H}_{BB} \end{bmatrix} \begin{Bmatrix} \mathbf{P} \\ \mathbf{F}_{B1} \end{Bmatrix} \quad (\text{C.18a})$$

$$\mathbf{u}_{B2} = \mathbf{G}_{BB} \mathbf{F}_{B2} \quad (\text{C.18b})$$

where  $\mathbf{H}_{ij}$  are the layer's  $2 \times 2$  transfer functions for the displacement at  $i$  due to a load applied at  $j$ ;  $\mathbf{G}_{BB}$  is the  $2 \times 2$  transfer function for a driving-point response on the surface of the halfspace (i.e. surface B).

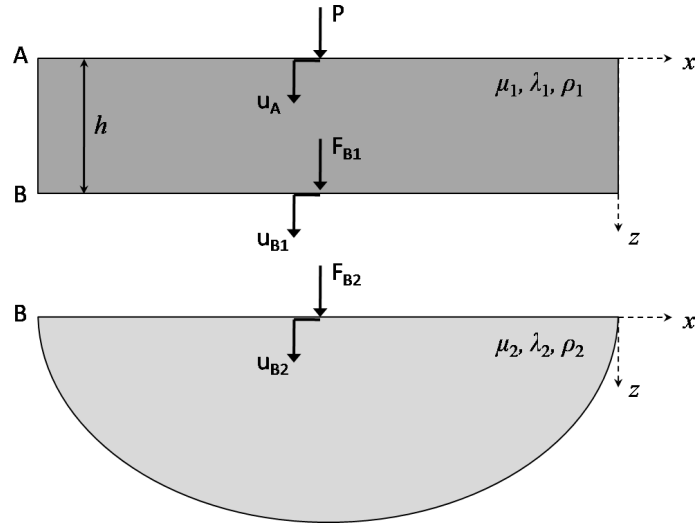


Figure C.4: Layered halfspace subjected to a surface load separated into its subsystems showing internal displacements and internal loads

Displacement compatibility and force equilibrium require

$$\mathbf{u}_{B1} = \mathbf{u}_{B2} = \mathbf{u}_B \quad (\text{C.19a})$$

$$\mathbf{F}_{B1} = -\mathbf{F}_{B2} \quad (\text{C.19b})$$

Subbing these requirements into Equation C.18 results in the coupled equations for the displacement at the layer interface due to a load applied at the surface of the horizontally layered halfspace

$$\mathbf{u}_B = (\mathbf{I} + \mathbf{H}_{BB}\mathbf{G}_{BB}^{-1})^{-1} \mathbf{H}_{BA}\mathbf{P}. \quad (\text{C.20})$$

## C.4 Layered Halfspace - Buried Load, Observation at Surface

To validate the TLM model for tunnel loading, the analytical transfer function for the response at the surface of a layered halfspace due to a buried load is required. When the systems are separated as depicted in Figure C.5, the equations of motions for a given

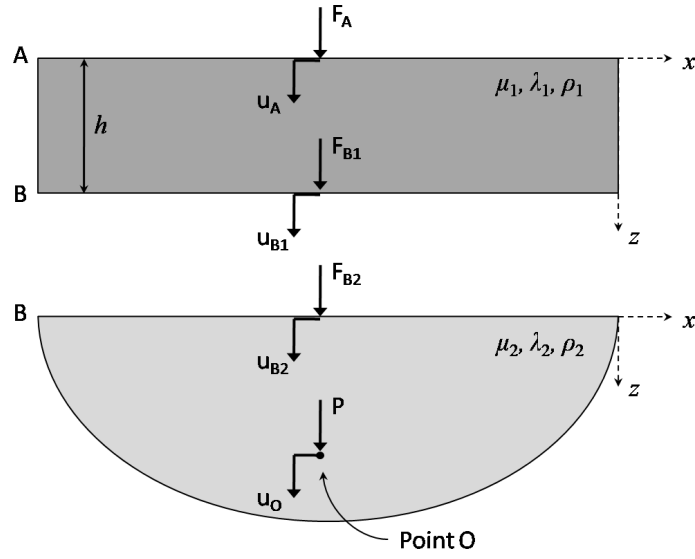


Figure C.5: Layered halfspace subjected to a buried load separated into its subsystems showing internal displacements and internal loads

wavenumber  $k_n$  and frequency  $\omega$  can be written as follows

$$\begin{Bmatrix} \mathbf{u}_A \\ \mathbf{u}_{B1} \end{Bmatrix} = \begin{bmatrix} \mathbf{H}_{AA} & \mathbf{H}_{AB} \\ \mathbf{H}_{BA} & \mathbf{H}_{BB} \end{bmatrix} \begin{Bmatrix} \mathbf{F}_A \\ \mathbf{F}_{B1} \end{Bmatrix} \quad (\text{C.21a})$$

$$\begin{Bmatrix} \mathbf{u}_{B2} \\ \mathbf{u}_O \end{Bmatrix} = \begin{bmatrix} \mathbf{G}_{BB} & \mathbf{G}_{BO} \\ \mathbf{G}_{OB} & \mathbf{G}_{OO} \end{bmatrix} \begin{Bmatrix} \mathbf{F}_{B1} \\ \mathbf{P} \end{Bmatrix} \quad (\text{C.21b})$$

where  $\mathbf{H}_{ij}$  are the  $2 \times 2$  transfer functions for the displacement at  $i$  due to a load applied at  $j$ ;  $\mathbf{G}_{ij}$  are the halfspace's  $2 \times 2$  transfer functions for a displacement at  $i$  due to a load applied at  $j$ .

Displacement compatibility and force equilibrium require

$$\mathbf{u}_{B1} = \mathbf{u}_{B2} = \mathbf{u}_B \quad (\text{C.22a})$$

$$\mathbf{F}_A = 0 \quad (\text{C.22b})$$

$$\mathbf{F}_{B1} = -\mathbf{F}_{B2} \quad (\text{C.22c})$$

Subbing these requirements into Equation C.21 results in the coupled equations for the displacement at the surface of a layered halfspace due to a load applied at depth in the lower-halfspace

$$\mathbf{u}_A = \mathbf{H}_{AB} (\mathbf{H}_{BB} + \mathbf{G}_{BB})^{-1} \mathbf{G}_{BO} \mathbf{P}. \quad (\text{C.23})$$



# Appendix D

## Boundary Element Method in Plane Strain Dynamics

The boundary element method (BEM) in dynamics is a numerical technique based on integral equation formulations of the equations of motion for an elastic continuum using basic field variables (i.e. displacements, tractions, etc.)<sup>[22]</sup>. The characteristic benefit to the BEM is that only the boundary needs to be discretized opposed to full-domain techniques such as finite element methods (FEM) or finite difference methods (FDM) which require discretization of the entire domain. Numerous books have been written on the subject of BEM in dynamics including Dominguez<sup>[22]</sup>, Becker<sup>[10]</sup> and Manolis *et al.*<sup>[100]</sup>. This appendix is meant only to introduce the method to the reader; please refer to the reference material for full details.

## D.1 Fundamental Solution and the Boundary Integral Formulation

The general field equation for the elastodynamics fullspace in plane strain subjected to a unit line load can be written as<sup>[22]</sup>

$$c_1^2 \nabla \nabla \mathbf{u} - c_2^2 \nabla \times \nabla \times \mathbf{u} - \frac{\partial^2 \mathbf{u}}{\partial t^2} = -\delta(r) \quad (\text{D.1})$$

where  $c_1$  is the P-wave velocity,  $c_2$  is the S-wave velocity, and  $\lambda$  and  $\mu$  are Lamé constants as defined in Appendix A. The remaining properties are the material density  $\rho$ , the Dirac delta function  $\delta$ , the distance between the load point and observation point  $r$ , and the displacement vector  $\mathbf{u}$ . The above equations hold when damping is included using complex material properties, as outlined in Appendix A.

Equation D.1 can be solved by assuming the loading and resultant displacement are harmonic and decomposing  $\mathbf{u}$  into its irrotational and equivoluminal parts as follows

$$u_{ik}^* = \frac{1}{4\pi\rho c_2^2} \left[ \psi \delta_{ik} - \chi \frac{\partial r}{\partial l} \frac{\partial r}{\partial k} \right] \quad (\text{D.2a})$$

$$\begin{aligned} p_{ik}^* &= \frac{1}{4\pi} \left[ \left( \frac{d\psi}{dr} - \frac{\chi}{r} \right) \left( \delta_{ik} \frac{\partial r}{\partial n} + \frac{\partial r}{\partial k} \frac{\partial n}{\partial l} \right) \right. \\ &\quad - \frac{2\chi}{r} \left( \frac{\partial n}{\partial k} \frac{\partial r}{\partial l} - 2 \frac{\partial r}{\partial l} \frac{\partial r}{\partial k} \frac{\partial r}{\partial n} \right) - 2 \frac{\partial \chi}{\partial r} \frac{\partial r}{\partial l} \frac{\partial r}{\partial k} \frac{\partial r}{\partial n} \\ &\quad \left. + \left( \frac{c_1^2}{c_2^2} - 2 \right) \left( \frac{\partial \psi}{\partial r} - \frac{\partial \chi}{\partial r} - \frac{2\chi}{r} \right) \frac{\partial r}{\partial l} \frac{\partial n}{\partial k} \right] \end{aligned} \quad (\text{D.2b})$$

where  $u_{ik}^*$  is the displacement in the  $k$ -direction due to a unit load applied in the  $l$ -direction,  $p_{ik}^*$  is the traction component in the  $k$ -direction on a surface whose unit external normal is  $\mathbf{n}$  due to a unit load applied in the  $l$ -direction,  $\delta_{ik}$  is the Kronecker delta function, and  $r$  is the distance from the point of interest to the load point (see

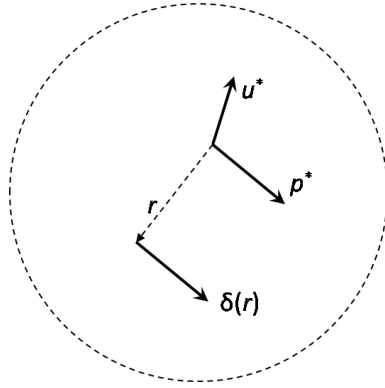


Figure D.1: Depiction of the resultant displacement vector  $\mathbf{u}^*$  and traction vector  $\mathbf{p}^*$  due to a unit line load  $\delta(r)$  acting at a distance  $r$  in a fullspace

Figure D.1). The displacement and traction parameters are starred because these are the solutions for a unit load in a fullspace and are therefore commonly referred to as the Green's functions of the formulation.

Now let  $\Omega$  represent an elastic region within the plane strain fullspace with a boundary defined by  $\Gamma$ . If body forces are ignored (valid assumption since vibrations are small amplitude about an equilibrium position), the integral representation of the displacement response  $\mathbf{u}$  at an internal point  $i$  is<sup>[22]</sup>

$$u_i^i + \int_{\Gamma} p_{lk}^* u_k d\Gamma = \int_{\Gamma} u_{lk}^* p_k d\Gamma \quad (\text{D.3})$$

where  $u_k$  and  $p_k$  are the displacement and traction vectors on the boundary of  $\Omega$  in the  $k$ -direction, and  $u_{lk}^*$  and  $p_{lk}^*$  are the fundamental solutions for displacements and tractions in a fullspace along a path defined by  $\Gamma$ .

Since Equation D.3 is valid for every point in  $\Omega$ , including those on  $\Gamma$ , this expression can be applied to every point on the boundary to produce a system of equations which, once solved, gives the boundary values. However, when point  $i$  is taken to the boundary the integrals develop a singularity. Dominguez<sup>[22]</sup> shows that a Cauchy Principal Value integral can be applied which transforms Equation D.3 to

$$c_{lk}^i u_k^i + \int_{\Gamma} p_{lk}^* u_k d\Gamma = \int_{\Gamma} u_{lk}^* p_k d\Gamma \quad (\text{D.4})$$

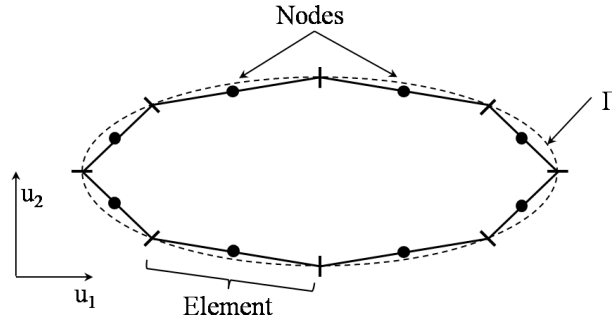


Figure D.2: Two-dimensional body divided into constant boundary elements

where  $c_{lk}^i = \frac{1}{2}\delta_{lk}$  is valid for boundary nodes.

## D.2 Numerical Solution

For a plane strain problem, the displacement and traction vectors are defined as

$$\mathbf{u} = \begin{Bmatrix} u_1 \\ u_2 \end{Bmatrix} \quad ; \quad \mathbf{p} = \begin{Bmatrix} p_1 \\ p_2 \end{Bmatrix} \quad (\text{D.5})$$

and the Green's functions of the formulation as

$$\mathbf{u}^* = \begin{bmatrix} u_{11}^* & u_{12}^* \\ u_{21}^* & u_{22}^* \end{bmatrix} \quad ; \quad \mathbf{p}^* = \begin{bmatrix} p_{11}^* & p_{12}^* \\ p_{21}^* & p_{22}^* \end{bmatrix} \quad (\text{D.6})$$

hence Equation D.4 can be written as

$$\frac{1}{2}\mathbf{u}^i + \int_{\Gamma} \mathbf{p}^* \mathbf{u} d\Gamma = \int_{\Gamma} \mathbf{u} * \mathbf{p} d\Gamma \quad (\text{D.7})$$

Let the boundary  $\Gamma$  be discretized into  $N$  elements. Numerous shape functions can be applied to define the variation in field variable across the element<sup>[10]</sup>; for simplicity assume a constant shape function meaning each element is defined by a single, central node and the field variable is constant over the whole element as shown in Figure D.2.

This allows Equation D.7 to be written as

$$\frac{1}{2}\mathbf{u}^i + \sum_{j=1}^N \left[ \int_{\Gamma_j} \mathbf{p}^* d\Gamma \right] \mathbf{u}^j = \sum_{j=1}^N \left[ \int_{\Gamma_j} \mathbf{u}^* d\Gamma \right] \mathbf{p}^j \quad (\text{D.8})$$

where the boundary integrals have been written as a summation of integrals along the elements, and the elemental displacements and tractions ( $\mathbf{u}^j$  and  $\mathbf{p}^j$ ) can be taken outside the integrals as they are constant over the element.

The integrals can be recognized as  $2 \times 2$  matrices which relate the node of interest  $i$  with the node of the integration element  $j$  allowing Equation D.8 to be written in matrix form as

$$\sum_{j=1}^N \mathbf{H}^{ij} \mathbf{u}^j = \sum_{j=1}^N \mathbf{G}^{ij} \mathbf{p}^j \quad \text{for } i = 1, 2, \dots, N \quad (\text{D.9})$$

where

$$\mathbf{H}^{ij} = \begin{cases} \int_{\Gamma_j} \mathbf{p}^* d\Gamma + \frac{1}{2} & ; \quad i = j \\ \int_{\Gamma_j} \mathbf{p}^* d\Gamma & ; \quad i \neq j \end{cases} \quad (\text{D.10a})$$

$$\mathbf{G}^{ij} = \int_{\Gamma_j} \mathbf{u}^* d\Gamma \quad (\text{D.10b})$$

When Equation D.9 is applied to all boundary elements, the resulting system of equations is given by

$$\mathbf{HG} = \mathbf{UP} \quad (\text{D.11})$$

where the influence matrices  $\mathbf{H}$  and  $\mathbf{G}$  are  $2N \times 2N$ . The computation of the influence coefficients integrals is generally done numerically as they contain a mixture of Bessel functions which makes an analytical solution difficult to find (see Dominguez<sup>[22]</sup> for a computationally efficient Gaussian-quadrature method).

The final consideration is the application of the boundary conditions; at some nodes the displacement may be constrained while at others the known tractions may be applied. Standard matrix algebra is applied to move all unknowns to the left-hand side of

Equation D.11 and all known parameters to the right, resulting in a standard system of equations

$$\mathbf{AX} = \mathbf{F} \quad (\text{D.12})$$

where  $\mathbf{X}$  represents all unknowns (i.e. displacements and tractions) in the problem.

# Appendix E

## The PiP Derivation in 3D

A long tunnel of circular cross-section buried in a fullspace can be conceptualized as an infinitely long tube surrounded by soil of infinite extent. This arrangement can be simulated as shown in Figure E.1 using an inner pipe (i.e. the tunnel) coupled to an outer pipe with infinite outer radius (i.e. the soil). Since the wall thickness of the inner pipe is thin compared to its radius, cylindrical thin-shell theory is used to model the tunnel's response. The thick-shell response of the tunnel is modeled using elastic continuum equations. The following sections show the derivation of the coupled tunnel-soil model as developed by Forrest<sup>[33]</sup>.

### E.1 3D Cylindrical Shell Equations

The general dynamic equations for a three-dimensional cylindrical shell made of linear elastic, homogeneous, isotropic materials are given by Forrest<sup>[33]</sup> as reproduced below. These equations are based on the general shell equations derived by Volmir<sup>[154]</sup> and Flügge<sup>[32]</sup>. Each of the three equations represents dynamic equilibrium in one of the three principal cylindrical directions.

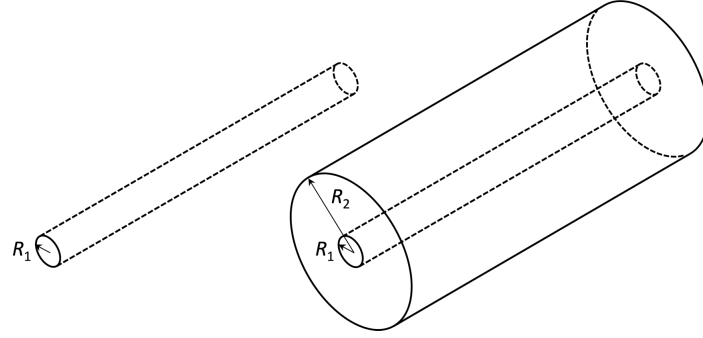


Figure E.1: Schematic of the pipe-in-pipe arrangement: inner pipe representing the tunnel modeled as a thin-walled cylinder (left) and outer pipe representing the soil with outer radius  $R_2 = \infty$  (right)

Longitudinal direction:

$$\begin{aligned}
 & a \frac{\partial^2 u}{\partial x^2} + \frac{(1-\nu)}{2a} \frac{\partial^2 u}{\partial \theta^2} + \frac{(1+\nu)}{2} \frac{\partial^2 v}{\partial x \partial \theta} - \nu \frac{\partial w}{\partial x} \\
 & + \frac{h^2}{12} \left[ \frac{(1-\nu)}{2a^3} \frac{\partial^2 u}{\partial \theta^2} + \frac{\partial^3 w}{\partial x^3} - \frac{(1-\nu)}{2a^2} \frac{\partial^3 w}{\partial x \partial \theta^2} \right] \\
 & + a \frac{(1-\nu^2)}{Eh} q_x - \rho a \frac{(1-\nu^2)}{E} \frac{\partial^2 u}{\partial t^2} = 0
 \end{aligned} \tag{E.1}$$

Tangential direction:

$$\begin{aligned}
 & \frac{(1+\nu)}{2} \frac{\partial^2 u}{\partial x \partial \theta} + a \frac{(1-\nu)}{2} \frac{\partial^2 v}{\partial x^2} + \frac{1}{a} \frac{\partial^2 v}{\partial \theta^2} - \frac{1}{a} \frac{\partial w}{\partial \theta} \\
 & + \frac{h^2}{12} \left[ \frac{3(1-\nu)}{2a} \frac{\partial^2 v}{\partial x^2} + \frac{(3-\nu)}{2a} \frac{\partial^3 w}{\partial x^2 \partial \theta} \right] \\
 & + a \frac{(1-\nu^2)}{Eh} q_y - \rho a \frac{(1-\nu^2)}{E} \frac{\partial^2 v}{\partial t^2} = 0
 \end{aligned} \tag{E.2}$$

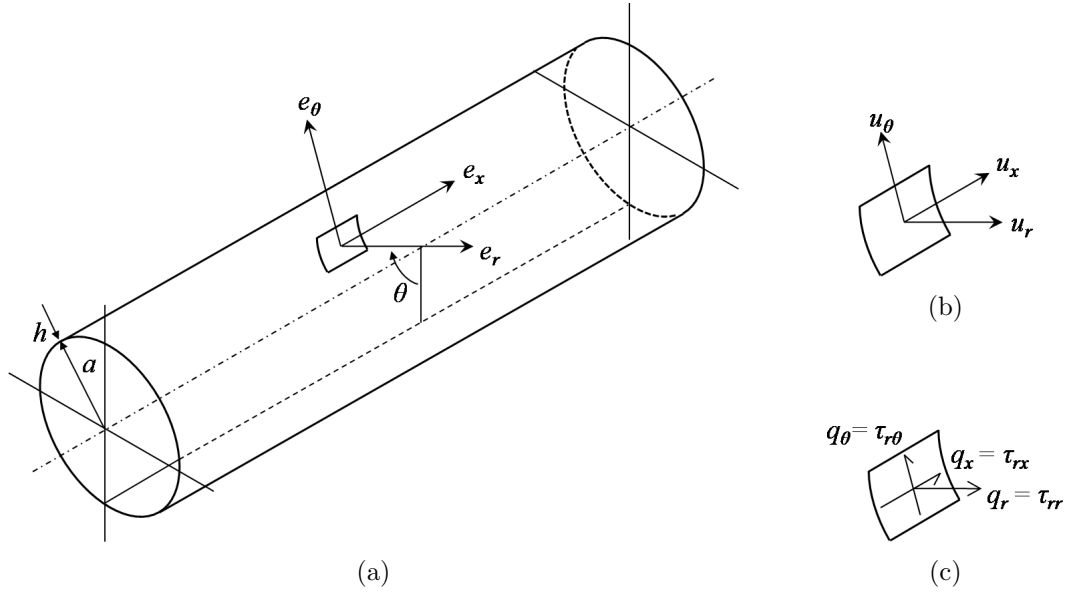


Figure E.2: Coordinate system for three-dimensional cylindrical shell equations showing (a) the principle directions for a typical element of the shell, (b) the corresponding displacement components and (c) the corresponding surface stress components.

Radial direction:

$$\begin{aligned}
 & \nu \frac{\partial u}{\partial x} + \frac{1}{a} \frac{\partial v}{\partial \theta} - \frac{1}{a} w - \frac{h^2}{12} \left[ a \frac{\partial^4 w}{\partial x^4} + \frac{2}{a} \frac{\partial^4 w}{\partial x^2 \partial \theta^2} + \frac{1}{a^3} \frac{\partial^4 w}{\partial \theta^4} \right] \\
 & - \frac{h^2}{12} \left[ \frac{\partial^3 u}{\partial x^3} - \frac{(1-\nu)}{2a^2} \frac{\partial^3 u}{\partial x \partial \theta^2} + \frac{(3-\nu)}{2a} \frac{\partial^3 v}{\partial x^2 \partial \theta} + \frac{1}{a^3} w + \frac{2}{a^3} \frac{\partial^2 w}{\partial \theta^2} \right] \\
 & + a \frac{(1-\nu^2)}{Eh} q_z - \rho a \frac{(1-\nu^2)}{E} \frac{\partial^2 w}{\partial t^2} = 0
 \end{aligned} \tag{E.3}$$

The displacement components  $u_x$ ,  $u_\theta$  and  $u_r$  vary with time  $t$  and correspond to the  $x$ ,  $\theta$  and  $r$  directions, respectively (see Figure E.2(b)). The shell is of radius  $a$  and thickness  $h$  and has material defined by elastic modulus  $E$ , Poisson's ratio  $\nu$  and density  $\rho$ . The net applied stress components acting on the inside surface of the shell (i.e. the difference between the interior and exterior surface stresses) are described using two shear tractions  $q_x$  and  $q_\theta$ , and one normal stress  $q_r$  (see Figure E.2(c)).

The loading applied to the infinitely long cylindrical shell is assumed to be harmonic

in both space and time and provided the loading is symmetric (e.g. longitudinal and radial loading) it takes the form

$$\begin{aligned} q_x &= \tilde{Q}_{xn} \cdot \cos n\theta \cdot e^{i(\omega t + \xi x)} \\ q_\theta &= \tilde{Q}_{\theta n} \cdot \sin n\theta \cdot e^{i(\omega t + \xi x)} \\ q_r &= \tilde{Q}_{rn} \cdot \cos n\theta \cdot e^{i(\omega t + \xi x)}. \end{aligned} \quad (\text{E.4})$$

The resulting displacements can be written in the form

$$\begin{aligned} u_x &= \tilde{U}_{xn} \cdot \cos n\theta \cdot e^{i(\omega t + \xi x)} \\ u_\theta &= \tilde{U}_{\theta n} \cdot \sin n\theta \cdot e^{i(\omega t + \xi x)} \\ u_r &= \tilde{U}_{rn} \cdot \cos n\theta \cdot e^{i(\omega t + \xi x)}. \end{aligned} \quad (\text{E.5})$$

The coefficients  $\tilde{U}_{xn}$ ,  $\tilde{U}_{\theta n}$ ,  $\tilde{U}_{rn}$ ,  $\tilde{Q}_{xn}$ ,  $\tilde{Q}_{\theta n}$  and  $\tilde{Q}_{rn}$  are functions of frequency  $\omega$ , longitudinal wavenumber  $\xi$ , and ring-mode  $n$ . For clarity the capitalization of the coefficients indicates the frequency domain, the tilde indicates the wavenumber domain, and the subscript  $n$  indicates the ring-mode domain.

Substituting equations E.4 and E.5 into E.1, E.2 and E.3 results in the following relationship

$$\left[ \tilde{\mathbf{A}} \right] \begin{Bmatrix} \tilde{U}_{xn} \\ \tilde{U}_{\theta n} \\ \tilde{U}_{rn} \end{Bmatrix} = \frac{-a(1-\nu^2)}{Eh} \begin{Bmatrix} \tilde{Q}_{xn} \\ \tilde{Q}_{\theta n} \\ \tilde{Q}_{rn} \end{Bmatrix} \quad (\text{E.6})$$

where the  $[\tilde{\mathbf{A}}]$  matrix is  $3 \times 3$  whose elements are calculated by

$$\begin{aligned}
a_{11} &= \frac{\rho a(1-\nu^2)}{E} \omega^2 - a \xi^2 - \frac{(1-\nu)}{2a} n^2 - \frac{(1-\nu)}{2a} \frac{h^2}{12a^2} n^2 \\
a_{12} &= \frac{(1+\nu)}{2} i \xi n \\
a_{13} &= -\nu i \xi + \frac{h^2}{12} (i \xi)^3 + \frac{h^2}{12a^2} \frac{(1-\nu)}{2} i \xi n^2 \\
a_{21} &= -\frac{(1+\nu)}{2} i \xi n \\
a_{22} &= \frac{\rho a(1-\nu^2)}{E} \omega^2 - \frac{a(1-\nu)}{2} \xi^2 - \frac{1}{a} n^2 - \frac{a(1-\nu)}{2} \frac{h^2}{4a^2} \xi^2 \\
a_{23} &= \frac{1}{a} n + \frac{h^2}{12} \frac{(3-\nu)}{2a} \xi^2 n \\
a_{31} &= \nu i \xi - \frac{h^2}{12} (i \xi)^3 - \frac{h^2}{12a^2} \frac{(1-\nu)}{2} i \xi n^2 \\
a_{32} &= \frac{1}{a} n + \frac{h^2}{12} \frac{(3-\nu)}{2a} \xi^2 n \\
a_{33} &= \frac{\rho a(1-\nu^2)}{E} \omega^2 - \frac{h^2}{12} \left( a \xi^4 + \frac{2}{a} \xi^2 n^2 + \frac{1}{a^3} n^4 \right) - \frac{1}{a} + \frac{h^2}{6a^3} n^2 - \frac{h^2}{12a^3}
\end{aligned} \tag{E.7}$$

For simplicity this can be written as

$$\tilde{\mathbf{U}}_n = \tilde{\mathbf{H}}_{\text{tunnel}} \tilde{\mathbf{Q}}_n \tag{E.8a}$$

where

$$\tilde{\mathbf{H}}_{\text{tunnel}} = \frac{-a(1-\nu^2)}{Eh} [\tilde{\mathbf{A}}]^{-1} \tag{E.8b}$$

Hussein shows that if the applied loading is anti-symmetric about  $\theta = 0$  (e.g. circumferential loading)  $a_{12}$ ,  $a_{21}$ ,  $a_{23}$  and  $a_{32}$  must be multiplied by  $-1$ <sup>[61]</sup>.

## E.2 3D Elastic Continuum Equations

The general dynamic equations for a three-dimensional, linear elastic, homogeneous, isotropic solid in the form of a thick-walled cylinder with finite inner radius and infinite outer radius are given by Forrest<sup>[33]</sup> as reproduced below. These equations are based on the work of Gazis<sup>[43]</sup> and Köpke<sup>[84]</sup>. The 3D wave equation is given by Graff<sup>[47]</sup>, amongst others, as

$$(\lambda + \mu)\nabla\nabla \cdot \mathbf{u} + \mu\nabla^2\mathbf{u} + \rho\mathbf{f} = \rho\frac{\partial^2\mathbf{u}}{\partial t^2} \quad (\text{E.9})$$

where  $\mathbf{u}$  is the displacement vector,  $\mathbf{f}$  is the body force vector,  $t$  is time,  $\rho$  is density, and  $\lambda$  and  $\mu$  are Lamé's elastic constants. The standard elastic constants can be calculated from Lamé's constants as follows

$$\begin{aligned} E &= \mu \frac{3\lambda + 2\mu}{\lambda + \mu} \\ \nu &= \frac{\lambda}{2(\lambda + \mu)} \\ G &= \mu. \end{aligned} \quad (\text{E.10})$$

In the current investigation the only body forces present are due to gravity; since the dynamic solution of interest vibrates about the equilibrium position the effect of gravity can be neglected thus  $\mathbf{f}$  is set to zero. The wave equation can be solved using Lamé's potentials in cylindrical coordinates which describe the field transformation

$$\mathbf{u} = \nabla\phi + \nabla \times \mathbf{H} \quad (\text{E.11})$$

and

$$\nabla \times \mathbf{H} = F(\mathbf{r}, t) \quad (\text{E.12})$$

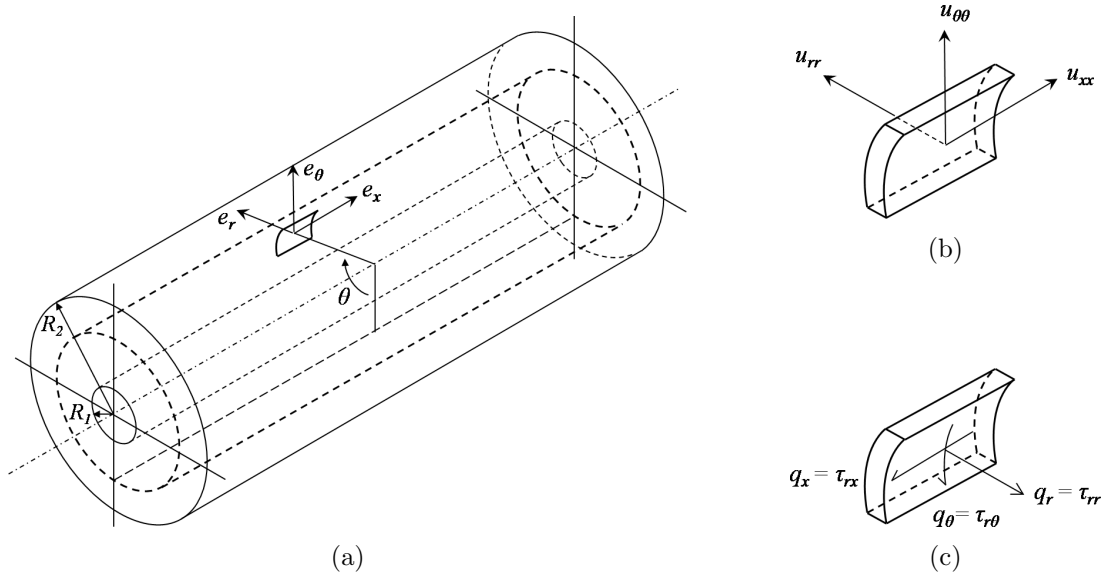


Figure E.3: Coordinate system for three-dimensional elastic continuum in cylindrical coordinates showing (a) the principle directions for a typical element, (b) the corresponding displacement components and (c) the corresponding surface stress components.

where  $F$  is an arbitrary scalar function and  $\mathbf{r}$  is the position vector  $(r, \theta, z)$ . The coordinate directions used to describe  $\mathbf{r}$ , with the corresponding displacement and stress directions, are given in Figure E.3.

The potentials satisfy the wave equation (E.9) if

$$\nabla^2 \phi = \frac{1}{c_1^2} \frac{\partial^2 \phi}{\partial t^2} \quad (\text{E.13})$$

and

$$\nabla^2 \mathbf{H} = \frac{1}{c_2^2} \frac{\partial^2 \mathbf{H}}{\partial t^2} \quad (\text{E.14})$$

where  $c_1 = \sqrt{(\lambda + 2\mu)/\rho}$  is the pressure wave speed of the medium and  $c_2 = \sqrt{\mu/\rho}$  is the shear wave speed of the medium. The potentials are assumed to be harmonic and

separable in the three space variables as follows

$$\begin{aligned}
 \phi &= f \cdot \cos n\theta \cdot e^{i(\omega t + \xi x)} \\
 H_r &= g_r \cdot \sin n\theta \cdot e^{i(\omega t + \xi x)} \\
 H_\theta &= g_\theta \cdot \cos n\theta \cdot e^{i(\omega t + \xi x)} \\
 H_x &= g_x \cdot \sin n\theta \cdot e^{i(\omega t + \xi x)}
 \end{aligned} \tag{E.15}$$

where  $f$  and  $g$  are functions of  $r$ ,  $\omega$ ,  $\xi$  and  $n$ . Substituting equation E.15 into E.13 and E.14 results in

$$\begin{aligned}
 r^2 f'' + r f' - \left[ \left( \xi^2 - \frac{\omega^2}{c_1^2} \right) r^2 + n^2 \right] f &= 0 \\
 r^2 g_x'' + r g_x' - \left[ \left( \xi^2 - \frac{\omega^2}{c_2^2} \right) r^2 + n^2 \right] g_x &= 0 \\
 r^2 g_\theta'' + r g_\theta' - \left[ \left( \xi^2 - \frac{\omega^2}{c_2^2} \right) r^2 + n^2 + 1 \right] g_\theta + 2n g_r &= 0 \\
 r^2 g_r'' + r g_r' - \left[ \left( \xi^2 - \frac{\omega^2}{c_2^2} \right) r^2 + n^2 + 1 \right] g_r + 2n g_\theta &= 0.
 \end{aligned} \tag{E.16}$$

The first two equations of E.16 are modified Bessel equations of order  $n$ . To solve the last two equations Forrest makes use of the arbitrary scalar function in equation E.12 by setting  $g_r = -g_\theta$ , which results in a modified Bessel equation of order  $(n + 1)$

$$r^2 g_r'' + r g_r' - \left[ \left( \xi^2 - \frac{\omega^2}{c_2^2} \right) r^2 + (n + 1)^2 \right] g_r = 0. \tag{E.17}$$

For more information regarding this derivation refer to Forrest<sup>[33]</sup>, Gazis<sup>[43]</sup>, or Morse and Feshbach<sup>[104]</sup>.

Thus, the solutions to  $f$ ,  $g_x$ ,  $g_\theta$  and  $g_r$  can be determined from equations E.16 and

E.17 as

$$\begin{aligned}
 f &= AI_n(\alpha r) + BK_n(\alpha r) \\
 g_x &= A_x I_n(\beta r) + B_x K_n(\beta r) \\
 g_r &= A_r I_{n+1}(\beta r) + B_r K_{n+1}(\beta r) = -g_\theta
 \end{aligned} \tag{E.18}$$

where  $\alpha^2 = (\xi^2 - \omega^2/c_1^2)$  and  $\beta^2 = (\xi^2 - \omega^2/c_2^2)$ , and  $I_n$  and  $K_n$  are modified Bessel functions of the first and second kinds of order  $n$ , respectively. The coefficients  $A$ ,  $B$ ,  $A_x$ ,  $B_x$ ,  $A_r$ ,  $B_r$  are to be determined from the boundary conditions.

Substituting equation E.15 into equation E.11 and using Hooke's laws of general stress-strain relations<sup>[148]</sup> the harmonic solutions for the displacement vector  $\mathbf{u}$  and stress vector  $\boldsymbol{\tau}$  can be written as follows

$$\begin{aligned}
 \mathbf{u} &= \begin{Bmatrix} u_{xx} \\ u_{\theta\theta} \\ u_{rr} \end{Bmatrix} = [\mathbf{S}] \cdot [\tilde{\mathbf{U}}] \cdot \mathbf{C}e^{i(\omega t + \xi x)} \\
 \boldsymbol{\tau} &= \begin{Bmatrix} \tau_{rx} \\ \tau_{r\theta} \\ \tau_{rr} \\ \tau_{\theta\theta} \\ \tau_{\theta x} \\ \tau_{xx} \end{Bmatrix} = \begin{bmatrix} \mathbf{S} & \mathbf{0} \\ \mathbf{0} & \mathbf{S} \end{bmatrix} \cdot [\tilde{\mathbf{T}}] \cdot \mathbf{C}e^{i(\omega t + \xi x)}
 \end{aligned} \tag{E.19}$$

where

$$[\mathbf{S}] = \begin{bmatrix} \cos n\theta & 0 & 0 \\ 0 & \sin n\theta & 0 \\ 0 & 0 & \cos n\theta \end{bmatrix} \quad (\text{E.20})$$

$$\mathbf{C} = \left\{ A \ B \ A_x \ B_x \ A_r \ B_r \right\}^T$$

The coefficients for the  $3 \times 6$  matrix  $[\tilde{\mathbf{U}}]$  and  $6 \times 6$  matrix  $[\tilde{\mathbf{T}}]$  are given at the end of this section.

The displacements and surface stresses of the elastic continuum can be written in the wavenumber-frequency domain in a similar way to the shell results (E.6)

$$\begin{Bmatrix} \tilde{U}_{xxn} \\ \tilde{U}_{\theta\theta n} \\ \tilde{U}_{rrn} \end{Bmatrix} = [\tilde{\mathbf{U}}] \cdot \mathbf{C} \quad \text{and} \quad \begin{Bmatrix} \tilde{T}_{rxn} \\ \tilde{T}_{r\theta n} \\ \tilde{T}_{rrn} \end{Bmatrix} = [\tilde{\mathbf{T}}_r] \cdot \mathbf{C} \quad (\text{E.21})$$

where the  $3 \times 6$  matrix  $[\tilde{\mathbf{T}}_r]$  is the top half of the  $6 \times 6$  matrix  $[\tilde{\mathbf{T}}]$  in E.19.

$$u_{11} = i\xi I_n(\alpha r)$$

$$u_{12} = i\xi K_n(\alpha r)$$

$$u_{13} = -\beta I_n(\beta r)$$

$$u_{14} = \beta K_n(\beta r)$$

$$u_{15} = 0$$

$$u_{16} = 0$$

$$u_{21} = -\frac{n}{r} I_n(\alpha r)$$

$$u_{22} = -\frac{n}{r} K_n(\alpha r)$$

$$u_{23} = i\xi I_{n+1}(\beta r)$$

$$u_{24} = i\xi K_{n+1}(\beta r)$$

$$u_{25} = -\frac{n}{r} I_n(\beta r) - \beta I_{n+1}(\beta r)$$

$$u_{26} = -\frac{n}{r} K_n(\beta r) + \beta K_{n+1}(\beta r)$$

$$u_{31} = \frac{n}{r} I_n(\alpha r) + \alpha I_{n+1}(\alpha r)$$

$$u_{32} = \frac{n}{r} K_n(\alpha r) - \alpha K_{n+1}(\alpha r)$$

$$u_{33} = i\xi I_{n+1}(\beta r)$$

$$u_{34} = i\xi K_{n+1}(\beta r)$$

$$u_{35} = \frac{n}{r} I_n(\beta r)$$

$$u_{36} = \frac{n}{r} K_n(\beta r)$$

$$t_{11} = 2\mu i \xi \frac{n}{r} I_n(\alpha r) + 2\mu i \xi \alpha I_{n+1}(\alpha r)$$

$$t_{12} = 2\mu i \xi \frac{n}{r} K_n(\alpha r) - 2\mu i \xi \alpha K_{n+1}(\alpha r)$$

$$t_{13} = -\mu \frac{n}{r} \beta I_n(\beta r) - \mu(\xi^2 + \beta^2) I_{n+1}(\beta r)$$

$$t_{14} = \mu \frac{n}{r} \beta K_n(\beta r) - \mu(\xi^2 + \beta^2) K_{n+1}(\beta r)$$

$$t_{15} = \mu i \xi \frac{n}{r} I_n(\beta r)$$

$$t_{16} = \mu i \xi \frac{n}{r} K_n(\beta r)$$

$$t_{21} = -2\mu \frac{(n^2 - n)}{r^2} I_n(\alpha r) - 2\mu \frac{n}{r} \alpha I_{n+1}(\alpha r)$$

$$t_{22} = -2\mu \frac{(n^2 - n)}{r^2} K_n(\alpha r) + 2\mu \frac{n}{r} \alpha K_{n+1}(\alpha r)$$

$$t_{23} = \mu i \xi \beta I_n(\beta r) - 2\mu i \xi \frac{(n+1)}{r} I_{n+1}(\beta r)$$

$$t_{24} = -\mu i \xi \beta K_n(\beta r) - 2\mu i \xi \frac{(n+1)}{r} K_{n+1}(\beta r)$$

$$t_{25} = \left( -2\mu \frac{(n^2 - n)}{r^2} - \mu \beta^2 \right) I_n(\beta r) + 2\mu \frac{\beta}{r} I_{n+1}(\beta r)$$

$$t_{26} = \left( -2\mu \frac{(n^2 - n)}{r^2} - \mu \beta^2 \right) K_n(\beta r) - 2\mu \frac{\beta}{r} K_{n+1}(\beta r)$$

$$t_{31} = \left( 2\mu \frac{(n^2 - n)}{r^2} - \lambda \xi^2 + (\lambda + 2\mu) \alpha^2 \right) I_n(\alpha r) - 2\mu \frac{\alpha}{r} I_{n+1}(\alpha r)$$

$$t_{32} = \left( 2\mu \frac{(n^2 - n)}{r^2} - \lambda \xi^2 + (\lambda + 2\mu) \alpha^2 \right) K_n(\alpha r) + 2\mu \frac{\alpha}{r} K_{n+1}(\alpha r)$$

$$t_{33} = 2\mu i \xi \beta I_n(\beta r) - 2\mu i \xi \frac{(n+1)}{r} I_{n+1}(\beta r)$$

$$t_{34} = -2\mu i \xi \beta K_n(\beta r) - 2\mu i \xi \frac{(n+1)}{r} K_{n+1}(\beta r)$$

$$t_{35} = 2\mu \frac{(n^2 - n)}{r^2} I_n(\beta r) + 2\mu \frac{n}{r} \beta I_{n+1}(\beta r)$$

$$t_{36} = 2\mu \frac{(n^2 - n)}{r^2} K_n(\beta r) - 2\mu \frac{n}{r} \beta K_{n+1}(\beta r)$$

$$t_{41} = \left( -2\mu \frac{(n^2 - n)}{r^2} + \lambda(\alpha^2 - \xi^2) \right) I_n(\alpha r) + 2\mu \frac{\alpha}{r} I_{n+1}(\alpha r)$$

$$t_{42} = \left( -2\mu \frac{(n^2 - n)}{r^2} + \lambda(\alpha^2 - \xi^2) \right) K_n(\alpha r) - 2\mu \frac{\alpha}{r} K_{n+1}(\alpha r)$$

$$t_{43} = 2\mu i \xi \frac{(n+1)}{r} I_{n+1}(\beta r)$$

$$t_{44} = 2\mu i \xi \frac{(n+1)}{r} K_{n+1}(\beta r)$$

$$t_{45} = -2\mu \frac{(n^2 - n)}{r^2} I_n(\beta r) - 2\mu \frac{n}{r} \beta I_{n+1}(\beta r)$$

$$t_{46} = -2\mu \frac{(n^2 - n)}{r^2} K_n(\beta r) + 2\mu \frac{n}{r} \beta K_{n+1}(\beta r)$$

$$t_{51} = -2\mu i \xi \frac{n}{r} I_n(\alpha r)$$

$$t_{52} = -2\mu i \xi \frac{n}{r} K_n(\alpha r)$$

$$t_{53} = \mu \frac{n}{r} \beta I_n(\beta r) - \mu \xi^2 I_{n+1}(\beta r)$$

$$t_{54} = -\mu \frac{n}{r} \beta K_n(\beta r) - \mu \xi^2 K_{n+1}(\beta r)$$

$$t_{55} = -\mu i \xi \frac{n}{r} I_n(\beta r) - \mu i \xi \beta I_{n+1}(\beta r)$$

$$t_{56} = -\mu i \xi \frac{n}{r} K_n(\beta r) + \mu i \xi \beta K_{n+1}(\beta r)$$

$$t_{61} = (\lambda \alpha^2 - (\lambda + 2\mu) \xi^2) I_n(\alpha r)$$

$$t_{62} = (\lambda \alpha^2 - (\lambda + 2\mu) \xi^2) K_n(\alpha r)$$

$$t_{63} = -2\mu i \xi \beta I_n(\beta r)$$

$$t_{64} = 2\mu i \xi \beta K_n(\beta r)$$

$$t_{65} = 0$$

$$t_{66} = 0$$

### E.3 The Coupled Tunnel-Soil Equations

The coupling of the thin-walled tunnel to the thick-walled soil require three sets of boundary conditions to be satisfied:

1. The stresses on the thin-shell are equal to the summation of the applied loading plus the reactionary stressed developed at the interface between the tunnel and soil (stress equilibrium)
2. The displacements of the tunnel shell and soil continuum must be equivalent at the interface (displacement compatibility)
3. The displacements of the soil continuum must decay to zero as the radius from the center of the tunnel approaches infinity (radiation condition)

Consider the third condition. Recall from E.21 that the displacement and stress components of the continuum are expressed in terms of modified Bessel functions (e.g.  $I_n$  and  $K_n$ ). Only the modified Bessel function of the second kind  $K$  decays for all arguments as  $r$  approaches infinity, thus all coefficients in E.21 associated with modified Bessel functions of the first kind  $I$  must be set to zero to satisfy the radiation condition

$$A = A_r = A_x = 0 \tag{E.22}$$

$$\Rightarrow \mathbf{C} = \{0 \ B \ 0 \ B_x \ 0 \ B_r\}^T$$

Therefore the displacements and stresses in a thick-shell continuum with infinite outer radius can be written as follows (note the coordinate system of the tunnel shell is adopted to simplify the coupling of the two systems)

$$\begin{Bmatrix} \tilde{U}_{xn} \\ \tilde{U}_{\theta n} \\ \tilde{U}_{rn} \end{Bmatrix} = \begin{Bmatrix} \tilde{U}_{xxn} \\ \tilde{U}_{\theta\theta n} \\ -\tilde{U}_{rrn} \end{Bmatrix} = \begin{bmatrix} u_{12} & u_{14} & u_{16} \\ u_{22} & u_{24} & u_{26} \\ -u_{32} & -u_{34} & -u_{36} \end{bmatrix} \begin{Bmatrix} B \\ B_x \\ B_r \end{Bmatrix} = [\tilde{\mathbf{U}}_\infty]_{r=r_1} \cdot \mathbf{B} \tag{E.23}$$

and

$$\begin{Bmatrix} \tilde{T}_{xn} \\ \tilde{T}_{\theta n} \\ \tilde{T}_{rn} \end{Bmatrix} = \begin{Bmatrix} -\tilde{T}_{rxn} \\ -\tilde{T}_{r\theta n} \\ \tilde{T}_{rrn} \end{Bmatrix} = \begin{bmatrix} -t_{12} & -t_{14} & -t_{16} \\ -t_{22} & -t_{24} & -t_{26} \\ t_{32} & t_{34} & t_{36} \end{bmatrix} \begin{Bmatrix} B \\ B_x \\ B_r \end{Bmatrix} = [\tilde{\mathbf{T}}_\infty]_{r=r_1} \cdot \mathbf{B} \quad (\text{E.24})$$

Combining Equations E.23 and E.24 allows the relationship to be written in standard form

$$\tilde{\mathbf{U}}_n = \tilde{\mathbf{H}}_{\text{soil}} \tilde{\mathbf{T}}_n \quad (\text{E.25a})$$

where

$$\tilde{\mathbf{H}}_{\text{soil}} = [\tilde{\mathbf{U}}_\infty]_{r=r_1} [\tilde{\mathbf{T}}_\infty]_{r=r_1}^{-1} \quad (\text{E.25b})$$

It should be noted that if the applied loading is anti-symmetric about  $\theta = 0$  (e.g. circumferential loading) coefficients 12, 13, 21, 32 and 33 of  $\tilde{\mathbf{U}}_\infty$  and  $\tilde{\mathbf{T}}_\infty$  must be multiplied by  $-1$ <sup>[61]</sup>.

Finally, combining the remaining boundary conditions and the equations of motion for the tunnel shell (E.8) and soil continuum (E.25), the coupled tunnel-soil equations to be written as follows

$$\tilde{\mathbf{U}}_n = \left( \mathbf{I} + \tilde{\mathbf{H}}_{\text{tunnel}} \tilde{\mathbf{H}}_{\text{soil}}^{-1} \right)^{-1} \tilde{\mathbf{H}}_{\text{tunnel}} \tilde{\mathbf{F}}_n \quad (\text{E.26})$$

where  $\tilde{\mathbf{F}}_n$  is the applied loading vector to the inside surface of the tunnel and  $\tilde{\mathbf{U}}_n$  is the displacement vector at the interface between the shell and continuum.

The transfer function at any radius  $R$  in the soil can be calculated simply by deriving  $[\tilde{\mathbf{U}}_\infty]$  at  $r = R$  resulting in

$$\tilde{\mathbf{U}}_{nR} = \tilde{\mathbf{H}}_{\text{soil}R} \tilde{\mathbf{T}}_n \quad (\text{E.27a})$$

where

$$\tilde{\mathbf{H}}_{\text{soil}R} = [\tilde{\mathbf{U}}_\infty]_{r=R} [\tilde{\mathbf{T}}_\infty]_{r=r_1}^{-1} \quad (\text{E.27b})$$



# Appendix F

## The PiP Derivation in 2D

### Plane-Strain

A problem can be considered plane-strain if it involves a long, prismatic body loaded by forces that are perpendicular to the longitudinal direction and do not vary along the length; under these conditions it may be assumed that all cross sections will experience the same conditions<sup>[148]</sup>. For a line-load acting in the PiP model the displacement components  $u_\theta$  and  $u_r$  are functions of  $\theta$  and  $r$  but are independent of the longitudinal coordinate  $x$ . Since the longitudinal displacement  $u_x$  is zero it follows that the strains normal to the  $\theta - r$  plane are zero (i.e.  $\varepsilon_{xx} = \varepsilon_{\theta x} = \varepsilon_{rx} = 0$ ) and shear stresses associated with the longitudinal direction are also zero (i.e.  $\tau_{x\theta} = \tau_{xr} = 0$ ). This 2D stress-strain state can be determined from the three-dimensional shell and continuum equations outlined in Sections E.1 and E.2 by simply setting the wavenumber  $\xi = 0$ . This is confirmed through comparison with the equations derived by Gazis<sup>[42]</sup> for plane-strain response of thick-walled shells.

## F.1 Thin-shell and Continuum Equations in 2D Plane-Strain

Converting the three-dimensional cylindrical shell equations E.4 to E.7 into plane-strain results in stress and displacement vectors

$$\begin{aligned} q_\theta &= Q_{\theta n} \cdot \sin n\theta \cdot e^{i\omega t} \\ q_r &= Q_{rn} \cdot \cos n\theta \cdot e^{i\omega t}. \end{aligned} \quad (\text{F.1})$$

and

$$\begin{aligned} u_\theta &= U_{\theta n} \cdot \sin n\theta \cdot e^{i\omega t} \\ u_r &= U_{rn} \cdot \cos n\theta \cdot e^{i\omega t}. \end{aligned} \quad (\text{F.2})$$

Notice the tildes have been omitted since the equations do not depend on the wavenumber  $\xi$ . The relationship between stress and displacement in plane-strain is given below

$$[\mathbf{A}]^{PS} \begin{Bmatrix} U_{\theta n} \\ U_{rn} \end{Bmatrix} = \frac{-a(1-\nu^2)}{Eh} \begin{Bmatrix} Q_{\theta n} \\ Q_{rn} \end{Bmatrix} \quad (\text{F.3})$$

where the elements of the  $2 \times 2$   $[\mathbf{A}]^{PS}$  matrix are calculated as follows

$$\begin{aligned} a_{11}^{PS} &= \frac{\rho a(1-\nu^2)}{E} \omega^2 - \frac{1}{a} n^2 \\ a_{12}^{PS} &= \frac{1}{a} n \\ a_{21}^{PS} &= \frac{1}{a} n \\ a_{22}^{PS} &= \frac{\rho a(1-\nu^2)}{E} \omega^2 - \frac{1}{a} - \frac{h^2}{12a^3} (n^4 + 2n^2 - 1). \end{aligned} \quad (\text{F.4})$$

Similarly the three-dimensional continuum equations can be converted into plane-

strain as follows

$$\mathbf{u} = \begin{Bmatrix} u_{\theta\theta} \\ u_{rr} \end{Bmatrix} = [\mathbf{S}] \cdot [\mathbf{U}]^{PS} \cdot \mathbf{C}e^{i\omega t}$$

$$\boldsymbol{\tau} = \begin{Bmatrix} \tau_{r\theta} \\ \tau_{rr} \\ \tau_{\theta\theta} \\ \tau_{xx} \end{Bmatrix} = \begin{bmatrix} \mathbf{S} & \mathbf{0} \\ \mathbf{0} & \mathbf{S} \end{bmatrix} \cdot [\mathbf{T}]^{PS} \cdot \mathbf{C}e^{i\omega t} \quad (\text{F.5})$$

where

$$[\mathbf{S}] = \begin{bmatrix} \sin n\theta & 0 \\ 0 & \cos n\theta \end{bmatrix}$$

$$\mathbf{C} = \left\{ A \ B \ A_r \ B_r \right\}^T. \quad (\text{F.6})$$

The coefficients for the  $2 \times 4$  matrix  $[\mathbf{U}]^{PS}$  and  $4 \times 4$  matrix  $[\mathbf{T}]^{PS}$  are given at the end of this section.

As before, the displacements and surface stresses of the elastic continuum can be written in the wavenumber-frequency domain in a similar way to the shell results (F.3)

$$\begin{Bmatrix} \tilde{U}_{xxn} \\ \tilde{U}_{\theta\theta n} \\ \tilde{U}_{rrn} \end{Bmatrix} = [\tilde{\mathbf{U}}] \cdot \mathbf{C} \quad \text{and} \quad \begin{Bmatrix} \tilde{T}_{rxn} \\ \tilde{T}_{r\theta n} \\ \tilde{T}_{rrn} \end{Bmatrix} = [\tilde{\mathbf{T}}_r] \cdot \mathbf{C} \quad (\text{F.7})$$

where the  $3 \times 6$  matrix  $[\tilde{\mathbf{T}}_r]^{PS}$  is the top half of the  $6 \times 6$  matrix  $[\tilde{\mathbf{T}}]^{PS}$  in F.5.

$$u_{11}^{PS} = -\frac{n}{r}I_n(\alpha r)$$

$$u_{12}^{PS} = -\frac{n}{r}K_n(\alpha r)$$

$$u_{13}^{PS} = -\frac{n}{r}I_n(\beta r) - \beta I_{n+1}(\beta r)$$

$$u_{14}^{PS} = -\frac{n}{r}K_n(\beta r) + \beta K_{n+1}(\beta r)$$

$$u_{21}^{PS} = \frac{n}{r}I_n(\alpha r) + \alpha I_{n+1}(\alpha r)$$

$$u_{22}^{PS} = \frac{n}{r}K_n(\alpha r) - \alpha K_{n+1}(\alpha r)$$

$$u_{23}^{PS} = \frac{n}{r}I_n(\beta r)$$

$$u_{24}^{PS} = \frac{n}{r}K_n(\beta r)$$

$$t_{11}^{PS} = -2\mu \frac{(n^2 - n)}{r^2} I_n(\alpha r) - 2\mu \frac{n}{r} \alpha I_{n+1}(\alpha r)$$

$$t_{12}^{PS} = -2\mu \frac{(n^2 - n)}{r^2} K_n(\alpha r) + 2\mu \frac{n}{r} \alpha K_{n+1}(\alpha r)$$

$$t_{13}^{PS} = \left( -2\mu \frac{(n^2 - n)}{r^2} - \mu \beta^2 \right) I_n(\beta r) + 2\mu \frac{\beta}{r} I_{n+1}(\beta r)$$

$$t_{14}^{PS} = \left( -2\mu \frac{(n^2 - n)}{r^2} - \mu \beta^2 \right) K_n(\beta r) - 2\mu \frac{\beta}{r} K_{n+1}(\beta r)$$

$$t_{21}^{PS} = \left( 2\mu \frac{(n^2 - n)}{r^2} + (\lambda + 2\mu) \alpha^2 \right) I_n(\alpha r) - 2\mu \frac{\alpha}{r} I_{n+1}(\alpha r)$$

$$t_{22}^{PS} = \left( 2\mu \frac{(n^2 - n)}{r^2} + (\lambda + 2\mu) \alpha^2 \right) K_n(\alpha r) + 2\mu \frac{\alpha}{r} K_{n+1}(\alpha r)$$

$$t_{23}^{PS} = 2\mu \frac{(n^2 - n)}{r^2} I_n(\beta r) + 2\mu \frac{n}{r} \beta I_{n+1}(\beta r)$$

$$t_{24}^{PS} = 2\mu \frac{(n^2 - n)}{r^2} K_n(\beta r) - 2\mu \frac{n}{r} \beta K_{n+1}(\beta r)$$

$$t_{31}^{PS} = \left( -2\mu \frac{(n^2 - n)}{r^2} + \lambda \alpha^2 \right) I_n(\alpha r) + 2\mu \frac{\alpha}{r} I_{n+1}(\alpha r)$$

$$t_{32}^{PS} = \left( -2\mu \frac{(n^2 - n)}{r^2} + \lambda \alpha^2 \right) K_n(\alpha r) - 2\mu \frac{\alpha}{r} K_{n+1}(\alpha r)$$

$$t_{33}^{PS} = -2\mu \frac{(n^2 - n)}{r^2} I_n(\beta r) - 2\mu \frac{n}{r} \beta I_{n+1}(\beta r)$$

$$t_{34}^{PS} = -2\mu \frac{(n^2 - n)}{r^2} K_n(\beta r) + 2\mu \frac{n}{r} \beta K_{n+1}(\beta r)$$

$$t_{41}^{PS} = \lambda \alpha^2 I_n(\alpha r)$$

$$t_{42}^{PS} = \lambda \alpha^2 K_n(\alpha r)$$

$$t_{43}^{PS} = 0$$

$$t_{44}^{PS} = 0$$

### F.1.1 The Coupled Tunnel-Soil Equations in 2D Plane-Strain

Applying the boundary conditions outlined in Section E.3 for stress equilibrium, displacement compatibility and the radiation condition results in

$$A = A_r = 0 \quad (F.8)$$

$$\Rightarrow \mathbf{C} = \{0 \quad B \quad 0 \quad B_r\}^T$$

Therefore the displacements and stresses in a plane-strain, thick-shell continuum with infinite outer radius can be written as follows (note the coordinate system of the tunnel shell is adopted to simplify the coupling of the two systems)

$$\begin{Bmatrix} \tilde{U}_{\theta n} \\ \tilde{U}_{rn} \end{Bmatrix} = \begin{Bmatrix} \tilde{U}_{\theta\theta n} \\ -\tilde{U}_{rrn} \end{Bmatrix} = \begin{bmatrix} u_{22} & u_{26} \\ -u_{32} & -u_{36} \end{bmatrix} \begin{Bmatrix} B \\ B_r \end{Bmatrix} = \left[ \tilde{\mathbf{U}}_{\infty} \right]_{r=r_1}^{PS} \cdot \mathbf{C} \quad (F.9)$$

and

$$\begin{Bmatrix} \tilde{T}_{\theta n} \\ \tilde{T}_{rn} \end{Bmatrix} = \begin{Bmatrix} -\tilde{T}_{r\theta n} \\ \tilde{T}_{rrn} \end{Bmatrix} = \begin{bmatrix} -t_{22} & -t_{26} \\ t_{32} & t_{36} \end{bmatrix} \begin{Bmatrix} B \\ B_r \end{Bmatrix} = \left[ \tilde{\mathbf{T}}_{\infty} \right]_{r=r_1}^{PS} \cdot \mathbf{C} \quad (F.10)$$

where the superscript PS signifies plane-strain. Finally the coupled tunnel-soil equations to be written as follows

$$\left[ \frac{-Eh}{a(1-\nu^2)} \left[ \tilde{\mathbf{A}} \right]^{PS} + \left[ \tilde{\mathbf{T}}_{\infty} \right]_{r=r_1}^{PS} \left( \left[ \tilde{\mathbf{U}}_{\infty} \right]_{r=r_1}^{PS} \right)^{-1} \right] \begin{Bmatrix} \tilde{U}_{\theta n} \\ \tilde{U}_{rn} \end{Bmatrix} = \begin{Bmatrix} \tilde{F}_{\theta n} \\ \tilde{F}_{rn} \end{Bmatrix} \quad (F.11)$$

where  $\tilde{\mathbf{F}}_n$  is the applied loading vector and  $\tilde{\mathbf{U}}_n$  is the displacement vector at the interface between the shell and continuum.

# Appendix G

## Equivalent internal source method in plane-strain

The equivalent internal source method (EIS) in plane-strain uses discrete line loads in a fullspace to reproduce the soil loading predicted by the standard pipe-in-pipe model subjected to an internal line load; this is shown schematically in Figure G.1. See Appendix F for more information on the plane-strain PiP method. Hussein<sup>[61]</sup> shows that the discrete line loads should be arranged in a circle whose radius  $r_{EIS}$  is smaller than that of the tunnel  $r_1$ .

Recall the standard pipe-in-pipe derivation in plain strain for a tunnel of outer radius  $r_1$  and thickness  $h$

$$\frac{-Eh}{(r_1)(1-\nu^2)}[\mathbf{A}]^{PS} \begin{Bmatrix} U_{\theta n} \\ U_{rn} \end{Bmatrix} = \begin{Bmatrix} Q_{\theta n} \\ Q_{rn} \end{Bmatrix} \quad (\text{G.1})$$

or

$$[\mathbf{A}_1]^{PS} \begin{Bmatrix} U_{\theta n} \\ U_{rn} \end{Bmatrix}_{tunnel} = \begin{Bmatrix} Q_{\theta n} \\ Q_{rn} \end{Bmatrix}_{tunnel} \quad (\text{G.2})$$

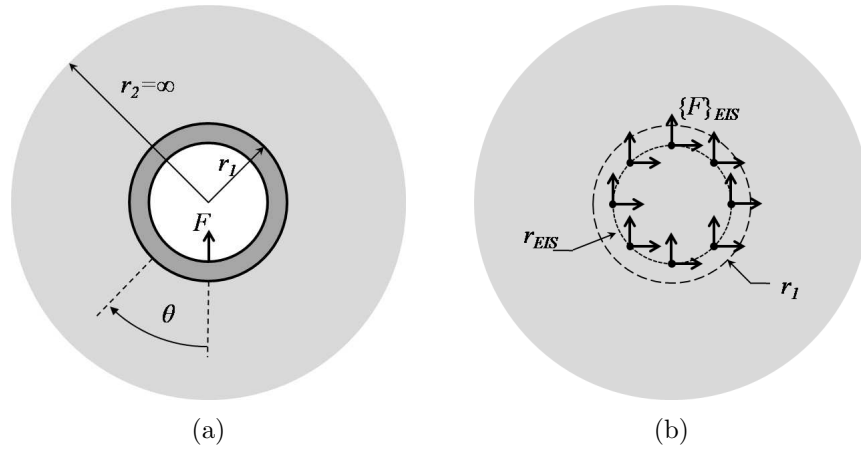


Figure G.1: Schematic of the PiP arrangement (left) and equivalent internal source arrangement (right) to simulate a tunnel buried in a fullspace under plane-strain loading.

and for the soil with inner radius  $r_1$

$$\begin{Bmatrix} U_{\theta\theta n} \\ U_{rrn} \end{Bmatrix}_{soil} = [\mathbf{U}_\infty]_{r_1}^{PS} \cdot \mathbf{C} \quad (\text{G.3})$$

$$\begin{Bmatrix} T_{r\theta n} \\ T_{rrn} \end{Bmatrix}_{soil} = [\mathbf{T}_\infty]_{r_1}^{PS} \cdot \mathbf{C}. \quad (\text{G.4})$$

The superscript  $PS$  signifying these are plane-strain derivations will be omitted for clarity throughout the remainder of this section.

Enforcing continuity and equilibrium at the interface between the tunnel and soil results in the coupled equation

$$([\mathbf{A}_1] + [\mathbf{T}_\infty]_{r_1} [\mathbf{U}_\infty]_{r_1}^{-1}) \mathbf{U}_n = \mathbf{F}_n \quad (\text{G.5})$$

where  $\mathbf{F}_n = \{0 \quad f_n\}^T$  is a line load acting on the bottom of the tunnel invert. The value of this line load is determined using delta function form<sup>[33] [61]</sup> and can be decomposed

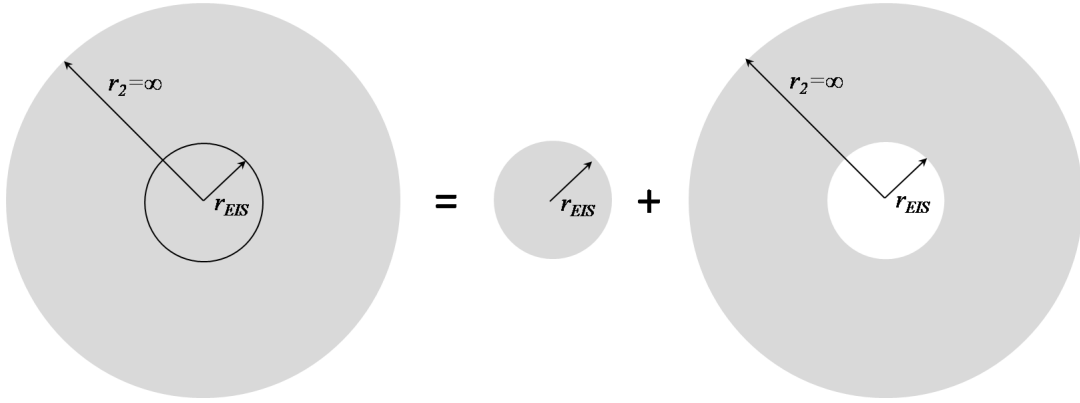


Figure G.2: The core-in-pipe arrangement: a solid core of radius  $r_{EIS}$  coupled to the inside of a hollow cylinder with inner radius  $r_{EIS}$  and infinite outer radius; this arrangement simulates a fullspace.

into a Fourier series around a cylinder of radius  $r_1$  as

$$\frac{\delta(\theta)}{r_1} e^{i\omega t} = \sum_{n=0}^{\infty} f_n \cos(n\theta) \cdot e^{i\omega t} \quad (\text{G.6})$$

where  $f_0 = \frac{1}{2\pi r_1}$ ,  $f_n = \frac{1}{\pi r_1}$  for  $n \geq 1$ , and  $\theta$  measured as shown in Figure G.1.

## G.1 Fullspace core-in-pipe model

Consider now a fullspace modeled using the pipe-in-pipe arrangement: a solid inner cylinder with outer radius  $r_{EIS}$  coupled to an outer pipe with infinite outer radius and inner radius  $r_{EIS}$  as detailed in Figure G.2. Both the inner cylinder (core) and outer cylinder (soil) are given the same soil properties.

The equations of motion G.3 and G.4 are used for the outer pipe with  $r = r_{EIS}$

$$\left\{ \begin{array}{c} U_{\theta\theta n} \\ U_{rrn} \end{array} \right\}_{r_{EIS}} = [\mathbf{U}_{\infty}]_{r_{EIS}} \cdot \mathbf{C} \quad (\text{G.7})$$

$$\left\{ \begin{array}{c} T_{r\theta n} \\ T_{rrn} \end{array} \right\}_{r_{EIS}} = [\mathbf{T}_{\infty}]_{r_{EIS}} \cdot \mathbf{C}. \quad (\text{G.8})$$

The equations of motion for the core can be written in a similar form

$$\begin{Bmatrix} U_{\theta\theta n} \\ U_{rrn} \end{Bmatrix}_{r_{EIS}} = [\mathbf{U}_0]_{r_{EIS}} \cdot \mathbf{B} \quad (\text{G.9})$$

$$\begin{Bmatrix} T_{r\theta n} \\ T_{rrn} \end{Bmatrix}_{r_{EIS}} = [\mathbf{T}_0]_{r_{EIS}} \cdot \mathbf{B}. \quad (\text{G.10})$$

where the elements of  $[\mathbf{U}_0]_{r_{EIS}}$  and  $[\mathbf{T}_0]_{r_{EIS}}$  are calculated as in Appendix F in conjunction with a new boundary condition:

- the displacements of the soil continuum of the core must be finite as the radius of the cylinder approaches zero (boundedness condition).

Note that the modified Bessel functions of the second kind ( $K_n$ ) tend to infinity at zero arguments (i.e.  $r = 0$ ), therefore all coefficients associated with these functions must be set to zero to satisfy the boundedness condition.

For simplicity in coupling the core and pipe systems, the displacements and stresses of the continuum core are written in the coordinate system of the tunnel shell. Recall from Figure E.3(c) that the stress directions are defined from the outward normal direction. Since the outward normal of the core at the coupling interface is the opposite direction to that of the pipe, the stress vector must be multiplied by  $-1$ .

$$\begin{Bmatrix} U_{\theta n} \\ U_{rn} \end{Bmatrix} = \begin{Bmatrix} U_{\theta\theta n} \\ -U_{rrn} \end{Bmatrix} = \begin{bmatrix} u_{21} & u_{25} \\ -u_{31} & -u_{35} \end{bmatrix} \begin{Bmatrix} A \\ A_r \end{Bmatrix} = [\mathbf{U}_0]_{r_{EIS}} \cdot \mathbf{B} \quad (\text{G.11})$$

and

$$\begin{Bmatrix} T_{\theta n} \\ T_{rn} \end{Bmatrix} = \begin{Bmatrix} T_{r\theta n} \\ -T_{rrn} \end{Bmatrix} = \begin{bmatrix} t_{21} & t_{25} \\ -t_{31} & -t_{35} \end{bmatrix} \begin{Bmatrix} A \\ A_r \end{Bmatrix} = [\mathbf{T}_0]_{r_{EIS}} \cdot \mathbf{B}. \quad (\text{G.12})$$

Imposing displacement compatibility and stress equilibrium at the interface between

the core and the pipe results in the following boundary conditions

$$\mathbf{U}_{rEIS}^{core} = \mathbf{U}_{rEIS}^{pipe} \quad (\text{G.13a})$$

and

$$\mathbf{F}_{EIS} = \mathbf{T}_{rEIS}^{pipe} - \mathbf{T}_{rEIS}^{core}. \quad (\text{G.13b})$$

The first boundary condition gives

$$[\mathbf{U}_0]_{rEIS} \cdot \mathbf{B} = [\mathbf{U}_\infty]_{rEIS} \cdot \mathbf{C} \quad (\text{G.14})$$

and the second boundary condition gives

$$\mathbf{F}_{EIS} = [\mathbf{T}_\infty]_{rEIS} \cdot \mathbf{C} - [\mathbf{T}_0]_{rEIS} \cdot \mathbf{B}. \quad (\text{G.15})$$

Solving for  $\mathbf{B}$  in Eq. G.14 and subbing into Eq. G.15 gives

$$\mathbf{F}_{EIS} = ([\mathbf{T}_\infty]_{rEIS} - [\mathbf{T}_0]_{rEIS} [\mathbf{U}_0]_{rEIS}^{-1} [\mathbf{U}_\infty]_{rEIS}) \mathbf{C}. \quad (\text{G.16})$$

The value of  $\mathbf{C}$  can be determined by forcing the displacement at radius  $r_1$  to be equal to that calculated using the PiP formulation given in Eq. G.5 as

$$\mathbf{C} = [\mathbf{U}_\infty]_{r_1}^{-1} [\mathbf{U}_n]^{PiP}. \quad (\text{G.17})$$

Therefore, the final equation giving the EIS vector in terms of the PiP displacement vector at the tunnel-soil interface is

$$\mathbf{F}_{EIS} = ([\mathbf{T}_\infty]_{rEIS} - [\mathbf{T}_0]_{rEIS} [\mathbf{U}_0]_{rEIS}^{-1} [\mathbf{U}_\infty]_{rEIS}) [\mathbf{U}_\infty]_{r_1}^{-1} [\mathbf{U}_n]^{PiP}. \quad (\text{G.18})$$

The  $\mathbf{F}_{EIS}$  vector is in the ring mode domain for a radius of  $r_{EIS}$  (note the subscript

$n$  in Eq. G.18). The cartesian value of a particular force at a discrete location can be determined using a standard inverse Fourier expansion.

# References

- [1] [www-g.eng.cam.ac.uk/convurt](http://www-g.eng.cam.ac.uk/convurt) CONVURT Consortium Homepage (accessed June 2010).
- [2] [www.mottmac.com](http://www.mottmac.com) Mott MacDonald - expert in tunnel planning, design and construction (accessed June 2010).
- [3] *Tunnel vision - the future role of tunnels in transport infrastructure*. Parliamentary office of science and technology, 90, 1997.
- [4] *World Reference Base for Soil Resources*. Food and Agriculture Organization of the United Nations, Rome, 1998.
- [5] L. Andersen and C. Jones. Coupled boundary and finite element analysis of vibration from railway tunnels - a comparison of two- and three-dimensional models. *Journal of Sound and Vibration*, 293:611–625, 2006.
- [6] L. Andersen and S. Nielsen. Boundary element analysis of the steady-state response of an elastic half-space to a moving force on its surface. *Engineering Analysis with Boundary Elements*, 27:23–38, 2003.
- [7] P. Andrade. *Implementation of second-order absorbing boundary conditions in frequency-domain computations*. PhD thesis, University of Texas at Austin, 1999.
- [8] L. Bachelier. Theorie de la speculation. *Annales Scientifiques de l'Ecole Normale Suprieure*, 3:21–86, 1900.
- [9] K.-J. Bathe. *Finite element procedures in engineering analysis*. Prentice-Hall, 1982.
- [10] A. Becker. *The boundary element method in engineering: a complete course*. London, UK, 1992.
- [11] B. Berglund, T. Lindvall, D. Schwela, and G. Kee-Tai. Guidelines for community noise. *World Health Organization*, 2000.

- 
- [12] J. Blanch, H. Robertsson, and W. Symes. *Viscoelastic Finite Difference Modeling*. Computational and Applied Mathematics Department, Rice University, Texas, TR93-04, 1993.
- [13] D. Bland. *The Theory of Linear Viscoelasticity*. Academic Press, New York, 1980.
- [14] B. Budaev and D. Bogy. Rayleigh wave scattering by a wedge. *Wave Motion*, 22:129–257, 1995.
- [15] R. Christensen. *Theory of Viscoelasticity. An Introduction*. Academic Press, New York, 1982.
- [16] D. Clouteau, M. Arnst, T. Al-Hussaini, and G. Degrande. Freefield vibrations due to dynamic loading on a tunnel embedded in a stratified medium. *Journal of Sound and Vibration*, 283:173–199, 2005.
- [17] J. Collins and W. Thompson. The eigenvalue problem for structural systems with statistical properties. *American Institute of Aeronautics and Astronautics Journal*, 73(4):642–648, 1969.
- [18] S. Conte and C. deBoor. *Elementary Numerical Analysis*. McGraw-Hill, New York, 1972.
- [19] C. Costantino. Finite element approach to stress wave problem. *Journal of Engineering Mechanics ASCE*, 93(EM2):153–176, 1967.
- [20] G. Degrande, D. Clouteau, R. Othman, M. Arnst, H. Chebli, R. Klein, P. Chatterjee, and B. Janssens. A numerical model for ground-borne vibrations from underground railway traffic based on a periodic finite element - boundary element formulation. *Journal of Sound and Vibration*, 293:645–666, 2006.
- [21] D. Dinges, F. Pack, K. Williams, K. Gillen, J. Powell, G. Ott, C. Aptowicz, and A. Pack. Cumulative sleepiness, mood disturbance and psychomotor vigilance performance decrements during a week of sleep restricted to 4-5 hours per night. *Sleep*, 20(4):267–277, 1997.
- [22] J. Dominguez. *Boundary elements in dynamics*. Elsevier Applied Science, London, UK, 1993.
- [23] L. Drake. Love and Rayleigh waves in nonhorizontally layered media. *Bulletin of the Seismological Society of America*, 62(5):1241–1258, 1972.

- 
- [24] M. Duarte and M. Filho. Perception threshold of people exposed to sinusoidal vibration. *Proceedings of the Tenth International Congress on Sound and Vibration*, pages 3791–3798, 2003.
- [25] A. Einstein. Investigations on the theory of the brownian movement. *Annalen der Physik*, 17:549, 1915.
- [26] W. Ewing, W. Jardetzky, and F. Press. *Elastic waves in layered media*. McGraw-Hill Education, 1957.
- [27] M. Ferrara and L. De Gennaro. How much sleep do we need? *Sleep Medicine Reviews*, 5(2):155–179, 2001.
- [28] S. Fidell, D. Barber, and T. Schultz. Updating a dosage-effect relationship for the prevalence of annoyance due to general transportation noise. *Journal of the Acoustical Society of America*, 89:221–233, 1991.
- [29] J.M. Fields. Railway noise and vibration annoyance in residential areas. *Journal of Sound and Vibration*, 66(3):445–458, 1979.
- [30] J.M. Fields and J.G. Walker. The response to railway noise in residential areas in Great Britain. *Journal of Sound and Vibration*, 85(2):177–255, 1982.
- [31] W. Flügge. *Viscoelasticity*. Blaisdell Publishing Co., 1967.
- [32] W. Flügge. *Stresses in Shells*. 2nd ed., Springer-Verlag, Berlin, 1973.
- [33] J. Forrest. *Modeling of ground vibration from underground railways*. PhD thesis, University of Cambridge, 1999.
- [34] J. Forrest and H. Hunt. Ground vibration generated by trains in underground tunnels. *Journal of Sound and Vibration*, 294(4-5):706–736, 2006.
- [35] J. Forrest and H. Hunt. A three-dimensional model for calculating of train-induced ground vibrations. *Journal of Sound and Vibration*, 294(4-5):678–705, 2006.
- [36] F. Frederich. Effect of track geometry on vehicle performance. *Zeitschrift für eisenbahnwesen und vekehrstechnik - Glasers auualen*, 108(12):355–362, 1984.
- [37] A. Galaitsis and E. Bender. Wheel/rail noise - Part V: measurement of wheel and rail roughness. *Journal of Sound and Vibration*, 46(3):437–451, 1976.

- [38] P. Galvin and J. Dominguez. Analysis of ground motion due to moving surface loads induced by high-speed trains. *Engineering analysis with boundary elements*, 31(11):931–941, 2007.
- [39] A. Gautesen. Scattering of a rayleigh wave by an elastic wedge whose angle is greater than 180 degrees. *Journal of Applied Mechanics*, 68:476–479, 2001.
- [40] A. Gautesen. Scattering of a rayleigh wave by an elastic quarter space - revisited. *Wave Motion*, 35:91–98, 2002.
- [41] A. Gautesen. On scattering of an SH-wave by a corner comprised of two different elastic materials. *Mechanics of Materials*, 35:407–414, 2003.
- [42] D.C. Gazis. Exact analysis of the plane-strain vibrations of thick-walled hollow cylinders. *Journal of the Acoustical Society of America*, 30(8):786–794, 1958.
- [43] D.C. Gazis. Three-dimensional investigation of the propagation of waves in hollow circular cylinders. i. analytical foundations. *Journal of the Acoustical Society of America*, 31(5):568–573, 1959.
- [44] A. Ghali and A. Neville. *Structural analysis: a unified classical and matrix approach*. E and FN Spon, 1997.
- [45] R. Ghanem and P. Spanos. *Stochastic Finite Elements - A Spectral Approach*. Springer-Verlag, New York, 1991.
- [46] D. Ghiocel and R. Ghanem. Stochastic finite-element analysis of seismic soil-structure interaction. *Journal of Engineering Mechanics*, 128(1):66–77, 2002.
- [47] K. Graff. *Wave motion in elastic solids*. Dover Publications, 1991.
- [48] R. Greer and C. Manning. Vibration isolation for railways. *Acoustics Bulletin*, 23(3):13–17, 1998.
- [49] B. Griefahn, A. Marks, and S. Robens. Noise emitted from road, rail and air traffic and their effects on sleep. *Journal of Sound and Vibration*, 295:129–140, 2006.
- [50] S. Gupta, M. Hussein, G. Degrande, H. Hunt, and Clouteau. A comparison of two numerical models for the prediction of vibrations from underground railway traffic. *Soil Dynamics and Earthquake Engineering*, 27(7):608–624, 2007.

- 
- [51] S. Gupta, W.F. Liu, G. Degrande, G. Lombaert, and W.N. Liu. Prediction of vibrations induced by underground railway traffic in beijing. *Journal of Sound and Vibration*, 310:608–630, 2008.
- [52] S. Gupta, Y. Stanus, G. Lombaert, and G. Degrande. Influence of tunnel and soil parameters on vibration from underground railways. *Journal of Sound and Vibration*, 327(1-2):70–91, 2009.
- [53] G. Hart and J. Collins. The treatment of randomness in finite element modelling. *SAE Shock and Vibration Symposium, Society of Automotive Engineers*, pages 2509–2519, October 1970.
- [54] N. Haskell. The dispersion of surface waves on multi-layered media. *Bulletin of the Seismological Society of America*, 43(1):17–34, 1953.
- [55] M. Heckl, G. Hauck, and R. Wettschureck. Structure-borne sound and vibration from rail traffic. *Journal of Sound and Vibration*, 193(1):175–184, 1996.
- [56] M. Huber, A. Moellmann, A. Bárdossy, and P. Vermeer. Contributions to probabilistic soil modelling. *Proceedings of the 7th International Probabilistic Workshop, Delft*, pages 1–12, 2009.
- [57] S. Hull and E. Kausel. Dynamic loads in layered halfspaces. *Engineering Mechanics in Civil Engineering, Proceedings of the 5th Engineering Mechanics Division Specialty Conference, University of Wyoming*, 1:201–204, 1984.
- [58] H. Hung and Y. Yang. A review of researches on ground-borne vibrations with emphasis on those induced by trains. *Proceedings of the National Science Council*, 25(1):1–16, 2001.
- [59] H. Hunt. *Measurement and modeling of traffic-induced vibration*. PhD thesis, University of Cambridge, 1988.
- [60] H. Hunt and M. Hussein. *Ground-borne vibration transmission from road and rail systems - prediction and control*. Chapter 117.a in Handbook of noise and vibration control. John Wiley & Sons, New York, 2008.
- [61] M. Hussein. *Vibration from underground railways*. PhD thesis, University of Cambridge, 2004.
- [62] M. Hussein, S. Gupta, H. Hunt, G. Degrande, and J. Talbot. An efficient model for calculating vibration from a railway tunnel embedded in a half space. *Proceedings*

- from the 13th International Congress of Sound and Vibration, Vienna, Austria, 2006.*
- [63] M. Hussein and H. Hunt. A numerical model for calculating vibration from a railway tunnel embedded in a full-space. *Journal of Sound and Vibration*, 305(3):401–431, 2007.
- [64] M. Hussein and H. Hunt. A numerical model for calculating vibration due to a harmonic moving load on a floating-slab tracks with discontinuous slabs in an underground railway tunnel. *Journal of Sound and Vibration*, 321(1-2):363–374, 2009.
- [65] British Standards Institution. Guide to evaluation of human exposure to vibration in buildings (1Hz-80Hz). BS 6472-1:2008.
- [66] British Standards Institution. Human response to vibration. Measuring instrumentation. BS EN ISO 8041:2005.
- [67] British Standards Institution. Mechanical vibration - ground-borne noise and vibration arising from rail systems - part 1: general guidance. BS ISO 14837-1:2005.
- [68] British Standards Institution. Mechanical vibration and shock. Evaluation of human exposure to whole-body vibration. Guidelines for the evaluation of the effects of vibration and rotational motion on passengers and crew comfort in fixed-guideway transport systems. BS ISO 2631-4:2001.
- [69] E. Its and T. Yanovskaya. Propagation of surface waves in a half-space with vertical, inclined or curved interfaces. *Wave Motion*, 7:79–94, 1985.
- [70] M. Jaksa, K. Yeong, K. Wong, and S. Lee. Horizontal spatial variability of elastic modulus in sand from the dilatometer. *The 9th Australia New Zealand Conference on Geomechanics, Auckland NZ*, 1:289–294, 2004.
- [71] C. Jones and J. Block. Prediction of ground vibration from freight trains. *Journal of Sound and Vibration*, 193(1):205–213, 1996.
- [72] M. Katou, T. Matsuoka, O. Yoshioka, Y. Sanada, and T. Miyoshi. Numerical simulation study of ground vibrations using forces from wheels of a running high-speed train. *Journal of Sound and Vibration*, 318:830–849, 2008.

- [73] E. Kausel. *Fundamental Solutions in Elastodynamics*. Cambridge University Press, 2006.
- [74] E. Kausel. An explicit solution for the green functions for dynamic loads in layered media. Department of Civil Engineering, MIT, R81-13, 1981.
- [75] E. Kausel and R. Peek. Dynamic loads in the interior of a layered stratum: an explicit solution. *Bulletin of the Seismological Society of America*, 72(5):1459–1481, 1982.
- [76] E. Kausel and J Roësset. Semianalytic hyperelement for layered strata. *Journal of the engineering mechanics division, ASCE*, 103(EM4):569–588, 1977.
- [77] E. Kausel and J. Roësset. Stiffness matrices for layered soils. *Bulletin of the Seismological Society of America*, 71(6):1743–1761, 1981.
- [78] E. Kausel and S. Seale. Static loads in layered halfspaces. *Journal of Applied Mechanics*, 54:403–408, 1987.
- [79] J. Kim, D. Kim, S. Kim, J. Won, and W. Moon. Monitoring of urban land surface subsidence using psinsar. *Geosciences Journal*, 11(1):59–73, 2007.
- [80] R. Klæboe, E. Öhrström, I. Turunen-Rise, H. Bendtsen, and H. Nykänen. Vibration in dwellings from road and rail traffic - Part III: towards a common methodology for socio-vibrational surveys. *Applied Acoustics*, 64:111–120, 2003.
- [81] R. Klæboe, I. Turunen-Rise, L. Hårvik, and C. Madshus. Vibration in dwellings from road and rail traffic - Part II: exposure-effect relationships based on ordinal logit and logistic regression models. *Applied Acoustics*, 64:89–109, 2003.
- [82] W. Knight. Satellites spot city subsidence. *New Scientist*, 13 March, 2002.
- [83] K. Komiya, K. Takiyama, and H. Akagi. Settlement behaviour of a shield tunnel constructed in subsiding reclaimed area. *Proceedings of geotechnical aspects of underground construction in soft ground*, 2006.
- [84] U.G. Köpke. Transverse vibration of buried pipelines due to internal excitation at a point. *Proceedings IMechE, Part E: Journal of Process Mechanical Engineering*, 207(E1):41–58, 1993.
- [85] N. Kovacevic, R. Mair, and D. Potts. Finite element analyses of ground movements from tunneling below southwark park. *Building Response to Tunnelling: Case Studies from Construction of the Jubilee Line Extension, London*, 1:185–194, 2001.

- 
- [86] S. Kramer. *Geotechnical earthquake engineering*. Prentice-Hall, New Jersey, 1996.
- [87] K. Kryter. Community annoyance from aircraft and ground vehicle noise. *Journal of the Acoustical Society of America*, 72:1212–1242, 1982.
- [88] H. Lamb. On the propagation of tremors over the surface of an elastic solid. *Philosophic Transactions of the Royal Society (London)*, 203(Series A):1–42, 1904.
- [89] R. Langley. On quasi-stationary approximations to non-stationary random vibration. *Journal of Sound and Vibration*, 113(2):365–375, 1987.
- [90] S. Liao and J. Li. A stochastic approach to site-response component in seismic ground motion coherency model. *Soil Dynamics and Earthquake Engineering*, 22(9-12):813–820, 2002.
- [91] K. Lo. *Measurement and modeling of vibration transmission through piled foundations*. PhD thesis, University of Cambridge, 1994.
- [92] M. Loeve. *Probability Theory*. Springer-Verlag, New York, 1977.
- [93] G. Lombaert and G. Degrande. Ground-borne vibration due to static and dynamic axle loads of intercity and high-speed trains. *Journal of Sound and Vibration*, 319:1036–1066, 2009.
- [94] G. Lombaert, G. Degrande, J. Kognut, and S. François. The experimental validation of a numerical model for the prediction of railway induced vibrations. *Journal of Sound and Vibration*, 297:512–535, 2006.
- [95] J. Lysmer. Lumped mass method for rayleigh waves. *Bulletin of the Seismological Society of America*, 60(1):89–104, 1970.
- [96] J. Lysmer and L. Drake. The propagation of Love waves across nonhorizontally layered structures. *Bulletin of the Seismological Society of America*, 61(5):1233–1251, 1971.
- [97] J. Lysmer and R. Kuhlemeyer. Finite dynamic model for infinite media. *Journal of the engineering mechanics division, ASCE*, 95(EM4):859–877, 1969.
- [98] J. Lysmer and G. Waas. Shear waves in plane infinite structures. *Journal of the Engineering Mechanics Division, ASCE*, 98(EM1):85–105, 1972.

- 
- [99] R. Mair and R. Taylor. Elizabeth house: settlement predictions. *Building Response to Tunnelling: Case Studies from Construction of the Jubilee Line Extension, London*, 1:195–215, 2001.
- [100] G. Manolis and D. Beskos. *Boundary Element Methods in Elastodynamics*. Unwin Hyman, London, 1988.
- [101] H. Miedema and C. Oudshoorn. Annoyance from transportation noise: relationships with exposure metrics NDL and DENL and their confidence intervals. *Environmental Health Perspectives*, 109:409–416, 2001.
- [102] H. Miedema and H. Vos. Exposure-response relationships for transportation noise. *Journal of the Acoustical Society of America*, 104(6):3432–3445, 1998.
- [103] G. Miller and H. Pursey. On the partition of energy between elastic waves in a semi-infinite solid. *Proceedings of the Royal Society (London)*, 233(Series A):55–69, 1955.
- [104] P. Morse and H. Feshbach. *Methods of Theoretical Physics*. McGraw-Hill, New York, 1953.
- [105] S. Nakagiri and T. Hisada. Stochastic finite element method applied to structural analysis with uncertain parameters. *Proceedings for the International Conference on the Finite Element Method*, pages 206–211, August, 1982.
- [106] D. Newland. *An introduction to random vibrations, spectral and wavelet analysis*. Longman, Harlow, Essex, England, 1993.
- [107] S. Ng. *Transmission of ground-borne vibration from surface railway trains*. PhD thesis, University of Cambridge, 1995.
- [108] J. Nielsen and A. Igeland. Vertical dynamic interaction between train and track - influence of wheel and track imperfections. *Journal of Sound and Vibration*, 187(5):825–839, 1995.
- [109] A. Nour, A. Slimani, N. Laouami, and H. Afra. Finite element model for the probabilistic seismic response of heterogeneous soil profile. *Soil Dynamics and Earthquake Engineering*, 23(5):331–348, 2003.
- [110] R. Nyren, J. Standing, and J. Burland. Surface displacements at st. james’s park greenfield reference site above twin tunnels through the london clay. *Building Response to Tunnelling: Case Studies from Construction of the Jubilee Line Extension, London*, 2:387–400, 2001.

- 
- [111] E. Öhrström. Effects of exposure to railway noise - a comparison between areas with and without vibration. *Journal of Sound and Vibration*, 205(4):555–560, 1997.
- [112] E. Öhrström, L. Barregård, E. Andersson, and A. Skånberg. Annoyance due to single and combined sound exposure from railway and road traffic. *Journal of the Acoustical Society of America*, 122(5):2642–2652, 2007.
- [113] M. O’Reilly and B. New. Settlements above tunnels in the united kingdom - their magnitude and prediction. *Tunneling ’82, Institution of Mining and Metallurgy, London*, 1982.
- [114] I. Parcharidis, E. Lagios, and V. Sakkas. Subsidence monitoring within the athens basin (greece) using space radar interferometric techniques. *Earth Planets Space*, 58:505–513, 2006.
- [115] J. Park and E. Kausel. Impulse response of elastic half-space in the wave number-time domain. *Journal of Engineering Mechanics*, 130(10):1211–1222, 2004.
- [116] S. Park. *Methods for the numerical analysis of wave motion in unbounded media*. PhD thesis, University of Texas at Austin, 2000.
- [117] R. Peck. Deep excavations and tunneling in soft ground. *Proceedings of the 7th International Conference on Soil Mechanics and Foundation Engineering, Mexico*, 1969.
- [118] K. Phoon and F. Kulhawy. Characterization of geotechnical variability. *Canadian Geotechnical Journal*, 36:612–624, 1999.
- [119] K. Phoon and F. Kulhawy. Evaluation of geotechnical property variability. *Canadian Geotechnical Journal*, 36:625–639, 1999.
- [120] Lord Rayleigh. On waves propagated along the plane surface of an elastic solid. *Proceedings of the London Mathematical Society*, 17:4–11, 1885.
- [121] P. Remington. Wheel/rail noise - Part I: characterization of the wheel/rail dynamic system. *Journal of Sound and Vibration*, 46(3):359–379, 1976.
- [122] P. Remington. Wheel/rail noise - Part IV: rolling noise. *Journal of Sound and Vibration*, 46(3):419–436, 1976.
- [123] G. Rennie. Monitoring earth’s subsurface from space. *Science and technology review*, April:4–11, 2005.

- 
- [124] F. Rizzo and D. Shippy. An application of the correspondence principle of linear viscoelasticity theory. *SIAM Journal on Applied Mathematics*, 21(2):321–330, 1971.
- [125] S. Rokhlin and L. Wang. Stable recursive algorithm for elastic wave propagation in layered anisotropic media: stiffness matrix method. *Journal of the Acoustical Society of America*, 112(3):822–834, 2002.
- [126] M. Rudd. Wheel/rail noise - Part II: wheel squeal. *Journal of Sound and Vibration*, 46(3):381–394, 1976.
- [127] M. Schevenels, G. Lombaert, G. Degrande, D. Degrauwe, and B. Schoors. The green’s functions of a vertically inhomogeneous soil with a random dynamic shear modulus. *Probabilistic Engineering Mechanics*, 22:100–111, 2007.
- [128] J. Schlue. Finite element matrices for seismic surface waves in three-dimensional structures. *Bulletin of the Seismological Society of America*, 69(5):1425–1437, 1979.
- [129] T. Schultz. Synthesis of social surveys on noise annoyance. *Journal of the Acoustical Society of America*, 64:377–405, 1978.
- [130] C. Seo, C. Yun, and J. Kim. Three-dimensional frequency-dependent infinite elements for soil-structure interaction. *Engineering Structures*, 29:3106–3120, 2007.
- [131] X. Sheng, C. Jones, and D. Thompson. A comparison of a theoretical model for quasi-statically and dynamically induced environmental vibration from trains with measurements. *Journal of Sound and Vibration*, 267(3):621–635, 2003.
- [132] X. Sheng, C. Jones, and D. Thompson. Prediction of ground vibration from trains using the wavenumber finite and boundary element methods. *Journal of Sound and Vibration*, 293:575–586, 2006.
- [133] M. Shinozuka and J. Astill. Random eigenvalue problems in structural analysis. *American Institute of Aeronautics and Astronautics Journal*, 10(4):456–462, 1972.
- [134] M. Shinozuka and E. Lenoe. A probabilistic model for spatial distribution of material properties. *Engineering Fracture Mechanics*, 8(1):217–227, 1976.
- [135] P. Smithson, K. Addison, and K. Atkinson. *Fundamentals of The Physical Environment*. Routledge, London, 2002.

- 
- [136] M. Soulié, P. Montes, and V. Silvestri. Modeling spatial variability of soil parameters. *Canadian Geotechnical Journal*, 27:617–630, 1990.
- [137] P. Spanos and R. Ghanem. Stochastic finite element expansion for random media. *Journal of Engineering Mechanics ASCE*, 115(5):1035–1053, 1989.
- [138] A. Stamos and D. Beskos. 3D seismic response analysis of long lined tunnels in half-space. *Soil Dynamics and Earthquake Engineering*, 15(2):111–118, 1996.
- [139] A. Tadeu and J. António. Green’s function for 2.5d elastodynamic problems in a free solid layer formation. *Engineering Structures*, 24:491–499, 2002.
- [140] A. Tadeu, J. António, and L. Godinho. Green’s function for two-and-a-half-dimensional elastodynamic problems in a half-space. *Computational Mechanics*, 27:484–491, 2001.
- [141] A. Tadeu and E. Kausel. Green’s functions for two-and-a-half-dimensional elastodynamic problems. *Journal of Engineering Mechanics ASCE*, 126(10):1093–1097, 2000.
- [142] J. Talbot. *On the performance of base-isolated buildings: A generic model*. PhD thesis, University of Cambridge, 2001.
- [143] R. Taylor. *Groundborne noise from the operating railway*. A consultant report to Grand Central Studios regarding CROSSRAIL *not in the public domain*, February, 2007.
- [144] D. Thompson. *Wheel/rail noise - theoretical modelling of the generation of vibrations*. PhD thesis, University of Southampton, 1990.
- [145] D. Thompson, B. Hemsworth, and N. Vincent. Experimental validation of the TWINS prediction program for rolling noise, Part I: description of the model and method. *Journal of Sound and Vibration*, 193:123–135, 1996.
- [146] D. Thompson and C. Jones. A review of the modelling of wheel/rail noise generation. *Journal of Sound and Vibration*, 231(3):519–536, 2000.
- [147] W. Thomson. Transmission of elastic waves through a stratified soil medium. *Journal of Applied Physics*, 21:89–93, 1950.
- [148] S. Timoshenko and J.N. Goodier. *Theory of Elasticity*. 3rd ed., McGraw-Hill, New York, 1970.

- [149] I. Turunen-Rise, A. Brekke, L. Hårvik, C. Madshus, and R. Klæboe. Vibration in dwellings from road and rail traffic - Part I: a new Norwegian measurement standard and classification system. *Applied Acoustics*, 64:71–87, 2003.
- [150] E. Vanmarcke. Probabilistic modeling of soil profiles. *Journal of the Geotechnical Engineering Division ASCE*, 103(GT11):1227–1246, 1977.
- [151] E. Vanmarcke. *Random Fields*. The MIT Press, Massachusetts, 1983.
- [152] E. Vanmarcke and M. Grigoriu. Stochastic finite element analysis of simple beams. *Journal of the Geotechnical Engineering Division ASCE*, 109(5):1203–1214, 1983.
- [153] I. Vér, C. Ventres, and M. Myles. Wheel/rail noise - Part III: impact noise generation by wheel and rail discontinuities. *Journal of Sound and Vibration*, 46(3):395–417, 1976.
- [154] A.S. Volmir. *Nonlinear Dynamics of Plates and Shells*. Nauka, Moscow (in Russian), 1972.
- [155] G. Waas. *Linear two-dimensional analysis of soil dynamics problems in semi-infinite layered media*. PhD thesis, Engineering, University of California Berkeley, 1972.
- [156] J. Walker and M. Chan. Human response to structurally radiated noise due to underground railway operations. *Journal of Sound and Vibration*, 193(1):49–63, 1996.
- [157] W. White, S. Valliappan, and I. Lee. Unified boundary for finite dynamic models. *Journal of the Engineering Mechanics Division, ASCE*, 103(EM5):949–964, 1977.
- [158] J. Wolf. *Foundation vibration analysis using simple physical models*. Prentice-Hall, 1994.
- [159] J. Wolf and G. Darbe. Dynamic-stiffness matrix of soil by the boundary-element method: embedded foundation. *Earthquake Engineering and Structural Dynamics*, 12(3):401–416, 1984.
- [160] R. Woods. Screening of surface waves in soils. *Journal of the Soil Mechanics and Foundations Division ASCE*, SM4:951–979, 1968.
- [161] F. Yamazaki, M. Shinozuka, and G. Dasgupta. Neumann expansion for stochastic finite element analysis. *Journal of Engineering Mechanics*, 114(8):1335–1354, 1988.

- 
- [162] J. Yau. Response of a train moving on multi-span railway bridges undergoing ground settlement. *Engineering Structures*, 31:2115–2122, 2009.
- [163] C. Yeh and M. Rahman. Stochastic finite element methods for the seismic response of soils. *International Journal for Numerical and Analytical Methods in Geomechanics*, 22(10):819–850, 1998.